

Dissertation

Particle Accumulation in Incompressible Laminar Flows due to Particle-Boundary Interaction

ausgeführt zum Zwecke der Erlangung des akademischen Grades des
Doktors der technischen Wissenschaften (PhD)
unter der Leitung von

Univ.Prof. Dipl.-Phys. Dr.rer.nat. Hendrik C. Kuhlmann
Institutsnummer E322
Institut für Strömungsmechanik und Wärmeübertragung

eingereicht an der Technischen Universität Wien

Fakultät für Maschinenwesen und Betriebswissenschaften

von

MSc Francesco Romanò
Matrikelnummer 1228694
Pachmanngasse 17-21/4/19, 1140 Wien



Wien, 27. September 2016

Abstract

The accumulation of particles in laminar incompressible fluid flows is investigated. Boundary-driven closed systems are considered. We deal with a thermocapillary liquid bridge, a lid-driven cavity and a partially liquid-filled rotating drum. In all three the configurations we consider flows after the onset of a steady three-dimensional instability. The corresponding fluid dynamics systems are equivalent to a Hamiltonian system of 1.5 degrees of freedom and we consider flow parameters for which chaotic and regular regions coexist. Owing to the boundary-driving mechanism, the quasi-periodic streamlines (Kolmogorov-Arnold-Moser or KAM tori) are mainly located near the moving wall or the free-surface.

Finite-size particles with small Stokes numbers are introduced in these fluid flow systems to study the so-called particle accumulation structures (PAS). In the following we extend the classical framework of investigation of PAS, passing from thermocapillary to boundary-driven flows. We further aim at clarifying the fundamental mechanism PAS is based on, regardless of the specific system in which it is considered. The main flow features basically required in these set-ups are KAM tori located near the boundaries and particles of finite-size. The particles which move close to a wall or a free-surface may be transferred from the chaotic to the regular regions of the flow because of the repulsion exerted by the boundaries. The particle-boundary interaction represents the main dissipative mechanism responsible for the formation of PAS.

For simulating particles moving close to the driving boundaries we employ fully-resolved simulations produced via a discontinuous Galerkin finite element method (DG-FEM) in combination with the smoothed profile method (SPM). The simulations aim at clarifying the dependence of the lubrication gap width on particle size and density ratio after that a single particle is trapped (within a certain tolerance) in 2-D PAS. To this end, small particles in a shear-stress- and a lid-driven cavity are investigated. The fully-resolved simulation results are employed to improve an existing particle-boundary interaction (PSI) model. A one-way coupling approach which includes such an improved PSI model is used to simulate two- and three-dimensional particle-laden flows. A comparison of the numerically predicted PAS with experimental data is finally made to confirm the numerical results.

All the main phenomenological explanations given for understanding PAS will be commented and discussed in details. Our principal aim is to show that the strong correlation between particle accumulation structures and flow topology, together with the particle-boundary interaction dissipative effect, provides a universal mechanism for explaining PAS for all set-ups investigated.

alla mia famiglia ed a nonno Francesco
che quest'anno avrebbe compiuto cento anni

Acknowledgements

At first I would like to thank my PhD advisor Prof. Hendrik C. Kuhlmann for his support during these four years. I want to thank Hendrik in particular for having always been available for discussions and capable to inspire interesting and passionate conversations. Before joining his group I could not even imagine a so open and direct relation.

I would like to thank the reviewers of this thesis, Prof. Cristian Marchioli and Prof. Eckart Meiburg, for the attention they dedicated to it. Their helpful feedbacks and insightful comments helped me in improving this work.

Beside them I would like to thank the guys of my research group and, in particular, Behnaz and Saeed, who became good friends of mine in these four years. Their support was definitely precious during this time.

More in general, I would like to thank the persons of the Institute of Fluid Mechanics and Heat Transfer, TU Wien. Thanks to them it was so easy to integrate in a completely new surrounding and a special mention in this regards goes to Kathy.

Then, I want to thank the new and old friends who always supported me in these four years and, finally, I owe a special thank to my family for having been so close and for the precious care they gave me.

Contents

1. Introduction	1
1.1. Particle Accumulation Phenomena	1
1.2. Motivation	3
1.3. State of the Art of Particle Accumulation Structures	4
1.4. Thesis Outline	6
2. Problem Formulation	7
2.1. Liquid Bridge	7
2.2. Lid-Driven Cavity	9
2.3. Partially Liquid-Filled Rotating Drum	10
2.4. Particle Modelling	11
3. Numerical Method	15
3.1. h/p Discretization Methods	15
3.2. Evolution of Discontinuous Galerkin Finite-Element Method	16
3.3. Discrete Incompressible Navier–Stokes Equations	17
3.3.1. Temporal Discretization	18
3.3.2. Spatial Discretization	19
3.4. Methods for Particle-Laden Flows	21
3.5. Smoothed Profile Method	24
4. Particle–Boundary and Particle–Particle Interaction	29
4.1. Particle–Boundary Interaction	29
4.1.1. Particle–Surface Interaction Model	30
4.2. Particle–Free-Surface Interaction	31
4.2.1. Fully-Resolved Simulations	32
4.2.2. Comparison of One-Way Coupling and Fully-Resolved Simulations	38
4.3. Particle–Wall Interaction	40
4.3.1. Fully-Resolved Simulations	43
4.3.2. Comparison of One-Way Coupling and Fully-Resolved Simulations	49
4.4. Particle–Particle Interaction	49
4.4.1. Analysis Concepts for the Particle–Particle Interaction	49
4.4.2. Multiple-Particle Simulations	52
4.4.3. Results	53
4.4.4. Conceptual Extension to Three-Dimensions	58
5. Topology and Particle Accumulation Structures	61
5.1. Different Interpretations of Particle Accumulation Structures	61
5.1.1. Phenomenological Explanation of Particle Accumulation Structures	62
5.2. Liquid Bridge	63
5.2.1. Axisymmetric Liquid Bridge	64
5.2.2. Three-dimensional Liquid Bridge	69

5.3. Lid-Driven Cavity	79
5.3.1. Main Topological Elements	82
5.3.2. Regular and Chaotic Regions	85
5.3.3. Particle Accumulation Structures	87
5.3.4. Preliminary Comparison between Experiments and Simulations	94
5.4. Partially Liquid-Filled Rotating Drum	105
5.4.1. Main Topological Elements	106
5.4.2. Regular and Chaotic Regions	106
5.4.3. Particle Accumulation Structures	109
6. Summary and Conclusions	121
A. From Prototypical to Physical Domains	125
A.1. Transfinite Interpolation	125
A.2. Lattice generators	126
A.3. 2-D transfinite Lagrange interpolation	128
A.3.1. Edge Parametrization	128
A.3.2. Quadrilateral Mapping	129
A.3.3. Triangular Mapping	130
A.3.4. 2-D Mapping Benchmarks	131
A.4. 3-D Transfinite Lagrange Interpolation	131
A.4.1. Edge Parametrization	133
A.4.2. Hexahedral Mapping	133
A.4.3. Tetrahedral Mapping	135
A.4.4. 3-D mapping benchmarks	136
A.5. Distribution of Nodes	137
A.5.1. Quadrature Nodes	137
A.5.2. Interpolation Nodes	140
B. Numerical Solver: Benchmarks	143
B.1. Fluid Flow Benchmarks	143
B.1.1. Taylor–Green vortex	143
B.1.2. Von Kármán street	144
B.1.3. Lid-Driven Cavity	146
B.1.4. Thermocapillary-Driven Cavity	146
B.2. Multiphase Flow Benchmarks	151
B.2.1. Static Cylinder in a Channel Flow	151
B.2.2. Circular Cylinder Harmonically In-Line Oscillating	157
B.2.3. Circular Cylinder Harmonically Oscillatory Rotating	159
B.2.4. Cylinder Falling in a Channel	161
B.2.5. Cylinder Settling in a Bounded Geometry	163
B.2.6. Calibration of a Hot-Wire Probe	165
B.2.7. Heat Exchanger	167
C. One-Way Coupling Simulations	169
C.1. Fluid Flow Discretization	169
C.2. Verification of the Numerical Solver	170

1. Introduction

In this chapter the physical phenomenon of interest for the present thesis is introduced and discussed. A detailed overview on particle accumulation structures (PAS) is given, pointing out the different mechanisms which may lead to particle clustering. Thereafter we briefly present the theoretical background needed to understand PAS.

Experimental and numerical observations of particle accumulation in a liquid bridge are reported. The phenomenological interpretations proposed in literature for explaining PAS phenomena are presented and discussed, together with the motivations at the core of this thesis. Finally an outline of this dissertation is given.

1.1. Particle Accumulation Phenomena

Particle-laden flows are a class of multiphase flows in which an immiscible dispersed particulate phase is embedded in a continuous fluid phase. They occur in many industrial processes like steel making [260], biological applications [177] and combustion processes [63] as well as in natural phenomena such as volcanic ash flows, sand storms, debris flows [86]. It is therefore of crucial importance a deep understanding and an accurate prediction of the key phenomena which arise in this framework. Based on these reasons, particle-laden flows is a flourishing field of theoretical, experimental and computational fluid dynamics research.

In the following we will focus on particle accumulation phenomena observed in incompressible laminar flows. Various authors have considered such a matter, paying attention to the effect of inertia with respect to the temporal evolution of the particle distribution (see e.g. [6, 7, 112]) and investigating the accumulation pattern in correlation with chaotic and regular regions of the flow [41, 250, 288]. As we will see in the following, the direct correlation between particle clustering regions and the topology of the flow field is one of the key elements for understanding PAS phenomena. However, differently from the aforementioned investigations, inertia is playing a secondary role in the mechanisms we will investigate.

A fundamental step for understanding particle clustering in incompressible fluid flow systems consists in identifying the main source of dissipation for the particulate-phase system. Our focus will be on particle accumulation in steady three-dimensional flows and, under these conditions, the fluid dynamic system is equivalent to a Hamiltonian system of 1.5 degrees of freedom [12]. Owing to the solenoidal constraint, the Liouville's theorem states that the phase space volumes are conserved in the Hamiltonian system represented by the fluid flow. This implies that accumulation phenomena cannot be produced by simple advection of the particles with the flow, but there must be a dissipative mechanism which leads to particle clustering. In general, particle inertia, buoyancy effects and other dissipative mechanisms may lead to accumulation. In our case, among these dissipation sources, a dominant role is played by the particle–boundary interaction.

In the following we will deal with the so-called *particle accumulation structures*. They have been reported for the first time by Schwabe et al. [255], where an unexpected particle clustering

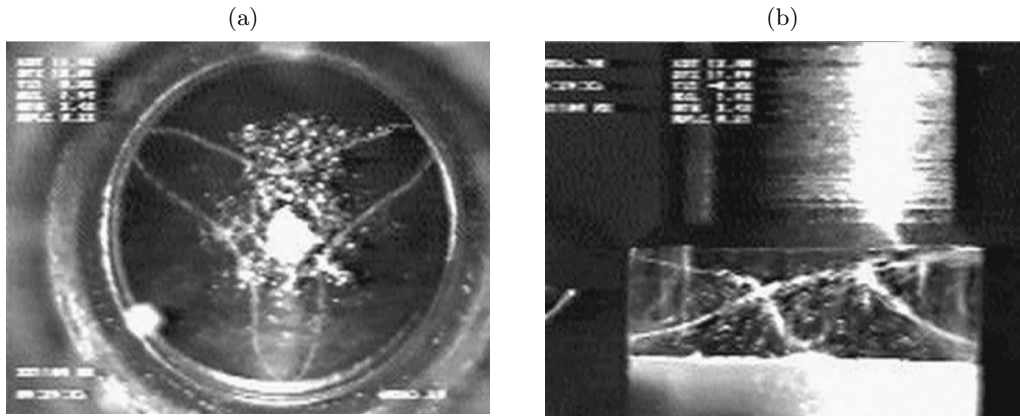


Figure 1.1.: Experimental evidence of particle accumulation structures reported in [256] under microgravity conditions. The snapshots represent top- (a) and side-view (b) of a thermocapillary liquid bridge seeded with particles. The tracers arranged themselves in a line-like pattern rotating with the hydrothermal wave occurring in the fluid flow.

is experimentally observed for very small Stokes numbers in a liquid bridge

$$\text{St} = \frac{2a_p^2}{9R^2}\varrho = \mathcal{O}(10^{-5}), \quad \varrho = \frac{\rho_p}{\rho_f} = \mathcal{O}(1), \quad (1.1)$$

where ρ_p and a_p are density and radius of the employed spherical particles, ρ_f and R denote the fluid density and the liquid bridge radius. It is significant that such a phenomenon is reported for “tracer particles” which, in other words, are particles supposed to almost perfectly follow the flow. As said, a perfect tracer cannot accumulate in non-dissipative flows and this explains the surprise of the authors in observing particle clustering in the liquid bridge. In the spirit of such an observation, we will keep on referring to small particles which accumulate on PAS as *tracers*.

Figure 1.1 depicts the top- and side-view of a liquid bridge heated from above where initially randomly distributed particles arranged themselves in a ordered line-like pattern [258]. This particle clustering phenomenon is known as PAS since the work of Schwabe et al. [255] and is attracting increasing interest of many authors who experimentally and numerically observe and investigate it (see e.g. [255, 254, 270, 258, 228, 126, 194, 190, 195, 197, 104, 102]).

Different patterns have been reported in dependence on the main non-dimensional groups of interest in the liquid bridge set-up. Among the main features highlighted by Schwabe et al. is the rapid de-mixing of initially randomly suspended particles which organize in tubular structures or closed threads after few convective time units. Moreover, almost all the particles present in the fluid are attracted to the periodic or quasi-periodic orbit without sensible changing of the shape of PAS due to particle–particle interaction. This may lead to speculate that the particle accumulation is, with good approximation, a single-particle phenomenon. Such a hypothesis is commonly exploited in the numerical prediction of PAS, where tracers are usually modeled as point-wise particles using a one-way coupled approach.

Two other aspects are still to be mentioned. First of all the peculiar feature of thermocapillary [152] flows produced by the shear stress driving along the liquid–gas interface. Owing to it, the highest velocities of the flow are reached at the interface and the resulting streamline crowding transports many particles very close to the free-surface. For this reason, understanding

PAS requires to take into account the role of particle–free-surface interactions (see [126, 194]) even though small particle volume fractions and very low Stokes numbers are involved in the phenomenon.

Moreover, the finite size of the particle is negligible when the tracer moves in a region far away from the boundaries, but essential when it moves very close to the free-surface. Indeed, the lubrication forces exerted from the boundary on the finite-size tracer produce a sensible change of the whole trajectory if compared to a zero-size particle one. Hence, an accurate prediction of the particle accumulation structures requires a thorough description of the particle–boundary interaction.

We anticipate that in this accumulation phenomenon inertial effects play a minor role [197]. Neglecting the particle–free-surface interaction in the numerical simulation of PAS produces unrealistic predictions (see [195]) and even a simply advected tracer whose motion near the free-surface is modeled via a dedicated theoretical particle–boundary interaction approach can qualitatively well reproduce experimental results [194]. However, as pointed out by Mukin & Kuhlmann [194], for an accurate prediction of particle accumulation structures, it is necessary to take into account the minimum lubrication gap width between the free-surface and the particle trapped in the periodic- or quasi-periodic attractor.

1.2. Motivation

Even though particle accumulation phenomena in a liquid bridge have been extensively demonstrated experimentally or reproduced numerically for more than two decades, the theoretical mechanisms which dominate the phenomenon are still subject of discussion. Aim of this work is to clarify the physical mechanism which produces the accumulation structures discussing and criticizing most of the theoretical explanations proposed so far. Summarizing some of the interpretations, among the proposed theories: the gathering effect of the cold corner on the free-surface [258], a resonance phenomenon combined with a Bernoulli-effect [255], the interaction between vorticity-waves and PAS [160], a particle-flow synchronization [228, 190] and the repeated interaction between particles and free-surface in combination with regular and chaotic regions of the flow topology [126, 194].

Apart from the last one, all the reported interpretations have been inferred from experimental or numerical observation and never rigorously demonstrated. We will provide other proofs in support of the theory of Kuhlmann et al. [126, 194] showing that this represents a phenomenological explanation of PAS universally valid for all the set-ups we investigate. The strong correlation between flow topology and particle accumulation structures will be further proven comparing PAS and regular regions for the flow. Apart from the liquid bridge, a two-sided antiparallel lid-driven cavity and a partially liquid-filled rotating drum are considered. These mechanically-driven systems are chosen on purpose to demonstrate PAS in the absence of a contracting-expanding free-surface and characteristic frequencies of the traveling wave instability. This way we aim at showing that the theoretical explanations of Schwabe et al. [258, 255], Pushkin & Melnikov et al. [228, 190], respectively, do not provide a universal argument for interpreting PAS in all the set-ups in which it is observed. Vice versa, the streamline crowding in proximity of the driving boundaries induces repeated particle–free-surface/wall interactions in all the considered systems. Moreover, considering the particle–boundary interaction as the main dissipative effect the numerical time is consistent with the experimental PAS formation time.

Thereafter, we aim at quantitatively compare numerical and experimental results both, in case of liquid-bridge and lid-driven-cavity flows. For the first time, an experimental observation

of PAS will be reported in set-ups different from the liquid bridge. To the best of the author's knowledge, this is the first time that a systematic comparison will be presented in terms of objective and reliably measurable quantities.

To that end we will determine a functional dependence of the minimum lubrication gap width between particle and free-surface/wall after that the particle has been trapped by the periodic attractor (within a certain tolerance). Parameters of the investigation will be the particle radius and the particle-to-fluid density ratio. Such a result will be used for numerically predicting PAS. Furthermore, it may guide future experiments estimating the window of particle radii to employ for observing particle accumulation. Moreover, ad-hoc cases will be selected to show that an accurate prediction of the lubrication gap may be essential even for a simple qualitative prediction of the particle accumulation experimentally observed in a liquid bridge.

Finally, the role of particle–particle interactions will be investigated comparing single-particle attractors with multiple particle accumulation. We aim at understanding if mutual particle interactions may induce loss of particles from an established particle accumulation structure.

1.3. State of the Art of Particle Accumulation Structures

Since the pioneering work of Schwabe et al. [255], PAS phenomena in a liquid bridge have triggered a series of experimental and numerical investigations aiming at understanding and giving a physical explanation of it. The first experimental evidence of PAS considered subcritical regimes for the liquid bridge under which the flow is steady and axisymmetric. Under these conditions particles heavier than the fluid tend to accumulate on toroidal structures very close to the free-surface. Very similar particle accumulation structures have been reported for different combinations of particle radii and particle-to-fluid density ratios (abstract of [255]).

PAS has been also found in case of supercritical conditions when the fluid flow instability arises in the form of a hydrothermal wave (see e.g. [266, 202, 291, 251, 167] for details about the fluid flow configuration after the onset of such instability). The shape of the periodic or quasi-periodic attractor is different from the subcritical case and the particles seem to cluster along line-like structures rotating with the same angular velocity of the hydrothermal wave. The accumulation structure winds m times around the thermocapillary vortex core, where m represents the azimuthal wave number of the hydrothermal wave [254]. Different forms of PAS are reported in dependence on the liquid bridge aspect ratio and the other non-dimensional groups of interest for the fluid flow. Figure 1.2 depicts two examples of periodic attractors for mode 2 (a) and mode 3 (b).

Owing to the limited hydrostatic stability, only small liquid bridges can be realized on the ground. Based on this reason, particle accumulation structures have been further investigated under microgravity conditions scaling up the typical length of a liquid bridge under normal gravity conditions (mm) to the orders of centimeters. Under weightlessness conditions (see fig. 1.1) it has been shown that particle accumulation structures may arise (see [256]), which proves that buoyancy effects are not necessary for the occurrence of such a phenomenon. During these experiences conducted under the MAXUS 6 flight, it was also found that the optimum parameters (i.e. aspect ratio, Reynolds numbers, particle radius) for observing PAS differ slightly between weightlessness and ground conditions.

Apart from the aforementioned studies conducted using a NaNO_3 liquid bridge, other experimental investigations using liquid bridges made out of silicone oil [280, 270, 1, 279, 2, 206, 103, 104] further enriched the patterns of observed accumulation structures varying the Prandtl number of the fluid and classifying existence regimes for the so-called SL-I- and SL-II-PAS.

Other periodic attractors are found in [258], where the authors report the PAS formation time

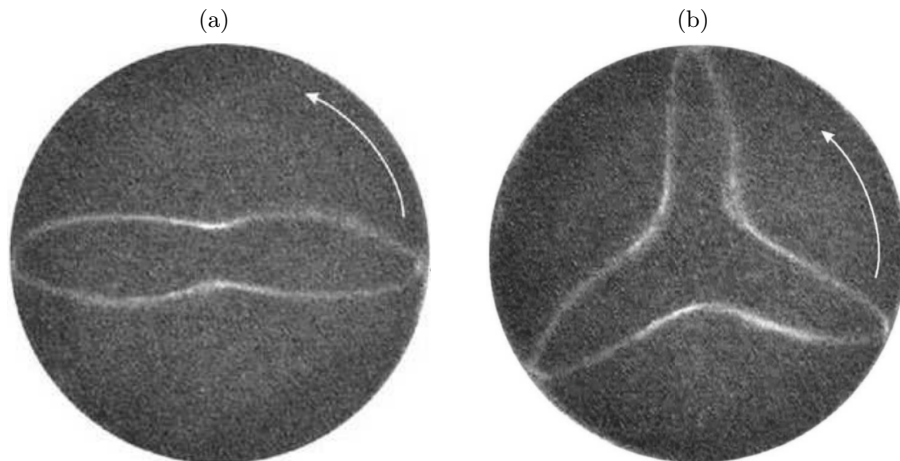


Figure 1.2.: Particle accumulation structures in a liquid bridge beyond the onset of a hydrothermal wave instability. The azimuthal wave numbers are $m = 2$ (a) and $m = 3$ (b) and the arrows depict the sense of rotation of the hydrothermal wave (and consequently of the particle accumulation structures). The two snapshots are reported in [254].

and suggest it as a fundamental quantity of interest for identifying the dominant mechanism responsible for PAS. A precise definition of the PAS formation time τ is currently matter of discussion and was defined by Schwabe et al. as “the time elapsed between a homogenization of the particle distribution and the moment when PAS can be recognized again by the observer”. This definition is certainly subjective, but may lead to estimate an order of magnitude of the clustering phenomenon formation time. In fact, the different accumulation mechanisms (inertia, particle–boundary interaction, etc...) sensibly differ in the time required to produce PAS and in the accumulation structures they produce [197]. Therefore an estimate of τ can be used to reliably identify the dominant effects from the secondary ones. In [258] it was also experimentally reported that the PAS formation time is function of the particle diameter and the particle density.

Moreover, experimental reconstruction of single-particle trajectories are reported in [270, 258, 279, 206, 104], which show how single particles follow the accumulation pattern, but travel with much slower azimuthal velocity than the phase velocity of the hydrothermal wave.

Once again we point out that the experimental evidence demonstrates that the shape of the accumulation pattern does not depend on the number of particles suspended in the liquid bridge. This observation may suggest that particle–particle interaction does not play an important role in determining PAS. However, as reported in [258], a transfer of particles from the line-like PAS to the bulk region of the flow has been observed. They proposed sedimentation and other causes to explain it, but the relevance of particle–particle interactions in the stability of PAS is still to be clarified.

Apart from experimental studies, the first attempts to numerically model particle accumulation structures are due to Domesi [69, 70]. He highlighted the strong deviation between zero-size and finite-size particle trajectories moving very close to the free-surface and suggested it as cause of the particle accumulation. This idea has been further developed in a more systematic manner by Hofmann & Kuhlmann [126]. These authors proved that particle–free-surface interactions can actually lead to an attracting periodic orbit for particle motion. Further improvements of this theory are proposed in [194], where the crucial role of coexisting chaotic and regular streamlines is pointed out. Moreover Mukin & Kuhlmann [194] highlighted the importance of estimating

the minimum lubrication gap width between particles and free-surface (after that particles accumulated along the periodic orbit) for a quantitatively accurate numerical prediction of the accumulation phenomenon.

Other numerical investigations included inertial effects for reproducing PAS either in a liquid bridge flow [190] or in an ad-hoc analytical model flow [228]. In both these papers a phenomenon of synchronization between particles and fluid flow is proposed as cause of PAS speculating the frequency lock-in between PAS and hydrothermal wave frequency. However, inertial effects involve much slower accumulation dynamics if compared to the experimental formation time [154, 149, 197]. Moreover Kuhlmann & Muldoon [153, 156] have brought to the discussion robust arguments against the interpretation of particle accumulation as result of a lock-in phenomenon. Their objections are based on the fact that synchronization may occur between two weakly-coupled systems [226], whereas the particle dynamical system is definitely driven by the fluid flow for the typically small Stokes numbers involved in the experiments. In this case the particle structures are moving in synchronous motion with the fluid flow, but do not induce frequency lock-in.

Still to be mentioned is another interpretation of PAS inferred in his numerical study by Lappa in [160]. He proposed the interaction between vorticity-waves as cause of PAS formation noticing that the particle attractors lie on axial vorticity isosurfaces. He also found particle accumulation in liquid bridges under standing wave instability [163], g-jitter conditions [162] and Rayleigh-Bénard convection [161]. These results are at least questionable due to the first-order scheme used for the time integration which, by itself, may produce PAS by accumulation of numerical errors. Moreover in the papers of Lappa it is not reported the strange implementation of the PSI model he employs (see [197]).

1.4. Thesis Outline

The present thesis is organized as follows.

Chapter 2 gathers the problem formulations for the three-dimensional flow configurations in which PAS is investigated: a liquid bridge, an antiparallel lid-driven cavity and a partially liquid-filled rotating drum. Equations, boundary conditions and different scalings are discussed to formally define the particle-laden flows to be investigated.

In Chapter 3 we present the numerical methods employed for dealing with fully-resolved particle-free-surface, particle-wall and particle-particle interactions. The choice will be motivated via a thorough comparison with other methods commonly employed in literature.

The accumulation phenomenon in the two-dimensional shear-stress-driven and lid-driven cavities is investigated in Chapter 4. After a complete accumulation, the minimum lubrication gap width between particle and boundary is calculated, relating it to the particle radius and the particle-to-fluid density ratio. Finally a phenomenological consideration on particle-particle interactions is conducted.

Chapter 5 presents the numerical prediction of particle accumulation structures in the three configurations defined in Chapter 2. A tight connection between PAS and flow topology will be demonstrated and the comparison between numerical and experimental data is considered for verifying our prediction whenever experimental data are available.

Finally, Chapter 6 is dedicated to summarize and discuss the results of the present work as well as to propose possible future investigations for better understanding and predicting particle accumulation structures.

2. Problem Formulation

Three different problem set-ups will be investigated herein presenting their mathematical formulation in this chapter. The non-dimensionalization is consequently adapted in dependence on the flow features, and the corresponding scalings are discussed in the following.

The first part of this chapter focuses on describing the fluid phase modelling. Three-dimensional thermocapillary and mechanically-driven flows are targeted: a liquid bridge, a lid-driven cavity and a partially liquid-filled rotating drum. The aim is to extend the usual framework of investigation of particle accumulation structures from thermocapillary- to boundary-driven systems.

The last part of this chapter is dedicated to the particulate phase modelling. A point-wise and a finite-size approach for dealing with the particles will be mathematically formulated and discussed. During this thesis both of them will be employed in dependence on the specific case to investigate.

2.1. Liquid Bridge

The first set-up we formulate consists of a liquid bridge of an incompressible Newtonian liquid. The liquid has density ρ_f , and both its thermal diffusivity and kinematic viscosity, $\kappa(T)$ and $\nu(T)$, are assumed temperature dependent. Two coaxial, cylindrical disks of radius R are placed at a mutual distance d . They are kept at constant temperatures $T_{\text{cold}} = T_0 - \Delta T/2$ and $T_{\text{hot}} = T_0 + \Delta T/2$ and represent the support of the liquid bridge. The hotter disk is heating the fluid from above.

Under micro-gravity conditions or for small characteristic scales, the principal driving is due to thermocapillary forces which arise from the surface-tension gradient induced by the temperature gradient. The surface tension between the ambient gas and the liquid bridge

$$\sigma = \sigma_0 - \gamma(T - T_0), \quad (2.1)$$

can be, in good approximation, represented as a linear function of the temperature, where σ_0 is the surface tension at the mean temperature $T_0 = (T_{\text{hot}} + T_{\text{cold}})/2$ and $\gamma = -\partial\sigma/\partial T|_{T=T_0}$ the negative surface tension coefficient. In fig. 2.1 a sketch of the problem is depicted.

Cylindrical coordinates (r, φ, z) are used to formulate the problem and a thermocapillary scaling is employed, non-dimensionalizing as follows

$$\mathbf{u} = \frac{\gamma\Delta T}{\rho_f\nu_0}\hat{\mathbf{u}}, \quad \mathbf{x} = d\hat{\mathbf{x}}, \quad t = \frac{d\rho_f\nu_0}{\gamma\Delta T}\hat{t}, \quad p = \frac{\gamma\Delta T}{d^2}\hat{p}, \quad T = \Delta T\hat{\theta}, \quad (2.2)$$

where $\mathbf{u} = ue_r + ve_\varphi + we_z$ and p are the velocity and pressure fields, respectively, $\mathbf{x} = (r, \varphi, z)$ denotes the space vector in cylindrical coordinates, t is the time and the caret indicates non-dimensional quantities. Dropping it and including the Boussinesq approximation, the non-dimensional Navier–Stokes system reads

$$\text{Re}(\partial_t + \mathbf{u} \cdot \nabla)\mathbf{u} = -\nabla p + \nabla \cdot (\nu/\nu_0 \nabla \mathbf{u}) + \text{Bd} \theta e_z, \quad (2.3a)$$

$$\nabla \cdot \mathbf{u} = 0, \quad (2.3b)$$

$$\text{Ma}(\partial_t + \mathbf{u} \cdot \nabla)\theta = \nabla \cdot (\kappa/\kappa_0 \nabla \theta), \quad (2.3c)$$

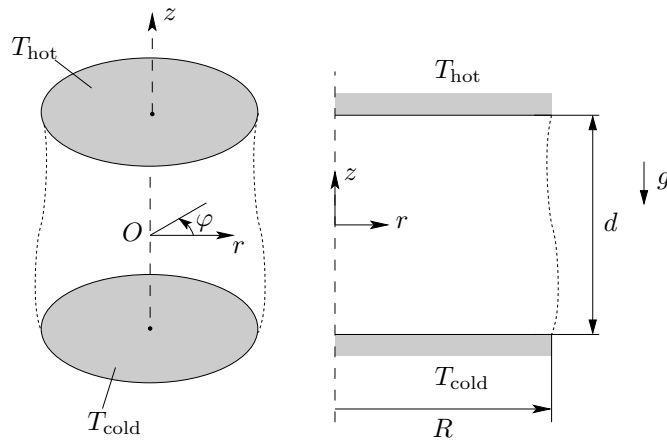


Figure 2.1.: Sketch of the liquid bridge.

where the non-dimensional groups of interest are the thermocapillary Reynolds number, Re , the Marangoni number, Ma , and the dynamic Bond number, Bd

$$Re = \frac{\gamma \Delta T d}{\rho_f \nu_0^2}, \quad Ma = \frac{\gamma \Delta T d}{\rho_f \nu_0 \kappa_0}, \quad Bd = \frac{\beta \rho_f g d^2}{\gamma}, \quad (2.4)$$

where g is the acceleration of gravity and β the thermal expansion coefficient. For convenience, instead of the Marangoni number, a reference Prandtl number, $Pr = \nu_0 / \kappa_0$, will be employed in combination with the thermocapillary Reynolds number, considering that $Ma = Re Pr$.

Assuming the case of large mean surface tension σ_0 , the flow-induced dynamic deformation of the interface can be neglected and the shape deformation problem is therefore independent of the internal liquid bridge flow. This corresponds to consider the asymptotic limit of a vanishing capillary number $Ca = \gamma \Delta T / \sigma_0 \rightarrow 0$, and reduces the normal-stress balance to the Young–Laplace equation

$$\Delta p_s = \nabla \cdot \mathbf{n} + Bo \, z, \quad (2.5)$$

where \mathbf{n} is the unit outward-pointing normal vector, Δp_s denotes the static pressure difference across the free-surface, and Bo is the static bond number

$$Bo = \frac{\rho_f g d^2}{\sigma_0}. \quad (2.6)$$

Owing to symmetry arguments, the shape of the liquid bridge $h(z)$ is axisymmetric and the two boundary value problem (2.5) can be solved supplementing (2.5) with a set of three boundary conditions. Fixing the volume ratio \mathcal{V} of the liquid bridge and assuming the contact line pinned to the sharp edges of the supporting rods, the following constraints are employed

$$h(z = \pm 1/2) = 1/\Gamma, \quad \mathcal{V} = \int_{-1/2}^{1/2} h^2(z) dz, \quad (2.7)$$

where $\Gamma = d/R$ is the aspect ratio of the liquid bridge and the volume ratio is normalized by the volume $\pi R^2 d$ of a cylindrical liquid bridge.

Once the liquid bridge shape has been determined, to close the mathematical problem (2.3), no-slip and isothermal boundary conditions are employed on the support rods

$$z = \pm 1/2: \quad u = 0, \quad v = 0, \quad w = 0, \quad \theta = \pm 1/2. \quad (2.8a)$$

In case of an axisymmetric flow, the following conditions are enforced along the axis

$$r = 0: \quad u = \partial_r w = \partial_r \theta = 0. \quad (2.8b)$$

Neglecting the stresses exerted by the surrounding gas on the liquid bridge, the interface is assumed to be a conductive free-surface, modeled according to Newton's heat transfer law

$$r = h(z): \quad \mathbf{u} \cdot \mathbf{n} = 0, \quad (\mathbf{S} \cdot \mathbf{n}) \cdot \mathbf{t}_z = -\nabla \theta \cdot \mathbf{t}_z, \quad (2.9)$$

$$\nabla \theta \cdot \mathbf{n} = -\text{Bi}(\theta - \theta_a), \quad (\mathbf{S} \cdot \mathbf{n}) \cdot \mathbf{t}_\varphi = -\nabla \theta \cdot \mathbf{t}_\varphi, \quad (2.10)$$

where $\text{Bi} = ld/k$ is the Biot number, l the heat transfer coefficient, k the thermal conductivity, $\theta_a(z)$ the ambient temperature distribution, $\mathbf{S} = \nabla \mathbf{u} + (\nabla \mathbf{u})^T$ the viscous stress tensor and \mathbf{t}_z and \mathbf{t}_φ are the tangential unit vectors in the (r, z) - and (r, φ) -plane, respectively.

Two different flow conditions will be investigated in the case of a liquid bridge: a subcritical axisymmetric flow and a supercritical one for which a periodic traveling wave occurs. In both the cases experimental results are available and our numerical investigation aims at quantitatively reproduce the corresponding PAS-related experimental data. Further details on the parameters and the flow characteristics are given in Chapter 5 and for an extensive parametric study about flow configurations and instabilities occurring in dependence on the non-dimensional groups of interest we refer the reader to [205, 167, 147, 253, 290, 289, 291, 299].

2.2. Lid-Driven Cavity

The second case to investigate is an incompressible Newtonian fluid in a closed cavity of rectangular cross-section. Both the density and the kinematic viscosity, ρ_f and ν respectively, are here assumed constant and thermal effects are not included. The fluid flow is mechanically driven by two parallel sidewalls placed at a mutual distance d which slide in opposite direction with constant velocity U . The cavity has a cross-sectional height h in y -direction and is assumed infinitely long in z -direction. A sketch of it is depicted in fig. 2.2.

In this case, a viscous scaling is employed

$$\mathbf{u} = \frac{\nu}{h} \hat{\mathbf{u}}, \quad \mathbf{x} = h \hat{\mathbf{x}}, \quad t = \frac{h^2}{\nu} \hat{t}, \quad p = \frac{\rho_f \nu^2}{h^2} \hat{p} \quad (2.11)$$

where \mathbf{u} and p are the velocity and pressure fields, respectively, \mathbf{x} and t denote space and time coordinates, and the caret-sign represents non-dimensional quantities. Dropping it, the non-dimensional Navier–Stokes equations read

$$(\partial_t + \mathbf{u} \cdot \nabla) \mathbf{u} = -\nabla p + \nabla^2 \mathbf{u}, \quad (2.12a)$$

$$\nabla \cdot \mathbf{u} = 0. \quad (2.12b)$$

To close the mathematical problem, no-penetration and no-slip boundary conditions are enforced along the walls, whereas periodic conditions are set in z -direction

$$\mathbf{u}(y = \pm 1/2) = \mathbf{0}, \quad \mathbf{u}(x = \pm \Gamma/2) = \mp \text{Re} \mathbf{e}_y, \quad \mathbf{u}(z = \lambda/2) = \mathbf{u}(z = -\lambda/2), \quad (2.13)$$

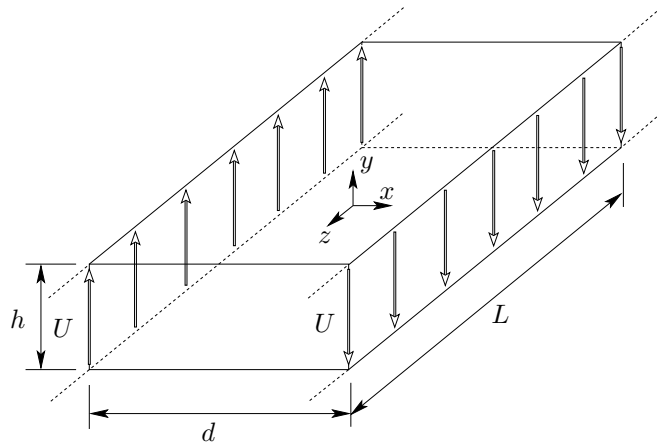


Figure 2.2.: Sketch of the two-sided anti-parallel lid-driven cavity.

where

$$\text{Re} = \frac{Uh}{\nu}, \quad \Gamma = \frac{d}{h} \quad \text{and} \quad \lambda = \frac{L}{h} \quad (2.14)$$

are the Reynolds number, the cross-sectional aspect ratio and the non-dimensional wavelength of the periodic domain, respectively.

Three different Reynolds numbers (beyond the onset of the flow instability) are targeted for this configuration, keeping the cross-sectional aspect ratio fixed. The period of the domain is selected to equal the critical wave length. For all the cases the instability arises in form of two steady mirror-symmetric orthogonal convection cell whose centres are located at $z_n = z_0 + n(\lambda/2)$ with $n \in \mathbb{Z}$ and no through-flow ($w = 0$) is present over the cell boundaries. More details about the onset and the different instability scenarios which can arise in this system can be found in [5, 3, 30, 157].

2.3. Partially Liquid-Filled Rotating Drum

The last set-up to investigate is a rotating cylindrical drum of radius R partially filled with an incompressible Newtonian liquid of constant density ρ_f and kinematic viscosity ν . The flow is driven by the constant rotational speed of the drum, Ω , and the system is assumed to be infinitely extended along its axial direction z . We consider the limit in which gravitational forces are dominant over centrifugal and capillary forces. Moreover we require that capillary forces dominate over inertia forces. This is realised if $\text{Fr} \ll 1$, $\text{Fr}/(\text{CaRe}) \ll 1$ and $\text{CaRe} \ll 1$, respectively. The limit we consider is $\text{Fr} \rightarrow 0$, $\text{Ca} \rightarrow 0$ with $\text{Fr}/\text{Ca} \rightarrow 0$ such that $\text{Re} = O(1)$ and in this limit, the gas-liquid interface remains flat and perpendicular to the gravity vector. The liquid level has maximum depth h and the liquid- and passive gas-phases are decoupled from each other. In the following only the liquid phase (gray color in fig. 2.3) will be object of the investigations.

A convective scaling is adopted

$$\mathbf{u} = \Omega R \hat{\mathbf{u}}, \quad \mathbf{x} = R \hat{\mathbf{x}}, \quad t = \frac{1}{\Omega} \hat{t}, \quad p = \rho_f \Omega^2 R^2 \hat{p}. \quad (2.15)$$

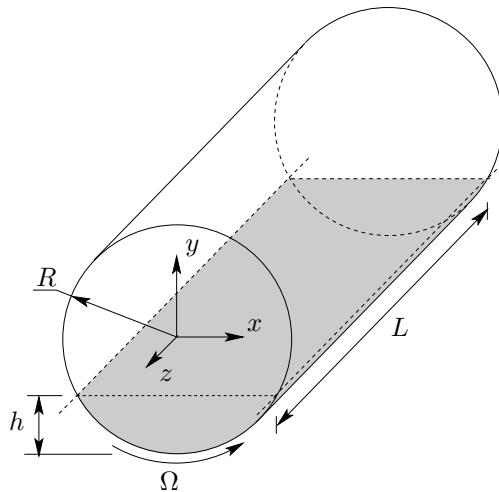


Figure 2.3.: Sketch of the rotating drum problem. In grey the liquid-phase in the cavity is depicted.

Dropping the caret, the non-dimensional Navier–Stokes equations read

$$(\partial_t + \mathbf{u} \cdot \nabla) \mathbf{u} = -\nabla p + \text{Re}^{-1} \nabla^2 \mathbf{u}, \quad (2.16a)$$

$$\nabla \cdot \mathbf{u} = 0. \quad (2.16b)$$

where

$$\text{Re} = \frac{\Omega R^2}{\nu} \quad (2.17)$$

is the convective Reynolds number.

No-penetration and no-slip boundary conditions are set along the moving wall, periodic conditions are imposed in z -direction

$$\mathbf{u}(r=1) = \mathbf{e}_\varphi, \quad \mathbf{u}(z=\lambda/2) = \mathbf{u}(z=-\lambda/2), \quad (2.18)$$

and along the free-surface a zero-tangential-stress boundary condition is enforced

$$y = -1 + \Gamma: \quad \mathbf{u} \cdot \mathbf{n} = 0, \quad (\mathbf{S} \cdot \mathbf{n}) \cdot \mathbf{e}_z = 0, \quad (\mathbf{S} \cdot \mathbf{n}) \cdot \mathbf{e}_x = 0, \quad (2.19)$$

where

$$\Gamma = \frac{h}{R} \quad \text{and} \quad \lambda = \frac{L}{R} \quad (2.20)$$

are the non-dimensional liquid depth and wavelength of the periodic domain, respectively. Once again we consider an instability which arises in form of steady two mirror-symmetric periodic cells whose boundaries are located at $z_n = z_0 + n\lambda/2$ with $n \in \mathbb{Z}$.

For fixed Γ and λ , three Reynolds numbers beyond the onset of hydrodynamic instability will be investigated in Chapter 5. For a detailed study about the scenarios experimentally observed in this configuration we refer to [274, 24].

2.4. Particle Modelling

Particle-laden flows are belonging to a class of multiphase flows in which two phases only are considered. The dispersed phase consists of particles, herein assumed rigid, and it is immersed in the continuously connected fluid phase.

2. PROBLEM FORMULATION

The equations presented so far are valid for modelling single-phase flows or the fluid-phase of particle-laden flows. Hence, including the particulate phase implies modelling particle–fluid and, if needed, particle–particle interactions.

Different approaches are used in dependence on the characteristic length and time scales of the two-phases. Hereinafter we target small Stokes numbers and particle volume fractions. In the following we employ either a one-way coupling or a fully-resolved simulation. They consider three levels of rising complexity and, consequently, of increasing computational cost. (a) The one-way coupling approach neglects the feedback of the particulate phase on the fluid as well as the particle–particle interactions. (b) Single-particle fully-resolved simulations include the effect of the particle on the fluid phase, but neglect the interactions between particles. (c) When multiple-particle simulations are carried out the interactions between particles are considered. Since the particulate-phase is assumed always immersed in the fluid phase and no dewetting phenomena are modelled, particle contacts will not arise.

The coupling between fluid- and particulate-phase is obtained via the no-slip and no-penetration conditions all over the solid-fluid interface. The equations of rigid body motion are used to compute the particle trajectories, integrating forces and torques, \mathbf{F} and \mathbf{R} , exerted by the fluid on the i -th particle

$$\mathbf{F}_i = M_i \dot{\mathbf{V}}_i, \quad \mathbf{R}_i = \mathbf{I}_i \cdot \dot{\boldsymbol{\Omega}}_i \quad (2.21)$$

where M_i , \mathbf{I}_i , \mathbf{V}_i and $\boldsymbol{\Omega}_i$ are the mass, inertia tensor, translational velocity and rotational rate of the i -th particle, respectively.

When a one-way coupling approach is employed, the particles are typically modelled as spherical particles immersed in a non-uniform Stokes flow (relatively to the fluid flow motion). Under such assumptions, the Maxey–Riley equation [189] holds and we employ a simplified version of it [10], neglecting the Basset term and the Saffmann and Faxén corrections. The scaling will be adapted case by case to the fluid-flow scaling; the Maxey–Riley in thermocapillary scaling reads

$$\ddot{\mathbf{y}} = \left(\frac{1}{\varrho + 1/2} \right) \left[-\frac{\varrho}{\text{St}} (\dot{\mathbf{y}} - \mathbf{u}) + \frac{3}{2} \frac{D\mathbf{u}}{Dt} - \frac{\varrho - 1}{\text{Fr}^2} \mathbf{e}_z \right], \quad (2.22)$$

where \mathbf{y} is the position of the particle and D/Dt is the Lagrangian derivative moving with the fluid. Three non-dimensional groups arise: the particle-to-fluid density ratio, the Stokes number and the Froude number

$$\varrho = \frac{\rho_p}{\rho_f}, \quad \text{St} = \varrho \text{Re} \frac{2a^2}{9d^2}, \quad \text{Fr} = \frac{\gamma \Delta T}{\nu_0 \rho_f \sqrt{gd}}, \quad (2.23)$$

where a is the particle radius, d the characteristic dimension of the flow system and Re the thermocapillary Reynolds number of the fluid flow. In the limit of $\text{St} \rightarrow 0$, if gravity is negligible, $\varrho = 1$ and the particle is initially velocity-matched with the fluid, the Maxey–Riley equation reduces to a pure advection equation and the particle becomes a perfect tracer and behaves like a fluid element. Typical particle parameters of this study and the experiments we target are $\varrho \in [1, 2]$ and $\text{St} \in [10^{-5}, 10^{-2}]$.

The three terms considered on the rhs of in 2.22 account for the forces exerted by the undisturbed fluid on the sphere ($1/(\varrho + 1/2)D_t\mathbf{u}$), the Stokes drag due to the viscosity of the fluid ($-1/(\varrho + 1/2)\varrho/\text{St}(\dot{\mathbf{y}} - \mathbf{u})$), the added-mass term which includes the effect of the relative motion of the particle in the fluid ($1/2(\varrho + 1/2)D_t\mathbf{u}$) and the buoyancy force ($1/(\varrho + 1/2)(\varrho - 1)/\text{Fr}^2\mathbf{e}_z$).

Even if we included the Saffmann and Faxén corrections, 2.22 could not accurately take into account particle–boundary interaction effects when the sphere moves nearby a wall or a free-surface. Moreover the lubrication effects we aim at considering in case of particle trajectories very close to a wall or a free-surface, may be crucial in making an accurate prediction. In

Chapter 4 and 5 this point will be extensively discussed, comparing point-particles and fully-resolved numerical results, proposing a particle–boundary interaction model and validating it with experimental data.

3. Numerical Method

The methods chosen to numerically simulate particle-laden flow phenomena are discussed in this chapter. Their main features and the reasons to opt for them will be highlighted, comparing these methods with other possible options already broadly established in literature.

This chapter is basically divided in two main parts: the first one which refers to the discretization method used in space, DG-FEM (discontinuous Galerkin finite element method), applied to a stiffly-stable splitting scheme in time. The second one which includes the rigid dispersed particulate phase in the flow domain, SPM (smoothed-profile method). An extension of the algorithms available in the literature is presented in order to include thermal and variable-viscosity effects in the numerical simulation.

The reader is referred to the Appendix for a collection of the most significant benchmarks included for validation and verification purpose.

3.1. h/p Discretization Methods

The numerical method we are going to employ, discontinuous Galerkin finite element method (DG-FEM), belongs to the class of h/p -methods and in the following we will discuss about the reasons why we chose it.

One of the main strengths of classic h/p spectral methods (see [139, 138, 36, 38, 37]) is the so-called p -convergence. It consists of approaching the exact solution by increasing the degrees of freedom of a single element employed to discretize the domain. For an infinitely smooth solution, the p -convergence is faster than any polynomial convergence and increasing the polynomial order can therefore be very efficient. The p -refinement flexibility may be further extended considering different orders of approximation for different elements. This leads not just to a global p -refinement capability of the method, but also to its local p -adaptivity [67, 68].

In addition to the p -type, the name h/p methods refers to a second kind of convergence: the h -convergence. Since the computational domain is described in an element-wise approach, the convergence of the numerical solution to the exact one may be obtained by reduction of the elements size, h . Thereafter, an element-wise approach guarantees a high flexibility either in describing complex geometries or in locally refining the solution accuracy. In general a suitable combination of h - and p -refinements guarantees high accuracy for a relatively cheap computational cost.

These features of classic h/p spectral we would certainly like to keep in our numerical method. For limiting numerical stability constraints, we plan to apply an implicit time discretization; considering that we would not have any advantage by using an explicit discretization approach (mass matrix not to be inverted), the implicit discretization is certainly recommended. On the other hand, classic spectral element methods (SEM) typically employ symmetric basis functions, which are the best choice for dealing with problems dominated by symmetric terms (diffusive terms), but numerical stability issues may occur when the dominant effect is due to convection (see [123]). This point has been extensively considered in literature and many techniques have been proposed to cure such a drawback of the classic FEM/SEM approach, e.g. introducing a suitable numerical viscosity or using an enriched functional space including bubble functions capable to self-adapt to the local advection direction (see e.g. [234]).

This consideration represents a discriminant for us since the phenomena we are interested in are highly dominated by convective terms. For them the upwinding technique employed in finite difference (FDM) and finite volume methods (FVM) represents the most natural discretization approach. The choice of merging h/p spectral and finite volume methods results, as natural consequence, in the discontinuous Galerkin finite element method, which combines the space functions used by h/p approaches with a FVM-like sense in satisfying the discrete equations.

A typical choice for including the local approach in h/p methods consists in duplicating the variables along the shared faces between different elements. This results, for a nodal approach, in doubling the degrees of freedom at the internal faces (see fig. 3.1) and connecting the adjacent elements via preservation of the numerical flux across each shared edge. The latter operation ensures globally meaningful results and it is nothing but the reconstruction step proper of the finite volume methods [123]. The main drawback of the discontinuous approach in comparison with a continuous Galerkin one is the increment of the degrees of freedom, which induces larger discrete systems and, consequently, higher computational effort in the solving process. On the other hand, a typically sparser matrix is obtained by DG-FEM if compared with classic h/p methods and raising the degrees of freedom affects the computational cost less and less the higher the polynomial order is. For this reason, the latter disadvantage of the discontinuous approach seems not to be so effective for the simulations of main interest herein.

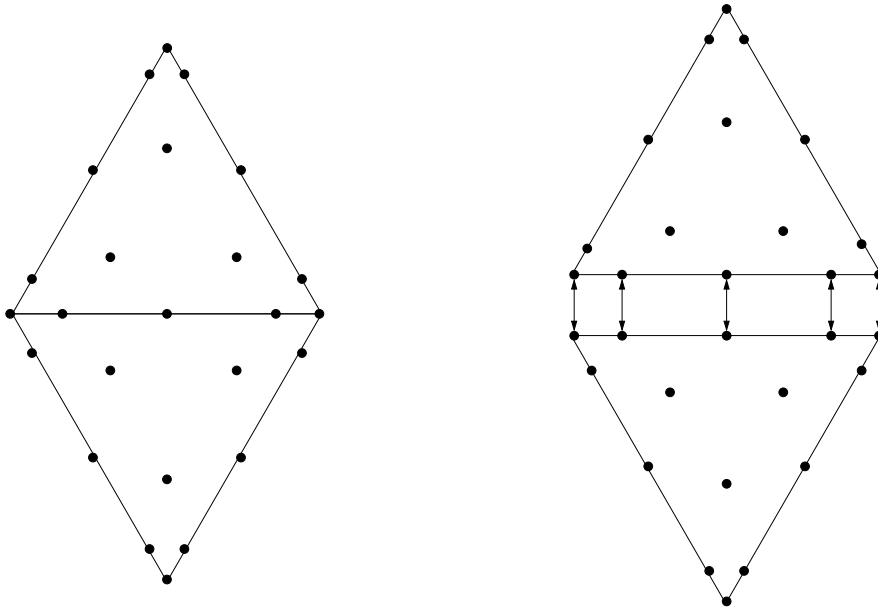


Figure 3.1.: Degrees of freedom in a classic h/p method (left) and in a DG-FEM (right).

In conclusion, because of accuracy and flexibility, either in a geometrical or in a numerical flux designing sense, the discontinuous Galerkin finite element method appears as the best candidate for simulating the cases of interest for the present thesis.

3.2. Evolution of Discontinuous Galerkin Finite-Element Method

The introduction of DG-FEM can be traced back to the work of Reed & Hill [240] who used it for dealing with neutron transport problems. Successively, an intensive effort was spent

in the analysis and the development of DG’s theoretical basis including convergence studies for smooth [165, 136, 223] and non-smooth solutions [171, 48], post-processing [56, 64, 247], limiting [229, 233, 230, 231, 232, 183] and various numerical stability issues.

Even though the method has been introduced in the 70’s, the main development effectively started only in the 90’s and because of the flexibility in designing the numerical fluxes, hyperbolic equations and conservation laws became natural candidates for the employment of DG-FEM [44, 43, 57, 58, 55, 49]. Therefore, electromagnetism (e.g. [294]), acoustics (e.g. [9]), elasticity (e.g. [74]), shallow water (e.g. [89]) and plasma physics (e.g. [170]) have been extensively investigated by the means of discontinuous Galerkin methods.

Mainly due to the work of Bassi & Rebay, Baumann, Cockburn & Shu, DG methods focused on inviscid, compressible fluid dynamics [60, 21] and have been successively generalised to diffusion, convection–diffusion and compressible Navier–Stokes problems [20, 22, 59, 208, 23, 180, 181, 42, 127, 221, 307, 115, 114]. More recently, a further improvement consisted in applying RANS and LES modelling to compressible Navier–Stokes equations [19, 17, 203, 209, 159, 282, 287], and discontinuous Galerkin methods have also been successfully employed for incompressible Navier–Stokes equations [176, 53, 51, 50, 193, 168, 16, 18, 263, 192, 241, 52, 204, 78, 77].

Among all these authors, three main approaches for the numerical flux design arose, i.e. interior penalty, local discontinuous Galerkin and Bassi-Rebay methods. A comparison between them was derived in [8] and, in the present thesis only the former one will be implemented. The interior penalty method uses nothing but a penalization technique in order to induce a certain smoothness in the numerical solution, and the same approach is then used to apply Dirichlet boundary conditions, enforced via a so-called spectral penalty method (see [83, 84, 85, 120, 117, 118, 121, 119, 122]).

To the author’s knowledge, the quoted literature can give a detailed summary of the potential of discontinuous Galerkin finite element methods, especially when applied to fluid dynamics. However, giving an exhaustive overview about the method is not within the scope of this dissertation. We refer to [8, 54, 225, 140, 123, 241] for a far more complete overview of DG-FEM, keeping in mind that, owing to the intensive investigation recently carried out in such a field, it appears to be a continuously active research area (e.g. hybridizable DG methods [204]).

3.3. Discrete Incompressible Navier–Stokes Equations

In the following section a discontinuous Galerkin method with interior penalty approach will be applied to the incompressible Navier–Stokes equations. One of the main difficulties of numerically simulating this system of equations is that velocity and pressure are coupled via the incompressibility constraint. In order to overcome such an obstacle, when a primitive variable formulation is employed, Chorin & Temam introduced the projection methods [45, 272]. These methods belong to the fractional/splitting methods and their efficiency comes from approaching the incompressible Navier–Stokes equations in a sequence of steps that decouples pressure and velocity unknowns.

After their introduction, many improvements and approaches have been developed and three main classes of projection methods can be identified: pressure-correction [93, 275, 283, 142], velocity-correction [109, 210, 141] and consistent splitting methods [108].

In the following, just one velocity-correction approach will be employed and, for an extensive review about projection methods and their comparison, we refer to [107].

3.3.1. Temporal Discretization

A stiffly stable velocity-correction splitting scheme will be implemented in order to deal with the incompressible Navier–Stokes equations. Different from the pressure-correction fractional step method, the chosen algorithm belongs to the so-called high-order projection methods because it is proved to be numerically stable even for third or higher order in time. Furthermore, it is one of the most employed schemes for h/p spectral methods and it has been extensively tested.

Because of these reasons, following Karniadakis et al. [141], we consider a three-stages projection method: the first step integrates the convective terms, written in a conservative form, via an Adam-Bashforth second-order scheme; the second step represents the projection of the resulting velocity components onto a weakly divergence-free functional space and the third step includes the viscous terms.

In case the viscous scaling is employed, the time-discrete system of continuity, Navier–Stokes and energy equations read

$$\begin{aligned} \frac{\gamma_0 \tilde{\mathbf{u}} - \alpha_0 \mathbf{u}^n - \alpha_1 \mathbf{u}^{n-1}}{\Delta t} &= -\beta_0 [\mathbf{N}(\mathbf{u}^n, \mathbf{u}^n) - \text{Gr} \theta^n \mathbf{e}_y] \\ &\quad - \beta_1 [\mathbf{N}(\mathbf{u}^{n-1}, \mathbf{u}^{n-1}) - \text{Gr} \theta^{n-1} \mathbf{e}_y] \end{aligned} \quad (3.1a)$$

$$\frac{\gamma_0 \tilde{\theta} - \alpha_0 \theta^n - \alpha_1 \theta^{n-1}}{\Delta t} = -\beta_0 \mathbf{N}(\mathbf{u}^n, \theta^n) - \beta_1 \mathbf{N}(\mathbf{u}^{n-1}, \theta^{n-1}) \quad (3.1b)$$

$$\nabla^2 \bar{p}^{n+1} = \frac{\gamma_0}{\Delta t} \nabla \cdot \tilde{\mathbf{u}} \quad (3.1c)$$

$$\begin{aligned} \frac{\partial \bar{p}^{n+1}}{\partial \hat{n}} &= -\beta_0 \hat{\mathbf{n}} \cdot \left(\frac{D\mathbf{u}^n}{Dt} + \nabla \times \boldsymbol{\omega}^n - \text{Gr} \theta^n \mathbf{e}_y \right) \\ &\quad - \beta_1 \hat{\mathbf{n}} \cdot \left(\frac{D\mathbf{u}^{n-1}}{Dt} + \nabla \times \boldsymbol{\omega}^{n-1} - \text{Gr} \theta^{n-1} \mathbf{e}_y \right) \end{aligned} \quad (3.1d)$$

$$-\nabla^2 \mathbf{u}^{n+1} + \frac{\gamma_0}{\Delta t} \mathbf{u}^{n+1} = \frac{\gamma_0}{\Delta t} \tilde{\mathbf{u}} - \nabla \bar{p}^{n+1} \quad (3.1e)$$

$$-\nabla^2 \theta^{n+1} + \frac{\gamma_0 \text{Pr}}{\Delta t} \theta^{n+1} = \frac{\gamma_0 \text{Pr}}{\Delta t} \tilde{\theta}, \quad (3.1f)$$

where $\boldsymbol{\omega}$ is the vorticity vector field, n identifies the current time, Δt is the time step, $\mathbf{N}(\mathbf{u}, *)$ represent the non-linear term written in a conservative form as follows

$$\mathbf{N}(\mathbf{u}, \mathbf{u}) = \begin{pmatrix} N_u \\ N_v \\ N_w \end{pmatrix} = \nabla \cdot \begin{pmatrix} \mathbf{F}_u \\ \mathbf{F}_v \\ \mathbf{F}_w \end{pmatrix} = \begin{pmatrix} \frac{\partial(u^2)}{\partial x} + \frac{\partial(uv)}{\partial y} + \frac{\partial(uw)}{\partial z} \\ \frac{\partial(uv)}{\partial x} + \frac{\partial(v^2)}{\partial y} + \frac{\partial(vw)}{\partial z} \\ \frac{\partial(uw)}{\partial x} + \frac{\partial(vw)}{\partial y} + \frac{\partial(w^2)}{\partial z} \end{pmatrix} \quad (3.2a)$$

$$N(\mathbf{u}, \theta) = \nabla \cdot \mathbf{F}_\theta = \frac{\partial(u\theta)}{\partial x} + \frac{\partial(v\theta)}{\partial y} + \frac{\partial(w\theta)}{\partial z} \quad (3.2b)$$

and (3.1d) represents a pressure boundary condition to employ when Dirichlet boundary conditions are set on velocity and it is obtained using the so-called *curl – curl* formulation.

Owing to the second-order backward scheme in time, the velocity-correction cannot be a self-starting method. The first time step is then performed via a simpler implicit Euler method. A straightforward way to implement it consists in suitably defining the constant coefficients of the algorithm as follows

$$\gamma_0 = 0, \quad \alpha_0 = 1 \quad , \quad \alpha_1 = 0, \quad \beta_0 = 1 \quad , \quad \beta_1 = 0, \quad \text{if } n = 1 \quad (3.3a)$$

$$\gamma_0 = \frac{3}{2}, \quad \alpha_0 = 2 \quad , \quad \alpha_1 = \frac{1}{2}, \quad \beta_0 = 2 \quad , \quad \beta_1 = -1, \quad \text{if } n > 1 \quad (3.3b)$$

Moreover the explicit treatment used for the non-linear terms is very efficient, because there is no need of implementing an iterative non-linear solver for dealing with the convective terms. Finally, owing to the stability properties of the scheme, it does not impose very severe constraints on the time step Δt and an appropriate design of the discrete convective fluxes can even more increase the stability performance of the projection method.

As is clear from (3.1), the solution of the incompressible Navier–Stokes equations is reduced to solve two Helmholtz problems in terms of temperature and velocity, and one Poisson problem in terms of pressure.

3.3.2. Spatial Discretization

Once the temporal discretization is provided by the splitting method, a DG approach is used to discretize in space. Following the strategy outlined in [123], the non-linear advection terms are treated via an upwind scheme of the numerical fluxes, derived from the Lax–Friedrichs/Rusanov scheme. The variational form adopted for such a purpose is:

find N_* such that

$$\begin{aligned} (\phi_h, N_*)_{\Omega_h^k} &= (\phi_h, \nabla \cdot I_N F_*(\mathbf{u}_h, *))_{\Omega_h^k} \\ &\quad - \frac{1}{2} (\phi_h, \mathbb{J} I_N F_*(\mathbf{u}_h, *) \mathbf{K})_{\partial \Omega_h^k}, \quad \forall \phi_h \in V_h \\ &\quad + \frac{\lambda}{2} (\phi_h, \hat{\mathbf{n}} \cdot \mathbf{J} \mathbf{u}_h \mathbf{K})_{\partial \Omega_h^k} \end{aligned} \quad (3.4)$$

where the subscript h indicates the performed spatial discretization, $*$ is a generic symbol employed to generalize the notation among the different non-linear terms, i.e. u_h, v_h, w_h or θ_h , $\{\phi_h\}$ is the test function basis, $V_h = \bigoplus_{k=1}^K \mathbb{P}_N(\Omega_h^k)$, Ω_h^k is the k -th element of the spatial mesh, $\mathbb{P}_N(\Omega_h^k)$ is the functional space used for the k -th element, $I_N f$ is the N -th-order interpolation of f , $\mathbf{J} \cdot \mathbf{K} = (\cdot|_{e\ell^1}) - (\cdot|_{e\ell^2})$ refers to the jump operator and λ is nothing but the penalty multiplier for the local Lax–Friedrichs scheme and it is evaluated by the usage of the trace values. Along the Dirichlet boundaries for velocity and temperature, the boundary conditions are included in the non-linear term by the mean of the relative positive trace.

The second stage of the algorithm implies the solution of a Poisson equation in terms of pressure. An interior penalty approach is used for the discontinuous Galerkin discretization and, along the velocity Dirichlet boundaries, pressure Neumann boundary conditions are applied via the so-called *rotational approach* introduced in (3.1d). The current step can be then formulated as:

find $p_h^{n+1} \in V_h$ such that

$$\begin{aligned}
 & (\nabla \phi_h, \nabla p_h^{n+1})_{\Omega_h^k} - \frac{1}{2} (\hat{\mathbf{n}} \cdot \nabla \phi_h, \hat{\mathbf{n}} \cdot \mathbf{J} p_h^{n+1} \mathbf{K})_{\partial \Omega_h^k \setminus \partial \Omega_h} \\
 & - (\phi_h, \hat{\mathbf{n}} \cdot \{ \{ \nabla p_h^{n+1} \} \})_{\partial \Omega_h^k \setminus \partial \Omega_h} + (\tau^k \phi_h, \hat{\mathbf{n}} \cdot \mathbf{J} p_h^{n+1} \mathbf{K})_{\partial \Omega_h^k \setminus \partial \Omega_h} \\
 & - (\hat{\mathbf{n}} \cdot \nabla \phi_h, (p_h^{n+1})^-)_{\partial \Omega_h^k \cap \partial \Omega_h^{\text{pDir}}} - (\phi_h, 2 \hat{\mathbf{n}} \cdot \nabla (p_h^{n+1})^-)_{\partial \Omega_h^k \cap \partial \Omega_h^{\text{uDir}}} \\
 & + (\tau^k \phi_h, (p_h^{n+1})^-)_{\partial \Omega_h^k \cap \partial \Omega_h^{\text{pDir}}} = \\
 & - (\hat{\mathbf{n}} \cdot \nabla \phi_h, p^{\text{pDir}})_{\partial \Omega_h^k \cap \partial \Omega_h^{\text{pDir}}} + \left(\phi_h, -\frac{\gamma_0}{\Delta t} \nabla \cdot \tilde{\mathbf{u}}_h \right)_{\Omega_h^k} \\
 & + \left(\phi_h, \beta_0 \frac{\partial p_h^n}{\partial \hat{\mathbf{n}}} + \beta_1 \frac{\partial p_h^{n-1}}{\partial \hat{\mathbf{n}}} \right)_{\partial \Omega_h^k \cap \partial \Omega_h^{\text{uDir}}} + (\tau^k \phi_h, p^{\text{pDir}})_{\partial \Omega_h^k \cap \partial \Omega_h^{\text{pDir}}}, \quad \forall \phi_h \in V_h, \quad (3.5)
 \end{aligned}$$

where the superscript $-$ indicates the negative trace, $\{ \{ \cdot \} \} = \frac{1}{2} (\cdot|_{el^1}) + \frac{1}{2} (\cdot|_{el^2})$ is the average operator, τ^k is the penalty factor for the k -th element which is chosen in dependence on the element size h^k and the number of nodes per edge, the superscripts pDir and uDir refer to the pressure and the velocity Dirichlet boundaries, respectively.

Because the linear system resulting from such a discretization, as for the remaining Helmholtz problems, is described by a sparse matrix whose non-zero entries are located according to the connectivity between the elements, it is computationally convenient to employ a reordering strategy such to reduce the bandwidth of the matrix. To this end the reverse Cuthill–McKee algorithm [65] is adopted. Moreover, because the Poisson matrix is Hermitian and positive definite, Cholesky factorization is used to solve the reordered linear system in an efficient way.

The last stage of the splitting algorithm consists of two equations formally identical to each other (see (3.1e) and (3.1f)), with the only difference of the pressure gradient contribution. Therefore, the interior penalty DG formulation will be presented only for the x -momentum equation.

Find $u_h^{n+1} \in V_h$ such that

$$\begin{aligned}
 & (\nabla \phi_h, \nabla u_h^{n+1})_{\Omega_h^k} + \frac{\gamma_0}{\Delta t} (\phi_h, u_h^{n+1})_{\Omega_h^k} - \frac{1}{2} (\hat{\mathbf{n}} \cdot \nabla \phi_h, \hat{\mathbf{n}} \cdot \mathbf{J} u_h^{n+1} \mathbf{K})_{\partial \Omega_h^k \setminus \partial \Omega_h} \\
 & - (\phi_h, \hat{\mathbf{n}} \cdot \{ \{ \nabla u_h^{n+1} \} \})_{\partial \Omega_h^k \setminus \partial \Omega_h} + (\tau^k \phi_h, \hat{\mathbf{n}} \cdot \mathbf{J} u_h^{n+1} \mathbf{K})_{\partial \Omega_h^k \setminus \partial \Omega_h} \\
 & - (\hat{\mathbf{n}} \cdot \nabla \phi_h, (u_h^{n+1})^-)_{\partial \Omega_h^k \cap \partial \Omega_h^{\text{uDir}}} - (\phi_h, \hat{\mathbf{n}} \cdot \nabla (u_h^{n+1})^-)_{\partial \Omega_h^k \cap \partial \Omega_h^{\text{uNeu}}} \\
 & + (\tau^k \phi_h, (u_h^{n+1})^-)_{\partial \Omega_h^k \cap \partial \Omega_h^{\text{uDir}}} = \\
 & - (\hat{\mathbf{n}} \cdot \nabla \phi_h, u^{\text{uDir}})_{\partial \Omega_h^k \cap \partial \Omega_h^{\text{uDir}}} + \left(\phi_h, \frac{\gamma_0}{\Delta t} (\tilde{u}_h - \Delta t \nabla p_h^{n+1}) \right)_{\Omega_h^k} \\
 & + \left(\phi_h, \frac{\partial u_h^{n+1}}{\partial \hat{\mathbf{n}}} \right)_{\partial \Omega_h^k \cap \partial \Omega_h^{\text{uNeu}}} + (\tau^k \phi_h, -u^{\text{uDir}})_{\partial \Omega_h^k \cap \partial \Omega_h^{\text{uDir}}}, \quad \forall \phi_h \in V_h. \quad (3.6)
 \end{aligned}$$

The combination of all these stages brings to one complete temporal step of the projection method. A well-known problem of projection schemes is the possible occurrence of spurious pressure modes whose explanation can be referred to a classic saddle point problem (see [234]).

This occurs when the same functional space V_h is used for discretizing pressure and velocity. In order to cure these non-physical pressures, a typical FEM/SEM strategy is to choose a richer functional space for the velocity than for the pressure field. In this case it is common to consider $\mathbb{P}_N - \mathbb{P}_{N-2}$ functional spaces for velocity and pressure, respectively. More in general, a suitable choice that respects the Ladyzhenskaya–Babuška–Brezzi (LBB) or *inf-sup* condition will guarantee the absence of parasite pressures [34, 11]. Whereas the same functional space is used for pressure and velocity, a stabilization technique has to be implemented for classic continuous Galerkin approaches. This is not necessary in the case of DG-FEM because the penalty factor used in the pressure step (second stage) of the splitting method can be designed such to considerably affect the pressure spurious modes. Furthermore, as discussed in [107], their importance decreases as the order of discretisation increases and choosing high-order polynomial basis (i.e. polynomial order ≥ 4), parasite pressures are not considerably effective in the solution accuracy. Because of these reasons, the same functional space is used for both, pressure and velocity, and 5th or higher polynomial order will be selected in the following simulations.

3.4. Methods for Particle-Laden Flows

Many different approaches have been developed for dealing with multiphase and, specifically, particle-laden flows. A numerical method applied in this field is basically required to be accurate in the description of the particle trajectories and the respective macroscopic forces. Moreover, it must be efficient for simulating many particles immersed in the fluid-phase, possibly even complex shaped particles. In the following, a short overview about the most commonly used approaches is given to justify the choice of SPM (smoothed profile method) for dealing with finite-size particles. For implementation details and benchmark results, the reader is referred to the Appendix and to [245].

Treating finite-size particle-laden flows can be done via two different numerical approaches. The first class of methods simulate the particulate phase using a Lagrangian approach. In practice, it means that the computational mesh employed for this group of methods is deforming following the particle motion.

Among all the different Lagrangian descriptions for the particulate phase, two main methods have been successfully implemented in this field: the arbitrary Lagrangian-Eulerian (ALE) and the space-time finite element methods. In the latter case both, time and space variables, are discretized with a finite element method using a pure Lagrangian point of view, in which the spatial domain deformation is directly mirrored via a deformation in time of the computational mesh (see Johnson et al. [134, 135]). On the other hand, the ALE method introduced by Hirt [124, 125], employs both, Eulerian and Lagrangian descriptions, for solving the flow. In this case the Lagrangian representation can be arbitrary, in the sense that it is generally done considering a reference, fictitious domain [128, 129, 71, 178, 269, 131]. When the mesh deformation velocity coincides with the flow velocity, the ALE method reproduces a pure Lagrangian description.

Even though these approaches have been successfully applied for high-order methods in fluid–structure interactions [293, 296, 292, 27, 26, 182, 207, 220, 218] or particle-laden flows (up to 1000 particles, see [135]), they do not seem very efficient for the cases of interest in the present study. In fact we deal with dilute suspensions and the working hypothesis which is commonly applied states that the phenomena to investigate are not sensibly affected by particle–particle interactions. Hence, only one particle will be considered in most of the simulations for investigating particle–boundary interaction phenomena. Moreover a moving mesh method can be very expensive if one wants to keep the computational resolution nearby the particle almost constant. This is due to the motion of the particle which induce a rapid degrading of the mesh

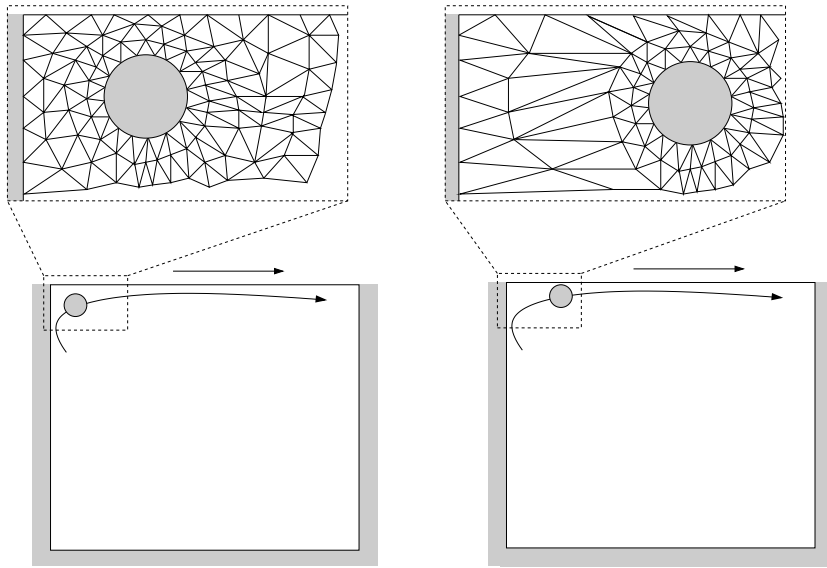


Figure 3.2.: Degrading of the computational mesh in Lagrangian descriptions due to the motion of a single particle in the domain.

in the fluid-phase domain. Consequently frequent re-meshing operations are needed. Figure 3.2 clarifies this issue.

The second class of methods for dealing with particle-laden flows employs an Eulerian description, simulating the interaction of the two phases on a fixed computational mesh. In this framework many different approaches have been developed for modeling the multiphase flow of interest. Differently from the Lagrangian methods, they do not require any re-meshing operation due to computational grid degradation induced by the particle motion (see fig. 3.3). However, if necessary, an adaptive grid can be employed.

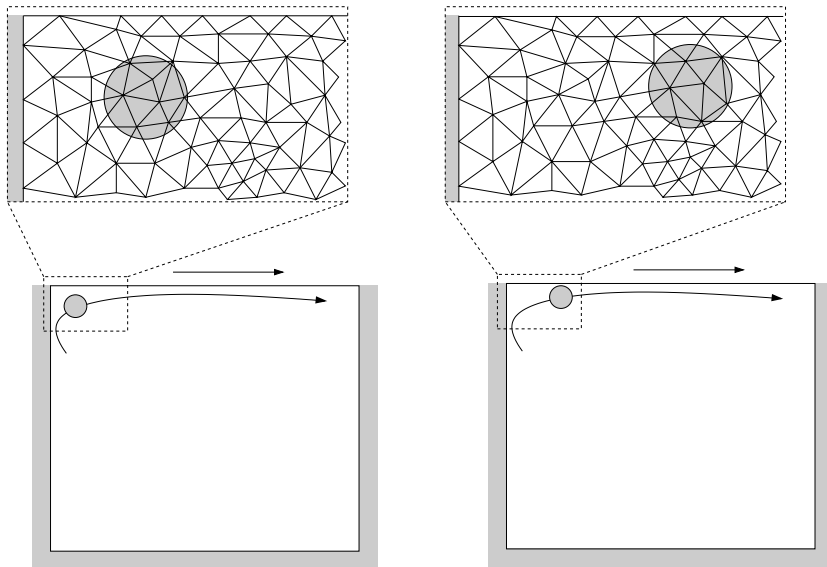


Figure 3.3.: Eulerian description of a single particle moving in the domain.

Some of these methods, like the distributed Lagrange multiplier (DLM) method introduced by Glowinski [90], impose an additional body force to maintain the rigid-body motion of the particles inside the particulate-phase domain and enforce the no-slip condition among the two phases. Such constraints are usually verified via velocity- [91, 92] or strain-rate-based [215] conditions added to the space of Lagrange multipliers.

Another Eulerian approach consists of representing the particle phase via a low-order expansion of force multipoles, i.e. Stokeslet, Stresslet, Rotlet, etc. This is the case for the force coupling method (FCM) introduced by Maxey et al. [188], in which a Taylor expansion of the Oseen tensor is employed and the non-zero-size particles are represented in the fluid-phase as distributed body forces [188, 179, 66]. However, even though FCMs give a very good approximation of the flow field far from the particles with a remarkable reduction of computational costs in comparison with full-scale simulations, their main drawback is that the flow is not fully resolved close to the particle surface. Therefore they exhibit a dramatic loss of accuracy in regions up to 25% of the radius far from the particle surface [47]. Hence, this aspect makes FCMs not suitable for an appropriate simulation of the phenomena the present investigation focuses on.

In both the latter cases, as well as for the method of virtual identity particles (VIP, see [175]), employing h/p methods guarantees that the spectral convergence is preserved [173, 174, 72]. Moreover, because of their efficiency, Eulerian methods have been successfully used for simulating up to 10000 and 1000 particles in 2-D and in 3-D, respectively [214, 213, 46].

Beside the simulation of the particulate phase via fictitious domain methods (DLM) or distributed body forces (FCM), other approaches can be employed such as a front tracking technique [276] or a semi-analytic method that iteratively matches the analytical and the numerical solutions for the flow field nearby and far away from the particles, respectively (see the implementation of Physalis introduced by Prosperetti & Oğuz [227, 268, 130, 305, 306]).

Finally, a last comment is reserved to the immersed boundary method (IBM). This approach belongs to the Eulerian class, as well, and it is widely employed in literature, specially by the finite-volume and finite-difference communities. The method is based on tracking the immersed boundary, which moves with the flow velocity, via a series of Lagrangian markers. Modeling the elastic/rigid properties (see [80, 28] for rigid-bodies) of the immersed boundary consists in determining the singular force distribution exerted on the flow in the regions nearby the Lagrangian markers. For this purpose, regularized Dirac delta functions have been introduced by Peskin [222]. Recent developments of the method consist in its extension to a second-order scheme [158] and implementation of different approaches for the interaction between Eulerian and Lagrangian representation (see virtual boundary method and direct forcing method [94, 76, 281]). A slightly different approach was then proposed via the immersed interface method (IIM) which includes the interface jump conditions into the discrete equations (see [166, 169, 164]) rather than considering the immersed boundary actions in a continuous fashion.

This short summary about the methods typically used to deal with particulate flows is concluded here motivating the choice of the smoothed profile method and comparing it with the aforementioned approaches. SPM describes the particle–fluid-phase interaction by means of an interface layer into which the rigid-body equations used for modelling the particulate phase are smoothly converted in the equation for the fluid phase. In this sense, the numerical transition layer can be interpreted as a matching operation similar to the one implemented in Physalis. Like DLM, FCM, Physalis, IBM and IIM, also the SPM employs an Eulerian mesh; thus avoiding the need for re-meshing due to the mesh degrading phenomena discussed for Lagrangian approaches. In general, the smoothed profile method has characteristics in common with some of the discussed techniques. Like the FCM, the particles are represented as body forces and similar to IBM, the SPM enforces approximate boundary conditions. Another common point

between SPM, FCM and IBM is that the particle volume is part of the computational domain and no internal constraints are enforced on it. For such a purpose, a penalty body force is adopted to ensure the rigidity of the particles and to integrate the relative translational and rotational velocities. This approach implicitly includes no-slip boundary conditions between the two phases and is responsible for the flow accuracy nearby the particle surfaces. In this sense it can be considered an improvement with respect to the body-force system employed in the FCM and, owing to it, it is possible to accurately simulate the colloidal forces and lubrication gaps of crucial importance for particle–boundary interaction phenomena [201]. Moreover, together with FCM and DLM, also SPM enjoys the spectral convergence if coupled with h/p methods [187].

Our last remark focuses on comparing the diffuse-interface and the sharp-interface methods. The transition between the particulate rigid phase and the fluid phase may be modelled using a numerically sharp border or smearing the coupling region in a diffuse interface. Techniques which employ body-fitted elements (see e.g. [135]) are clear examples of the former approach. However, also IBM can be implemented using a sharp interface (see e.g. [303, 88, 277, 261, 242]). Among the key issues in the latter case is the conservation of mass and energy, specially whether a cut-cell method is adopted. Contrary to body-fitted-element methods, SPM belongs by definition to the diffuse-interface methods and its interface thickness is typically governed by a scalar parameter ξ . Using a diffuse-interface approach is usually convenient to avoid numerical problems connected to the so-called *grid locking* [33]. The main drawback of diffuse-interface methods which is of interest for the present thesis work is the limited capability to describe refined regions nearby the solid-fluid interface. The coupling interactions between particles and fluid are smeared within the interface layer. This implies that simulations in which a particle is passing close to a domain boundary must make sure that the diffuse interface does not cross the boundary itself. On the other hand refining the interface thickness leads to a stiffer interaction between the particulate- and the fluid-phase which may even induce numerical instability. A thorough parameter tuning is therefore always required for diffuse-interface methods as SPM.

SPM has been intensively developed and tested in the last years passing from classic particle-laden flows (see e.g. [301, 198, 300, 200, 132]) to model electro-charged colloids and electrophoresis of dense dispersion (see [143, 145, 144, 199, 302, 184, 137]).

Apart from its efficiency in dealing with many particles [201, 301], a useful property of the smoothed profile method is the possibility of easily represent complex-shaped rigid bodies. In fact, SPM has been recently employed for describing stochastic roughness over the particle surfaces [304] and even the full rotating body of a waterjet propulsion system [185, 186]. In the present investigation we will only deal with circular/spherical particles, but the aforementioned references are relevant because SPM was tested for high Reynolds numbers up to turbulent regimes. Moreover SPM always exhibited excellent comparisons against moving-grids full-scales simulations and the dramatic cost reduction implied by SPM is typically considerable. Hence, it is hereinafter chosen for simulating the multiphase flows of interest.

3.5. Smoothed Profile Method

The smoothed profile method was originally proposed to resolve fluid- and particle-phase interactions in colloidal dispersions. It is based on the idea of representing the particles via a smooth concentration function, ϕ , (the so-called *smoothed profile*), which equals one in the particle domain and zero in the fluid-phase. Figure 3.4 shows a typical smooth variation (by gray-scale) of ϕ in a two-dimensional interface region.

The coupling of discontinuous Galerkin finite element and smoothed profile method is aiming at simulating the interactions between particulate- and fluid-phase. Therefore, the algorithm

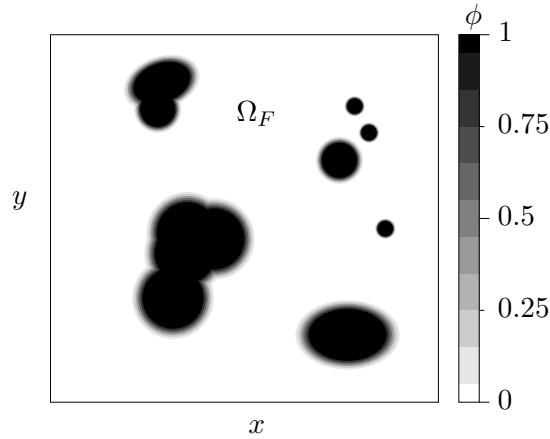


Figure 3.4.: Smoothed profile function ϕ for a complex-shaped particulate phase immersed in a fluid domain Ω_F .

presented in eq. 3.1 can be extended in order to consider the forces exerted by the fluid on the particles, their consequent rigid-body motion, as well as the perturbation field due to the particulate phase. Once again we point out that employing an Eulerian approach is the reason why the algorithm adopted remains substantially unchanged for the fluid phase domain.

The first quantity to define is the smoothed profile ϕ , which represents a concentration field to describe the whole particulate phase. Following the approach proposed by Nakayama et al. [201]. For the single particle we employ

$$\phi_i(\mathbf{x}, t) = \frac{1}{2} \left[\tanh \left(\frac{-d_i(\mathbf{x}, t)}{\xi_i} \right) + 1 \right], \quad (3.7)$$

where ϕ_i is the smoothed profile of the i -th particle, d_i is the signed distance to the i -th particle surface, which is positive outside and negative inside the particle and ξ_i is the interface thickness parameter for the i -th particle. A more detailed investigation on the choice of the smooth function employed to realize the transition between fluid- and particulate-phase can be found in [245]. Figure 3.5 depicts a one-dimensional smoothed profile of radius a and centred in x_p for different ξ .

Starting from the single indicator functions ϕ_i , under the hypothesis of non-overlapping particles¹, the global concentration field ϕ can be obtained by direct superposition. For N_p rigid bodies

$$\phi(\mathbf{x}, t) = \sum_{i=1}^{N_p} \phi_i(\mathbf{x}, t). \quad (3.8)$$

Referring to [201], the rigid-body motion of the particles reads

$$\phi(\mathbf{x}, t) \mathbf{u}_p(\mathbf{x}, t) = \sum_{i=1}^{N_p} [\mathbf{V}_i + \boldsymbol{\Omega}_i \times (\mathbf{x} - \mathbf{P}_i)] \phi_i, \quad (3.9)$$

where \mathbf{u}_p is the particle velocity field and \mathbf{P}_i , \mathbf{V}_i and $\boldsymbol{\Omega}_i$ are i -th particle centroid, translational and rotational rate, respectively. Moreover, due to the non-overlapping condition and since \mathbf{u}_p

¹This hypothesis is only approximated employing (3.7), but other smoothed-profile functions may be chosen if required, see [245]

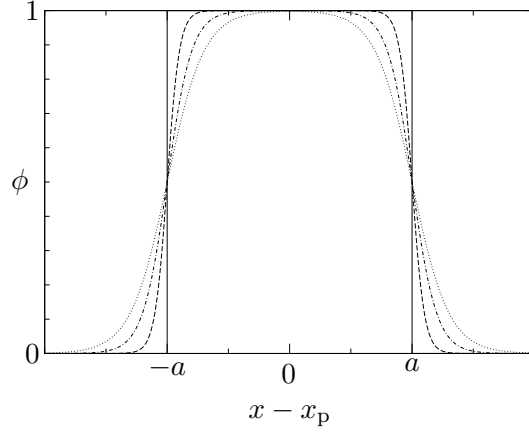


Figure 3.5.: Smoothed profile function ϕ in 1-D. Four interface thickness are depicted: $\xi = 0$ (solid line), $0.05a$ (dashed line), $0.1a$ (dashed-dotted line), $0.15a$ (dotted line).

is obtained by superimposition of rigid-body motions, SPM guarantees that the particle velocity field is identically divergence-free [201]. This is certainly a good property of the method because it assures that the spatial approximation introduced by the smoothed profile technique does not induce numerical dissipation due to violation of the incompressibility constraint. This is a crucial point to avoid particle accumulation structures induced as an artefact of the numerical technique. Finally, as shown in [201] and [187], no-slip and no-penetration conditions are automatically verified by the smoothed profile approach and the global velocity field can be obtained as a combination of particle- and fluid-phase velocities (\mathbf{u}_p and \mathbf{u}_f , respectively)

$$\mathbf{u}(\mathbf{x}, t) = \phi(\mathbf{x}, t)\mathbf{u}_p(\mathbf{x}, t) + [1 - \phi(\mathbf{x}, t)] \mathbf{u}_f(\mathbf{x}, t). \quad (3.10)$$

Using the same stiffly-stable splitting scheme of (3.1) (with the viscous scaling), and coupling it with the smoothed profile method as done in [245], the algorithm reads

$$\mathbf{P}_i^{n+1} = \mathbf{P}_i^n + \Delta t \sum_{k=0}^K a_k \mathbf{V}_i^{n-k} \quad (3.11a)$$

$$\mathbf{O}_i^{n+1} = \mathbf{O}_i^n + \Delta t \sum_{k=0}^K a_k \mathbf{\Omega}_i^{n-k} \quad (3.11b)$$

$$\begin{aligned} \frac{\gamma_0 \tilde{\mathbf{u}} - \alpha_0 \mathbf{u}^n - \alpha_1 \mathbf{u}^{n-1}}{\Delta t} &= -\beta_0 [\mathbf{N}(\mathbf{u}^n, \mathbf{u}^n) - \text{Gr}\theta^n \mathbf{e}_y] \\ &\quad - \beta_1 [\mathbf{N}(\mathbf{u}^{n-1}, \mathbf{u}^{n-1}) - \text{Gr}\theta^{n+1} \mathbf{e}_y] \end{aligned} \quad (3.11c)$$

$$\frac{\gamma_0 \tilde{\theta} - \alpha_0 \theta^n - \alpha_1 \theta^{n-1}}{\Delta t} = -\beta_0 N(\mathbf{u}^n, \theta^n) - \beta_1 N(\mathbf{u}^{n-1}, \theta^{n-1}) \quad (3.11d)$$

$$\nabla^2 p^* = \frac{\gamma_0}{\Delta t} \nabla \cdot \tilde{\mathbf{u}} \quad (3.11e)$$

$$\begin{aligned} \frac{\partial p^*}{\partial \hat{n}} &= -\beta_0 \hat{n} \cdot \left(\frac{D\mathbf{u}^n}{Dt} + \nabla \times \boldsymbol{\omega}^n - \text{Gr}\theta^n \mathbf{e}_y \right) \\ &\quad - \beta_1 \hat{n} \cdot \left(\frac{D\mathbf{u}^{n-1}}{Dt} + \nabla \times \boldsymbol{\omega}^{n-1} - \text{Gr}\theta^{n-1} \mathbf{e}_y \right) \end{aligned} \quad (3.11f)$$

$$-\nabla^2 \mathbf{u}^* + \frac{\gamma_0}{\nu \Delta t} \mathbf{u}^* = \frac{\gamma_0}{\Delta t} \tilde{\mathbf{u}} - \nabla p^* \quad (3.11g)$$

$$-\nabla^2 \theta^{n+1} + \frac{\gamma_0 \text{Pr}}{\Delta t} \theta^{n+1} = \frac{\gamma_0 \text{Pr}}{\Delta t} \tilde{\theta} \quad (3.11h)$$

$$\mathbf{F}_i^n = \frac{1}{\Delta t} \int_{\Omega} \phi_i^{n+1} (\mathbf{u}^* - \mathbf{u}_p^n) d\mathbf{x} \quad (3.11i)$$

$$\mathbf{R}_i^n = \frac{1}{\Delta t} \int_{\Omega} \mathbf{r}_i^{n+1} \times [\phi_i^{n+1} (\mathbf{u}^* - \mathbf{u}_p^n)] d\mathbf{x} \quad (3.11j)$$

$$\mathbf{V}_i^{n+1} = \mathbf{V}_i^n + M_i^{-1} \Delta t \sum_{k=0}^K a_k \mathbf{F}_i^{n-k} \quad (3.11k)$$

$$\mathbf{\Omega}_i^{n+1} = \mathbf{\Omega}_i^n + I_i^{-1} \Delta t \sum_{k=0}^K a_k \mathbf{R}_i^{n-k} \quad (3.11l)$$

$$\phi^{n+1} \mathbf{u}_p^{n+1} = \sum_{i=1}^{N_p} \phi_i^{n+1} [\mathbf{V}_i^{n+1} + \mathbf{\Omega}_i^{n+1} \times (\mathbf{x} - \mathbf{P}_i^{n+1})] \quad (3.11m)$$

$$\nabla^2 p_p = \gamma_0 \nabla \cdot \left[\frac{\phi^{n+1} (\mathbf{u}_p^{n+1} - \mathbf{u}^*)}{\Delta t} \right] \quad (3.11n)$$

$$\frac{\partial p_p}{\partial \hat{\mathbf{n}}} = \frac{\gamma_0}{\Delta t} (\phi^{n+1} (\mathbf{u}_p^{n+1} - \mathbf{u}^*)) \cdot \hat{\mathbf{n}} \quad (3.11o)$$

$$\frac{\gamma_0 \mathbf{u}^{n+1} - \gamma_0 \mathbf{u}^*}{\Delta t} = \frac{\gamma_0 \phi^{n+1} (\mathbf{u}_p^{n+1} - \mathbf{u}^*)}{\Delta t} - \nabla p_p, \quad (3.11p)$$

where \mathbf{O}_i , \mathbf{r}_i , \mathbf{F}_i and \mathbf{R}_i are orientation, distance vector from the instantaneous centre of rotation, forces and torques on the i -th particle, the subscript p refers to the perturbation fields induced by the particle, * refers to the flow field obtained without updating the particle perturbations, a_k originates from the backward differentiation formulae adopted for integrating the particle positions and velocities and the total pressure field can be reconstructed by the relation $p^{n+1} = p^* + p_p$.

Different from the single-phase flow, two thermal diffusivity coefficients have to be considered for including the thermal coupling. Therefore, the Prandtl number is not constant in the domain. To model such an aspect, the concentration function ϕ is employed in a more convenient definition of a global Prandtl number

$$\text{Pr} = \phi(\mathbf{x}, t) \text{Pr}_p + [1 - \phi(\mathbf{x}, t)] \text{Pr}_f. \quad (3.12)$$

where $\text{Pr}_p = \nu / \kappa_p$ and $\text{Pr}_f = \nu / \kappa_f$.

4. Particle–Boundary and Particle–Particle Interaction

The modelling of the motion of non-zero-size tracers in thermocapillary- or mechanically-driven flows can be extremely challenging when the particles are advected close to any boundary. This is the case for the configurations presented in Chapter 2, where the streamlines are very dense near the boundaries. It implies that if we have an initially random distribution of particles, a significant amount of tracers will pass in the close vicinity of the driving boundary within a given time. Thus, modelling the particle–boundary interaction may be of crucial importance for predicting the particle trajectories with a reasonable accuracy using a one-way coupling approach.

One of the main issues of simulating particle-laden flows consists of modelling the local particle–boundary interaction. This may have a global impact on the prediction of particle accumulation structures as reported in [194, 195]. In this framework one-way-coupled simulations are commonly employed modelling the particle–boundary interaction as an inelastic collision in normal direction to the boundary. However, to improve the accuracy of such predictions, the particle-to-fluid density ratio and the particle size are of major importance and therefore they will be investigated in this chapter for simplified two-dimensional problems. The main goal of the corresponding fully-resolved simulations is to improve the inelastic collision model including a prediction of the minimum lubrication gap width in the state of a stationary accumulation structure. The last part of this chapter is concerned with the role of particle–particle interactions in PAS phenomena.

4.1. Particle–Boundary Interaction

One of the main goals of simulating particle-laden flows consists in accurately predicting the particle trajectories. Moreover, considering closed flows for which the streamlines cluster towards the driving boundary, the particle–boundary interaction phenomena become more and more important because a high volume flux is concentrated in a thin layer nearby such boundaries.

The particles will move so close to the driving boundary that the thickness of the lubrication gap formed between their surface and the boundary itself may possibly be several times smaller than the particle radius. In such scenario it is obviously not possible to neglect the particle size effects (as done in a point-wise particle approach), but all the relevant scales need to be solved (fully-resolved simulations) or, at least, modelled.

Hofmann & Kuhlmann [126] proposed to mimic the particle–free-surface interaction with the so-called PSI (particle–surface interaction) model. Motivated by experimental observations (see e.g. [270, 255]), it is nothing but a rebound scheme. Along the free-surface normal direction the velocity of the particle is set to zero if the velocity vector points out of the fluid domain. It is shown by many authors (see e.g. [195, 126, 194, 151]) that particle accumulation phenomena can be well captured employing such a model. Even though these authors are aware of the importance of properly modelling the lubrication gap width (see e.g. [194]), at the time being it is commonly neglected in their numerical simulations. In fact they set the minimum distance between particle centroid and driving boundary equal to the particle radius.

The fully-resolved approach does not require any modelling operation. Therefore, it can be used to obtain a prediction of the lubrication gap width to be included in the PSI model for improving the point-wise particle results.

4.1.1. Particle-Surface Interaction Model

In case a one-way coupled approach is employed, the Maxey–Riley equation is solved to calculate the particle trajectories and no feedback effect from the particulate- to the fluid-phase is included. Moreover, as discussed in Chapter 2, the Maxey–Riley equation refers to a sphere in a non-uniform flow. In general, the Faxén and Saffmann corrections are considered for taking into account the trajectory curvature effect and the lift effect of a free-surface, respectively. However these corrections are not valid very close to the boundaries.

These considerations highlight the necessity to model the particle–boundary interaction and in the following we will introduce the PSI model. It assumes that when a particle is approaching a boundary there is a region of the fluid domain which cannot be accessed by the particle centroid due to the tracer’s finite-size. Indeed, if the distance between the particle centroid and a free-surface (assumed undeformable) or a wall equals the particle radius, this means that the particle experiences a collision with the boundary. Assuming the lubrication gap negligible, this condition implies that the particle centroids are not allowed to explore a region closer than the particle’s radii to the boundaries (the so-called *prohibited region*).

The assumption of the particle–surface interaction model is that, after such a collision, the particle slides along the boundary with zero surface-normal velocity since it is pushed towards the free-surface/wall. As soon as the particle velocity measured at its centroid is inward-pointing in normal direction to the boundary, the PSI model stops being effective on the particle trajectory until the next collision occurs.

A theoretical improvement of the model has been proposed by Mukin & Kuhlmann [194], who pointed out the sensitivity of PAS predictions to the size of the prohibited region and, therefore, the importance of including the lubrication gap width in the PSI model. The notion of *interaction length* Δ was consequently developed as the particle radius plus the minimum lubrication gap width, measured after the particle accumulated on a PAS. Operatively it indicates the thickness of the prohibited region measured from the boundaries of the fluid domain.

A sketch of the PSI model is depicted in fig. 4.1 for a two-dimensional flow field. The “collision” between particle and boundary is Δ far from the top wall/free-surface and represents the point of discontinuity between the trajectory predicted by the Maxey–Riley equation only and the one affected by the PSI model. A smooth release point is always characteristic of the model, as depicted in fig. 4.1.

Even though the notion of interaction length Δ was proposed in [194], it has never been applied because of the difficulty in giving an estimate of the minimum lubrication gap width δ . Therefore Δ has been approximated with the particle radius a , so far.

The improvement which can be introduced with the fully-resolved simulations consists in giving an estimate of $\delta = \Delta - a$ for obtaining better predictions from the Maxey–Riley equation plus PSI model. Moreover, a fully-resolved trajectory can give a qualitative measure of the errors committed employing a one-way coupled approach plus the particle–surface interaction model.

Owing to the inelastic character of the collision, an important drawback of the PSI model is that it cannot accurately predict the particle accumulation dynamics. This limit cannot be overcome improving the prediction of Δ and therefore the accumulation dynamics predicted by fully-resolved and one-way coupled approaches differs sensibly.

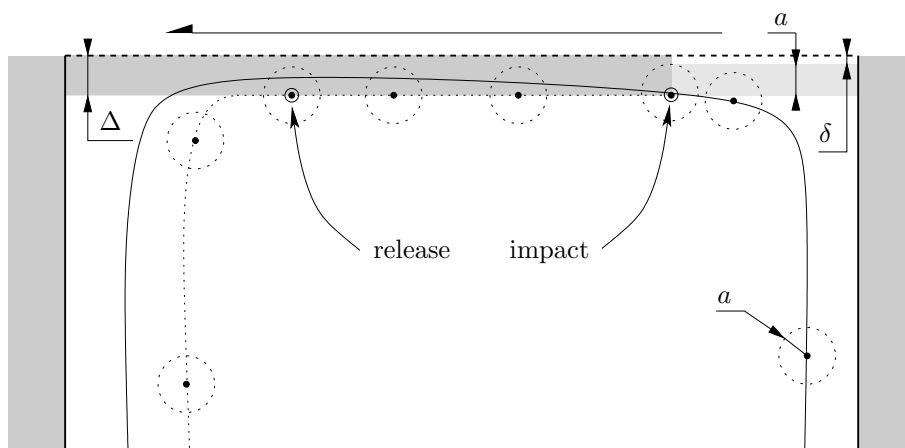


Figure 4.1.: Sketch of the particle–surface interaction (PSI) model. The full line represents the trajectory predicted by the Maxey–Riley equation without any particle–boundary interaction model. The dotted line is obtained enforcing the PSI model after the collision between the particle and the boundary.

4.2. Particle–Free-Surface Interaction

The first case we consider is the interaction of a single particle with a free-surface. A numerical solution to the three-dimensional problem of particle motion in a liquid bridge is extremely demanding. However, for the interaction of particles with the free-surface, the local radius of curvature of the interface is much bigger than the particle radius. Then a good approximation may be obtained by considering the interface as flat. A further simplification we include is to deal with the two-dimensional thermocapillary flow in the limit of $Ca \rightarrow 0$. We therefore consider a square cavity of linear length L with one free-surface. For $Pr \rightarrow 0$ and if buoyancy is neglected the temperature field is linear (conductive) and the shear stress on the free-surface is constant. Figure 4.2 shows a sketch of this shear–stress-driven cavity.

In the limit $Pr \rightarrow 0$ we use a viscous scaling for which the Reynolds number is the thermocapillary Reynolds number defined as in (2.4) with $d = L$. The non-dimensional Navier–Stokes equations are expressed by (2.12). In dimensionless form, the flow field boundary conditions read as

$$x = \pm 1/2 : \quad u = v = 0, \quad (4.1a)$$

$$y = -1/2 : \quad u = v = 0, \quad (4.1b)$$

$$y = 1/2 : \quad \partial_y u = -Re, \quad v = 0. \quad (4.1c)$$

Fixing the Reynolds number to 1000 and considering circular particles, the investigated parameters will be defined by the particle radius, $a = a_p/L$, and the particle-to-fluid density ratio, $\varrho = \rho_p/\rho_f$ where a_p and ρ_p are the particle radius and density, respectively.

A preliminary simulation is made for reaching a steady-state flow field. Thereafter, a single particle is instantaneously released. This creates a initial numerical mismatch in the part of the domain where the particle is suddenly inserted because of the rigidity constraint. Owing to the small Stokes numbers under investigation, the effect of the initial numerical mismatch is negligible (see [244]).

For finite-size particles heavier than the fluid, two main mechanisms make the particle trajectory differ from a streamline initialized in the same position: inertia and particle–boundary

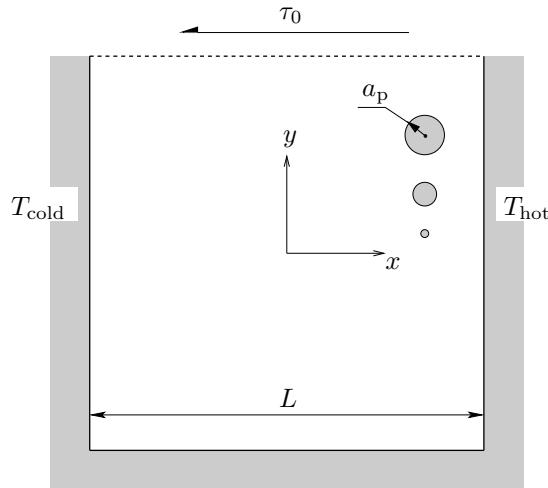


Figure 4.2.: Sketch of the two-dimensional shear-stress-driven cavity. The three particle sizes which are simulated via fully-resolved simulations are depicted in scale.

interaction. These two counteracting actions can lead the particle to become trapped in a limit cycle which represents an approximation (non-interacting particles) of two-dimensional PAS. After computing the limit cycle trajectory via fully-resolved simulations, it will be possible to extract the Δ from it and compare such a two-dimensional PAS with the one predicted via one-way coupling plus PSI model.

4.2.1. Fully-Resolved Simulations

All the simulations reported below are obtained using a functional space of 5th-order polynomials for the DG-FEM discretization and employing an interface layer thickness $\xi = 0.05a$. The time discretization adapts the time step Δt as function of ξ in order to minimize the numerical error (see [187]).

The scales of the flow, the particle and the lubrication gap are fully resolved. The trajectories are calculated in two separated steps. When the particle passes close to the free-surface the h -adaptivity of our numerical method is employed for solving up to the smallest scales (lubrication gap) present during the particle-boundary interaction phenomenon, see fig. 4.3a. After the tracer moved away from the free-surface, the smallest scales to resolve are the particle scales and the entire flow field is spectrally interpolated on a new grid (fig. 4.3b). The new distribution of the elements is more refined along the expected particle trajectory, considering that for small Stokes numbers it will not differ much from a streamline (see fig. 4.4).

Poincaré Maps

As depicted in fig. 4.4, the driving boundary represents a region of the flow field where the streamlines are dense. To investigate the effect of inertia and particle-free-surface interaction a Poincaré section is employed at $y = y_P$. Selecting y_P sufficiently close to the free-surface, the deviation of the particle trajectories from a streamline will be strongly affected by the particle-boundary interaction if the particle moves in $y > y_P$. Viceversa, if $y < y_P$ the inertial effect will be dominant.

In describing the particle dynamics by mean of a Poincaré map we make the hypothesis that the Poincaré points only depend on (x_{in}, y_P) for the given dynamical system, where x_0 is

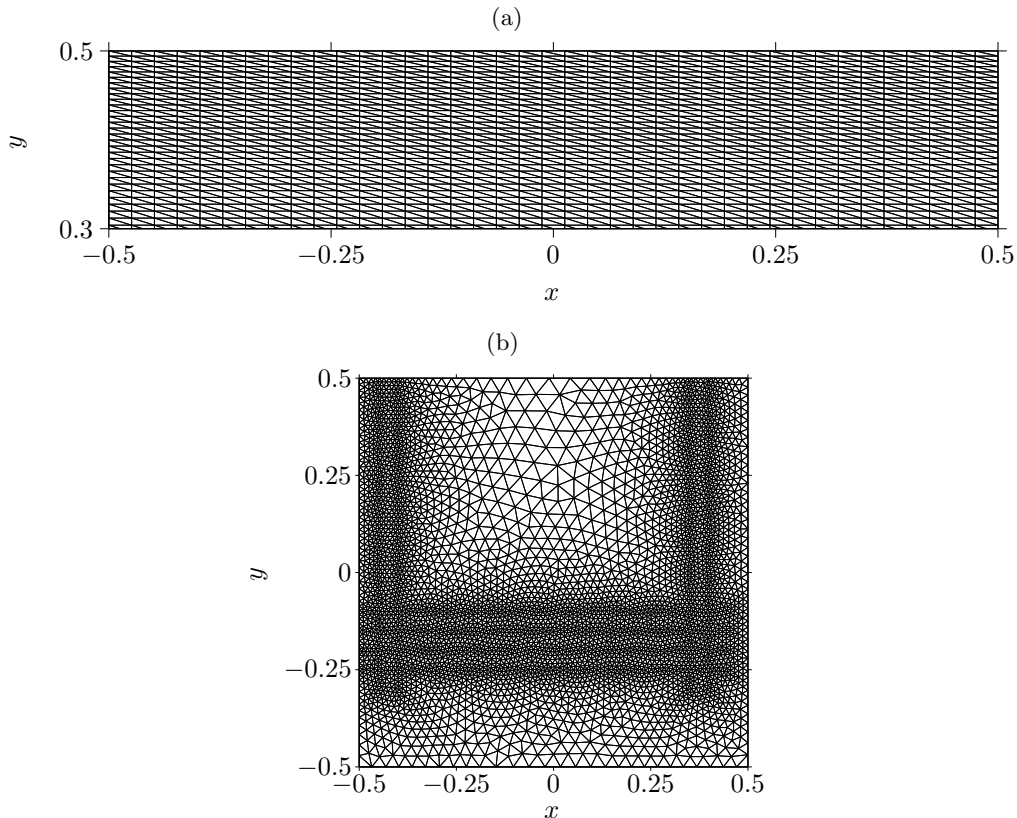


Figure 4.3.: Example of the computational mesh used for the fully-resolved simulations in the case of $a = 0.03$. Figure 4.3a shows a cut-off of the grid employed when the particle moves close to the free-surface (the actual numerical results are produced on a six-times finer computational mesh). The computational grid employed for the particle trajectory in the bulk region is depicted in (b).

the initial position of the particle. In fact, owing to the small Stokes numbers, the relaxation time of the particle is very short if compared with the fluid flow time scale. This means that regardless of the initial velocity of the particle, its trajectory can be reliably computed just knowing the position where the particle has been initialized (see [244]). The Poincaré sections are obtained initializing the particle at $\Delta y = 0.1$ from y_P with its centroid velocity-matched with the unperturbed fluid. The initial conditions for the free-surface and the bulk mappings are denoted with y_s^{fs} and y_s^{b} , respectively. Selecting $y_P = 0.3$ assures that all the trajectories of interest in determining the limit cycle are covered and that boundary and inertia effects are almost decoupled.

The Poincaré maps are constructed linking the first intersection of the particle trajectory with $y = y_P$ to the second ordered return on the Poincaré line

$$P^{\text{fs}}(x) : x_{\text{in}}^{\text{fs}} \rightarrow x_{\text{out}}^{\text{fs}}, \quad P^{\text{b}}(x) : x_{\text{in}}^{\text{b}} \rightarrow x_{\text{out}}^{\text{b}}. \quad (4.2)$$

Combining the Poincaré maps which result from the two parts of the particle trajectory ($P^{\text{fs}}(x)$ and $P^{\text{b}}(x)$ for free-surface and bulk, respectively), an oriented Poincaré map

$$P(x) : x_n \rightarrow x_{n+1} = P^{\text{b}}[P^{\text{fs}}(x)] \quad (4.3)$$

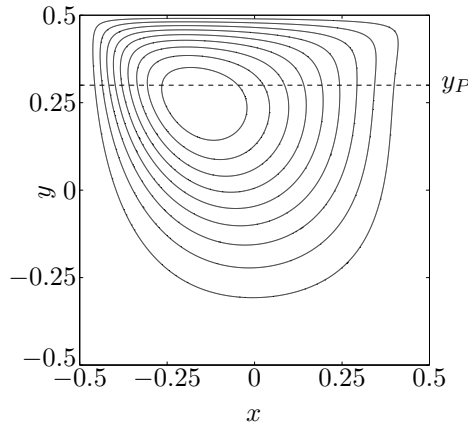


Figure 4.4.: Streamlines of the shear-stress-driven cavity for $Re = 1000$.

is obtained in order to describe the particle dynamics. Figure 4.5 makes clear how to construct the three mappings.

Existence of a Stable, Global Limit Cycle

Employing a fully-resolved approach for describing the particle dynamics we can demonstrate whether a limit cycle exists in a certain set-up. Moreover, analyzing the oriented Poincaré map it is possible to describe the character of such a limit cycle, determining if it is global or local, stable or unstable. The first parametric study investigates three particle radii, $a = 0.01, 0.03, 0.05$, for the particle-to-fluid density ratio $\varrho = 2$.

The free-surface and bulk mappings are combined in fig. 4.6 for all the considered particle radii. An example of how to employ the two maps for building the iterative Poincaré map is depicted in the case of particle radius $a = 0.05$ (triangles). A particle which starts at $(x, y) = (0.255, 0.3)$ (open diamonds) is mapped by the free-surface mapping at $(x, y) = (-0.39, 0.3)$ on the vertical axis (A and B segments on the graph). Starting from this position the particle will move in the bulk region for completing its first return (C and D segments on the graph), up to the coordinates $(x, y) = (0.318, 0.3)$ (full diamond). Therefore, the Poincaré map will consist of the corresponding connection between the open and the full diamonds.

A first remark can be made considering the free-surface and the bulk mappings for the finite-size tracers, P^{fs} and P^{b} respectively, compared to the fluid element mappings (indicated by the subscript ψ). For the latter case each initial position of the perfect tracer is mapped in itself after an ordered return and $P_{\psi}^{\text{fs}} = [P_{\psi}^{\text{b}}]^{-1} = P_{\psi}$. Owing to the asymmetry of the flow, the free-surface mapping compresses the fluid element trajectories along x ($[P_{\psi}^{\text{fs}}]' < 1$) and the bulk mapping completely recovers such a compression ($[P_{\psi}^{\text{b}}]^{-1} = P_{\psi}^{\text{fs}}$). The comparison between the slopes of P^{fs} and $[P^{\text{b}}]^{-1}$ for all the investigated finite-size particles shows a higher absolute value slope of $[P^{\text{b}}]^{-1}$ with respect to $[P_{\psi}^{\text{b}}]^{-1}$ and a lower one for P^{fs} . This is due to inertia effects which centrifuge out the particle trajectory (dominant in the bulk) and finite-size effects which repel the particle from the free-surface because of viscous lubrication forces.

P^{fs} and $[P^{\text{b}}]^{-1}$ intersect in one point only. This represents a fixed point for the iterative Poincaré map which uniquely determines the limit cycle. Moreover, the combined map reported in fig. 4.7 for all the particle sizes, is a monotonic continuous function with $0 < P'(x) < 1$, which characterize the limit cycle as stable and globally attracting.

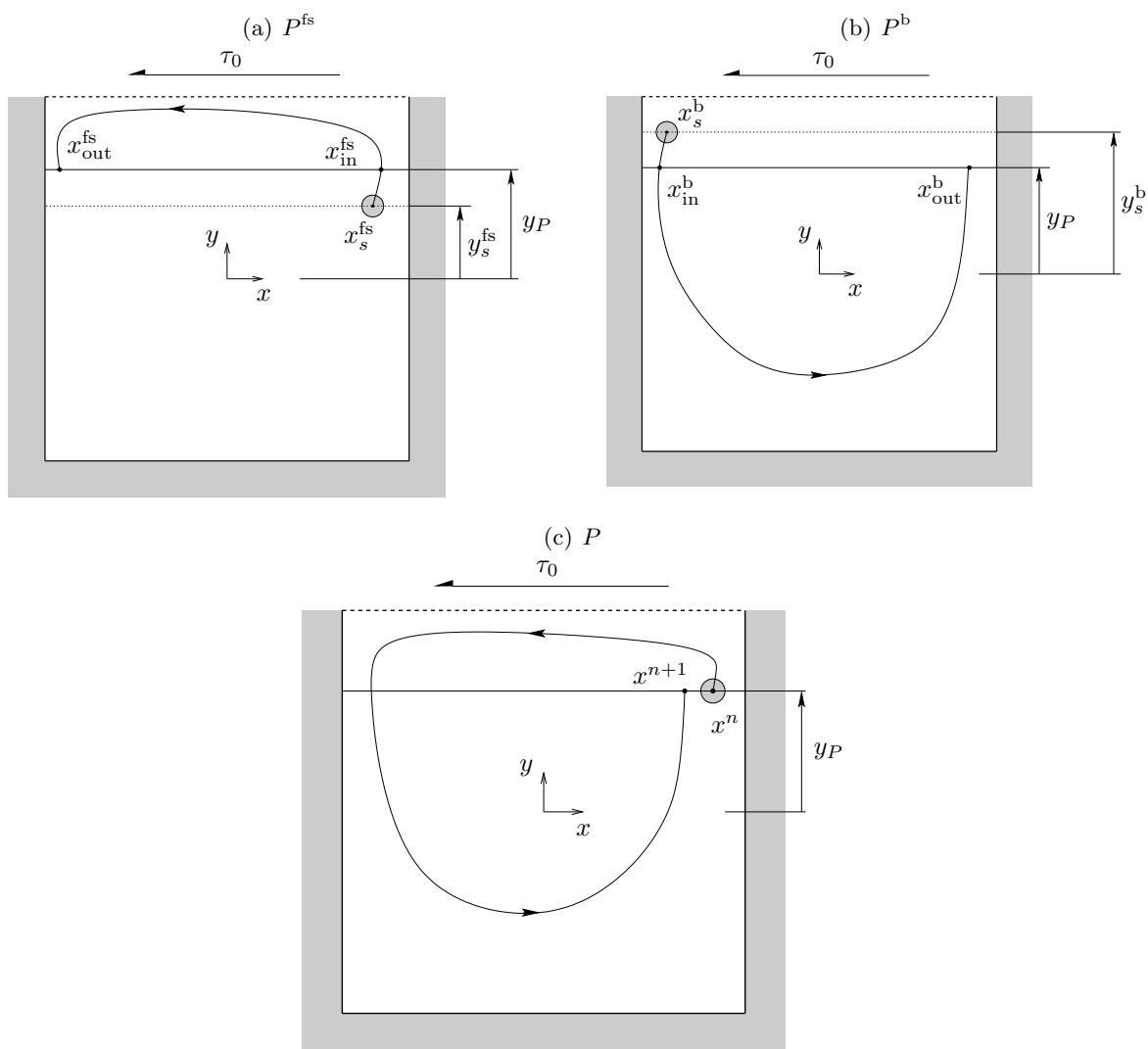


Figure 4.5.: Schematic representation of free-surface P^{fs} , bulk P^{b} and iterative maps P , respectively (a), (b) and (c).

This result can be understood if we consider that for heavy particles ($\varrho > 1$) the inertia effect is dominant far away from the boundaries and tends to centrifuge the particle out from the vortex core. On the contrary, when a particle approaches the free-surface, the repulsion of the boundaries due to lubrication effects dominates and induces a net centripetal effect on the particle trajectory. The equilibrium between the two effects is reached when the particle moves on the limit cycle. Along with this argument it is expected that the attraction to the limit cycle from the interior is due to inertial effects which, in two-dimensional flows, are the only process which can push a particle towards the periodic attractor from inside. Therefore, in the limit of particle-to-fluid density ratio $\varrho \downarrow 1$, the degeneration of the limit cycle to a fixed point is expected for a non-zero sized particle. Experimental evidence of this case is reported in [257], where also particles lighter than the fluid are considered. As a further remark, fig. 4.7 shows that the bigger the particle the higher its attraction rate to the limit cycle.

In literature (see e.g. [151]) the existence of a single, stable, global limit cycle is reported

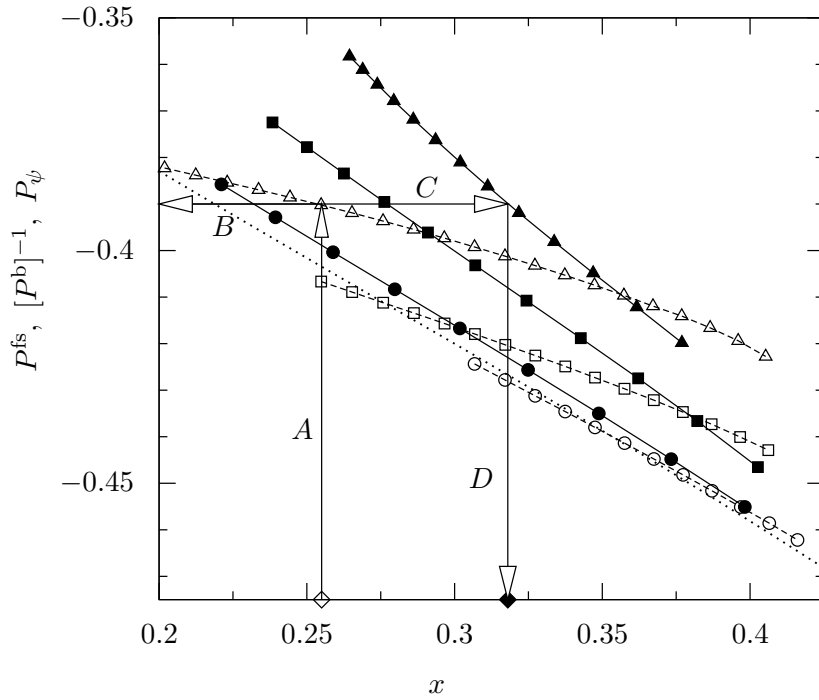


Figure 4.6.: Free-surface (open symbols) and bulk (full symbols) mappings for three particle radii: $a = 0.01$ (\circ), 0.03 (\square) and 0.05 . (\triangle). The thick dotted-line indicates the fluid element mapping P_ψ , whereas the arrows show how to employ the two mappings to build the iterative Poincaré map (open diamond to full diamond) in a representative case for $a = 0.05$. Referring to fig. 4.5, the open diamonds would represent $x_{\text{in}}^{\text{fs}}$, the left arrow head of BC is $x_{\text{out}}^{\text{fs}}$ and x_{in}^{b} , the full diamond is $x_{\text{out}}^{\text{b}}$.

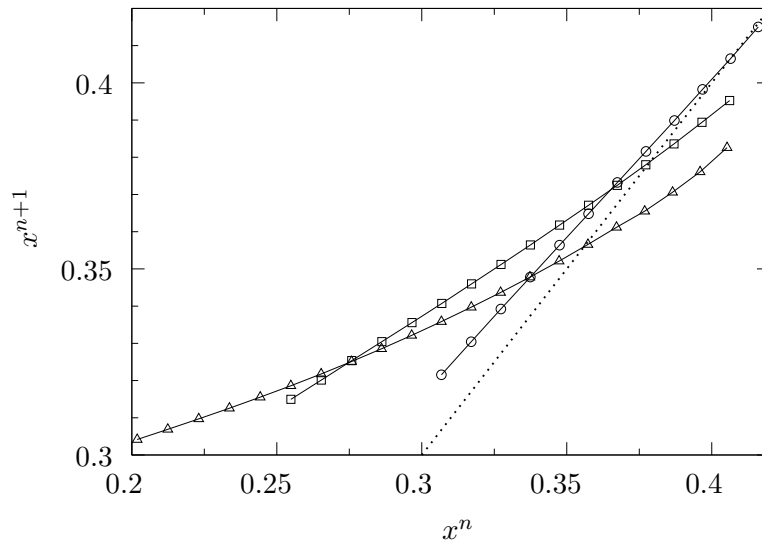


Figure 4.7.: Iterative Poincaré map $x_{n+1} = P(x_n)$ at $y_0 = 0.3$ for $\text{Re} = 1000$, $\varrho = 2$ and $a = 0.01$ (\circ), 0.03 (\square) and 0.05 (\triangle) in a shear-stress-driven cavity flow. The dotted line indicates the bisector and its intersection with the Poincaré map defines the fixed point, i.e. a point on the limit cycle.

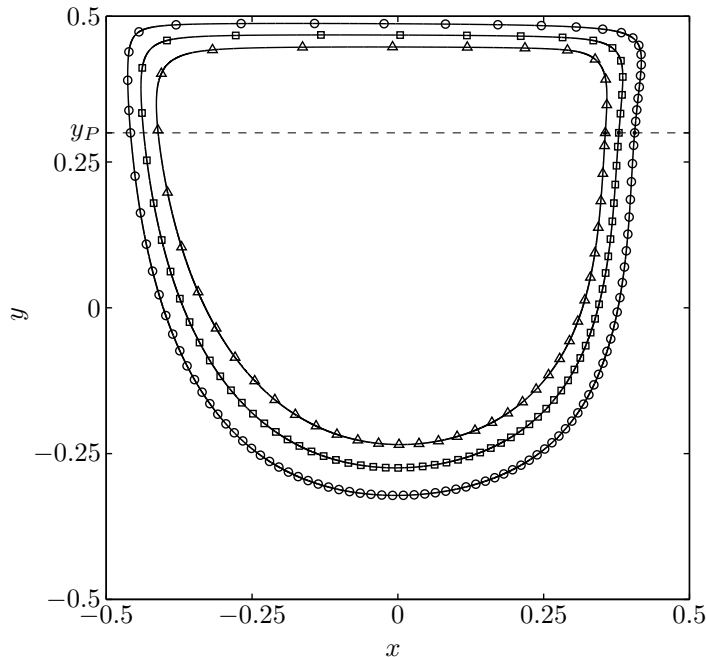


Figure 4.8.: Limit cycles for particles with $\varrho = 2$ and $a = 0.01$ (\circ), 0.03 (\square), 0.05 (\triangle) in a shear-stress-driven cavity for $\text{Re} = 1000$.

for the case of a three-dimensional axisymmetric liquid-bridge flow for which a two-dimensional PAS is observed. In Chapter 5 we investigate this case and compare with experiments, testing the improvement which is obtained by employing the fully-resolved simulation results in the PSI model.

Parameter Dependence of the Limit Cycle

The unique intersection between the iterative maps and the bisector line defines $x_n = x_{n+1} = x^*$ such that a particle placed at $(x, y) = (x^*, y_P)$ moves along the limit cycle. Figure 4.8 shows the limit cycles for $\text{Re} = 1000$, $\varrho = 2$ and $a \in \{0.01, 0.03, 0.05\}$. In vicinity of the free-surface the particles move almost parallel to it. This is a first confirmation of the good approximation made by the PSI model in assuming an inelastic collision between particle and boundary. Moreover, for the three investigated cases, the minimum lubrication film thickness δ between the particle's surface and the free-surface is one or two orders smaller than the particle radius itself.

Referring to [194], the interaction length $\Delta = a + \delta$ (minimum distance between the free-surface and the particle centroid) is a key parameter of the PSI model. Employing the fully-resolved approach, the interaction length is straightforward to compute once the limit cycles are obtained.

In order to compare the results for different particle radii, the interaction length is plotted in fig. 4.9 normalizing it with the particle radius. It can be noticed that the minimum normalized lubrication gap width δ/a is strongly depending on the particle radius a . The smaller the particle the less it is capable to squeeze the lubrication gap.

A second parameter of investigation is the particle-to-fluid density ratio. In this case the particle radius has been fixed to $a = 0.05$ and nine different density ratios $\varrho \in [1.2, 2]$ are considered for $\text{Re} = 1000$. The complete Poincaré map P is employed as before to determine the fixed points and the corresponding limit cycles. Figure 4.10b depicts the iterative maps

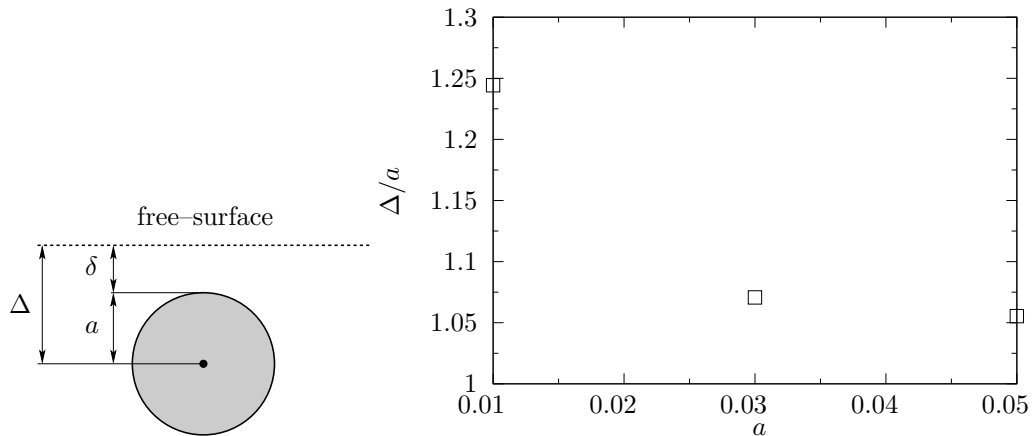


Figure 4.9.: Normalized interaction length Δ/a as function of the particle radius a for a particle-free-surface interaction in a shear-stress-driven cavity with $\text{Re} = 1000$ and $\varrho = 2$.

for all the investigated density ratios and shows the strong dependence of the fixed point on ϱ . Thereafter, comparing the slopes of the iterative maps in proximity of the corresponding fixed points, they do not sensibly depend on ϱ . Hence the asymptotic rate of attraction to the limit cycle, $P'(x^*)$, is a weak function of the particle-to-fluid density ratio.

As done in the previous case, computing the trajectories of particles initialized in $(x, y) = (x^*, y_P)$ each periodic orbit is calculated and depicted in fig. 4.10c. As ϱ increases the limit cycles become larger. This smooth trend results in period orbits for light particles which are completely nested in limit cycles for heavier particles.

Once again the interaction length Δ is obtained from the periodic orbits and fig. 4.11 depicts it, normalized with the particle radius, as function of the particle-to-fluid density ratio. The dependence of the minimum lubrication gap on ϱ is even stronger than the one observed as function of the particle radius. Indeed δ covers a wide range of scales passing from two orders of magnitude smaller than the particle radius ($\varrho = 2$) to the same order of a ($\varrho = 1.2$). Hence, the heavier the particle the more it is capable to squeeze the lubrication gap.

In case of a particle-free-surface interaction, the dependence of the interaction length $\Delta = f(a, \varrho)$ on the particle radius and density ratio has been determined. Table 4.1 lists the fixed-point x^* , the minimum lubrication gap width δ and the orbit time τ for all limit cycles computed for $\text{Re} = 1000$. In the next section these results are employed to improve the one-way coupled prediction including in the PSI model the lubrication gap width calculated via fully-resolved simulations.

4.2.2. Comparison of One-Way Coupling and Fully-Resolved Simulations

The comparison between one-way coupling and fully-resolved simulations is hereinafter made in terms of the prediction of the periodic orbits. Integrating the Maxey-Riley equation (2.22) and applying the PSI model using the fully-resolved estimate of the interaction length Δ , the one-way-coupled limit cycles are computed. Figure 4.12 demonstrate the influence of correctly predicting the interaction length as function of the particle radius for $\varrho = 2$ and $\text{Re} = 1000$. For $a = 0.05$ (fig. 4.12a) the fully-resolved and one-way-coupled results are in good agreement, for $a = 0.03$ (fig. 4.12b) they still well compare and for $a = 0.01$ (fig. 4.12c) the agreement is good. Hence the periodic orbits obtained for the present choice of parameters can be well approximated employing a one-way coupling approach and modeling the particle-free-surface interaction via

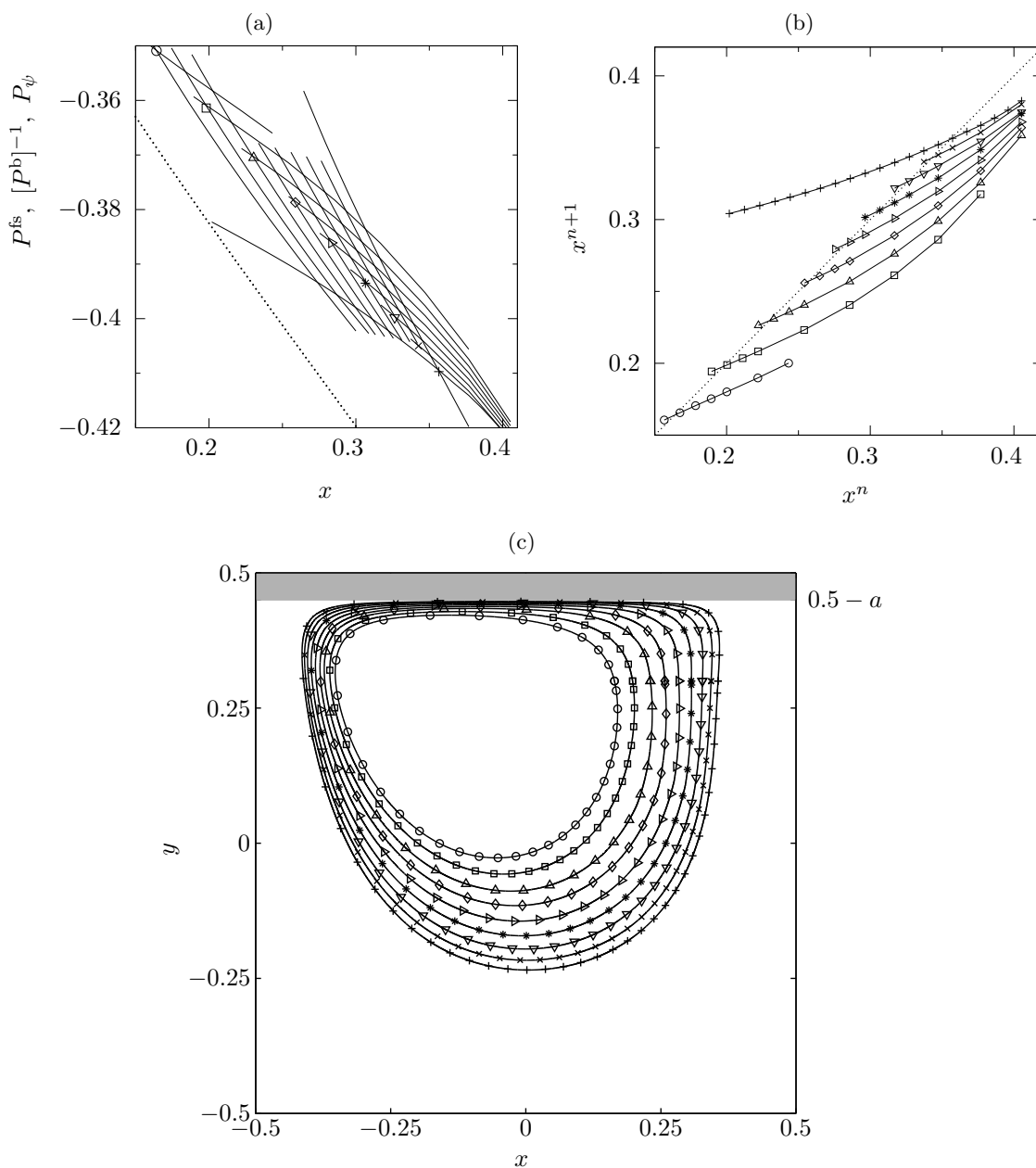


Figure 4.10.: Free-surface and bulk, iterative maps and limit cycles are plotted in (a), (b) and (c), respectively, for a shear-stress-driven cavity flow for $\text{Re} = 1000$, $a = 0.05$ and $\varrho \in [1.2, 2.0]$. Nine different particle-to-fluid density ratios are selected: $\varrho = 1.2$ (\circ), $\varrho = 1.3$ (\square), $\varrho = 1.4$ (\triangle), $\varrho = 1.5$ (\diamond), $\varrho = 1.6$ (\triangleright), $\varrho = 1.7$ ($*$), $\varrho = 1.8$ (∇), $\varrho = 1.9$ (\times) and $\varrho = 2$ ($+$). The dotted lines indicate the fluid element mapping and the bisector line in (a) and (b), respectively.

an improved PSI model. A further remark has to be made concerning the particle-boundary interaction model. The dashed lines in fig. 4.12 depicts the one-way coupling trajectories whether no PSI model is applied and, in these cases, no limit cycles were reached.

In order to show the improvement obtained in the one-way coupled trajectories plus PSI

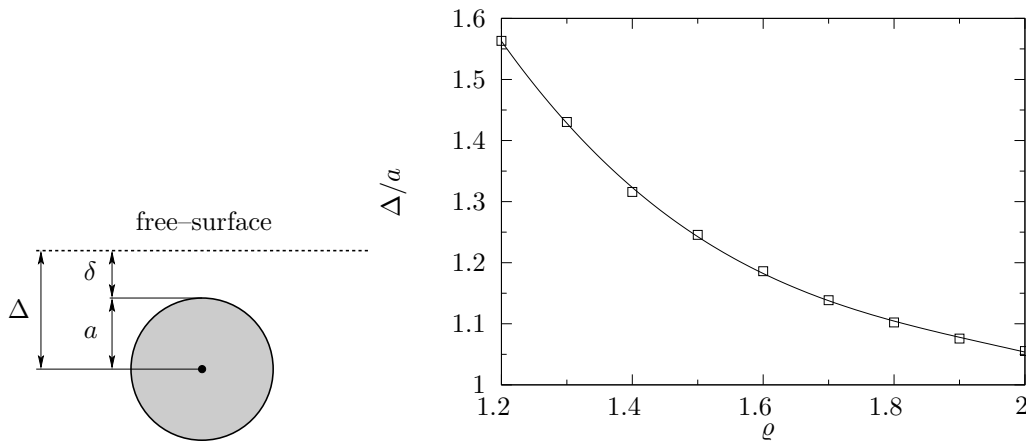


Figure 4.11.: Normalized interaction length Δ/a as function of the particle-to-fluid density ratio ρ for the particle–free-surface interaction in a shear–stress-driven cavity with $\text{Re} = 1000$ and $a = 0.05$. The markers represent fully-resolved simulation results and the solid line is obtained via a cubic best fit with homogeneous fitting weights.

model if the lubrication gap width is included, we compare the limit cycle for different particle-to-fluid density ratios ρ . Figure 4.13 depicts only the region near the free-surface and the periodic orbits obtained via fully-resolved simulations (marked line), the classical PSI model with $\Delta = a$ (dashed line) and the improved PSI model with $\Delta = a + \delta$ obtained from fig. 4.11 (solid line). Reducing the particle relative density the minimum lubrication gap width increases and the improvement obtained including the fully-resolved results in the PSI model becomes more and more important. Figure 4.13e shows that a one-way-coupled approach cannot predict with reasonable accuracy the reference trajectory obtained via fully-resolved simulations by the original PSI model. Hence, we further confirmed that an accurate evaluation of the minimum lubrication-gap width may be of crucial importance for accurately predicting PAS.

From the various comparisons reported we can conclude that the PSI model qualitatively well describes the particle–free-surface interaction if used in combination with a one-way coupling approach. More accurate predictions can be obtained if the minimum lubrication gap width is taken into account including the fully-resolved simulation results. However, modeling the interaction as an inelastic collision cannot, by definition, capture the dynamics of attraction of the particles to the limit cycle. Indeed, particles which are initially located in a region outside the limit cycle are instantaneously mapped on the limit cycle once they are released after “colliding” for the first time with the free-surface. As shown in the fully-resolved iterative maps, the particles approach the periodic orbit only asymptotically after multiple returns. On the contrary, if a particle is initialized inside the limit cycle, it will spiral towards it because of its inertia. This is taken care of by the Maxey–Riley equation.

4.3. Particle–Wall Interaction

The second case under consideration deals with the interaction between a single circular particle and a moving-wall. Owing to the small radius of the particle, even in the case of a curved moving wall the local curvature of the boundary is neglected and the particle–wall interaction can be investigated with good approximation considering a flat moving-wall. As done in the previous case, we study a two-dimensional configuration. The Reynolds number is of the order

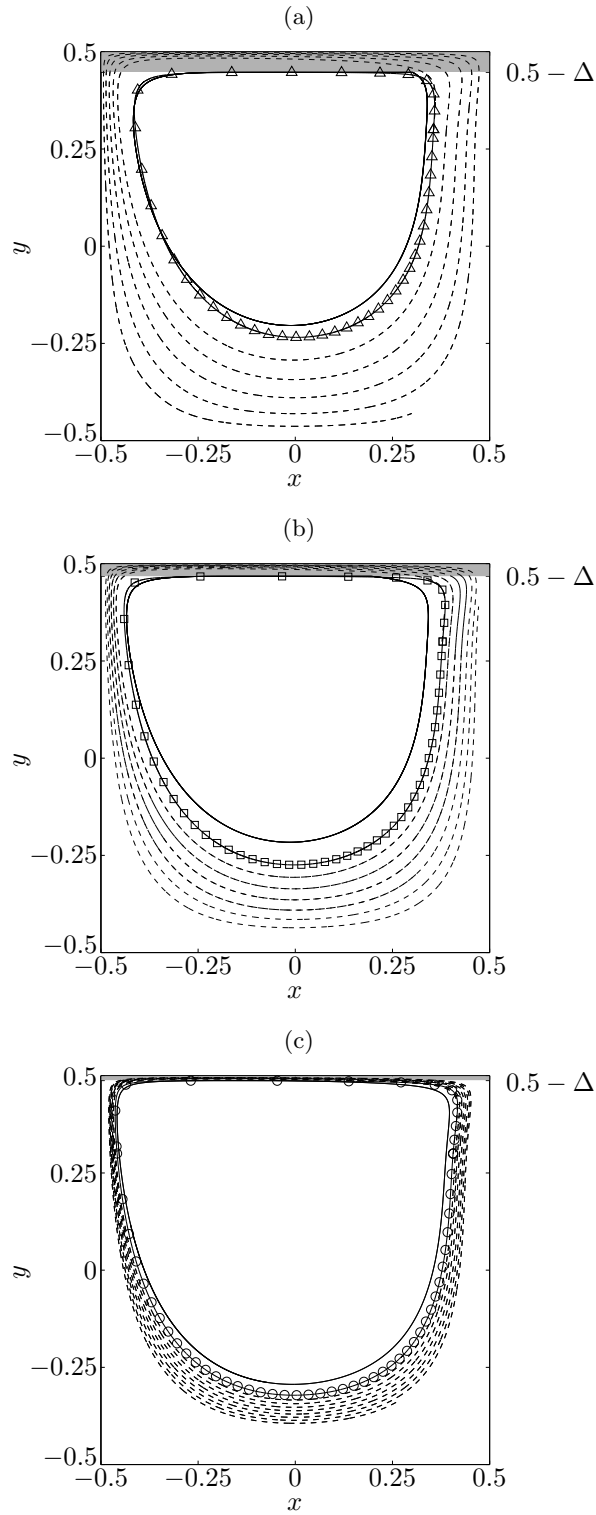


Figure 4.12.: Particle trajectories for three different particle radii, $a = 0.05, 0.03$ and 0.01 (a), (b) and (c) respectively. The marked and the solid lines depict fully-resolved simulations and Maxey–Riley equation plus PSI model results, respectively. The dashed line represents a one-way coupled trajectory for $t \in [0, 2]$ obtained initializing the particle at $(x, y) = (x^*, y_P)$. Without applying the PSI model no periodic orbit is reached.

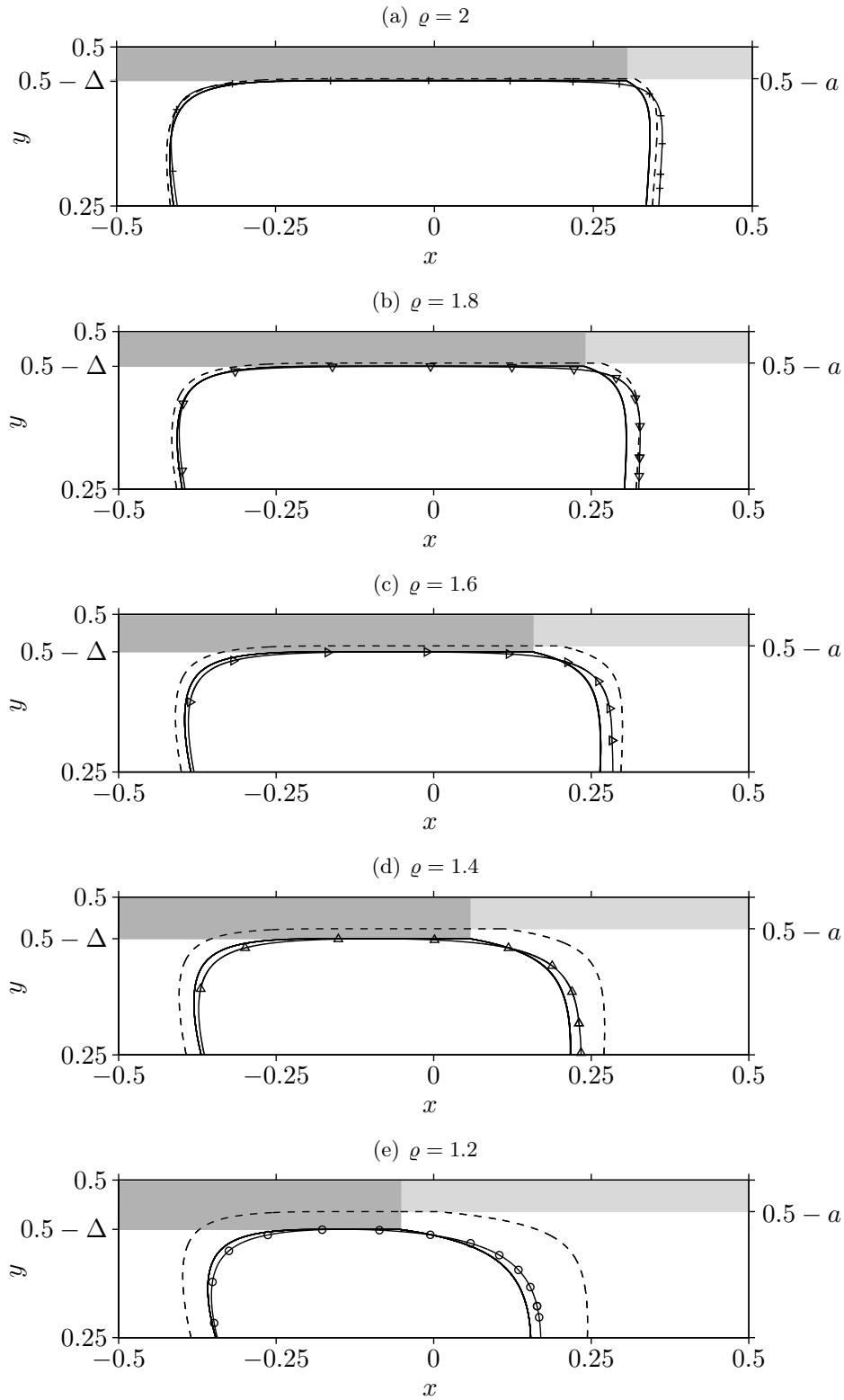


Figure 4.13.: Limit cycles for a shear-stress-driven cavity for $\text{Re} = 1000$, $a = 0.05$ and $\varrho \in [1.2, 2]$. Dashed and solid lines indicates the limit cycles obtained using a one-way coupling plus PSI model in which as interaction length $\Delta = a$ and $\Delta = a + \delta$ are selected, respectively. The markers show the reference periodic orbit obtained via the fully-resolved simulation.

Table 4.1.: Fixed-point x^* , minimum lubrication gap width δ and orbit time τ for the computed limit cycles in a shear–stress-driven cavity for $\text{Re} = 1000$.

a	ϱ	x^*	δ	τ
0.05	1.2	0.164	0.0282	0.0587
0.05	1.3	0.198	0.0215	0.0638
0.05	1.4	0.230	0.0158	0.0702
0.05	1.5	0.257	0.0123	0.0765
0.05	1.6	0.283	0.0093	0.0845
0.05	1.7	0.306	0.0069	0.0936
0.05	1.8	0.327	0.0051	0.1032
0.05	1.9	0.343	0.0038	0.1129
0.05	2.0	0.356	0.0028	0.1227
0.03	2.0	0.379	0.0021	0.1438
0.01	2.0	0.406	0.0024	0.1853

of the ones which will be investigated in the next chapter for the three-dimensional flows. A lid-driven square cavity of linear dimension L is considered; the moving-wall is located at the top and it moves tangentially to itself with constant velocity U . Figure 4.14 depicts a sketch of the lid-driven cavity.

The convective scaling is employed and the non-dimensional Navier–Stokes equations read as in (2.16) where the Reynolds number is

$$\text{Re} = \frac{UL}{\nu}. \quad (4.4)$$

The mathematical problem is closed by the non-dimensional boundary conditions

$$x = \pm 1/2 : \quad u = v = 0, \quad (4.5a)$$

$$y = -1/2 : \quad u = v = 0, \quad (4.5b)$$

$$y = 1/2 : \quad u = 1, \quad v = 0. \quad (4.5c)$$

The Reynolds number is fixed to 100, the particle-to-fluid density ratio $\varrho = \rho_p/\rho_f = 2$ and the particle radius, $a = a_p/L$, is assumed as parameter. The particles are instantaneously initialized in the steady-state flow field (see fig. 4.15) and the inertia and particle–boundary interaction effects will be investigated via Poincaré maps produced from the fully-resolved simulation results.

4.3.1. Fully-Resolved Simulations

As done for the case of a particle–free-surface, also for the particle–wall interaction 5th-order polynomials and interface layer thickness $\xi = 0.05a$ are employed for the fully-resolved simulations. In order to resolve all the relevant scales of the flow, a similar structure of the computational grids presented fig. 4.3 is employed. In the specific case of a particle moving away from the wall, the mesh has been adapted to the streamlines depicted in fig. 4.15. The DG-FEM element distribution in the bulk is very similar to the one shown in fig. 4.3b for the shear–stress-driven cavity.

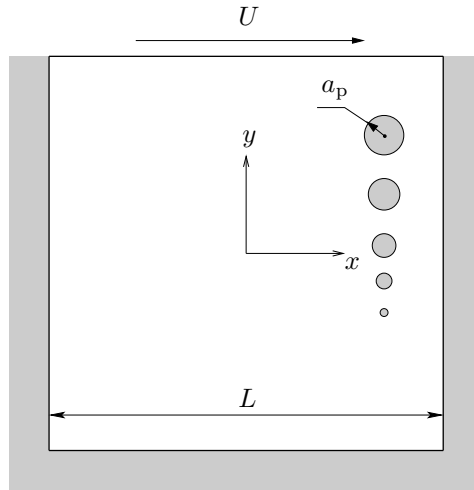


Figure 4.14.: Sketch of the two-dimensional lid-driven cavity. The five different particle sizes targeted in this investigation are depicted to scale.

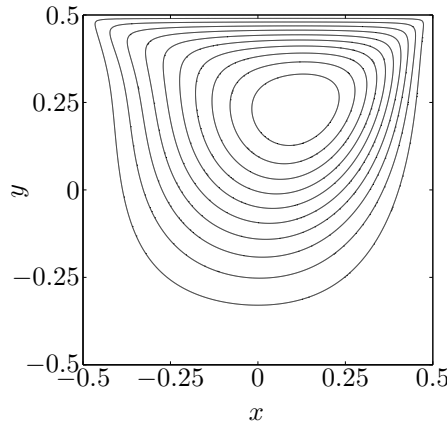


Figure 4.15.: Streamlines of the lid-driven cavity flow for $Re = 100$.

Poincaré Maps and Existence of a Stable, Global Limit Cycle

The Poincaré maps along the line $y = y_P$ are employed to investigate the particle motion in a lid-driven cavity. Choosing an ordinate on which to construct them which is close enough to the moving-wall (where the streamlines are dense), the inertial and particle-boundary interaction effects can be almost decoupled as done in the previous section. To do so we select $y_P = 0.3$ and we derive two complementary mappings, $P^w(x)$ and $P^b(x)$, which respectively describe the dynamics of a particle along $y = y_P$ in case the particle moves in $y > y_P$ (wall mapping) or in $y < y_P$ (bulk mapping)

$$P^w(x) : x_{in}^w \rightarrow x_{out}^w, \quad P^b(x) : x_{in}^b \rightarrow x_{out}^b. \quad (4.6)$$

Moreover, owing to the small Stokes numbers, the phase space of a particle consists with good approximation on its coordinates only. Once again, to avoid any dependence on the initial numerical transient due to the instantaneous particle injection in the steady flow field,

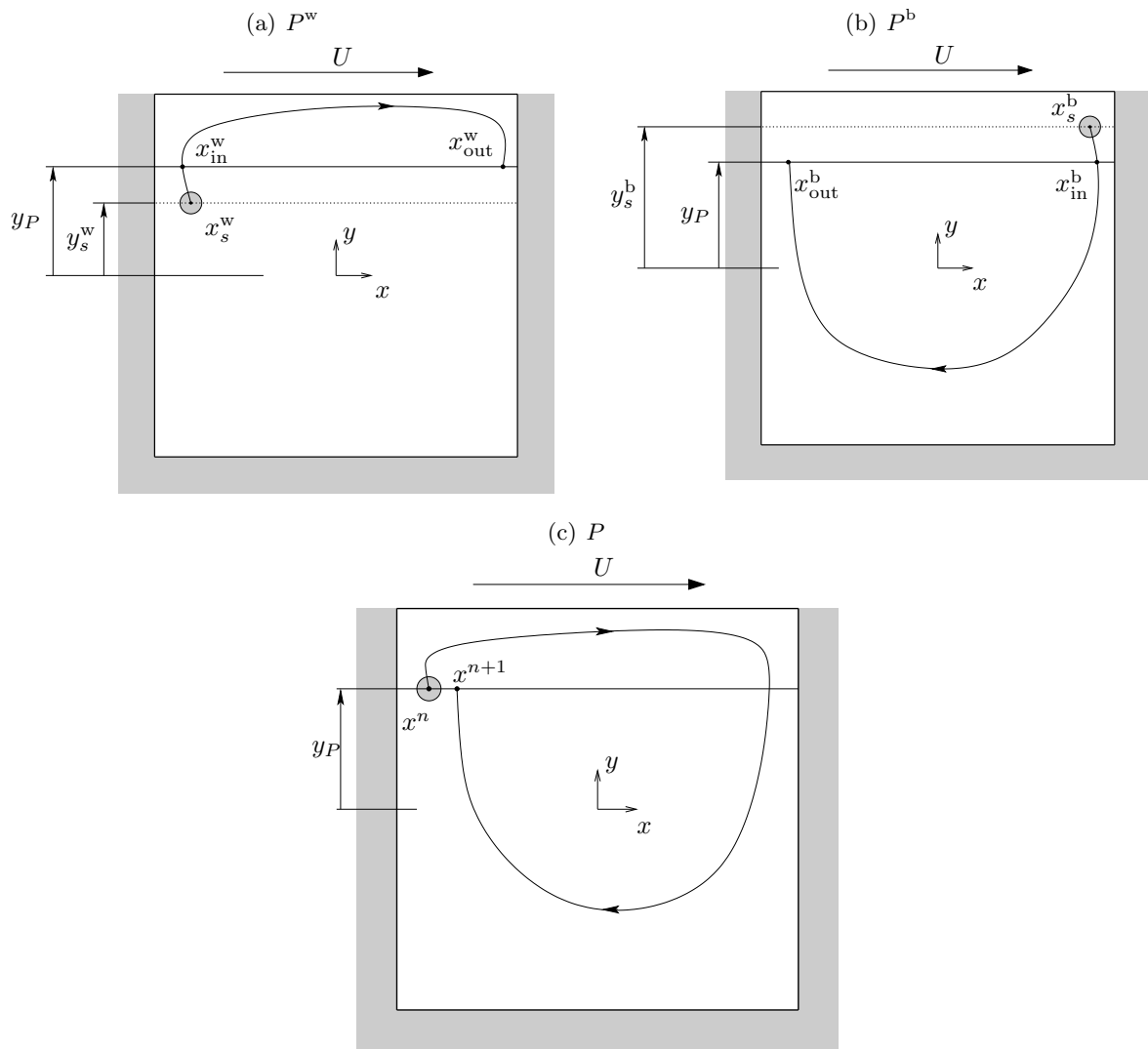


Figure 4.16.: Conceptual sketch of wall, bulk and iterative maps.

we initialize the particles at an ordinate y_s which is $\Delta y = 0.1$ far from y_P ($y_s^b = y_P + 0.1$, $y_s^w = y_P - 0.1$).

From the combination of the two Poincaré maps for the particle–wall interaction and bulk motion, a first oriented return Poincaré map $P(x) = P^b[P^w(x)]$ is obtained for defining the particle dynamics along y_P . The whole process is analogous to the one used for the shear–stress–driven cavity, with the only difference that the driving boundary is here producing a clockwise main vortex. A representative sketch of the three mapping operations is depicted in fig. 4.16.

As in the previous section, the existence of limit cycle can be demonstrated by fully-resolved simulations. Moreover, from the trend of the oriented Poincaré map it is possible to characterize such a periodic orbit. We want to understand if the basin of attraction of the limit cycle is a sub-space of the domain or if the whole domain is attracted by it. Moreover by fully-resolved simulation we will clarify if the limit cycle is a stable or unstable attracting periodic orbit.

Five particle radii are considered in this investigation: $a = 0.01, 0.02, 0.03, 0.04$ and 0.05 .

Both the wall and the bulk maps are presented in fig. 4.17, combining them as done for the shear–stress-driven cavity. The results are in complete analogy with the ones reported in the previous section: the bulk mapping tends to centrifuge out the particle and the particle–wall interaction acts compressing them owing to finite-size effects. The closer the particle moves to the wall the more dominant the particle–boundary interaction effects dominate on the inertial ones. This is shown by the slope of the wall map which is lower (in absolute value) than the bulk mapping slope. The two curves intersect, for each particle size, in just one point which determines the equilibrium between compression and expansion of the particle trajectories along x . In terms of oriented Poincaré map this can be observed in the fixed point for which the iterative map intersects with the bisector line. As aforementioned, this represents one of the two abscissae $x_{n+1} = x_n = x^*$ where to initialize the particle on $y = y_P$ such that its trajectory coincides with the attracting periodic orbit.

Figure 4.18 depicts the oriented Poincaré map and shows a monotonic trend for which $0 < P'(x) < 1$; this property of the iterative map derivative has been observed in the case of a particle motion in a shear–stress-driven cavity as well and defines the stable and global attracting character of the periodic orbit. Moreover, the bigger the particle the higher its attraction rate to the limit cycle. This conclusion can be drawn observing that $P'(x)$ becomes smaller and smaller the bigger the particle radius.

In fig. 4.19 the periodic orbits in the square lid-driven cavity for $Re = 100$, $\varrho = 2$ and $a \in [0.01, 0.05]$ are depicted. We focus on the region nearby the moving-wall where the particle motion is almost parallel to the driving boundary. This confirms that, even for particle–wall interactions, the assumption of a normal inelastic collision is a good local approximation. In the considered cases, the minimum thickness of the lubrication gap passes from one order smaller up to the same order of magnitude of the particle radius.

Comparison between Free-Surface and Wall Interaction Length

A first comparison between particle–wall and particle–free-surface interaction is made in terms of the attraction rate to the periodic orbit. For $\varrho = 2$ and $a = 0.05$ fig. 4.20 compares the two iterative Poincaré maps obtained in this and the previous section. $P'(x)$ for the periodic orbit in a lid-driven cavity is evidently greater than the one of the same particle accumulating in a shear–stress-driven cavity (for comparable Reynolds numbers). This demonstrate the higher attraction rate to the limit cycle for the particle in the shear-driven cavity. The same trend is found for the formation time of particle accumulation structures experimentally observed in a liquid bridge and a lid-driven cavity. For comparable Reynolds numbers, the accumulation in a liquid bridge is faster than in a lid-driven cavity.

Once the limit cycles for the considered particle radii are calculated, the minimum distance between the particle’s centroid and the moving-wall (interaction length Δ) can be computed. This quantity has already been described as the input for improving the PSI model, but it is also a measure of comparison between particle–wall and particle–free-surface interactions.

Figure 4.21 depicts the interaction length normalized with the particle radius ($\Delta/a = 1 + \delta/a$) for both, the lid-driven and the shear–stress-driven cavity. The normalized lubrication gap δ/a is strongly depending on the particle radius. An important quantitative difference, however, is reported in fig. 4.21 which shows δ/a to be one order of magnitude larger for a particle–wall interaction. It is concluded that a rigid boundary exerts a much stronger repulsion on the particle than a shear–stress boundary for comparable Re . Hence the interaction length of the PSI model is strongly depending on the particle radius. Such a trend is in agreement with what observed for the repulsion forces exerted on a sphere moving towards a wall or a free-surface. In this case it is well known that the forces exerted in normal direction from a free-surface are

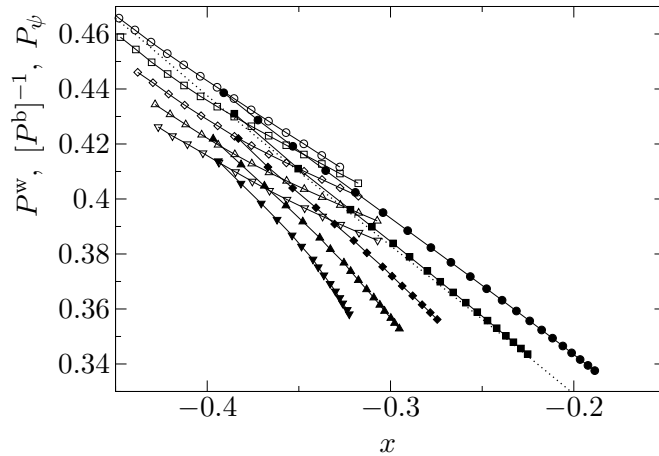


Figure 4.17.: Wall (open symbols) and bulk (full symbols) mappings for five particle radii: $a = 0.01$ (\circ), 0.02 (\square), 0.03 (\diamond), 0.04 (\triangle), and 0.05 (∇). The dotted line indicates the streamline mapping.

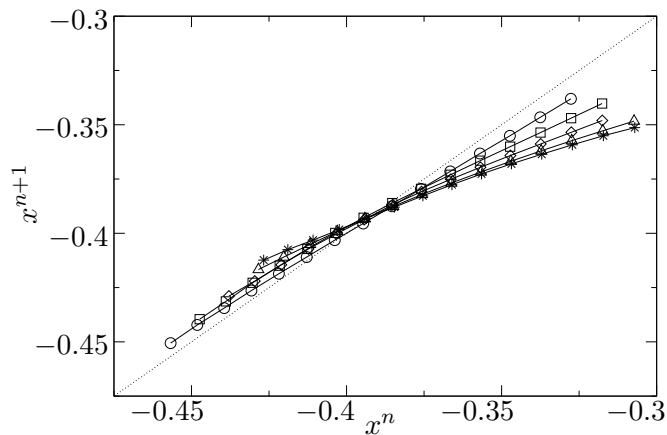


Figure 4.18.: Iterative Poincaré map $x_{n+1} = P(x_n)$ at $y_P = 0.3$ for $\text{Re} = 100$, $\varrho = 2$ and $a = 0.01$ (\circ), 0.02 (\square), 0.03 (\diamond), 0.04 (\triangle) and 0.05 ($*$) in a lid-driven cavity flow. The intersection of the Poincaré maps with the bisector (dotted line) defines the fixed point for each iterative map.

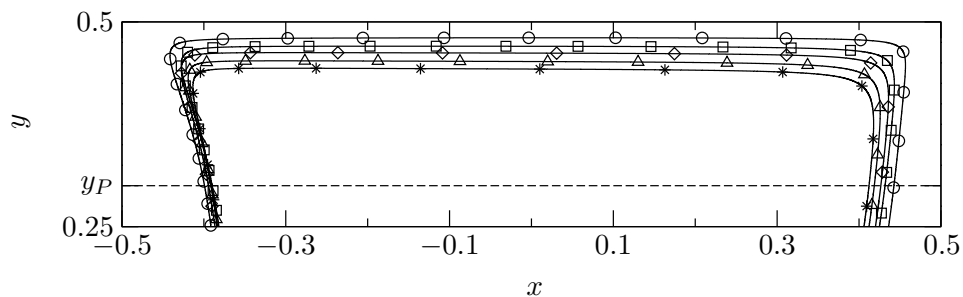


Figure 4.19.: Periodic orbits nearby the moving-wall for particles with $\varrho = 2$ and $a = 0.01$ (\circ), 0.02 (\square), 0.03 (\diamond), 0.04 (\triangle) and 0.05 ($*$) in a lid-driven cavity for $\text{Re} = 100$.

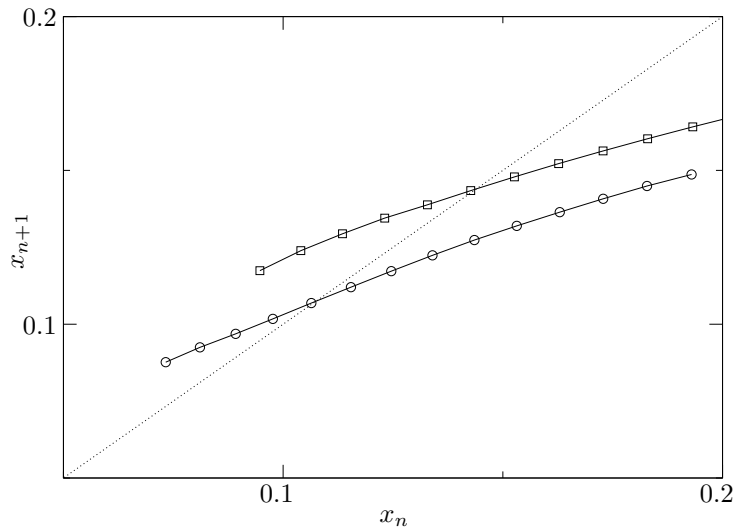


Figure 4.20.: Comparison of the Poincaré maps obtained for $a = 0.05$ and $\varrho = 2$ in the shear-stress-driven (\square) and the lid-driven (\circ) cavity. The bisector is shown as dashed line.

1/4 of the normal repulsion forces exerted by a wall for the same sphere.

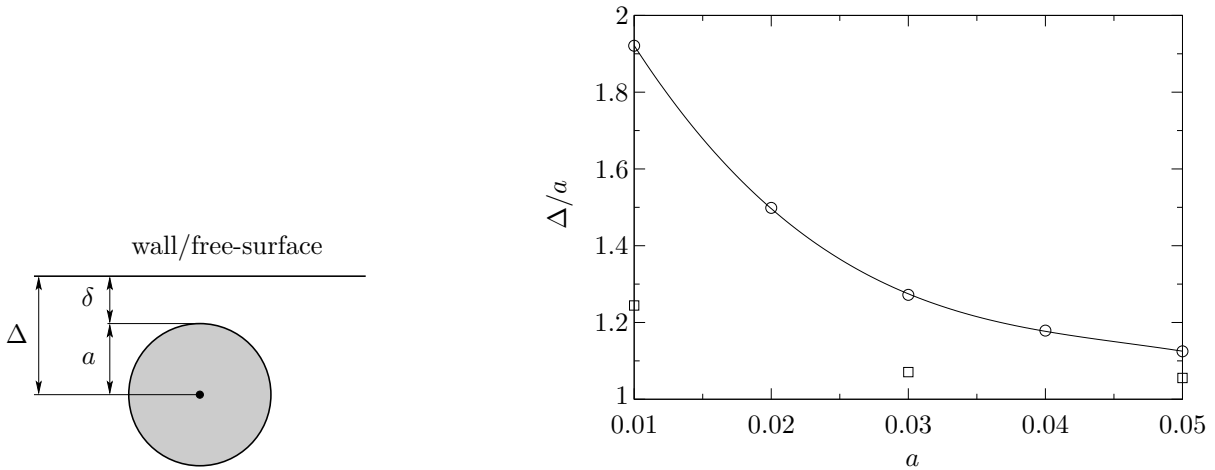


Figure 4.21.: Comparison between the normalized interaction length Δ/a as function of the particle radius a for a particle-wall (\circ) and a particle-free-surface (\square) interaction for $\varrho = 2$. A cubic fit, indicated in solid line, is used for the particle-wall interaction length.

This quantitative information will be tested by comparing the periodic orbit obtained by the PSI model in a one-way coupling approach with the reference trajectories computed by fully-resolved simulations.

4.3.2. Comparison of One-Way Coupling and Fully-Resolved Simulations

The periodic orbits obtained by one-way coupling and fully-resolved simulations are compared for all the five particle radii considered in the present investigation. We will not further demonstrate the importance of an appropriate particle–boundary interaction model as essential ingredient of the prediction, but we focus on the improvement of the periodic orbit obtained including the lubrication gap determined via the fully-resolved simulations.

Figure 4.22 depicts the three limit cycles obtained via one-way coupling (using $\Delta = a$ and $\Delta = a + \delta$ in the PSI model) and fully-resolved simulations. The strong curvature of the trajectory nearby the sliding lid indicated a strong acceleration/deceleration in x -direction during the approaching/releasing phase. The first conclusion which can be drawn from it is that the particle trajectory has essentially two time scales: a slow one in the approaching/releasing phase and a fast one, in the sliding phase. The same scenario has been observed in the shear–stress-driven cavity and justify the use of the PSI model which characterize the particle trajectory as a Filippov system applied to a fast–slow dynamical system. This aspect of the PSI model will be further commented in the next chapter because directly linked to the accumulation process.

The fully-resolved simulations are assumed as reference trajectories and two different interaction lengths are compared for the PSI model. The dashed lines are used to indicate results in which the lubrication gap is not taken care of ($\Delta = a$), whereas the solid lines depict the one-way coupled simulation for which the PSI interaction length is $\Delta = a + \delta$. Figure 4.22 shows a remarkable improvement of the one-way coupling trajectories when the minimum lubrication gap width obtained from fully resolved simulations is included in the PSI model. It must be further stressed that, even if big particles are considered, the one-way coupling approach is still an adequate tool to simulate their trajectory. Especially in the case of PAS caused by particle–wall interactions, this remark will become useful in the next chapter where relatively big particles (i.e. $a \approx 0.04 \div 0.05$) are dealt with.

4.4. Particle–Particle Interaction

The last investigation we conduct in two dimensions deals with particle–particle interactions. We consider the experimental observation of transfer of particles from PAS to the chaotic bulk-flow reported by Schwabe et al. [258]. The authors attributed this phenomenon to multimode hydrothermalwaves, external disturbance, sedimentation of particles and centrifugal forces. Moreover another mechanism of particle loss from PAS was numerically identified in [194] in the framework of the PSI model. Mukin & Kuhlmann pointed out that particle loss may occur as a single-particle phenomenon for relatively large particles owing to the geometry of the accumulation structure near the boundary. Hereinafter we address another mechanism which may induce particle transfer from PAS to the chaotic bulk-flow region: the particle–particle interaction among the particles which accumulate about the PAS.

4.4.1. Analysis Concepts for the Particle–Particle Interaction

In the following we will formulate a conceptual explanation of the particles’ transfer phenomenon. Assumptions will be discussed in order to motivate a simplified conceptual approach. This section represents a first idea for a more detailed investigation.

For the small Stokes numbers typically characterizing the particle, the velocity degrees of freedom in the phase space dynamics are neglected in the following¹. Hence, without the particle

¹For the flows under investigation, the velocity gradient is bounded and sufficiently smooth far from the singular corners. Therefore, in neighbourhoods of non-zero-size single-particle trajectories \mathcal{H} the velocity of the

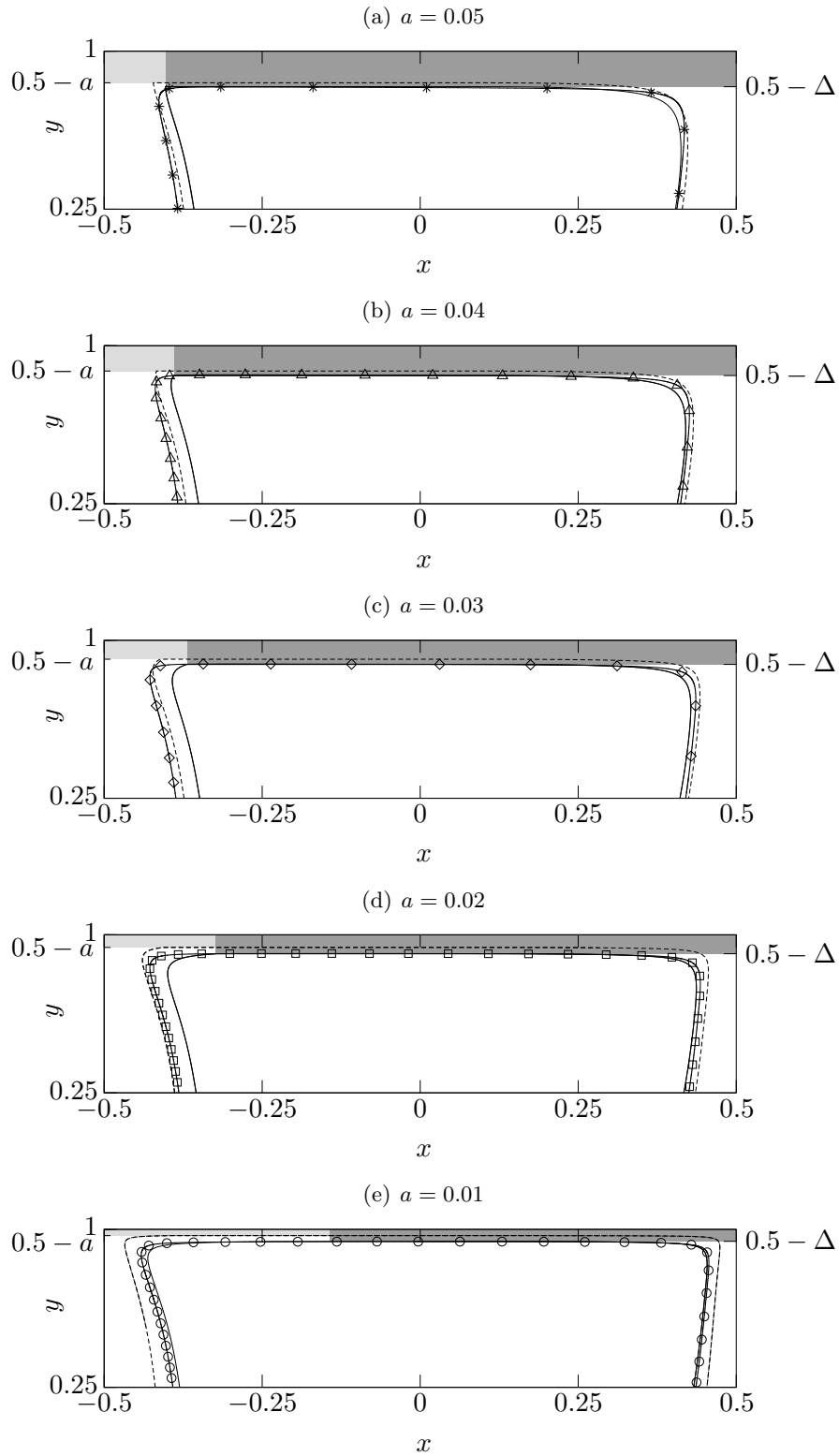


Figure 4.22.: Periodic orbits for a lid-driven cavity flow for $Re = 100$, $\varrho = 2$ and $a \in [0.01, 0.05]$. One-way coupling results (plus PSI model) are indicated with dashed and solid lines assuming as interaction lengths $\Delta = a$ and $\Delta = a + \delta$, respectively. The fully resolved simulations are depicted using markers.

velocities, the reduced phase space for the motion of n_p tracers is $(n_{\text{dim}} \times n_p)$ -dimensional, where n_{dim} are the fluid-flow dimensions. Therefore, chaotic dynamics and strange attractors are plausible for multiple-particle motion, even in planar flows. We remark that under the simplifying assumption of negligible effects connected to the particle velocities relative to the fluid the connected dissipation and the eventual strange attractors are neglected. We analyse the transfer of particles from PAS to the chaotic bulk-flow region employing a *Poincaré-like stability*, defined as follows

Let \mathcal{H} be the single-particle limit cycle and $\mathcal{H}_i(\mathbf{x}_i(t))$ the i -th particle trajectory.

$$\mathcal{H}_i(\mathbf{x}_i(t)) \text{ is Poincaré-like } (\epsilon, \tau)\text{-stable} \Leftrightarrow d_i = \text{dist}(\mathbf{x}_i(t), \mathcal{H}) \leq \epsilon, \quad \forall t \in [0, \tau] \quad (4.7)$$

where ϵ is a small, non-infinitesimal tolerance normal to \mathcal{H} about the single-particle periodic attractor (see fig. 4.23). It is to be remarked that the so-defined Poincaré-like stability differs from the classic Poincaré stability because it depends on the time-window we select, $[0, \tau]$, and on the tolerance ϵ and is just a monitoring quantity. At the end of this section we will propose a suitable way to define such a tolerance in order to infer some stability properties for the three-dimensional line-like PAS. In principle one would let $t \rightarrow \infty$, but because of numerical reasons, only the short-term dynamics will be investigated.

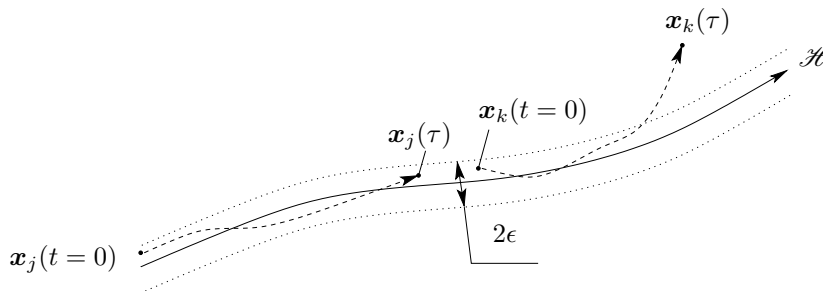


Figure 4.23.: Conceptual sketch of the Poincaré-like stability within the time window $t \in [0, \tau]$ for two particle trajectories, \mathcal{H}_j and \mathcal{H}_k . According to the definition given in eq. 4.7 the j - and the k -particles are Poincaré-like stable and unstable, respectively.

The problem is further formulated in terms of an occupation ratio of particles along the attracting limit cycle. Considering particles of the same size, their occupation ratio along a limit cycle is defined as

$$\phi^{\text{PAS}} = \frac{2a}{l_{\text{PAS}}} \cdot n_p \quad (4.8)$$

where l_{PAS} is the length of the single-particle limit cycle and n_p the number of particles moving in its vicinity (to uniquely define such a neighborhood of \mathcal{H} one may use the tolerance ϵ). An implicit simplification is herein included in selecting ϕ^{PAS} as the only non-dimensional group to investigate. In particular, the exclusion of the non-dimensional particle radius a_p/d from the following analysis must be justified. Owing to the typically small particle-Reynolds numbers, the perturbation introduced by each particle can be represented, with good approximation, as a creeping flow. For spherical particles in Stokes flow, the strength of the perturbation field decays as $\sim r_p^{-1}$, where r_p is the distance from the particle centroid. Hence we speculate that the projection of the particle–particle interaction along the single-particle attractor may be taken

particle is bounded. This guarantees that considerations about the phase space may be made dealing with the coordinate phase space only.

into account employing only ϕ^{PAS} , regardless of the non-dimensional particle radius. However, in order to neglect the particle radius as investigation parameter, we must limit the local curvature of the single-particle limit cycle, χ^{PAS} , with respect to the particle size, $a_p \chi^{\text{PAS}} \ll 1$.

If $\max_i(\text{dist}(\mathbf{x}_i, \mathcal{H})) = \epsilon$, ϕ^{PAS} equals the threshold occupation ratio for the i -th particle $\phi_{c,i}^{\text{PAS}}(\epsilon)$. Beyond $\phi_{c,i}^{\text{PAS}}(\epsilon)$ the single-particle limit cycle does coincide with the i -th-particle trajectory within the tolerance ϵ . Considering circular particles of the same density and size, the PAS Poincaré-like stability can be inferred considering the particle occupation ratio. We aim at finding ϕ_c^{PAS} such that the projection of the phase-space attractor onto each (x_i, y_i) -plane coincides with the single-particle limit cycle within an arbitrary transversal tolerance ϵ for a definite time window starting from definite initial conditions

$$\phi^{\text{PAS}} \leq \phi_c^{\text{PAS}}(\epsilon) = \min(\phi_{c,i}^{\text{PAS}}). \quad (4.9)$$

Owing to the far-field perturbation typical of two-dimensional flows, the particle–particle interaction experienced by each tracer is stronger than it would be if they were spherical tracers of the same radius at the same mutual distance. Therefore, we speculate that our estimate of the maximum stable particle occupation ratio along the attractor can be considered as a conservative supremum of the three-dimensional ϕ_c^{PAS} for line-like PAS.

If particle–particle interactions were negligible, the tracers would keep moving on the single-particle periodic attractor and their trajectories would coincide. In this case a simple shift in time would be enough to univocally link the particle trajectories. Along the same argument, the similarity among the particle orbits can be measured in terms of the turn-over time τ_i required by the i -th particle to complete a single revolution on the attractor.

4.4.2. Multiple-Particle Simulations

Under the assumption that the main particle–particle interaction can be approximated by considering the nearest neighbours only, three particles are simulated. This working hypothesis is violated if PAS instability (defined as above) occurs, but it is still expected to hold in the limit of $\phi^{\text{PAS}} \uparrow \phi_c^{\text{PAS}}$. The shear–stress-driven cavity for $\text{Re} = 1000$ is chosen as flow field for this investigation and fig. 4.24 depicts the aforementioned conceptual approximation.

The particles have $a = 0.01$ and $\varrho = 2$ and are initially distributed along the limit cycle calculated in Section 4.2.1 for a single particle. Owing to the variation of the velocity along the single-particle limit cycle, the tracers are arranged in a non-uniform distribution. The mutual distance between the particles will be smaller where the flow is slower and larger when the flow is faster. Therefore, in order to simulate a Poincaré stable configuration for a given ϕ^{PAS} , the particles are initialized at a constant frequency between each other $f^{\text{PAS}} = n_p / \tau^{\text{PAS}}$, where τ^{PAS} is the turn-over time² (assumed, in the limit, equal for all particles). The single-particle turn-over time $\tau^{\text{s-p}}$ is considered as a first estimate of τ^{PAS} . Simulating three particles only, we place the central one at (x^*, y_p) and calculate the initial location of the other two particles integrating backward and forward in time the single-particle trajectory up to $t = 1/f^{\text{PAS}}$. The three particles employed to investigate the stability of the attractor are labeled as in fig. 4.24.

Limiting our study to a relatively short time window (one turn-over time for the particle in the middle, τ_2), the data resulting from it will serve the purpose of investigating particle loss along the attractor for multiple particles because such a process is experimentally observed to be linked to the short-term dynamics of the system.

²The turn-over time is measured considering the Poincaré section of the particle trajectory with a line normal to its trajectory and passing from its initial position. The i -th particle turn-over time τ_i is the time between two successive ordered returns.

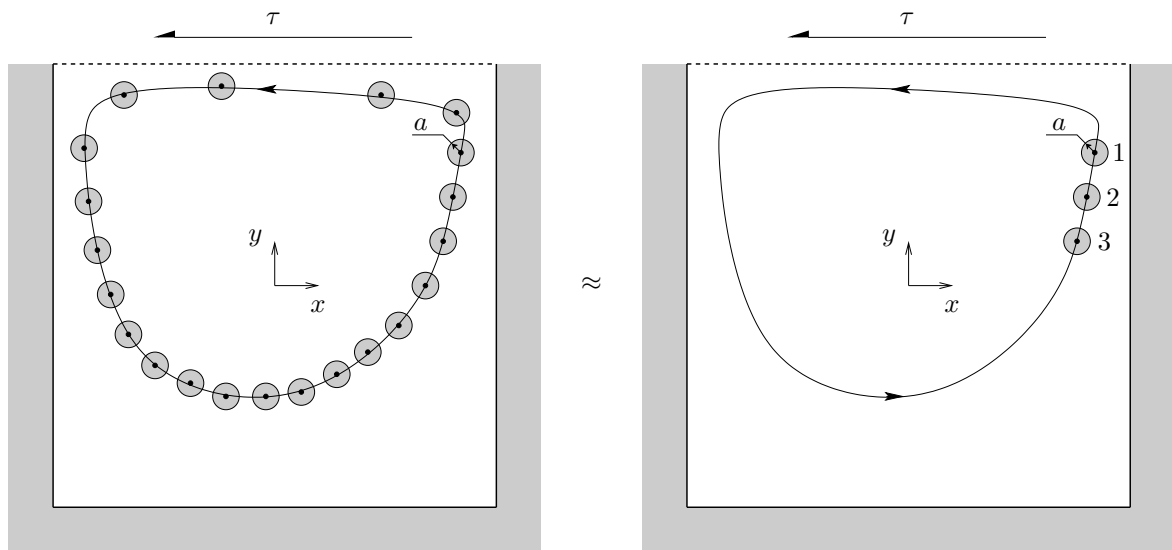


Figure 4.24.: Sketch of the simulation set-up (right) for investigating the occupation ratio of particles along the attractor such that particle–particle interaction does not induce Poincaré-like instability in a two-dimensional shear–stress-driven cavity for $\text{Re} = 1000$. Three particles are used to model the set of accumulated tracers (left) of the same size and density initially distributed along the single-particle attractor.

4.4.3. Results

Figure 4.25 compares the three particle trajectories with the single-particle limit cycle for $\phi^{\text{PAS}} = 0.9500$ (a), 0.7773 (b) and 0.6045 (c), respectively to 110, 90 and 70 particles, up to $t = \tau_2$. For $\phi^{\text{PAS}} = 0.9500$ the time window $t \in [0, \tau_2]$ does not suffice to reliably describe the particle dynamics (see fig. 4.26a). However the deviation of the multiple-particle trajectories (dashed, dashed-dotted, and dotted lines) from the single-particle limit cycle can already be observed in the first phase of the system evolution (fig. 4.26b). This violates the working hypothesis schematically depicted in fig. 4.24 and the resulting dynamics does not represent a good approximation of a 110-particles system evolution ($\phi^{\text{PAS}} = 0.9500$). Figure 4.26b depicts a numerical two-dimensional version of the bursts experimentally observed when the particles are leaving the region near the free-surface (see fig. 16b in [258]).

The minimum distance between the i -th particle centroid and the periodic attractor for a single particle, d_i , is shown as function of time in fig. 4.27, integrating up to $t = \tau_2$. The different lines refer to the three particles employed in the simulations. A remarkable decrease of the order of magnitude for d_i (note the scales of the axes) can be observed passing from $\phi^{\text{PAS}} = 0.9500$ (a) to 0.6045 (c) and the latter case can already be considered as Poincaré-like (ϵ, τ_2) -stable with a $\epsilon = 3.56 \times 10^{-3}$. Moreover, an important information can be extracted if the distance from the single-particle limit cycle is averaged among the three particles, $\langle d_i \rangle$. Tracking the particles and considering the solid line in fig. 4.27, $\langle d_i \rangle$ increases when the particles approach the free-surface. When particle–particle interactions are present, the free-surface has an ambivalent role: it focuses the tracers towards the single-particle limit cycle if particle–particle interaction is weak, whereas it defocuses from the periodic orbit when the mutual interaction between particles plays a major role. The latter behavior is shown by the initial temporal trend of $\langle d_i \rangle$ for $t \in [0, \tau_2]$ (solid line in fig. 4.27).

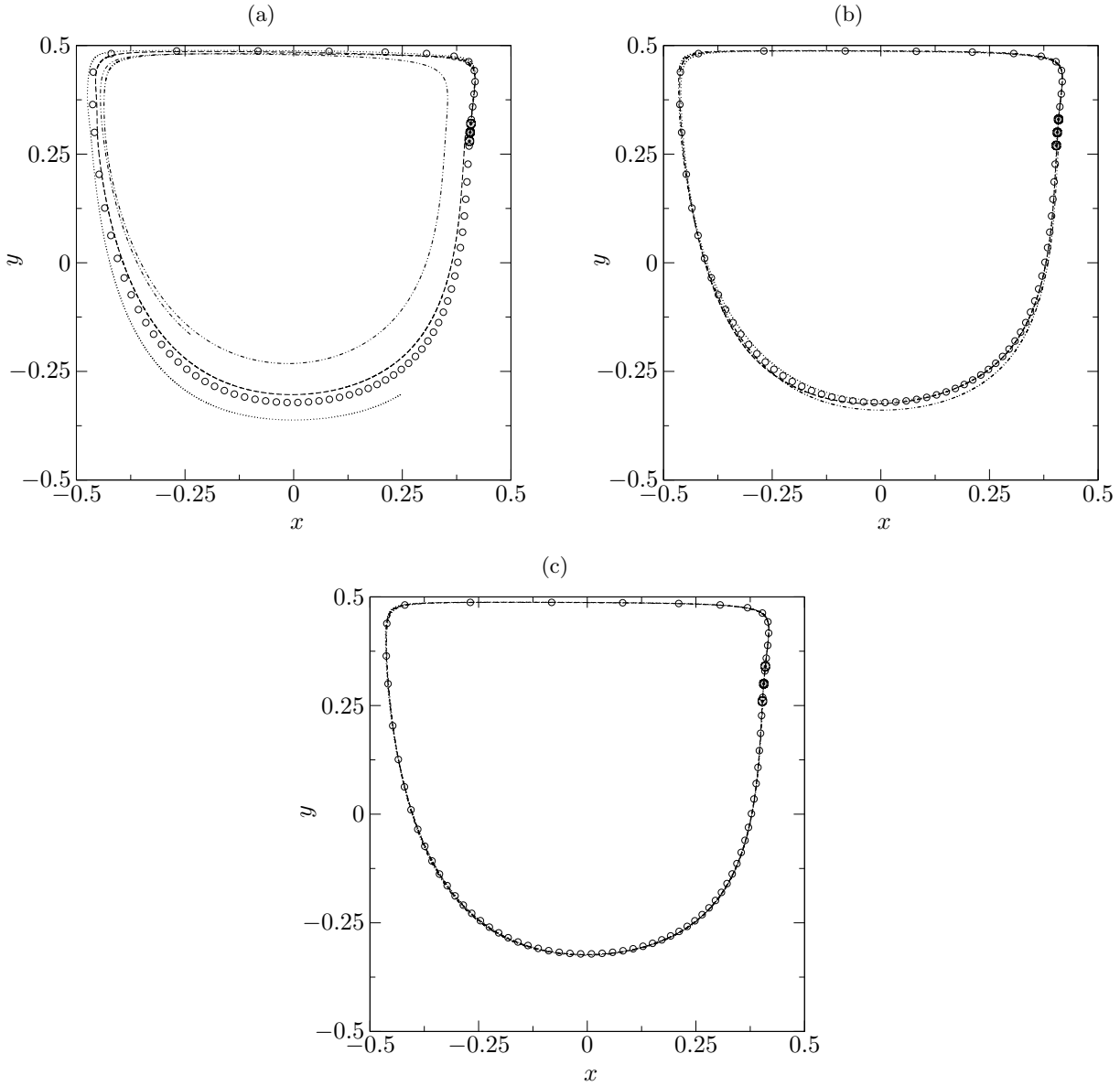


Figure 4.25.: Particle trajectories for three different occupation ratios $\phi^{\text{PAS}} = 0.9500$ (a), 0.7773 (b) and 0.6045 (c). The dashed-dotted, dashed and dotted lines refer to particle 1, 2 and 3, respectively, whereas the markers indicate the single-particle periodic attractor. Particle trajectories are integrated up to $t = \tau_2$.

Table 4.2 and fig. 4.28 give more quantitative comparisons between the single-particle periodic orbit and the multiple-particle trajectories. As function of the occupation ratio ϕ^{PAS} , fig. 4.28a depicts the turn-over time, τ_i (markers), for each particle compared with the single-particle turn-over time (solid line). Moreover, fig. 4.28b shows the maximum distance of the particle trajectories from the single-particle limit cycle as function of ϕ^{PAS} .

Table 4.2 lists the mean turn-over time, $\langle \tau_i \rangle$, as well as the mean maximum distance of the three particle trajectories from the single-particle limit cycle, $\langle \max(d_i) \rangle$. In both the cases the mean values are calculated averaging over the particle values. These data are given as function of the occupation ratio ϕ^{PAS} and the number of particles n_p . As already discussed, the case of

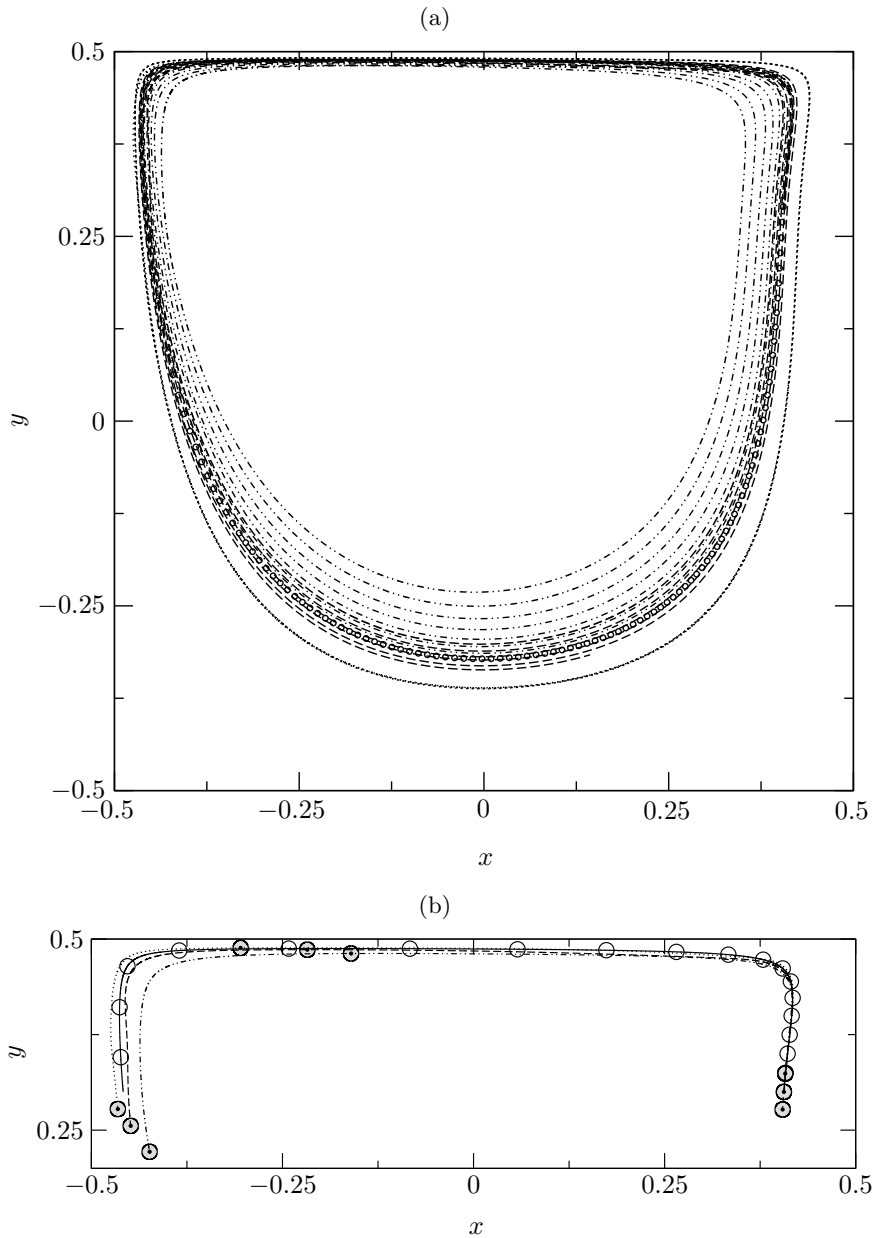


Figure 4.26.: Long-term evolution of the particle trajectories for occupation ratio $\phi^{\text{PAS}} = 0.9500$ (a) and two-dimensional burst of the particle trajectories after the first interaction with the free-surface (b). The dashed-dotted, dashed and dotted lines refer to particle 1, 2 and 3, respectively, whereas the markers indicate the single-particle periodic attractor. The time window of (a) is $t \in [0, 6\tau_2]$.

$\phi^{\text{PAS}} = 0.9500$ cannot be reliably represented simulating three particles only and this warning is indicated in table 4.2 highlighting the corresponding row in gray.

The turn-over time for each particle τ_i , and consequently the mean turn-over time $\langle \tau_i \rangle$, are increasing if the occupation ratio increases from $\phi^{\text{PAS}} = 0.6045$ to 0.7773. This can have two causes: (a) particle–particle interaction projected along the single-particle periodic attractor and (b) deviation of the tracers from the single-particle limit cycle. Only the central particle among the three experiences the interaction with both the nearest neighbour tracers. Even though this

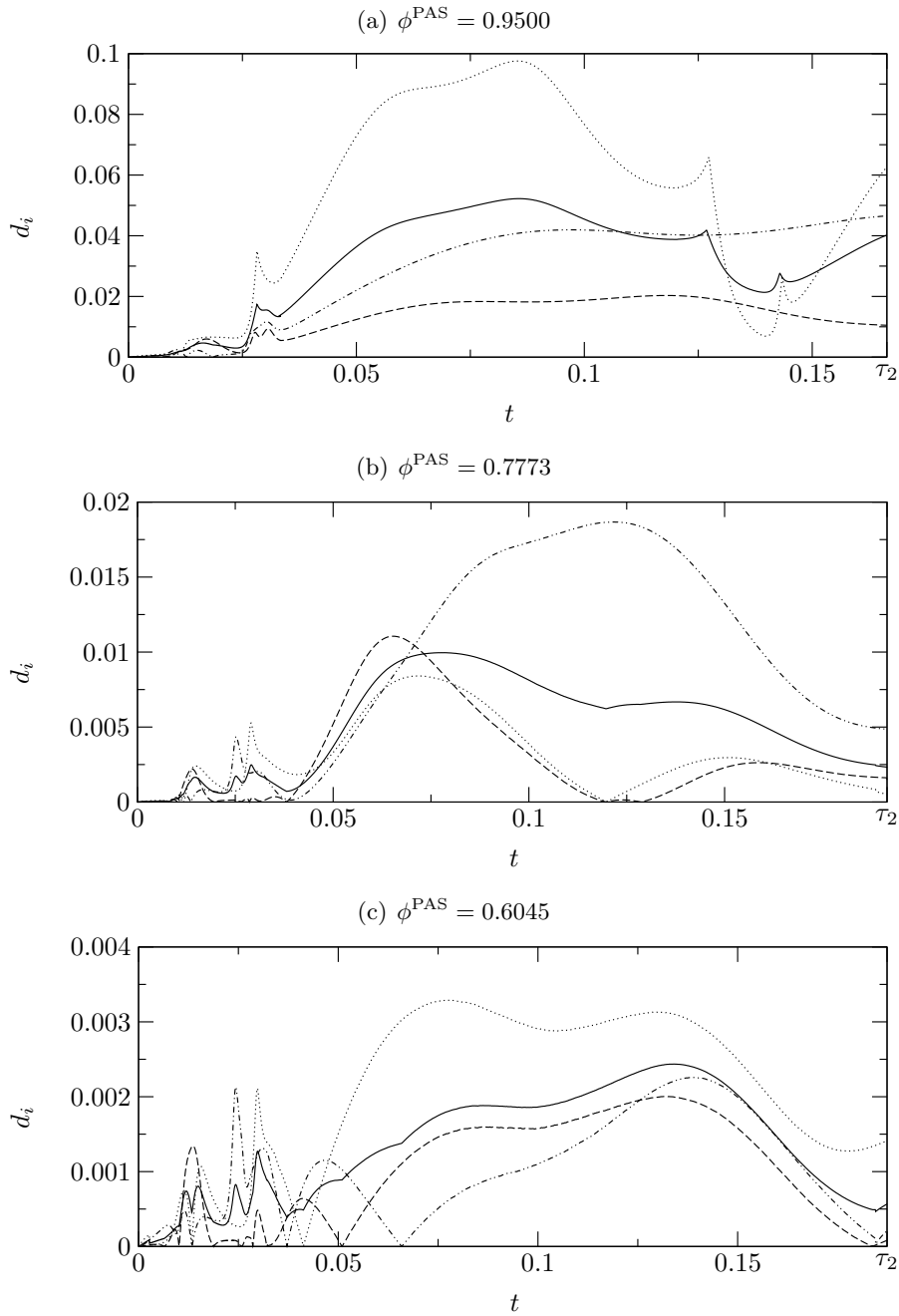


Figure 4.27.: Minimum distance function of the i -th particle trajectory, d_i , from the single-particle periodic attractor. The dashed-dotted, dashed and dotted line refer to particle 1, 2 and 3, respectively, whereas the solid line indicates the average among the particle of d_i . Three occupation ratios are depicted: $\phi^{\text{PAS}} = 0.9500$ (a), 0.7773 (b) and 0.6045 (c).

is the case, fig. 4.28a shows that the turn-over times of all particles are very similar to each other. Moreover, considering fig. 4.28, when the distance between each trajectory and the single-particle attractor increases, τ_i increases as well. This observation may lead to conclude that increasing d_i makes the multiple-particle turn-over times deviate from the period of single-particle limit cycle.

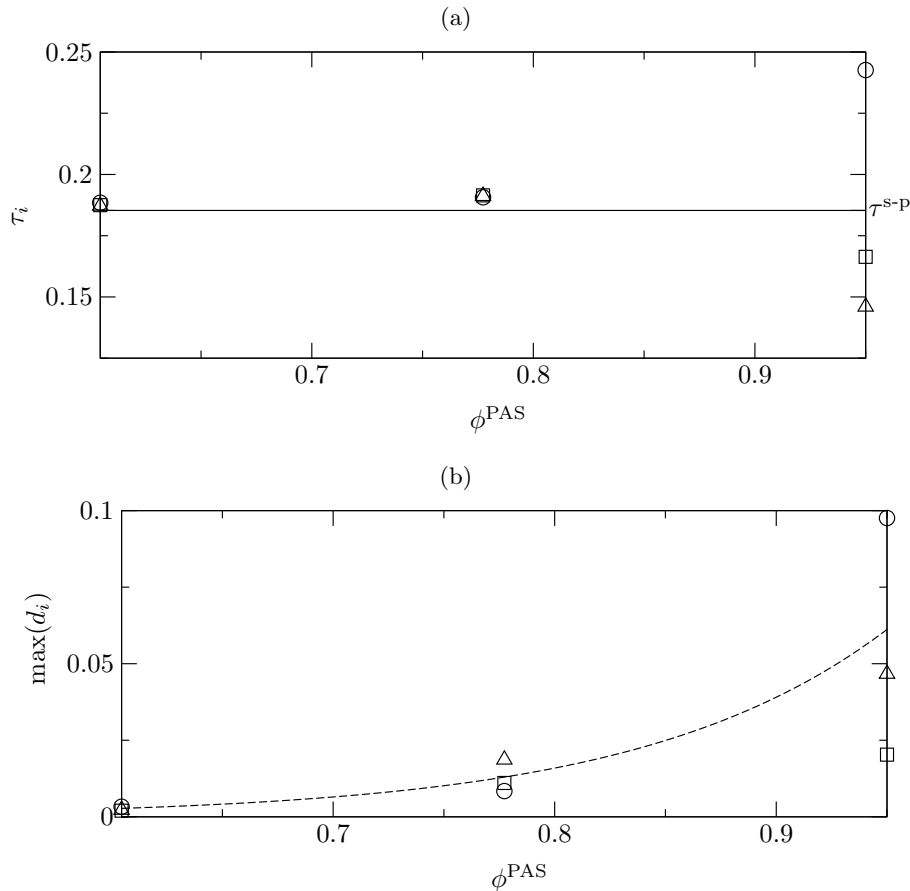


Figure 4.28.: Turn-over time τ_i (a) and maximum d_i (b) for the i -th particle as function of the occupation ratio ϕ^{PAS} . The circle, triangle and square refer to the particles 1, 2 and 3, respectively. The dashed line denotes an exponential fit for the root-mean-square of $\max(d_i)$ as function of ϕ^{PAS} .

Table 4.2.: Single-particle, $\tau^{\text{s-p}}$, compared with the averaged multiple-particle turn-over time, $\langle \tau_i \rangle$ as function of the occupation ratio of particles along the attractor ϕ^{PAS} . The averaged maximum distance of the multiple-particle trajectories from the single-particle limit cycle, $\langle \max(d_i) \rangle$, is computed up to $t = \tau_2$. All the particles are equal to each other ($a = 0.01$, $\varrho = 2$) and move in a shear–stress-driven cavity for $\text{Re} = 1000$. The gray color indicates that the last row does not give reliable data for interpreting the behavior of 110 particles with the only simulation of three of them.

ϕ^{PAS}	n_{p}	f^{PAS}	$\tau^{\text{s-p}}$	$\langle \tau_i \rangle$	$\langle \max(d_i) \rangle$	τ_2
0.6045	70	377.84	0.1853	0.1877	0.002516	0.1874
0.7773	90	485.79		0.1911	0.012712	0.1915
0.9500	110	593.75		0.1850	0.054863	0.1664

4.4.4. Conceptual Extension to Three-Dimensions

To conclude we will apply these concepts to three-dimensional particle accumulation structures. In Chapter 5 the strong correlation between particle attractors and regular regions of a steady fluid flow will be discussed. A single non-zero-sized particle does not perfectly follow the flow, but the small Stokes numbers and density ratios typically considered make its trajectory very similar to a streamline. As already discussed, this statement does not hold in the close vicinity of the boundaries.

In a three-dimensional flow it is therefore important to define in which regions of the domain a one-way coupled particle trajectory has a chaotic motion and where it moves along a periodic or quasi-periodic orbit. These regular regions for the single-particle trajectory will be approximated in the following discussion by the regular regions for the flow streamlines of a three-dimensional steady flow.

Figure 4.29 depicts a conceptual sketch of a generic tubular regular region for the fluid flow. Far enough from it a single tracer moves in a chaotic fashion. We consider the case of a single-particle accumulating on a closed trajectory inside the regular region of the flow (we make the assumption that the attracting limit cycle does not sensibly differ from the closed streamline). The curvilinear coordinate along the periodic attractor is denoted with s and the minimum distance of it from the boundary between regular and chaotic regions in each cross-section normal to s is called d^{s-P} .

If we give a clear description of the line-like PAS and the flow topology, the minimum acceptable tolerance for the system to be Poincaré-like stable may heuristically be approximated by $\min(d^{s-P})$. In fact, requiring that the particle trajectory coincides with the closed streamline within a tolerance $\epsilon = \min(d^{s-P})$ means that the particle will always move within the regular region. Hence, for the corresponding threshold occupation ratio, this condition would yield

$$\min(d^{s-P}) = \max(d_i) \Rightarrow \phi^{\text{PAS}} \leq \phi_c^{\text{PAS}}. \quad (4.10)$$

From (4.10) it results a conservative estimate of the stability boundary for particle accumulation structures in steady three-dimensional flows. Evaluating $\min(d^{s-P})$ we can determine an infimum of ϕ_c^{PAS} and the corresponding number of particles which can safely accumulate about the single-particle line-like PAS without causing loss of particles along the accumulation structure.

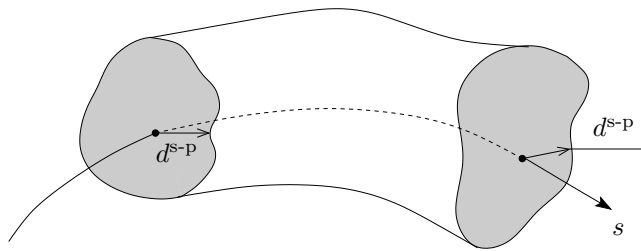


Figure 4.29.: Sketch of a part of the regular regions for the flow about a line-like PAS. The coordinate s is defined along the periodic attractor (closed trajectory assumed approximated by a closed streamline) and the gray areas represent the sections of the tubular regular region. The minimum distance between the periodic attractor and the boundary of a section of the regular region is indicated by d_{\min} and, in general, is function of t and s .

We finally remark that the mechanism we propose phenomenologically agrees with experimental observations of the loss of particles along PAS. Indeed, in the initial phase of the accu-

mulation, the occupation ratio along the attractor is very small. The more particles accumulate, the higher ϕ^{PAS} becomes. This holds up to the threshold ϕ_c^{PAS} at which the PAS Poincaré-like instability occurs and the accumulation structure loses particles to regions in which the streamlines are chaotic. This explains the contribution of particle–particle interactions to the loss of particles along the accumulation structure without making any reference to fluid-flow induced causes (e.g. multimode hydrothermalwaves). Such a mechanism takes into account the low Stokes numbers which are usually employed in the experiments and the corresponding negligible effect that particles have on the fluid, supposed to be almost insensitive to ϕ^{PAS} .

5. Topology and Particle Accumulation Structures

Inertia and particle–boundary interaction effects may lead to accumulation of particles in specific regions of the flow domain. We will consider either fluid-flow systems in which both effects are necessary to attract particles to global and stable PAS or systems in which the inertial effect can be neglected and the particle accumulation is determined by the only particle–boundary interaction. The case of particles clustering due to the only inertial effect has been extensively studied in literature (see e.g. [267]) and we will not deal with it in the present thesis.

The first part of this chapter considers PAS in a liquid bridge, either for axisymmetric or three-dimensional flows. The focus will be on the accurate prediction as function of the parameters of PAS and on the improvement derived from including the lubrication gap width in the PSI model. We will show how accurate the fully-resolved two-dimensional estimate can be in quantitative comparison with experimental results.

The second part of the chapter investigates a two-sided antiparallel lid-driven cavity for which PAS are reported here for the first time. A comparison with experimental investigations is also presented.

The last section includes a numerical prediction of PAS for a partially liquid-filled rotating drum in which there is no experimental evidence of particle accumulation structures, so far. The aim of such a section is to predict a suitable range of Reynolds numbers and particles sizes for which PAS may occur.

5.1. Different Interpretations of Particle Accumulation Structures

A numerical prediction of particle accumulation structures has been targeted by various research groups (see e.g. [190, 160, 194, 195]) and the accumulation mechanism itself is currently debated. Among the proposed interpretations, some authors tend to attribute it to a particle–fluid synchronization process [190, 228], others correlate PAS to the vorticity field [160], whereas Kuhlmann et al. [126, 195, 194, 151] explain the particle attraction to periodic and quasi-periodic orbits as a phenomenon directly connected to the flow topology and the particle–boundary interaction.

An exhaustive comment by Kuhlmann & Muldoon [156] excluded the synchronization mechanism among the possible causes of PAS and a further proof of it will be given in the present chapter. Indeed, only one-way coupled simulations are used in the following and this implies that the particles are, by definition, slaves of the flow field. To have particle–fluid synchronization it is required a weak coupling between particulate- and fluid-flow systems (see e.g. [226]), which is absent in our simulations, the fluid-phase being not affected by the particles.

The debate developed observing the particle accumulation structures in a liquid bridge, which is the only experimental evidence of PAS reported so far. When a hydrodynamical instability occurs in the flow of the liquid bridge in form of a traveling hydrothermal wave, the traveling frequency of PAS equals the frequency of the hydrothermal wave. However, even if the flow has

a characteristic frequency which is also observed for the particle accumulation structures, such a frequency does not result from synchronization between PAS and fluid, but from a synchronous motion with which the particle accumulation structures follow the flow. Moreover, PAS are also present in systems which do not have any characteristic traveling wave frequency, e.g. in a lid-driven cavity flow, and we will demonstrate it herein for the first time.

Regarding the “vorticity thinking” proposed by Lappa, this is resulting from the numerical observation that PAS are traveling along axial vorticity isosurfaces ([160]). However it has never been rigorously demonstrated how the vorticity-wave interaction could lead to PAS. Moreover, this does not provide a clear framework for understanding when PAS can occur in dependence on the particle radius, even though PAS has been experimentally observed for very specific combinations of flow-field and particle parameters (see e.g. [258]).

A possible cause of such controversies may be due to a technical problem in simulating the particle motion nearby the domain boundaries. Integrating numerically the Maxey–Riley equation the particles moving near the boundaries may unphysically exit the domain or cluster along the three-phase contact line on the cold corner of the liquid bridge due to numerical error. Even if according to their theoretical explanations Lappa [160] and Melnikov et al. [190] do not need any particle–boundary interaction model for numerically reproducing PAS, both of them employ a rebound scheme to prevent the aforementioned unphysical scenarios for the particle motion (see e.g. [190, 160]). This is corresponding, in practice, to apply the PSI model proposed by Hofmann & Kuhlmann. Since Lappa and Melnikov et al. have considered it as a minor numerical artifact, they kept on attributing PAS to inertia, synchronization and vorticity wave interaction causes. For an extensive analysis on the role of numerical errors and rebound schemes in simulating PAS we refer to [196].

In this chapter we will provide further evidence in support of the theory of Kuhlmann et al. [126, 195, 194, 151] by computing the flow topology, simulating the particle accumulation structures and comparing them with the regular regions of the flow. The particle radius is assumed as a key parameter of the investigation. To the best of the author’s knowledge, this is the first time that such a clear proof is given for flow-field parameters which are targeted in experimental studies and a comparison with the available experiments is presented in the following whenever possible.

5.1.1. Phenomenological Explanation of Particle Accumulation Structures

Since many different phenomenological explanations have been proposed for interpreting PAS, the previous overview about them may have helped the reader to get oriented. In this subsection we aim at specializing the discussion about the theory of Kuhlmann et al., which we support in the present thesis. In the following we clarify it in its essential physical aspects and in the way we model them.

The first aspect to discuss is the correlation between particle accumulation structures and fluid flow topology. The particles we consider are not so heavy ($\varrho = \mathcal{O}(1)$) and characterized by small Stokes numbers. Moreover the investigated fluid flows are featured by very high streamline density nearby the driving boundary. These two considerations suggest that inertial and buoyancy effects do not play a major role if compared to finite-size effects when the particle passes very close to the boundaries. Moreover, in the flow configurations we consider, the major part of the domain (including the boundaries) is occupied by the chaotic region. Therefore, by ergodicity, each particle located in the chaotic sea will be advected to move nearby the boundaries and will experience strong interactions with free-surfaces/walls due to its finite size.

As mentioned, inertia and buoyancy effects are almost negligible for the particle parameters under investigation, hence the regular regions of the fluid flow (without particles) approximate

possible trapping sub-volumes for single particles. Moreover it is experimentally reported that particle–particle interactions do not sensibly affect the shape of the accumulation pattern. This means that KAM surfaces not only may represent a good approximation of trapping regions for single particles, but they also very well approximate PAS.

The second important point to discuss is the dissipation phenomenon which brings the particles to accumulate. Many dissipation mechanisms are actually acting on the particles such as inertia, buoyancy and particle–boundary interactions. In our framework of investigation, the latter dissipative effect is definitely dominant on the former ones and it determines the major part of the accumulation dynamics. The dissipation is introduced in the particulate dynamical system because of the lubrication forces which are responsible for the strongest particle–boundary interaction effects. Their importance is limited to a flow region in the vicinity of a wall or a free-surface. This is because the considered particles are very small and lubrication forces are effective when the particle centroid has a distance from the boundaries which is at most of the same order of its radius, $\Delta = \mathcal{O}(a)$.

The last feature required for having particle accumulation in the framework of PAS is the vicinity of KAM tori to the fluid flow boundaries. When a regular region is located near a wall or a free-surface the dissipation mechanism due to the particle finite size can transfer the particle from a chaotic to a regular sub-volume of the flow. Once the particle enters a regular region, it remains trapped in it contributing to the accumulation pattern which identifies the PAS.

Employing fully-resolved three-dimensional simulations for determining the particle trajectories would be infeasibly numerically expensive and modelling assumptions are required. The first assumption we do (experimentally confirmed) is that PAS is a single-particle phenomenon. Therefore, in the framework of point-wise particle simulations, we select a one-way coupled approach. The second assumption numerically validated in the previous chapter consists in modelling the particle motion in proximity of a wall or a free-surface using the PSI model. In terms of dynamical systems, this last step corresponds to employing a Filippov system [79] for the velocity vector field in which the particle is moving. The PSI model is therefore responsible for modelling the main dissipative contribution in the particles dynamical system (see e.g. [110]). As a simplified case we consider the dissipation produced by the PSI model on the phase space of a perfectly advected tracer in steady, three-dimensional flow. Marking a ring of fluid elements, when it “collides” with the PSI prohibited region, its area shrinks due to the discontinuity of velocity in normal direction to the boundary. This clarifies the dissipation source induced by the PSI model. Therefore, even if inertial and buoyancy effects are neglected in integrating the particle trajectory ($\dot{\mathbf{y}} = \mathbf{u}$), the *tracer particle* can still accumulate in the framework of our model because of the particle–boundary interaction dissipation.

5.2. Liquid Bridge

The first set-up considered herein for investigating particle accumulation structures is the liquid bridge. For the corresponding problem formulation we refer to Section 2.1. At first an axisymmetric liquid bridge configuration is dealt with because quantitative experimental results have been reported (see [246]). In this case the importance of accurately determining the lubrication gap width is investigated in the framework of the PSI model. The numerical and experimental results are compared considering the temporal evolution of a single particle trajectory in terms of its radial coordinate as function of time from the liquid bridge axis.

The second subsection is concerned with a three-dimensional hydrothermal wave in a liquid bridge. The corresponding experimental particle accumulation structures are published in [103] and they will serve as a reference for our numerical prediction of PAS.

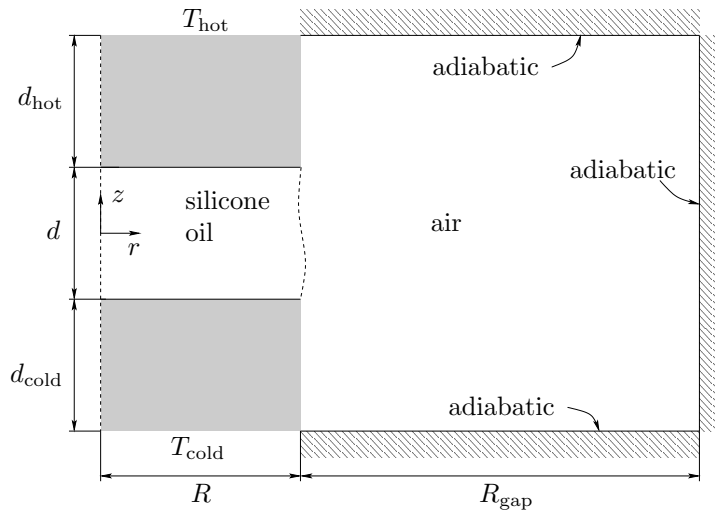


Figure 5.1.: Sketch of a conceptual model of the experimental set-up.

Table 5.1.: Thermo-physical properties of the test fluid at 25 °C.

ρ (kg/m ³)	ν (m ² /s)	κ (m ² /s)	σ_0 (N/m)	γ (N/(m K))	β (1/K)
8.71×10^2	2.0×10^{-6}	7.02×10^{-8}	18.3×10^{-3}	-7.0×10^{-5}	1.24×10^{-3}

The same experimental set-up has been used for both of the above cases. For further details we refer to [103]. The liquid employed in both cases is 2-cSt silicone oil (KF96L-2cs, Shin-Etsu Chemical, Co., Ltd., Japan) and its thermo-physical properties are reported in table 5.1. A simplified model for the numerical calculation is shown in fig. 5.1. The inclusion of the ambient gas enables to estimate the role of environmental conditions on the prediction of PAS.

The spherical particles employed in the experiments are gold-coated acrylic particles and the range of considered radii varies from 5 to 25 μm . In table 5.2 it is reported the mean density of the particles ρ_p for different particle radii a_p , as well as the mean particle-to-fluid density ratio $\varrho = \rho_p/\rho_f$ calculated at 25 °C. For more extensive details about the experimental apparatus and the relative test fluid and particles we refer to [103] and [246].

5.2.1. Axisymmetric Liquid Bridge

All the comparisons between numerical and experimental results in this section are based on the following liquid flow non-dimensional numbers

$$\text{Pr} = 28.5, \quad \text{Re} = 331, \quad \Gamma = 0.66, \quad \mathcal{V} = 1.0, \quad \text{Bd} = 0.40. \quad (5.1)$$

In order to demonstrate the fluid flow features fig. 5.2 depicts the corresponding temperature and Stokes streamfunction fields obtained employing a steady-state finite volume solver developed during this thesis. For more details we refer to the Appendix C, where an example of the grid distribution commonly employed is reported and discussed. For the following simulations 366×366 grid nodes are employed using an hyperbolic tangent stretching with stretching factor 1.05. The thermal boundary conditions are adiabatic ($\text{Bi} = 0$) with a statically deformed

Table 5.2.: Particle densities and density ratios, ρ_p and ϱ respectively, for different particles radii a_p at 25 °C.

a_p [μm]	5	7.5	$15^{+0}_{-0.35}$	25 ± 0.01
ρ_p [kg/m^3]	2.20×10^3	1.77×10^3	1.49×10^3	1.47×10^3
ϱ	2.52	2.03	1.71	1.69

free-surface. However, to take into account the heat transfer across the liquid-gas interface in predicting PAS, an extended multiphase solver will be also considered in the following subsections. In that case the free-surface boundary conditions described in Chapter 2 are implicitly extended in the solver, balancing stresses and energy across the interface.

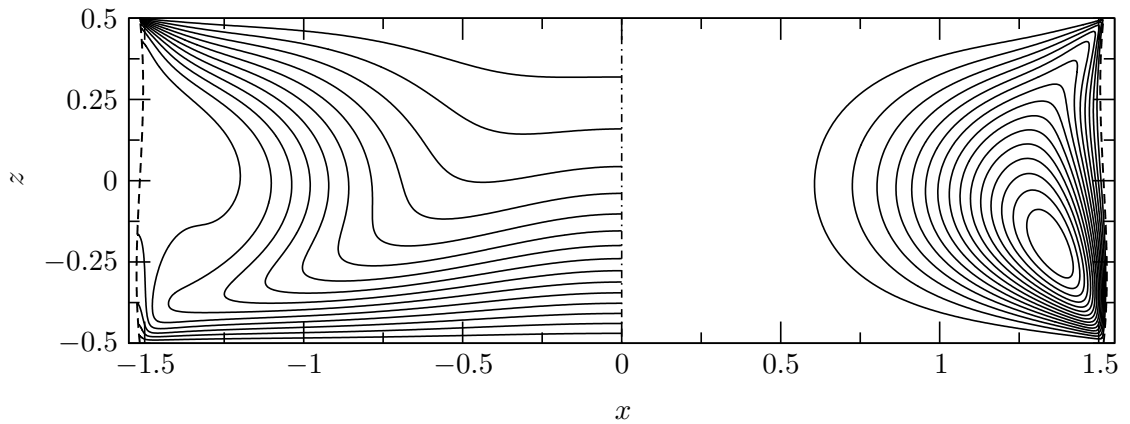


Figure 5.2.: Streamlines (right) and isothermal lines (left) for the axisymmetric flow in a liquid bridge with adiabatic free-surface for $\text{Pr} = 28.5$, $\text{Re} = 331$, $\Gamma = 0.66$, $\mathcal{V} = 1.0$ and $\text{Bd} = 0.40$. The dashed line depicts the free-surface of the liquid bridge and the dashed-dotted line denote its axis.

Experimental Evidence of the Existence of a Global Attractor

All the experiments presented in this section are carried out at Tokyo University of Science by Misa Ishimura under the supervision of Ichiro Ueno.

The experimental results are obtained making sure that the steady quasi-axisymmetric flow is reached and a period of 38 thermal time units, d^2/κ , is given to the system for asymptotically relax to it. Consequently, in order to make the comparison with numerical simulations independent on particle–particle interactions, one single particle is inserted in the liquid bridge through a hole in the external shield with a needle. The particle is kept on the needle because of electrostatic forces and will detach from it very close to the free-surface once the needle is retracted from the liquid bridge.

Having an axisymmetric flow, the whole flow-field domain is occupied by regular, periodic streamlines (see [211]) and, regardless of gravity, the only two mechanisms that may lead to a stable, global periodic attractor for the particle are centrifugation by inertia and repulsion by boundary forces. The phenomenon has been extensively discussed in Chapter 4 and in this subsection we aim at experimentally demonstrate the existence of such an attracting orbit.

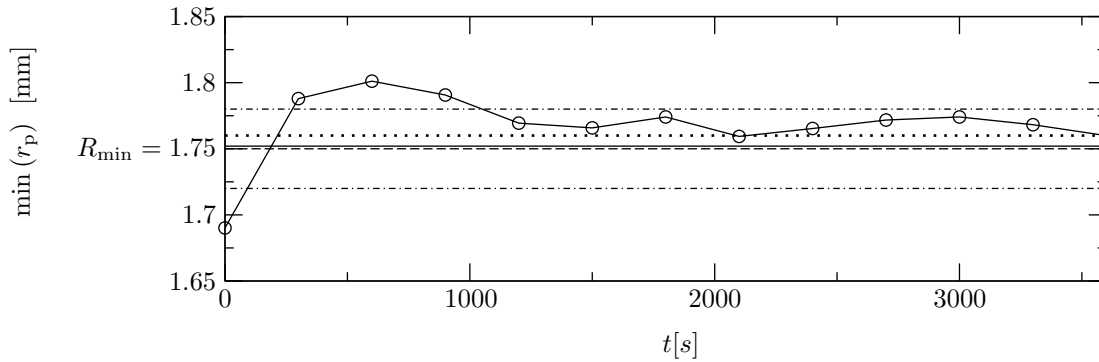


Figure 5.3.: Experimental evidence of the attraction of a single particle to the limit cycle (\circ) in a liquid bridge with $a_p = 25\mu\text{m}$, $\varrho = 1.69$, $d = 1.65\text{ mm}$, $\Gamma = 0.66$, $\text{Pr} = 28.5$, $\text{Re} = 331$ and $\text{Bd} = 0.40$. The dashed line denotes R_{\min} , calculated averaging three experimental runs in terms of $\min(r_p)$ after 60 minutes from the insertion of the particle. The maximum deviations of R_{\min} from the nominal value (measured averaging all the experimental runs) are indicated in dashed-dotted lines. The dotted and solid lines are the numerical predictions made considering a single-fluid solver (with adiabatic liquid bridges free-surface) and a two-fluids solver (which includes the ambient effects), respectively.

The radial position of the particle is measured by particle tracking for one hour (80 thermal time units ca.) and recorded for 4 seconds each 5 minutes. The attraction to the limit cycle is demonstrated in fig. 5.3 showing the minimum radial coordinate of the particle for each of the recording intervals, $\min(r_p)$, as function of time. A nominal value of $\min(r_p)$ after 60 minutes, R_{\min} , is obtained averaging the experimental results for different runs. In all of them the attraction to the limit cycle has been observed. Figure 5.3 demonstrates the very good agreement our numerical simulations with the experimental data of M. Ishimura & I. Ueno. More details about the numerical solvers are given in the next subsection.

Comparison between Experiments and Simulations

Experimental results are compared with one-way coupled particle trajectories integrated in the flow fields resulting from two different numerical solvers. The first one considers a simplified single-fluid model for which adiabatic free-surface is assumed, whereas a more sophisticated multiphase solver is employed to take into account the energy transfer effects on the flow and consequently on the particle accumulation structure. The fluids thermophysical properties assume as reference temperature 25°C and for the silicone oil we refer to [265] for modelling the temperature dependences of the fluid's viscosity and diffusivity. Figure 5.1 depicts the computational domain employed in the latter case, for which $d_{\text{cold}}/d = d_{\text{hot}}/d = 1$, $R_{\text{gap}}/R = 2$. The height of the test chamber does not correspond to the experimental set-up, but a sensitivity analysis has been conducted on $d_{\text{cold}}/d = d_{\text{hot}}/d$. Increasing $d_{\text{cold}}/d = d_{\text{hot}}/d$ beyond 1 does not considerably affect the fluid flow velocity in the liquid bridge, hence we select $d_{\text{cold}}/d = d_{\text{hot}}/d = 1$ in order to optimize the computational costs. In both cases, the thermocapillary scaling is adopted, statically deformed interface, temperature-dependency of kinematic viscosity and thermal diffusivity are taken into account.

Figure 5.4 shows the numerical particle trajectory after full convergence to the limit cycle corresponding to the largest particle available in the experiments ($a_p = 25\mu\text{m}$, $\varrho = 1.69$). Both,

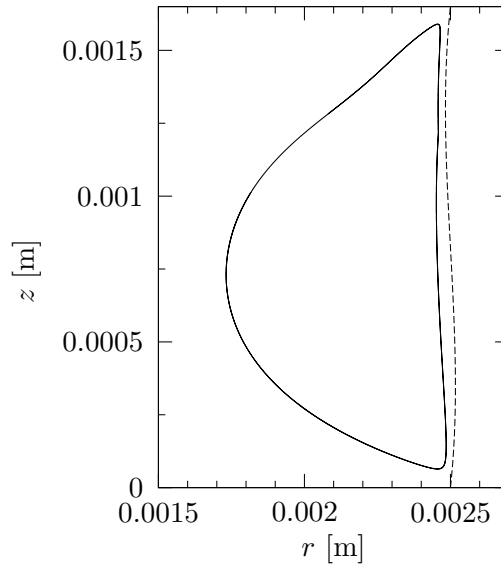


Figure 5.4.: Periodic attractor for the largest particle considered ($a_p = 25 \mu\text{m}$ and $\varrho = 1.69$) in an axisymmetric liquid bridge flow with $h = 1.65 \text{ mm}$, $\text{Pr} = 28.5$, $\text{Re} = 331$, $\Gamma = 0.66$, $\mathcal{V} = 1.0$ and $\text{Bd} = 0.40$. The trajectory is computed using the single-fluid solver. The liquid–gas interface is depicted in dashed line.

in case of the single-fluid and the two-fluids solver, the particle collision (in the framework of the PSI model) occurs at the hot corner, where the particle approaches closest the free-surface. Only a small portion of the particle trajectory along the liquid-gas interface is however affected by the inelastic collision model.

For a quantitative prediction of axisymmetric PAS, the only quantity which could be accurately measured from the experiment is the radial position of the particle as function of time. Moreover a one-way coupled approach in which the collision is modelled via PSI model is not suitable for describing the accumulation dynamics, but only the final stage of PAS. Hence our comparison will be based on the particle trajectory once it already accumulated on the periodic orbit. Three main scalar quantities characterize the orbit: the minimum radial coordinate of the particle, R_{\min} (see [270, 195, 194, 156]), the maximum radial coordinate of the particle, R_{\max} , and the turn-over time, $T_{\text{t-o}}$. Table 5.3 lists these quantities comparing experimental and numerical results in case a single-fluid or a two-fluids solvers is used. In the former case the focus is on showing the improvement of our prediction whether the PSI model is considering the lubrication gap width obtained in Chapter 4. The two-fluids solver is considered for the case of interaction length $\Delta = a + \delta$ only.

Furthermore, table 5.4 reports the relative difference between numerical and experimental data defined as follows

$$\Delta^{\text{rel}} = \left| \frac{s_{\text{exp}} - s_{\text{CFD}}}{s_{\text{exp}}} \right| \quad (5.2)$$

where s indicates the quantity to compare and exp and CFD refer to experimental measurements and numerical predictions, respectively. Such relative deviations are then compared with the relative experimental tolerance Δ^{expTol} obtained dividing the error bar by twice the nominal value s_{exp} .

We always find a good agreement with experimental data for which keeps $\Delta^{\text{rel}} < 10\%$ in

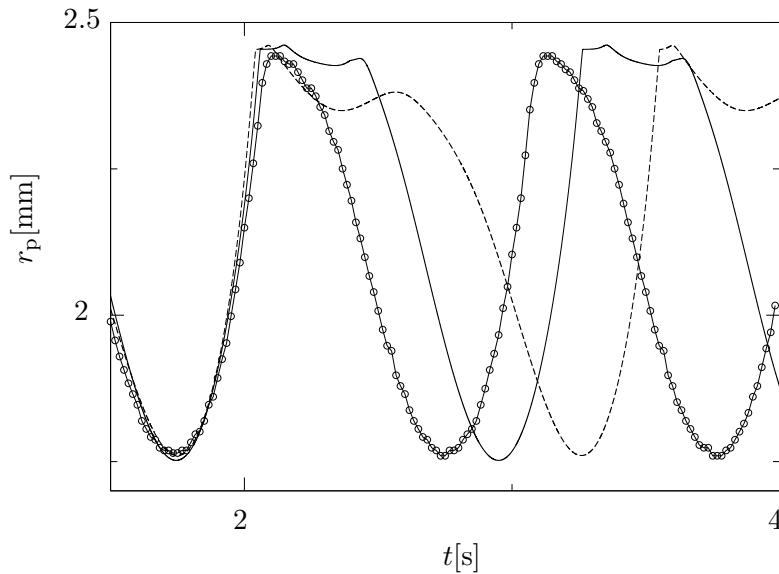


Figure 5.5.: Radial coordinate of the particle trajectory for $a_p = 25 \mu\text{m}$, $\varrho = 1.69$, after it accumulated along the periodic orbit in an axisymmetric liquid bridge for $h = 1.65 \text{ mm}$, $\text{Pr} = 28.5$, $\text{Re} = 331$, $\Gamma = 0.66$, $\mathcal{V} = 1.0$ and $\text{Bd} = 0.40$. The solid and dashed lines indicate numerical data obtained for the two-fluids and single-fluid solvers, respectively. Open circles indicate the experimental data obtained after 60 minutes from the insertion of the particle in the liquid bridge.

all the cases for R_{\min} and R_{\max} . This confirms that the simplest one-way coupled model we consider (single-fluid solver with adiabatic free-surface and interaction length $\Delta = a$) is already a good approximation of the experiments. However, including the lubrication gap width from the two-dimensional fully-resolved simulations of the previous chapter yields to an even better agreement. Even the single-fluid solver is capable to accurately reproduce the experimental results in terms of R_{\min} and R_{\max} . These quantities are not remarkably improved by considering the two-fluids solver (for larger particles the deviation between experimental and numerical results was already $< 2.5\%$), but the predicted turn-over time. Figure 5.5 depicts a comparison between experiments and numerical simulations for the particle trajectory along the periodic orbit. In the computational prediction the particle tends to stay close to the free-surface for a longer time than in the experiments. This explains why the two-fluid solver, for which the free-surface velocity is higher, gives a better prediction of the turn-over time than the single-phase adiabatic solver. The improved prediction of T_{t-o} is definitely better, specially if we consider the strong simplification introduced by the PSI model. Having considered all the possible factors which may have a significant role in the phenomenon, the remaining discrepancies can be attributed to a possibly over-simplified approach with which the particle–free-surface interaction is modelled or to experimental issues which may have caused a discrepancy between experiments and mathematical model (surfactants on the liquid-gas interface near the cold corner [191, 259], etc...).

From this study we can conclude that the axisymmetric particle accumulation structures can be accurately predicted employing a one-way coupling approach for which the particle trajectory is integrated using a Maxey–Riley equation corrected at the domain boundary via the PSI model. An accurate estimate of the minimum lubrication gap width is definitely important to obtain

Table 5.3.: Turn-over time, maximum and minimum radial coordinate of the limit cycles for heavy particles in a thermocapillary liquid bridge with $d = 1.65$ mm, $\Gamma = 0.66$, $\text{Pr} = 28.5$, $\text{Re} = 331$ and $\text{Bd} = 0.40$. The numerical results obtained via the single-fluid and the two-fluids solves are indicated with s-f_{CFD} and t-f_{CFD}, respectively.

a_p [μm]	R_{\max} [mm]	R_{\min} [mm]	T_{t-o} [s]	Source
15	2.471	1.592	1.292	t-f _{CFD} ($\Delta = a + \delta$)
	2.472	1.587	1.462	s-f _{CFD} ($\Delta = a + \delta$)
	2.485	1.555	1.464	s-f _{CFD} ($\Delta = a$)
	2.44 ± 0.02	1.68 ± 0.04	1.00	Experiments
25	2.461	1.752	1.205	t-f _{CFD} ($\Delta = a + \delta$)
	2.459	1.760	1.574	s-f _{CFD} ($\Delta = a + \delta$)
	2.479	1.587	1.488	s-f _{CFD} ($\Delta = a$)
	2.40 ± 0.03	1.75 ± 0.03	1.07	Experiments

Table 5.4.: Relative deviations in R_{\min} and R_{\max} between numerical and nominal experimental data compared with the relative experimental tolerance for axisymmetric PAS in a liquid bridge with $d = 1.65$ mm, $\Gamma = 0.66$, $\text{Pr} = 28.5$, $\text{Re} = 331$ and $\text{Bd} = 0.40$. The numerical results obtained via the single-fluid and the two-fluids solves are indicated with s-f_{CFD} and t-f_{CFD}, respectively.

a_p [μm]	$\Delta_{R_{\max}}^{\text{rel}}$	$\Delta_{R_{\max}}^{\text{expTol}}$	$\Delta_{R_{\min}}^{\text{rel}}$	$\Delta_{R_{\min}}^{\text{expTol}}$	Source
15	1.27%	0.8%	5.24%	2.3%	t-f _{CFD} ($\Delta = a + \delta$)
	1.31%		5.53%		s-f _{CFD} ($\Delta = a + \delta$)
	1.85%		7.44%		s-f _{CFD} ($\Delta = a$)
25	2.54%	1.3%	0.11%	1.7%	t-f _{CFD} ($\Delta = a + \delta$)
	2.46%		1.12%		s-f _{CFD} ($\Delta = a + \delta$)
	3.29%		8.79%		s-f _{CFD} ($\Delta = a$)

an accurate numerical prediction of R_{\min} and R_{\max} . Finally, including heat transfer effects the estimate of the particle turn-over time along the periodic orbit is sensibly improving, but still to be further investigated. In particular it must be clarified the role of a surfactant film near the cold corner in the early departure of the particle from the free-surface (compare experimental and numerical trajectories in fig. 5.5).

5.2.2. Three-dimensional Liquid Bridge

In this section we will consider a thermocapillary liquid bridge flow after the onset of instability in the form of a hydrothermal wave. Under normal gravity conditions, the flow parameters which will be kept constant in the following are

$$\text{Pr} = 28, \quad \Gamma = 0.68, \quad \mathcal{V} = 1.0, \quad \text{Ca} \rightarrow 0. \quad (5.3)$$

Two thermocapillary Reynolds numbers are considered: $\text{Re} = 1600$ and 1950 .

The choice of these parameters is motivated by published experimental data which have never been numerically reproduced before. Following the argument proposed in [194] for $\text{Pr} = 4$, a

detailed study of the relation between particle accumulation and flow topology will be presented. Considering $\text{Pr} = 28$ gives rise to a very thin thermal boundary layer which contributes to the challenge of simulating these flows.

Owing to the small free-surface deformation the liquid-gas interface is assumed statically (and dynamically) undeformed. Moreover thermal diffusivity and kinematic viscosity are considered constant only the liquid phase is simulated. To include the heat transfer we follow [194] and set $\text{Bi} = 0.30$ in Newton's law, assuming the ambient temperature $\theta_a = 0$.

An OpenFOAM[®] solver has been developed and benchmarked by Thomas Lemee in the framework of a dedicated FFG project [146] in order to deal with the thermocapillary flow of interest and the corresponding Marangoni boundary conditions. The thermal diffusion scaling is herein employed and the computational mesh is reported in fig. 5.7. A second-order implicit discretization is adopted in time and the simulations are stopped after that the hydrothermal wave has completely developed according to the following termination criterion in the rotating reference frame

$$\max_{x,i} \frac{|u_i(\mathbf{x}, t) - u_i(\mathbf{x}, t - \Delta t)|}{\text{Ma}\Delta t} \leq 10^{-5}. \quad (5.4)$$

In order to characterize the flow we refer to fig. 5.2 for demonstrating the features of the basic state. Figure 5.6 depicts the projection of the velocity vectors for $\text{Re} = 1600$ on the (r, φ) - and (r, z) -planes after the onset of the hydrothermal wave. The selected parameters lead to a hydrothermal wave with fundamental azimuthal wave number $m = 3$. Non-linear interactions generate also higher harmonics. The flow field for both the investigated Reynolds numbers is periodic in time, all the spectral components have the same phase velocity and we can assume the flow field stationary in a reference frame rotating with the hydrothermal wave. For $\text{Re} = 1600$ and 1950 the travelling wave has rotation rate $\Omega_{\text{HTW}} = 116.230$ and 123.218, respectively.

Main Topological Elements

The topology of the liquid bridge flow after the onset of the hydrothermal wave is here investigated via a Lagrangian representation of the flow kinematics. Owing to the periodicity of the flow, in a reference frame rotating with Ω_{HTW} , the flow is steady with $m = 3$ in azimuthal direction. The motion of the infinitesimal fluid element is governed by

$$\frac{d\mathbf{X}}{dt} = \mathbf{u}_{\Omega_{\text{HTW}}}(\mathbf{X}). \quad (5.5)$$

where \mathbf{X} is the fluid element location, $\mathbf{X}(t=0)$ its initial position and $\mathbf{u}_{\Omega_{\text{HTW}}}$ the fluid flow velocity in the reference frame rotating with the angular velocity Ω_{HTW} .

Equation 5.5 is integrated numerically employing the 4th/5th-order Runge–Kutta Dormand–Prince method [73], which consists in an explicit integration of the fluid element trajectory employing for each time step both, the 4th- and 5th-order Runge–Kutta scheme. By difference of the two solutions an error estimate is produced and the Δt is then adapted in order to keep the estimated absolute and relative errors always lower than 10^{-7} .

Passing from the Eulerian fluid flow description adopted so far to the Lagrangian frame of reference an interpolation of the flow velocity $\mathbf{u}_{\Omega_{\text{HTW}}}$ on the particle location has to be included. First order interpolation is used to compute the chaotic streamlines. A more accurate quadratic interpolant is adopted for computing streamlines in the regular regions of the flow. The two intersections between the axis and the cylindrical rods are critical points. They become saddle foci $s_{1,2}$ after the onset of instability.

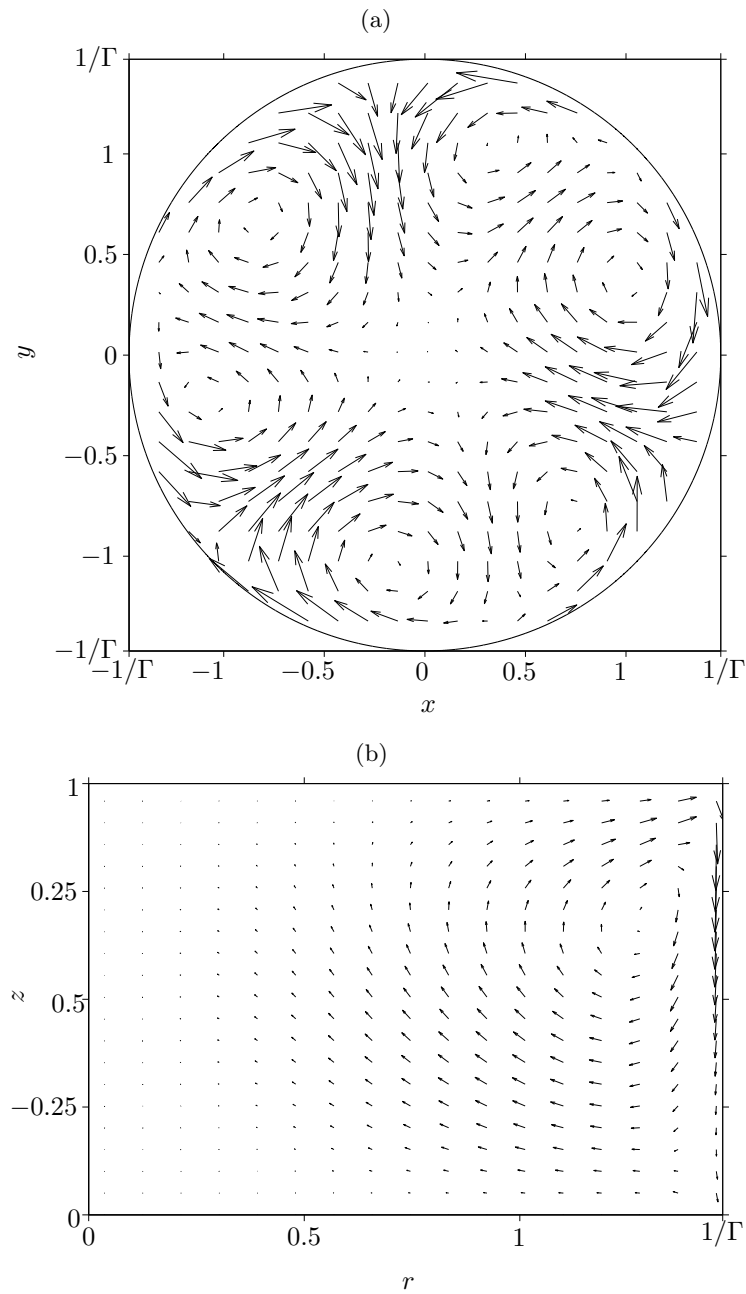


Figure 5.6.: Velocity vectors for $\text{Re} = 1600$ projected on (r, φ) - (a), (r, z) -planes (b) in a reference frame rotating with the angular velocity of the hydrothermal wave Ω_{HTW} .

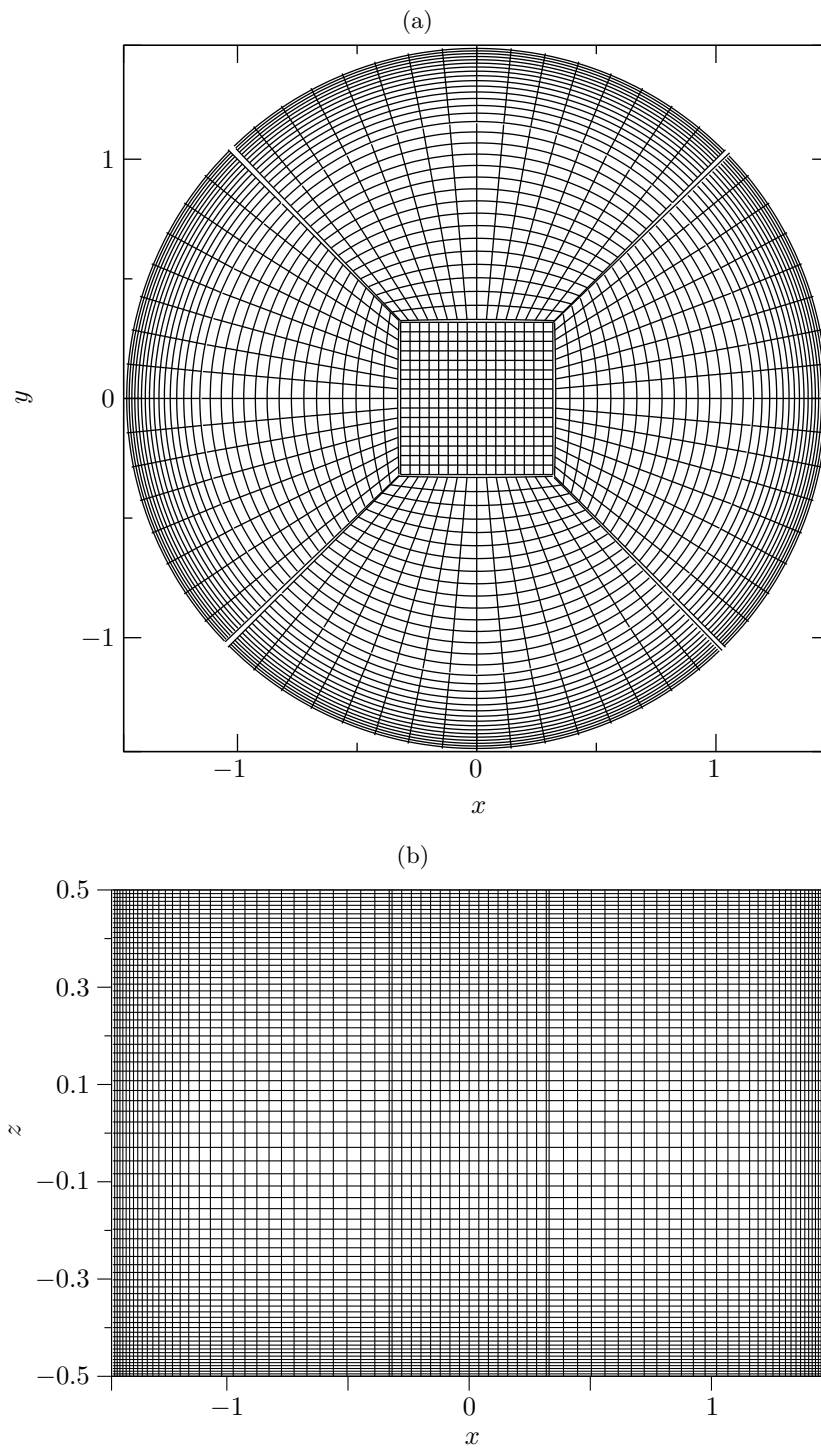


Figure 5.7.: Distribution of the finite volume cells for each cross-section (a) and on the (x, z) plane (b). The grid employed for the simulation presented in the following is 5 times finer than the one depicted in this figure, consisting of ≈ 20 million grid points. The double lines indicate the main blocks of the mesh.

In order to characterize the saddle foci on the hot and cold walls, the streamlines are computed for $\text{Re} = 1600$ at $|z| = 0.5 - 10^{-3}$ setting $w = 0$. The corresponding flow is therefore planar, but not incompressible. It can be considered as good approximation of the streamlines for $z \rightarrow \pm 0.5$. It characterizes both the critical points as spiralling-out saddle foci. For demonstration purpose, fig. 5.8 depicts the motion of a fluid element initialized in the vicinity of the saddle focus on the hot rod.

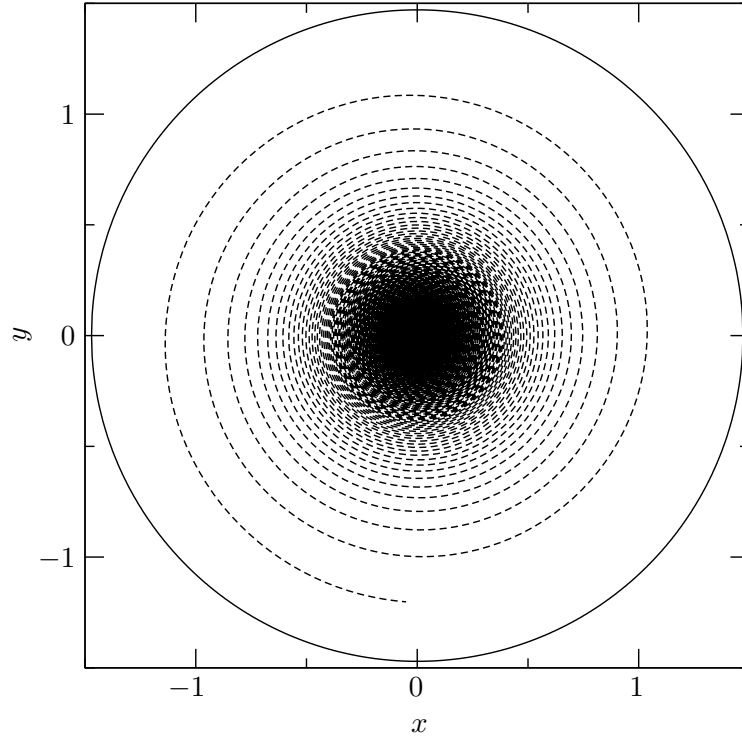


Figure 5.8.: Spiralling-out (dashed line) motion of a fluid element over the hot rod. The streamlines are computed at $z = 0.499$ for $\text{Re} = 1600$ integrating forward in time up to $t = 0.5$ a fluid element initialized at $(r, \varphi) = (0.001, 0)$ setting $w = 0$.

The same character of the two saddle foci can be explained by a separated region in the flow. Owing to the positive temperature gradient in z -direction and the thermophysical properties of silicone oil ($\partial_z \theta > 0$ and $\partial_\theta \sigma < 0$), thermocapillary effects drive the flow over the free-surface from top to bottom. In the vicinity of the cold corner, the flow raises with a sharp turn and a separated region appears at the cold corner. Further investigations are currently in progress to identify the intersection of the separation region with the cold rod. However, based on fig. 5.8, we speculate that the separation region invades the whole or most of the bottom rod. Under microgravity conditions such a recirculation zone is definitely small (see e.g. [205, 248]). It is larger in three-dimensional buoyant flows, but also exists under weightlessness for $\text{Pr} = 4$ [126]. From the streamlines on the cold rod we can conclude that in the case under investigation it invades the whole rod. To estimate the size of the separated region we plot the axial velocity w along the liquid bridge axis (see fig. 5.9).

On the separated surface there is another critical point c which plays a major role in the flow topology of the liquid bridge. It is a complex spiralling-in saddle focus and around such a free point the chaotic sea is distributed. To further investigate the kinematics of the chaotic streamlines we integrate forward and backward in time two fluid elements located $(r_c, \varphi_c, z_c \pm 10^{-2})$. The blue and red lines in fig. 5.10 depict the fluid element trajectories from the hot

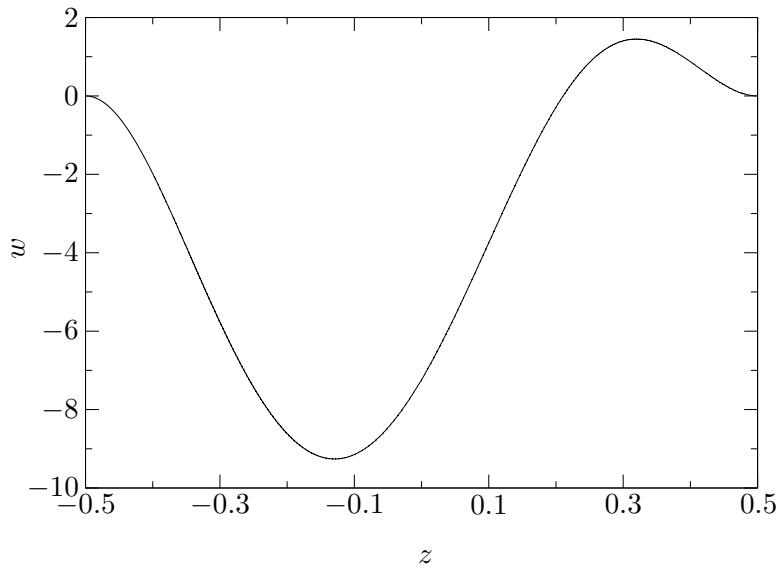


Figure 5.9.: Axial velocity w along the liquid bridge axis. The changing of sign of w along z identifies the intersection of the separated region with the liquid bridge axis at $z = 0.21067$.

and cold rods, respectively. On the free-surface, the streamlines are moving from top to bottom and then released nearby the edge of the separation region at the cold rod. Thereafter they are attracted by the spiralling-in saddle-node c and ejected along its unstable manifolds towards the spiralling-out saddle foci on the hot (blue dashed line) and cold (red solid line) walls.

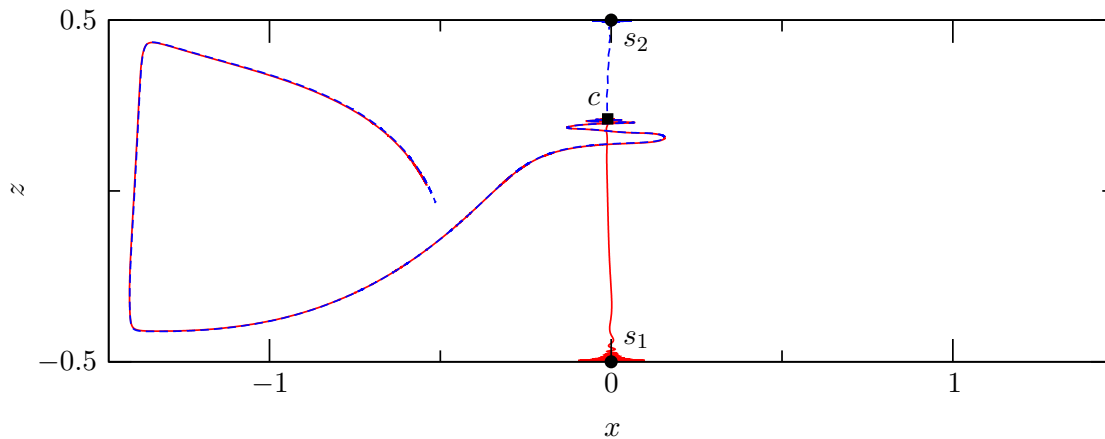


Figure 5.10.: Chaotic dynamics of two fluid elements integrated forward and backward in time from $(r_c, \varphi_c, z_c \pm 10^{-2})$. The shift of c from the liquid bridge axis results from the non perfect ($m = 3$)-periodicity of the flow. Full circles indicate the spiralling-out saddle foci, whereas the square marker denote the spiralling-in saddle point.

A conceptual sketch of the main topological elements for the liquid bridge in supercritical conditions is presented in fig. 5.11. A fluid element initially in the neighbourhood of s_2 will spiral out past the hot rod being attracted to the saddle limit cycle w_2 . Thereafter it moves along the free-surface which connects the two saddle limit cycles w_2 and w_c . From the latter the streamline is ejected in the bulk over the separation surface along which it will be attracted by

the complex saddle focus c . Thereafter the fluid element is further ejected along the unstable manifold of c and attracted once again by s_2 . With respect to the cold rod basically two cases may occur. If the chaotic streamlines lie within the separated region, they do not move along the free-surface but start crawling the separation surface once they arrive at w_c . On the other hand, if a streamline is moving along the free-surface (above the separated region), it will be attracted by the spiralling-in saddle focus c and may be successively ejected towards s_1 along the unstable manifold on c (black solid line in fig. 5.11). The fluid elements are attracted by c and ejected along its unstable manifold towards s_1 . Our speculation based on this evidences is that the chaos in the system is originated by the saddle-limit cycle at the cold corner w_c and the complex saddle focus in the bulk c . A detailed and dedicated study would be required for proving this assumption and further investigations are currently in plan.

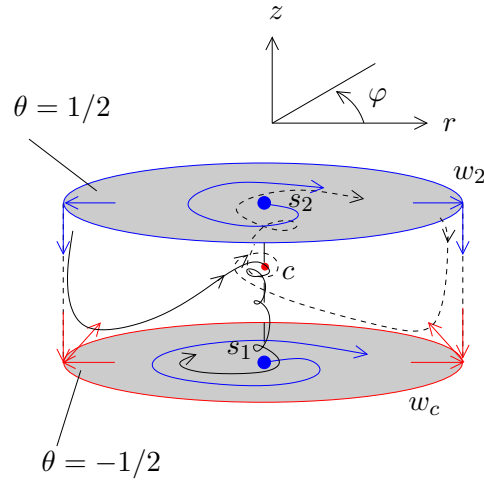


Figure 5.11.: Sketch of the major topological elements of the liquid bridge in supercritical conditions after the onset of a hydrothermal wave instability. The spiralling-in saddle focus (red dot) and the saddle limit cycle on $z = -1/2$ are denoted by c and w_c , respectively. The spiralling-out saddle foci and the saddle limit cycle on the other cell boundary (marked in blue) are indicated by $s_{1,2}$ and w_2 . The grey areas depict hot (top) and cold (bottom) rods.

Chaotic and Regular Regions

The aim of this topological study is to demonstrate the connection between periodic or quasi-periodic regular regions of the flow and the particle attractors experimentally observed. For a liquid bridge flow, Mukin & Kuhlmann [194] and Hofmann & Kuhlmann [126] have already numerically demonstrated it in case of $Pr = 4$. Herein we target the experimental parameter space and specific particle accumulations which have never been numerically reproduced before ($Pr = 28$ in normal gravity conditions). Our goal will consist in demonstrating how an accurate and systematic description of chaotic and regular regions is necessary for quantitatively predicting PAS.

In a reference frame rotating with the angular velocity of the hydrothermal wave, Ω_{HTW} , the flow is steady and three-dimensional. The fluid motion can be interpreted as an Hamiltonian with 1.5 degrees of freedom [12]. This statement implies that there may be a coexistence between chaotic regions and quasi-periodic sub-volumes (regular regions) of the fluid domain. Owing to the incompressibility of the flow field, the regular regions assume the shape of Kolmogorov-

Arnold-Moser tori (KAM tori, [106]). A typical condition the flow is arranged in is therefore a chaotic sea in which the KAM tori are embedded. Moreover, the higher the Reynolds number, the smaller the regular regions are expected to be.

To compute chaotic and regular streamlines, 20 fluid elements are evenly distributed along four vertical lines with a phase shift of $\Delta\varphi = \pi$ along $(r, z) = (1/\Gamma - 10^{-4}, z)$. The streamlines are integrated for $t = 3$ in thermal diffusive time units. For both the Reynolds numbers, $\text{Re} = 1600$ and 1950 , we produce a Poincaré section intersecting the fluid element trajectories with the (r, φ) -plane. A second integration is performed for the regular streamlines employing quadratic interpolation and setting the relative and absolute error estimate of the Runge–Kutta Dormand–Prince method to 10^{-9} . The integration time is chosen such that at least 20 oriented returns on the Poincaré plane are obtained.

We therefore identify the KAM surfaces and the corresponding closed trajectory which can be reliably computed; This is depicted in fig. 5.12 for both the investigated Reynolds numbers, including the projection on the (r, φ) -plane of the corresponding closed streamline (solid line). In fig. 5.12 chaotic (grey) and regular (indigo) regions of flow are characterized via a Poincaré section on the (r, φ) -plane. Increasing the Reynolds number the volume occupied by the widest regular region sensibly shrinks such that, at $\text{Re} = 1950$, we reliably identify a KAM torus just in a very narrow region about the closed trajectory and its Poincaré returns are within the marker size of the periodic orbit (\diamond). Moreover, passing from $\text{Re} = 1600$ to $\text{Re} = 1950$, three small KAM tori are created in the chaotic sea. A further remarkable difference between the two Reynolds numbers is the shape of their regular regions; passing from $\text{Re} = 1600$ to $\text{Re} = 1950$ the widest KAM torus winds six times around the apparent vortex center (see the streamlines in fig. 5.2) instead than three times only. To be noticed is also that the widest regular regions are located very close to the driving boundaries (i.e. free-surface in this case).

As pointed out in [194], the minimum distance from the boundaries of the closed widest streamline, L^{SL} , and the corresponding outermost KAM surface we reach to identify, T^{SL} , are key quantities for understanding and predicting the particle accumulation structures. They define the range of interaction lengths Δ which lead to particle accumulation structures embedded in the KAM tori (see e.g. [195, 194, 126]). Hence, these quantities are reported in table 5.5 together with the turn-over time of the widest closed streamline τ^{SL} . Moreover, in order to identify the corresponding periodic orbit we compute one of the respective elliptic fixed points of the Poincaré map carrying out a Newton–Raphson method up to a relative accuracy of 10^{-3} in the (r, φ) -plane.

Table 5.5.: List of the orbit times τ^{SL} for the closed streamlines L^{SL} and minimum distances Δ^{fs} and Δ^{w} from the free-surface and walls, respectively, for both, the periodic orbit, L^{SL} , and the outermost KAM surface, T^{SL} . To identify the radial coordinate of the closed streamlines, one of their fixed point locations on the Poincaré map over the (x, y) -plane is given.

Re	KAM/streamline	τ^{SL}	Δ^{fs}	Δ^{w}	Fixed point (x, y, z)
1600	T^{SL}	–	0.005648	0.031589	–
	L^{SL}	0.04631	0.011800	0.041935	(0.2554, 1.4254, 0)
1950	T^{SL}	–	0.004521	0.020698	–
	L^{SL}	0.04742	0.004549	0.020721	(0.2464, 0.6432, 0)

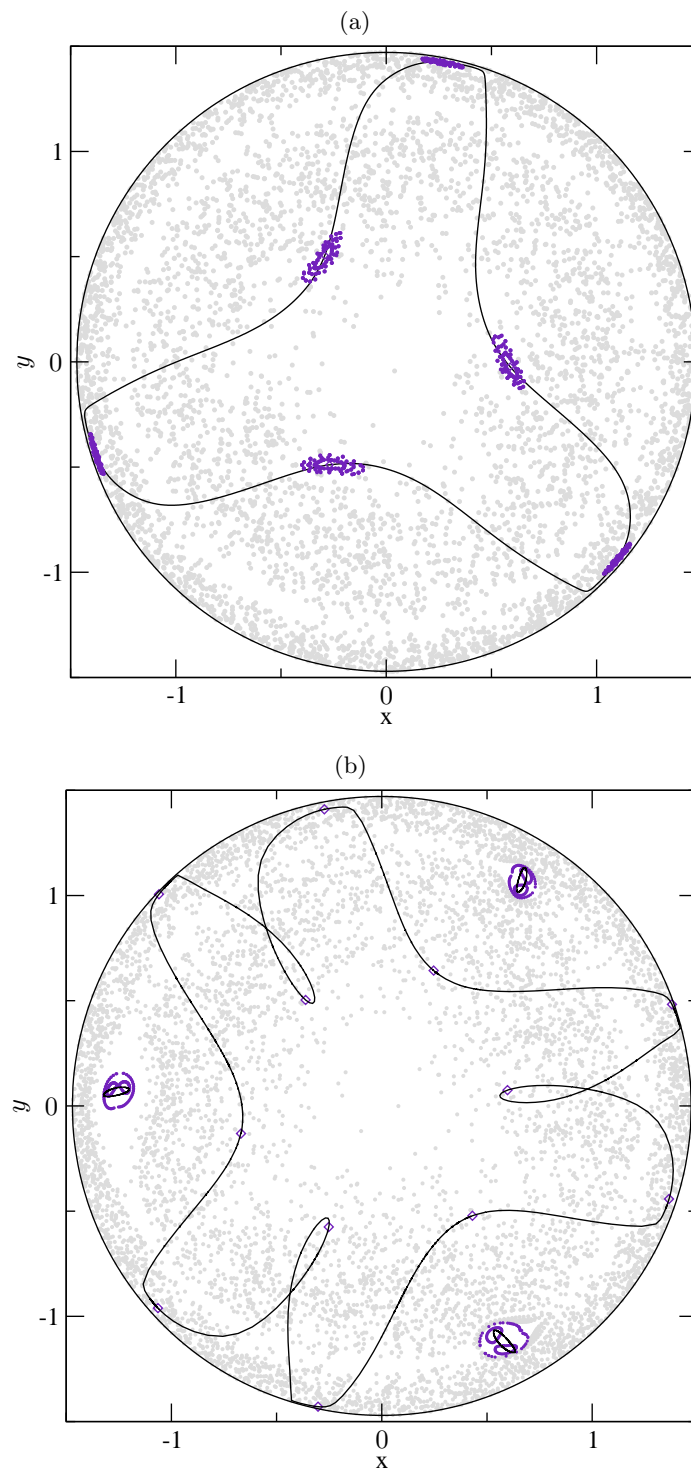


Figure 5.12.: Poincaré section of the KAM tori and the closed streamlines (indigo) embedded in the chaotic sea (grey) on the (r, φ) -plane for $\text{Re} = 1600$ (a) and $\text{Re} = 1950$ (b). The streamlines are computed in the rotating reference frame and the regular structures have period $m = 3$. The intersections of the periodic orbits with the Poincaré plane are marked by a diamond (\diamond). The solid line denotes the projection on the (r, φ) -plane of the closed streamlines.

Comparison Between Experiments and Simulations

Particle accumulation structures in a liquid bridge have been extensively studied numerically for flow conditions after the onset of hydrothermal wave instabilities (see e.g. [194, 190, 160]). Hence we will not focus on different scenarios of numerically predicted PAS, but we aim at demonstrating the importance of an accurate estimate of the minimum lubrication gap width between particles and boundaries, δ .

In Section 5.2.1 we investigated such a matter in an axisymmetric flow. Reliable quantitative data have been produced with an accurate particle tracking and single-particle experiments have been performed in order to exclude particle–particle interaction effects. At the time being a similarly accurate set of experimental data is not present for three-dimensional liquid bridge flows. Therefore the numerical results presented in the following will only be qualitatively compared with experiments. The two selected cases ($\text{Re} = 1600$ and 1950) have been chosen ad-hoc because of the high sensitivity their PAS has to the particle radius [278]. This will let us further understand the importance of δ in reliably predicting three-dimensional PAS.

The comparison with experiments is based on the accumulation patterns found carrying out the simulations up to $t = 3$ thermal diffusive time units. The Maxey–Riley equation supplemented with the PSI model have been employed for simulating the particle trajectories initializing 1000 randomly distributed tracers in the particle domain. A restricted initialization region \mathcal{V}^* is considered taking into account that the regions adjacent to the boundaries are not accessible for finite-size particles in the framework of the PSI model (see [126]). In cylindrical coordinates such a restricted domain reads

$$\mathcal{V}^* = [0, 1/\Gamma - \Delta_{\text{fs}}] \times [0, 2\pi] \times [-1/2 + \Delta_{\text{w}}, 1/2 - \Delta_{\text{w}}], \quad (5.6)$$

where Δ_{fs} and Δ_{w} are the interaction lengths in case of particle–free-surface and particle–wall interaction, respectively.

Table 5.6 lists flow and particle parameters of the two targeted experiments, as well as the interaction lengths adopted in the PSI model. Two different numerical simulations will be considered for both the experiments: the first case employs an interaction length which does not include the lubrication gap width ($\Delta = a$), whereas the second numerical simulation will take into account the predictions made in Chapter 4 regarding Δ_{fs} and Δ_{w} .

Table 5.6.: Flow and particle parameters employed for comparing experimental and numerical particle accumulation structures in three-dimensional flows in a liquid bridge under 1g conditions for $\text{Pr} = 28$ and $\Gamma = 0.68$.

Re	a_{p} [μm]	ϱ	$a_{\text{p}}/d = a$	Δ_{fs}	Δ_{w}
1600	7.5	2.03	0.004411765	0.005884	0.010042
1950	5	2.52	0.002941176	0.004420	0.007017

Figures 5.13 and 5.14 depict the comparison between numerical and experimental results for $\text{Re} = 1600$ and 1950 , respectively. Two different kinds of particle accumulation structures are shown: the so-called SL-I- (fig. 5.13) and SL-II-PAS (fig. 5.14). A first remarkable outcome resulting from the comparison is the essential role of a good estimate of the lubrication gap width δ . Indeed, the numerical simulations for which $\Delta = a$ is employed in the PSI model (see fig. 5.13a and 5.14a) do not predict any SL-I or SL-II, in contrast to what is experimentally observed. On the other hand, if Δ_{fs} and Δ_{w} are taken into account in the PSI model, the

comparison between numerical and experimental results is very convincing for both the cases. This confirms that the two-dimensional estimate of Δ is already good enough to reproduce experimentally observed PAS conditions very sensitive to the particle parameters.

A further remark has to be made about the toroidal core experimentally observed for $\text{Re} = 1600$ (see fig. 5.13). This is not observed in the numerical simulations and a possible reason is that it may be due to a very initial stage of the particle dynamics. Figure 5.13c is obtained averaging in time the recorded visualization and a weakly chaotic regions may give the impression of forming the toroidal PAS depicted in 5.13c if the experiment is recorded for too short time.

Comparing the regular structures of the flow topology and the patterns of accumulation one can clearly observe the connection of PAS with the KAM tori. To the best of the author's knowledge, this is the first time that SL-II-PAS is numerically reproduced for experimental conditions. Moreover the changing in shape of the closed streamline passing from $\text{Re} = 1600$ to $\text{Re} = 1950$ gives a clear explanation of why SL-I- turns into SL-II-PAS increasing the Reynolds number. Once again this statement confirms that PAS is strongly correlated with the flow topology and can be considered a further proof in support of the explanation of Kuhlmann et al. [126, 194].

Moreover, even if inertial and buoyancy effects are included in integrating the particle trajectories via the Maxey–Riley equation, the accumulation patterns almost coincide with the periodic and quasi-periodic orbits of a fluid element (indigo line in fig.s 5.13 and 5.14). This leads to speculate that inertial and buoyancy are minor effects regardless of which PAS phenomena are still well described in the investigated cases.

5.3. Lid-Driven Cavity

The second set-up we consider is a two-sided antiparallel lid-driven cavity for the mathematical formulation of which we refer to Chapter 2.

The aspect ratio of the cross section is set to $\Gamma = 1.7$, which corresponds to a critical Reynolds number $\text{Re}_c = 211.58$ and a critical wavelength $\lambda_c = 2.73$. Such a low Re_c guarantees the presence of steady, three-dimensional flow configurations for a relatively large interval of supercritical Reynolds numbers. The point symmetry with respect to each cell centres is a robust feature of the flow even after criticality, as experimentally confirmed by Blohm & Kuhlmann [30] for aspect ratio $\Gamma = 1.96$.

We refer to [3] for a complete description of the hydrodynamical instabilities one can observe in this configuration and to [4] and [243] for details about the numerical method employed for solving the Navier–Stokes system. Briefly, to give an idea of the accuracy employed for the flow solver, we mention that all the fluid flow simulations in this section are carried out with a collocated spectral method. Chebyshev–Gauss–Lobatto nodes are used in x - and y -direction, whereas Fourier modes are employed in z to implicitly verify the periodic boundary conditions. The solution is obtained using 128 modes in each direction and correcting the corners singularities with a second-order asymptotic solution (see [31, 4]). A second-order Adam–Bashforth backward–Euler scheme is adopted, employing a projection method conceptually similar to the one discussed in Chapter 3.

All the flow field data of this section have been provided by Stefan Albensoeder who carried out the simulations up to steadiness using the following termination criterion

$$\max_{x,i} \frac{|u_i(\mathbf{x}, t) - u_i(\mathbf{x}, t - \Delta t)|}{\Delta t |\text{Re}|} \leq 10^{-7}. \quad (5.7)$$

The streamlines integration is done according to the details given in Section 5.2.2 setting relative and absolute tolerance of the Dormand–Prince method to 10^{-10} . A linear interpolation

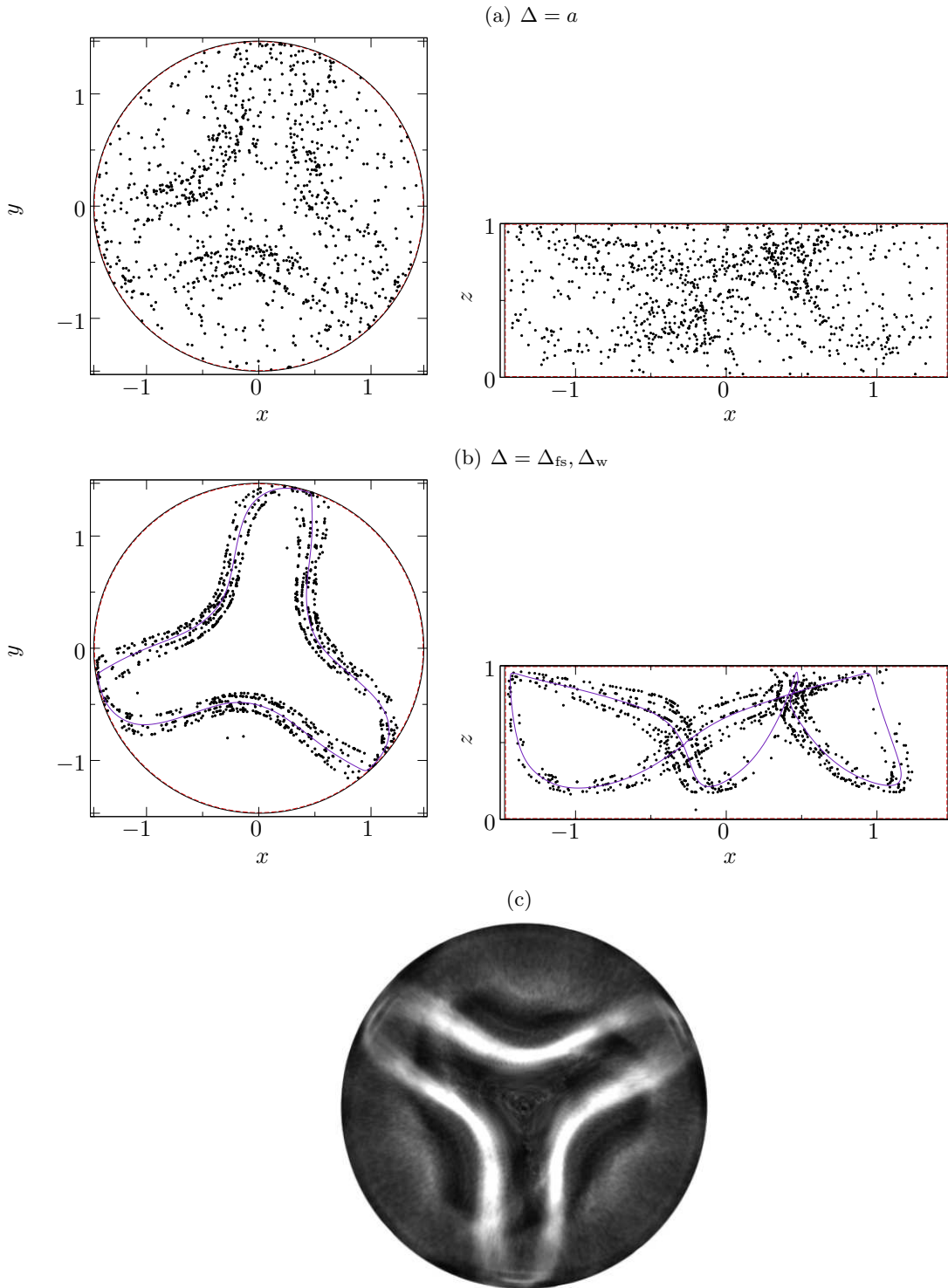


Figure 5.13.: Comparison between numerical, (a) and (b), and experimental, (c), results for PAS under 1g conditions for $Pr = 28$, $\Gamma = 0.68$ and $Re = 1600$. The integration time is $t = 3$ in thermal diffusion time units. If $\Delta = a$, initially randomly distributed particles do not form a clear SL-I (a) as in experiments (c). If the estimate of δ made in Chapter 4 is included (b), the tubular numerical SL-I-PAS very well resemble the experimental results (c). The indigo solid line represents the periodic orbit identified in the flow. The boundaries of \mathcal{V}^* are indicated with red dashed lines. The experimental results are produced at Tokyo University of Science under the supervision of Ichiro Ueno.

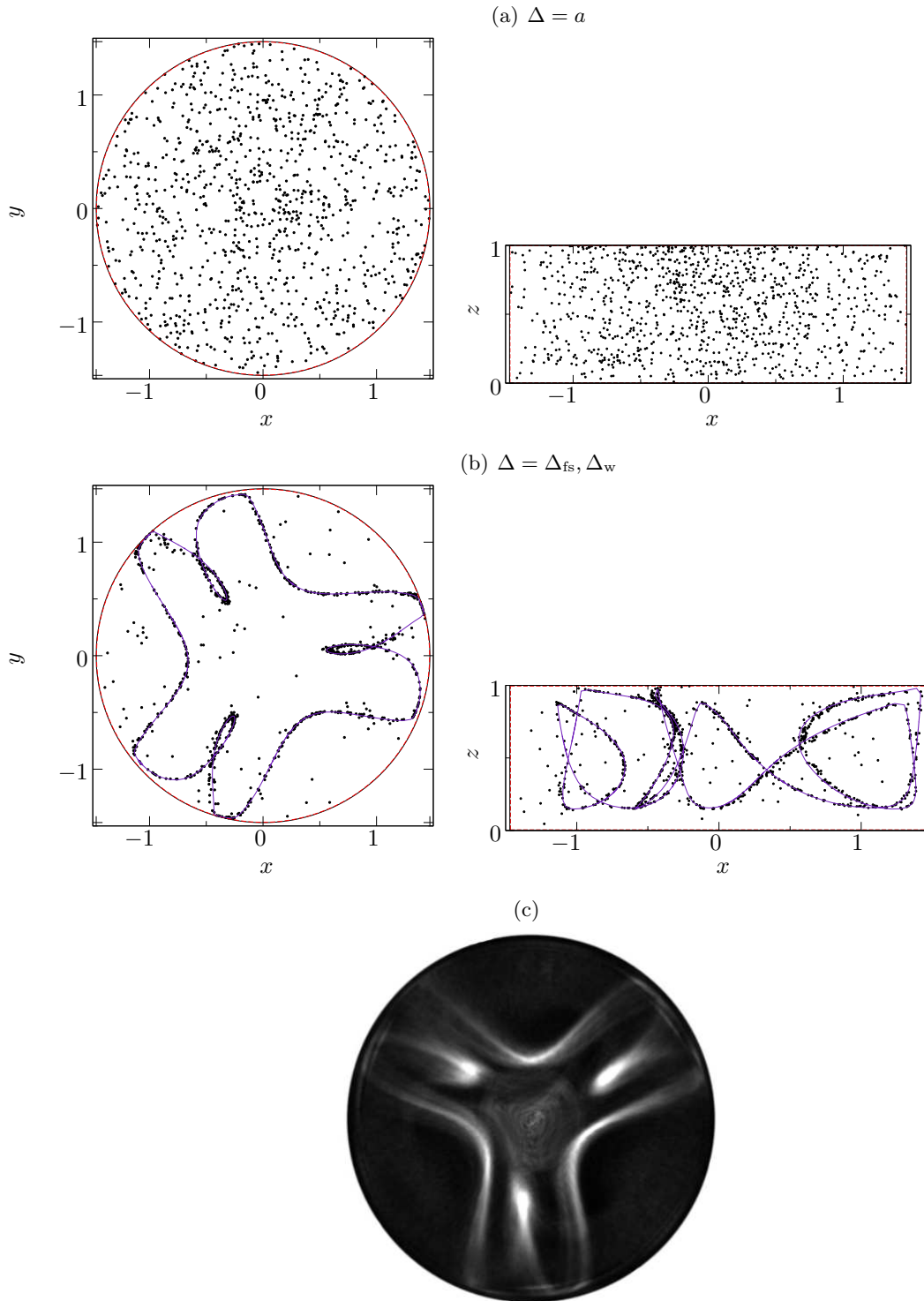


Figure 5.14.: Comparison between numerical, (a) and (b), and experimental, (c), results for PAS under 1g conditions for $Pr = 28$, $\Gamma = 0.68$ and $Re = 1950$. The integration time is $t = 3$ in thermal diffusion time units. If $\Delta = a$, initially randomly distributed particles do not accumulate (a). If the estimate of δ made in Chapter 4 is included (b), the line-like numerical SL-II-PAS very well resemble the experimental results (c). The indigo solid line represents the periodic orbit identified in the flow and almost coincide with the accumulation pattern. The boundaries of \mathcal{V}^* are indicated with red dashed lines. The experimental results are produced at Tokyo University of Science under the supervision of Ichiro Ueno.

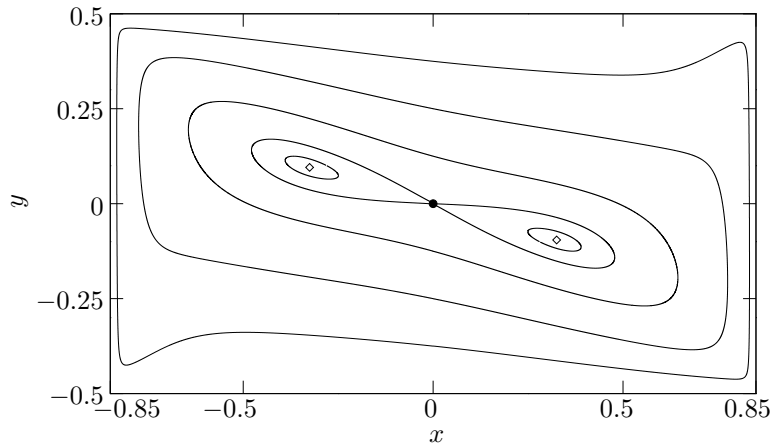


Figure 5.15.: Cat's-eye flow configuration occurring in the antiparallel lid-driven cavity at criticality for $\Gamma = 1.7$, $\lambda_c = 2.73$ and $\text{Re}_c = 211.58$. The markers indicate the hyperbolic point at the center of the cavity (\bullet) and the couple of elliptic points (\diamond) at $(x, y) = (\pm 0.3253, \mp 0.0955)$ which complete the cat's-eye configuration.

on the spectral grid is employed in computing chaotic streamlines, whereas the regular regions are obtained using a spectral interpolation over all the 128^3 modes of the mesh. For further details about the approximation introduced passing from an Eulerian solution for the flow to a Lagrangian description for the streamlines we refer to [243].

Three supercritical Reynolds numbers are here investigated: $\text{Re} = 400, 500$ and 700 . The peculiar cat's-eye flow configuration of the basic-state (see fig. 5.15) is lost slightly above criticality and the stationary flow field evolves from the elliptic instability presenting periodic cells delimited by $(z = \pm\lambda/4)$ -planes. The through-flow is absent on this planes ($w = 0$), but the planar velocity field is not incompressible. We anticipate that this gives rise to a spiralling-out saddle focus and an attracting limit cycle on the cell boundary.

For demonstrating the steady flow and its characteristic point symmetry, the velocity vectors for $\text{Re} = 500$ are plotted in fig. 5.16 projecting them on the planes $z = -\lambda/4$ (a), $z = 0$ (b), and $y = 0$ (c).

5.3.1. Main Topological Elements

In this subsection we aim at qualitatively present the main topological features of the flow for the supercritical conditions under investigation. For a quantitative and more detailed description of their evolution in dependence on the Reynolds number we refer to [243].

Owing to the point symmetry, at the centre of each periodic cell there is a stagnation point. It represents a complex saddle focus (c) around which the whole chaotic behaviour of the cavity arranges. Moreover, a critical point ($s_{1,2}$) characterised as simple saddle focus is located on each cell boundary.

The heteroclinic connection formed in the basic-state by a sequence of two elliptic and one hyperbolic points per cross-section (cat's-eye configuration) is suddenly broken slightly after the onset of the elliptic instability. Two saddle limit cycles ($w_{1,2}$) are consequently formed on the cell boundaries (see fig. 5.17) and a non-trivial saddle limit-cycle (w_c) is identified along the cavity walls (see fig. 5.18). The former are attracting in the cell boundary plane and repelling along the solid walls whereas the latter is attracting in z -direction along the walls and repulsive towards

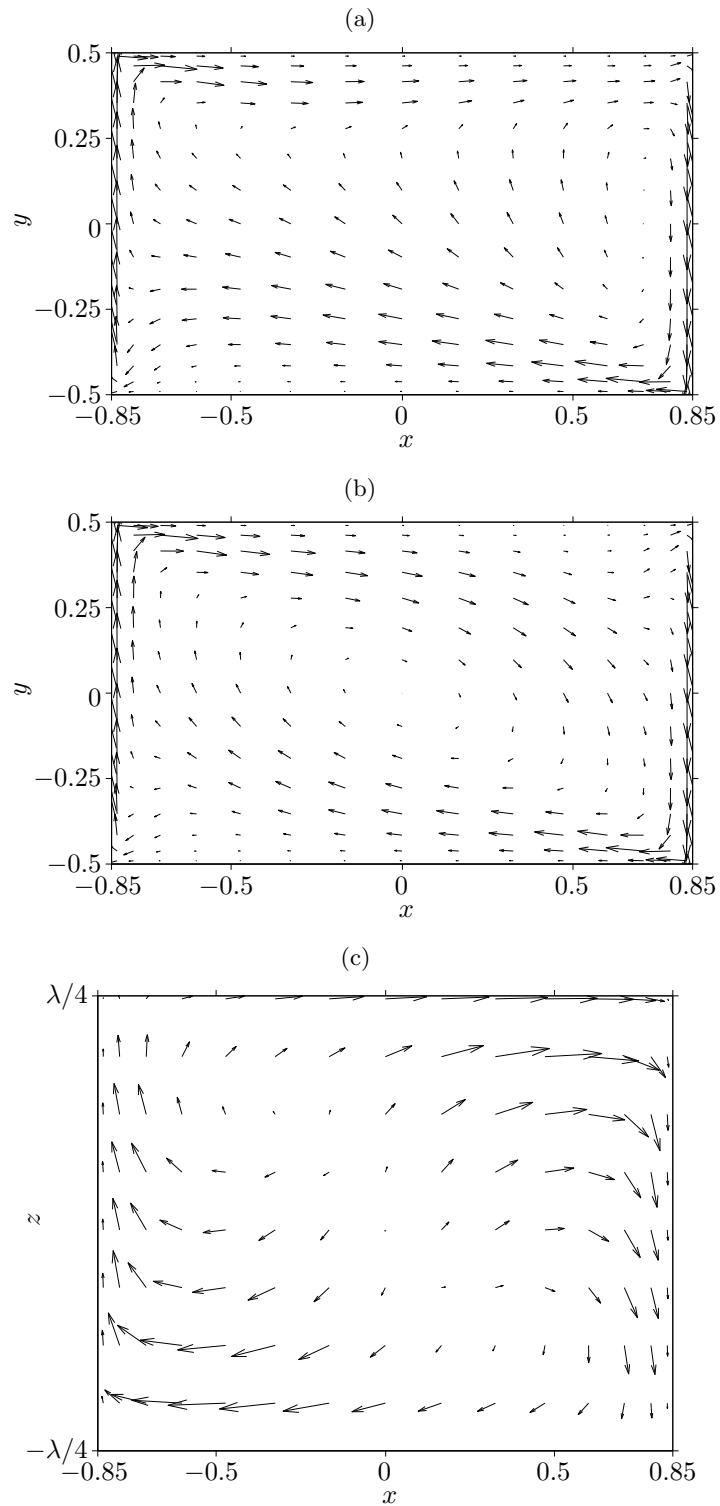


Figure 5.16.: Projection of the velocity vector field for $\text{Re} = 500$, $\Gamma = 1.7$ and $\lambda_c = 2.73$ on $(z = -\lambda/4)$ - (a), (x, y) (b) and (x, z) -plane (c). For visualization purposes, the vectors in (a) and (b) are magnified with respect to those of (c) by a factor of 1.5.

the cavity bulk region (see [243]). To show it we compute an approximation of the streamlines on the stationary walls, $y = \pm 0.5$, enforcing $v = 0$ and integrating the tracer trajectories on the planes $|y| = 0.5 - 1.5 \times 10^{-4}$. The streamlines are shown in fig. 5.18a and they are in good agreement with the deposition pattern of small particles observed by [29] (fig. 5.18b). There is no need to compute the streamlines on the moving walls because they are straight lines determined by the boundary conditions and are topologically connected with the fluid element trajectories on the stationary walls.

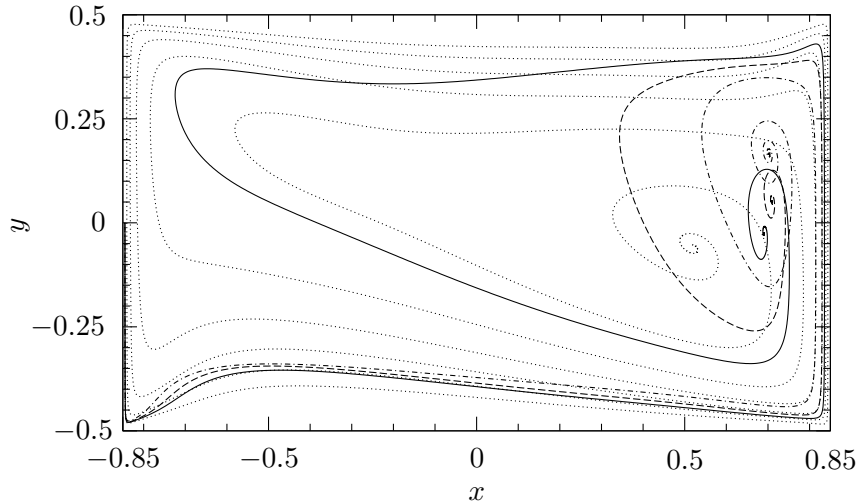


Figure 5.17.: Spiralling-out motion of a fluid element nearby the critical point s_2 on the cell boundary at $z = -\lambda/4$ for $\text{Re} = 240$ (dotted line), $\text{Re} = 400$ (solid line), $\text{Re} = 500$ (dashed line) and $\text{Re} = 700$ (dashed-dotted line). The degenerate saddle limit-cycle w_2 coincides with the cross-section boundaries.

In fig. 5.19 we report a proof of the broken heteroclinic connection showing a Poincaré sections on the (x, z) - and (y, z) -planes of the two-dimensional stable manifold of the spiralling-in-saddle focus at the cell center (red) together with the projections of the one-dimensional stable manifold of the spiralling-out-saddle foci on the cell boundaries (blue).

The chaotic dynamics in the system is organised around a heteroclinic tangling between the stable manifold of the central, complex saddle focus c and the unstable manifold of the saddle non-trivial limit cycle on the wall w_c . Integrating forward and backward in time 1000 streamlines from a small circle of radius 2×10^{-4} around the cell centre such a tangling is shown via a Poincaré section on the (x, z) -plane (see fig. 5.20). The red dots are obtained by backward integration in time and identify the stable manifold of the saddle focus, whereas the black dots are streamlines integrated forward in time. In the latter case the initial dynamics describe the one-dimensional unstable manifold of the central saddle focus: half of the conditions along the initial circle moves below the stable manifold, the other half moves above. The two bundles formed this way compactly move toward two of the cavity corners marking a Poincaré return each (marked as 1 in fig. 5.20). Two representative streamlines, colored in orange and magenta, are firstly advected nearby the cell boundary from where they are attracted by the saddle limit cycle w_c and successively ejected in the cavity. The stretching exerted on the two streamline bundles becomes evident after their first return nearby the central saddle point c . Hence, the black dots are also a good approximation of the unstable manifold of w_c , which intersect the central saddle stable manifold in a tangled fashion. As mentioned, the chaotic behaviour of the flow is strongly connected to such a heteroclinic tangle.

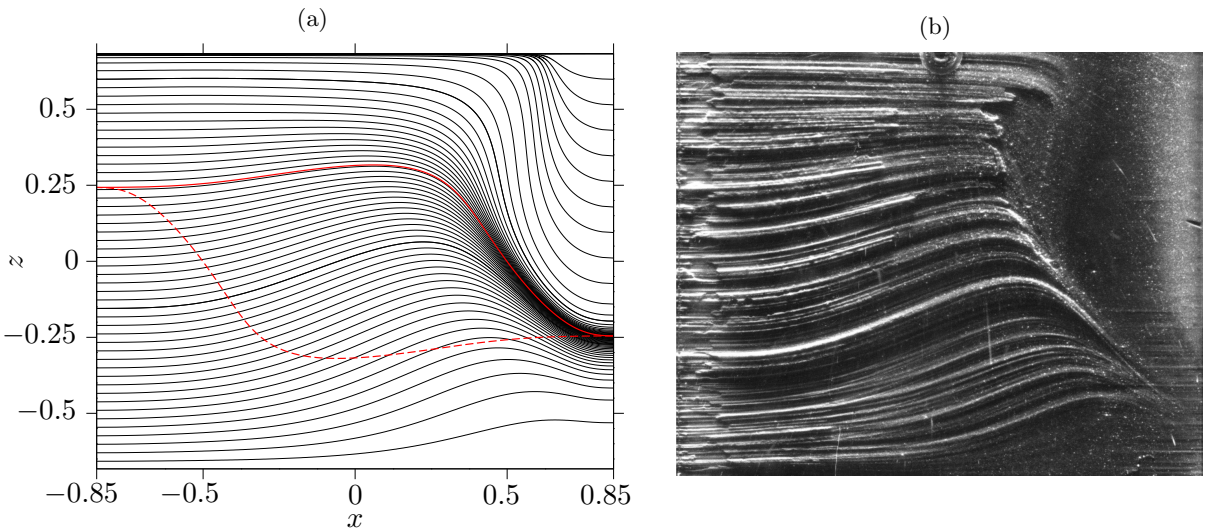


Figure 5.18.: Comparison between numerical wall streamlines at $y = -0.5$ for $\text{Re} = 500$ (a) and experimental deposition pattern (skin-friction lines) of small tracers (b) observed for a two-sided antiparallel lid-driven cavity with $\Gamma = 1.96$ after operating it for long time at $\text{Re} = 700$ (from [29]). The red line in (a) is the projection of the closed wall streamline w_c for $\text{Re} = 500$. In full and dashed lines it is indicated the part of w_c belonging to the bottom and top wall, respectively.

A sketch of the supercritical topological features is conceptually depicted in fig. 5.21.

5.3.2. Regular and Chaotic Regions

Reporting the main topological elements of the flow helps to understand the particle dynamics in the cavity, however, a more direct connection between flow topology and particle accumulation structures can be established determining the chaotic and regular regions.

As done in the case of the three-dimensional liquid bridge, the streamlines are integrated for identifying the chaotic see and, consequently, the largest reconstructible KAM surface in dependence on the Reynolds number. We initialize 2500 fluid elements evenly distributed on $(x, y) = (0, 0)$ and $z \in [-\lambda/4, \lambda/4]$ for $\text{Re} = 500$ and $\text{Re} = 400$, and on $(y, z) = (0, 0)$ within the interval $x \in [-0.85, 0]$ for $\text{Re} = 700$.

A preliminary Poincaré section is produced computing the streamlines up to $t = 1$ viscous time-units and intersecting them with the plane $x = 0$ regardless of the crossing direction. Observing their returns on the Poincaré section we identify the fluid elements which present a chaotic dynamics and the ones whose behaviour is periodic or quasi-periodic. Owing to the ergodicity of the flow, a fluid element belonging to the chaotic see will explore the whole chaotic region. Employing 2500 initial conditions and integrating for one viscous time unit is enough to have a good estimate of the chaotic see. A better description of the regular regions is given computing few streamlines up to $t = 2$ such that the boundary of the KAM tori are clearly shaped. Considering these regular fluid element trajectories, the outermost three-dimensional KAM surface and the corresponding closed streamline are computed for each torus. We select 100 equidistant points along the closed streamline; the intersection of the target KAM surface with the planes locally normal to the closed streamline is computed in each of the 100 points. These planar intersections are then interpolated on the corresponding cross-sectional plane using cubic splines. Finally, cubic Hermitian splines are employed to reconstruct the outermost KAM

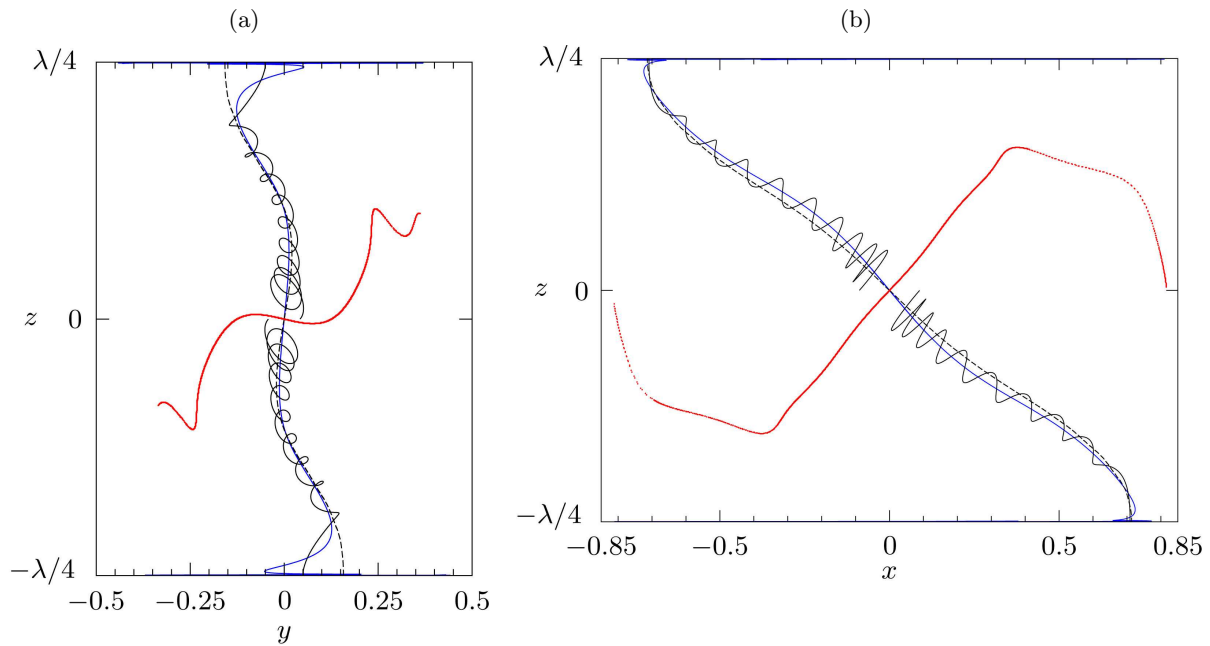


Figure 5.19.: The red line is the Poincaré section with the (y, z) - (a) and (x, z) -planes (b) of the central saddle two-dimensional stable manifold, whereas the blue line depicts the projections on (y, z) - and (x, z) -planes of the unstable manifold of c showing how a fluid element moves away from complex saddle focus towards the critical points $s_{1,2}$ on the cell-boundaries. The full black line depicts the stable manifold of the spiraling-out saddle foci $s_{1,2}$ projected on the (y, z) - (a) and (x, z) -planes (b). All the results are obtained for $\text{Re} = 500$.

surface from the 100 torus cross-sections.

For the smallest Reynolds number we consider, $\text{Re} = 400$, we identify two simply-periodic KAM tori which, owing to the features of the flow field, are point symmetric with respect to the cell center. Most of the domain is occupied by the chaotic sea organized around the central saddle focus. Figure 5.22 depicts the corresponding Poincaré section on the (y, z) -plane (a) and the three-dimensional reconstruction of the outermost KAM surface (b).

As the Reynolds number is further increased the chaotic region extends, as expected, and the two KAM tori become smaller for $\text{Re} = 500$. This trend can be observed comparing fig.s 5.22 and 5.23.

For $\text{Re} = 700$ the regular regions are even smaller and four KAM tori are found. Each point symmetric set consists of a simply-periodic and double-periodic torus, the latter of which winds around the major regular region. Figure 5.24 depicts them in purple and green respectively. The presence of a second type of regular structure (double-periodic KAM tori) for $\text{Re} = 700$ indicates that a splitting of the single-periodic tori identified for $\text{Re} = 500$ occurred at an intermediate Reynolds number. As further remark we notice that the regular regions are approximately located always in the same part of the periodic cell regardless of the Reynolds number.

For all the Reynolds numbers the closed streamlines are computed finding the elliptic fixed point of the Poincaré maps. The computation has been carried out using the Newton–Raphson method up to a relative accuracy of 10^{-4} in the (y, z) -plane. Figures 5.22, 5.23 and 5.24 show them with a diamond marker.

Figures 5.25 and 5.26 show the projection on the (y, z) - and (x, z) -plane, respectively, of the

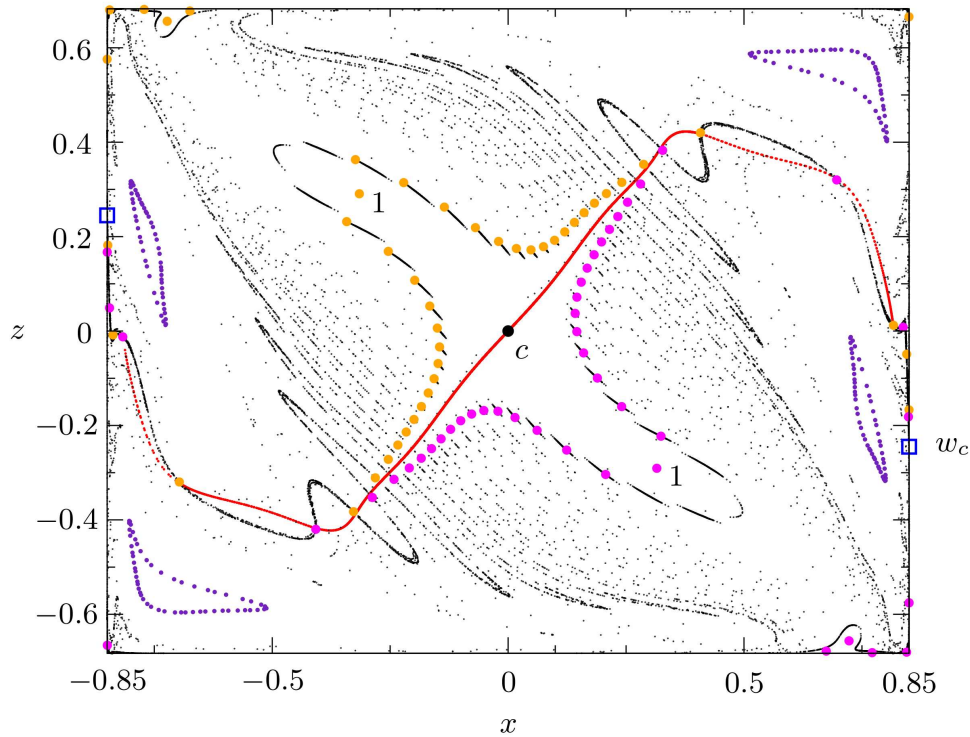


Figure 5.20.: Poincaré section of the central saddle two-dimensional stable manifold (red dots) and the one-dimensional unstable manifold (black dots) on the (x, z) -plane. The latter one approximate the unstable manifold of the wall limit-cycle w_c (blue squares). The data are obtained integrating backward and forward in time 1000 streamlines on a circle of radius 2×10^{-4} centered in c for $t = 2$ and $\text{Re} = 500$. Two representative streamlines are depicted in orange and magenta (first 55 returns): they initially move towards the cell boundaries at $z = 0.6825$ and $z = -0.6825$ marking a first return at ‘1’. The largest reconstructible regular region in the flow is depicted by the indigo dots, and further details about such KAM tori will be given in Section 5.3.2

closed streamlines identified inside the KAM tori. A remarkable feature is that the minimum distance from the cavity walls always occurs between the periodic trajectory and the moving walls at $x = \pm 0.85$.

As done in the case of the three-dimensional liquid bridge flow, we compute the minimum distance from the boundaries of the closed streamlines and the outermost KAM surface we identified. These quantities are of major importance for understanding the particle accumulation structures by mean of the particle–surface interaction model (see [195, 194, 126]). Table 5.7 reports such distances and the orbit time τ of the closed trajectory. Following [195], the outermost KAM surface and the respective closed trajectories are indicated as T_i and L_i , and the corresponding turn-over time will be τ_i . Owing to the point symmetry, we list such an information for the regular structures located in $z > 0$ only.

5.3.3. Particle Accumulation Structures

The numerical predictions of particle accumulation structures in the two-sided antiparallel lid-driven cavity are presented in the following. The attraction to periodic and quasi-periodic

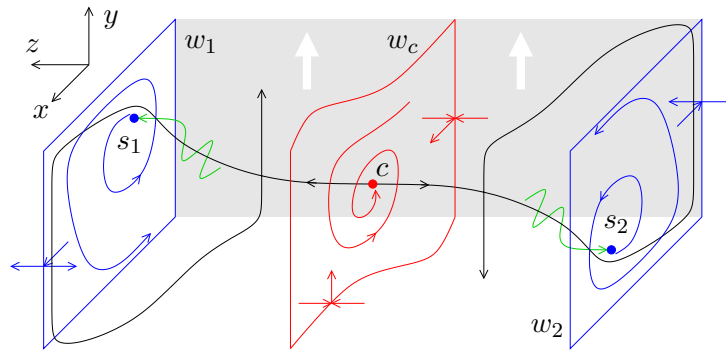


Figure 5.21.: Conceptual sketch of the main topological features of the fluid flow in supercritical conditions. The red and the blue lines represent the non-trivial saddle limit-cycle (w_c) and the limit cycles on the cell boundaries ($w_{1,2}$), respectively. The central saddle focus c is depicted with a red dot, whereas the boundary saddle foci $s_{1,2}$, are shown as blue dots. The grey rectangle with white arrows in the background is showing the upward moving wall.

Table 5.7.: List of the orbit times τ for the closed streamlines L_i and minimum distances Δ from the moving wall for both, the periodic attractors and the outermost KAM surface, T_i . To uniquely identify the closed streamlines, their fixed point location of the corresponding Poincaré section on the (y, z) -plane is reported.

Re	KAM/streamline	τ	Δ	Fixed point
700	T_1	–	0.0243	–
	L_1	0.0198	0.0264	(0, 0.2809, 0.5345)
	T_2	–	0.0233	–
	L_2	0.0457	0.0244	(0, 0.2210, 0.5838)
500	T_1	–	0.0359	–
	L_1	0.0272	0.0493	(0, 0.2497, 0.5348)
400	T_1	–	0.0349	–
	L_1	0.0342	0.0711	(0, 0.2257, 0.5153)

orbits by the only mean of particle–boundary interaction is herein investigated. Hence the trajectory of particles density-matched with the fluid are computed. Investigating PAS for density-matched particles is motivated by experimental evidence of particle accumulation for $\varrho = 1$ [258] conducted in a liquid bridge. In the next section a comparison between numerical predictions and experiments is presented for PAS. The experiments are carried out with almost neutrally buoyant particles and, to the best of the author’s knowledge, this is the first time that particle accumulation structures are experimentally reported in a configuration different from the liquid bridge.

To clearly show such a dissipative mechanism, a perfect tracer equation is solved for integrating the particle trajectories. Particle–particle interactions are neglected and the one-way coupled approach is completed by the PSI model, including the dependence of the lubrication gap width on the particle radius calculated in Chapter 4. It is indeed the PSI model which includes the dissipation needed to a perfect tracer for accumulating.

All the simulations have been carried out up to $t = 1$ initializing 2500 particles from a random

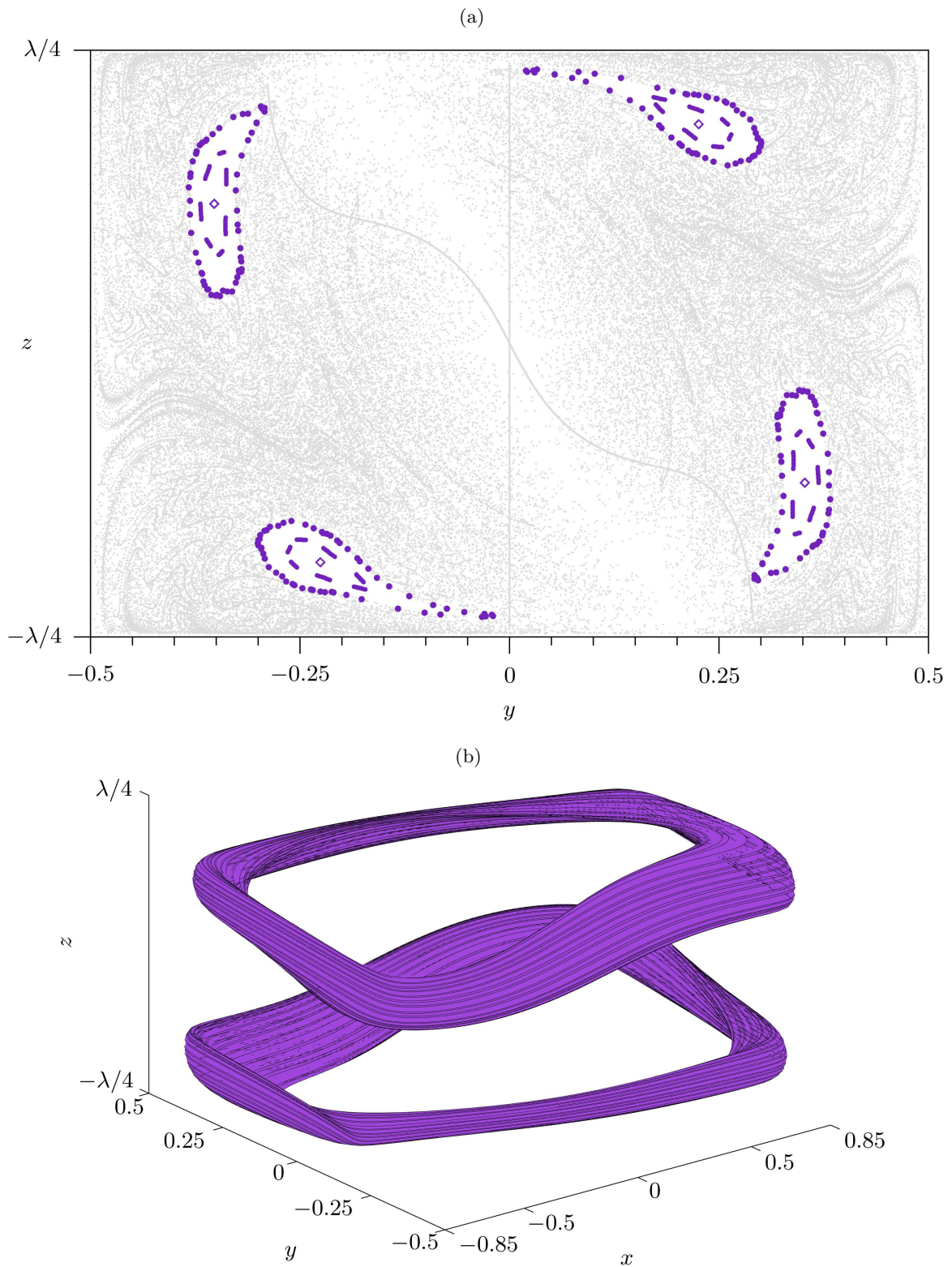


Figure 5.22.: Poincaré section of the KAM tori (indigo) embedded in the chaotic sea (grey) (a) on the (y, z) -plane for $Re = 400$. The two point-symmetric periodic orbits inside the KAM tori are marked by a diamond (\diamond). Three-dimensional reconstruction of the outermost KAM surfaces (b).

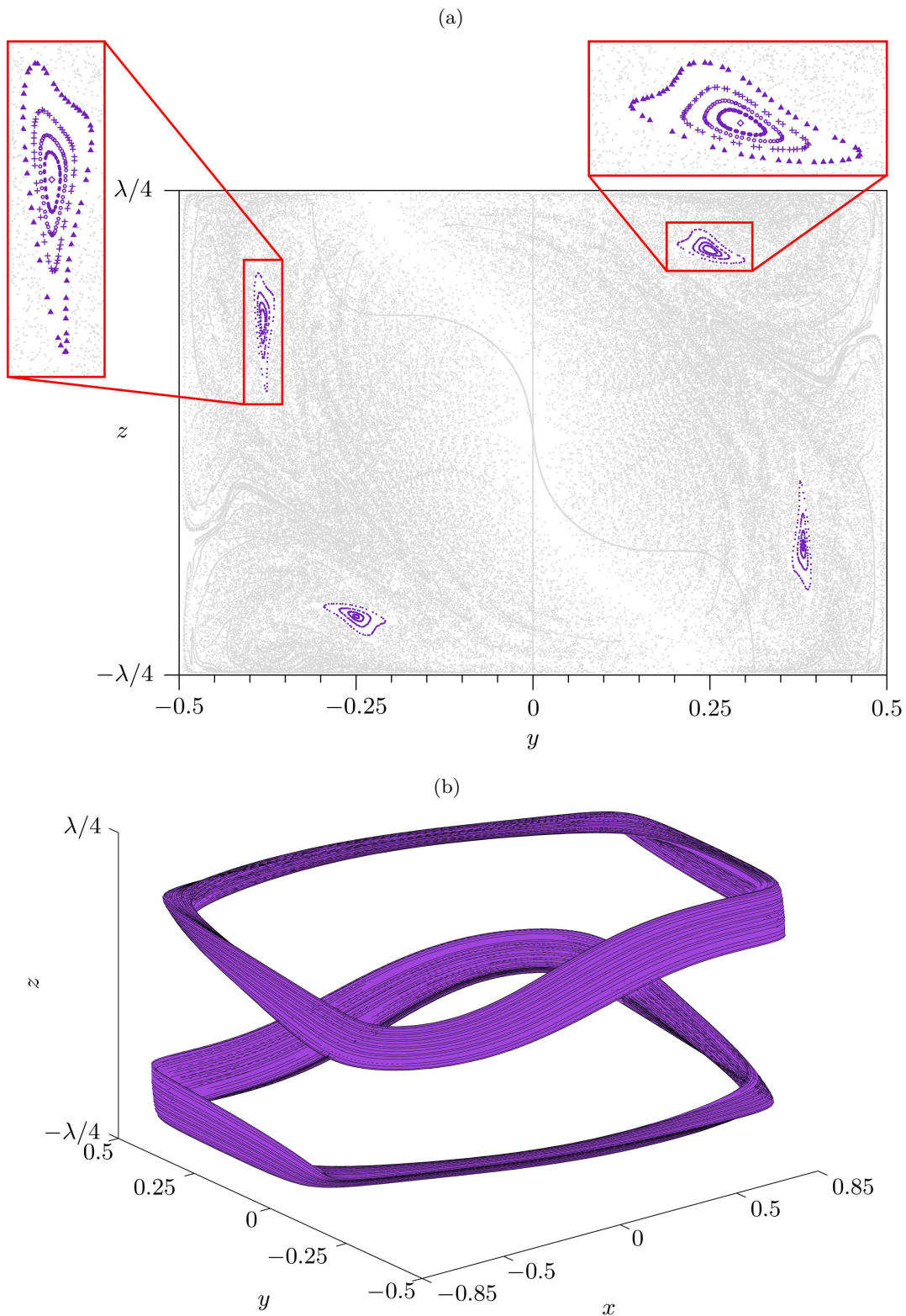


Figure 5.23.: Poincaré section of the KAM tori (indigo) embedded in the chaotic sea (grey) (a) on the (y, z) -plane for $\text{Re} = 500$. The two point-symmetric periodic orbits inside the KAM tori are marked by a diamond (\diamond). Three-dimensional reconstruction of the outermost KAM surfaces (b).

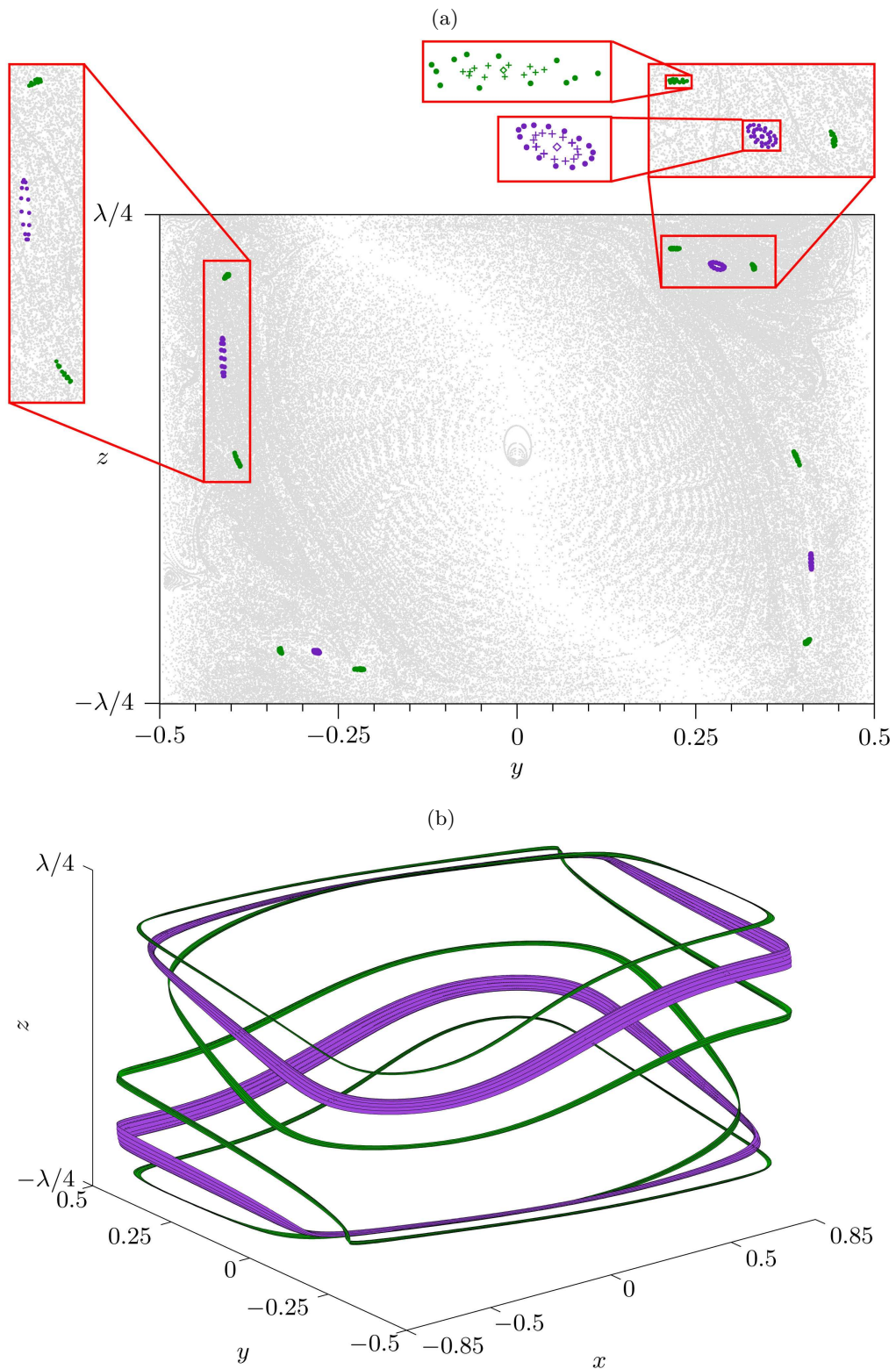


Figure 5.24.: Poincaré section of the KAM tori (indigo and green) embedded in the chaotic sea (grey) (a) on the (y, z) -plane for $\text{Re} = 700$. Two sets of point-symmetric KAM tori are found: a couple of single-periodic (indigo) and a couple of doubly-periodic KAM tori (green). The four point-symmetric closed streamlines are marked by a diamond (\diamond). Three-dimensional reconstruction of the outermost KAM surfaces (b).

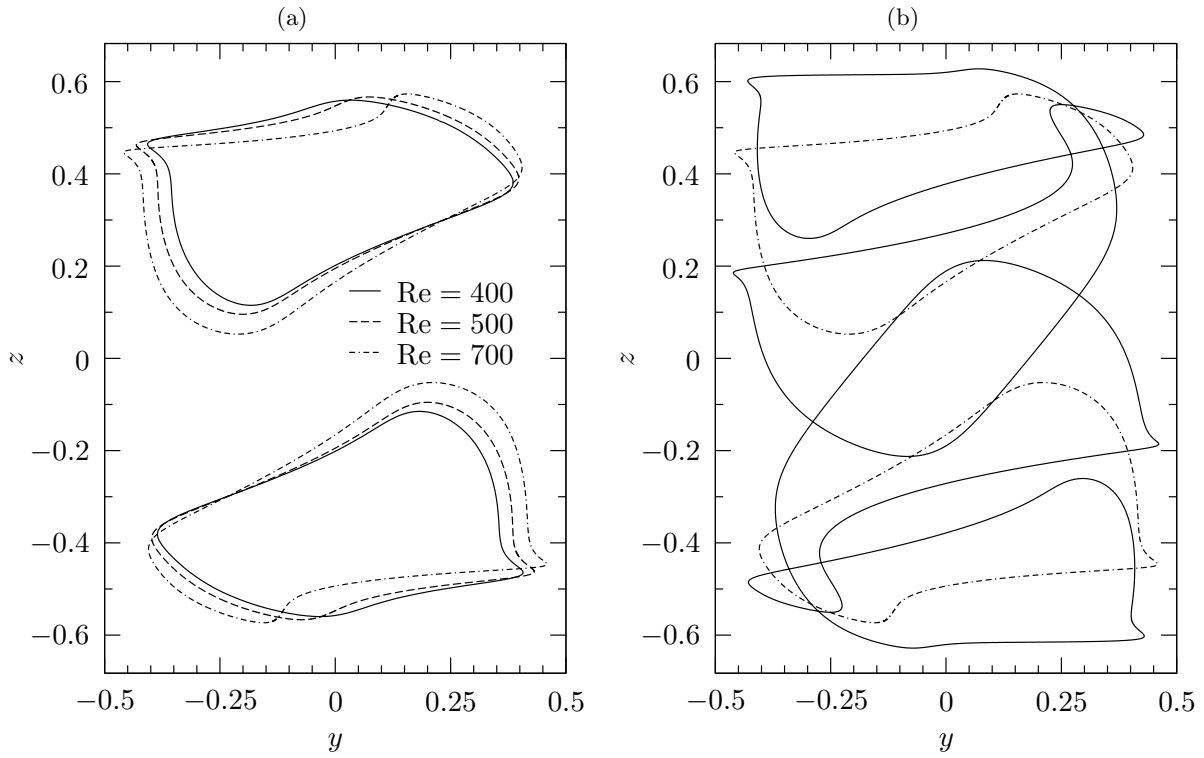


Figure 5.25.: Projection of the simple-periodic closed streamlines on the (y, z) -plane for $Re = 400, 500$ and 700 (a) and of the double-periodic orbit for $Re = 700$ (b).

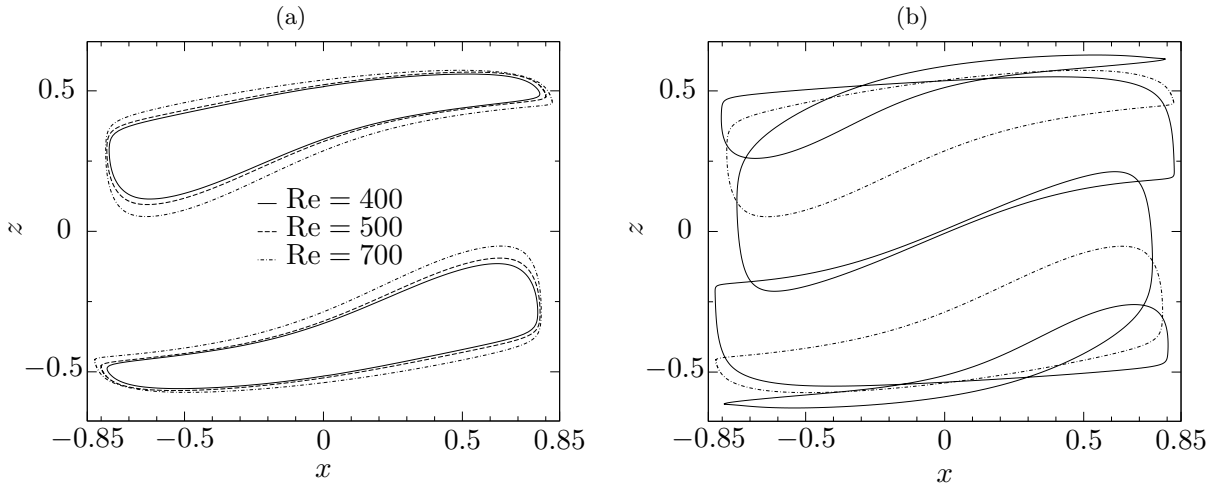


Figure 5.26.: Projection of the simple-periodic closed streamlines on the (x, z) -plane for $Re = 400, 500$ and 700 (a) and of the double-periodic orbit for $Re = 700$ (b).

distribution in one cell. The domain of initialization is such to exclude the regions which are not accessible to the particles in the PSI model framework (see [126])

$$\mathcal{V}^* = [-\Gamma/2 + \Delta, \Gamma/2 - \Delta] \times [-1/2 + \Delta, 1/2 - \Delta] \times [-\lambda/4, \lambda/4]. \quad (5.8)$$

Three scenarios are observed. (a) The first case is when the particles accumulate inside the

KAM tori, see fig.s 5.28,5.29,5.30 and 5.35. The resulting PAS has been termed *tubular PAS* in [126, 194]. After multiple interactions with the boundaries, the particles outside the regular region are mapped by the PSI model on the KAM surface which is tangent to the boundary of \mathcal{V}^* . The particles initially inside the tangent KAM surface do not experience any form of dissipation and, therefore, keep on moving along the periodic or quasi-periodic orbit they have been initialized on. A particularly high accuracy is required to calculate such trajectories in order to avoid particle accumulation structures due to dissipation by numerical errors (see e.g. [196]). The scenario described occurs for interaction lengths ranged in the interval between the minimum distance from the walls of the outermost KAM surface (Δ^{T_i}) and the one of the closed trajectory (Δ^{L_i})

$$\text{PAS inside KAM tori: } \Delta \in [\Delta^{T_i}, \Delta^{L_i}]. \quad (5.9)$$

A limit case of this accumulation is the so-called *line-like PAS* [126, 195]. It occurs when the interaction length Δ equals the minimum distance between the closed trajectory and the walls, Δ^{L_i} , and it reduces the domain of accumulation to the closed trajectory identical to the closed streamline only. To demonstrate it fig. 5.31, 5.36 and 5.37 show a comparison between the accumulation patterns (dots) and the corresponding periodic orbits computed in Section 5.3.2.

(b) A second scenario which may occur is obtained for $\Delta > \Delta^{L_i}$. If the interaction length is slightly larger than Δ^{L_i} a period doubling of the attractor is observed about the closed trajectory of the corresponding KAM torus (see fig. 5.32). Such phenomenon has been extensively discussed in the Appendix of [194] and can be explained considering the geometrical properties of the KAM surfaces and the mapping operation resulting from the PSI model. Experimental evidence of period doubling attractors have been reported in a liquid bridge flow (see [278]). The existence of such a phenomenon is however limited to a narrow interval of interaction lengths above Δ^{L_i} , and for $\Delta \gg \Delta^{L_i}$ no particles accumulation has been found.

(c) The third case considers $\Delta < \Delta^{T_i}$ for which the streamline hopping created by the PSI model cannot map the particle to a regular region of the flow. If the interaction length is slightly smaller than Δ^{T_i} a new set of attractors with period higher than one is found. Even though they are located outside the regular regions, they are still connected to the flow topology because the flow dynamics in proximity of the boundary between KAM tori and chaotic see is just weakly chaotic. The real part of Lyapunov exponents¹ measured comparing two initially close streamlines initialized right outside the border of a regular region is slightly bigger than zero. This means that after a complete turn-over, two particles initially close to each other will weakly diverge in terms of mutual distance, but staying still close to the KAM torus. The dissipation induced by the PSI model is, in these cases, capable to recover the weak divergence of their trajectories creating the attractors we observe in fig. 5.27, 5.33 and 5.34. This mechanism has been reported for the first time in the model flow of a liquid bridge [155]. If the interaction length is $\Delta \ll \Delta^{T_i}$ the numerical simulations do not predict any particle accumulation structure.

One conclusion which can be derived from the reported results is that particle accumulation structures can be caused by the dissipative effect provided by the only particle–boundary interaction. This was observed for the first time by Hofmann & Kuhlmann in [126] for a liquid bridge and it is here confirmed for a lid-driven cavity. Moreover, we demonstrated once again the strong correlation between particle accumulation structure and flow topology for all three

¹Considering two initially close conditions at distance $\Delta \mathbf{x}_0 = \Delta \mathbf{x}(t=0)$ along two distinct trajectories, the Lyapunov exponent Λ measures the mean exponential rate of divergence of the two orbits. Denoting with $\Delta \mathbf{x}(t)$ the distance between the two marked points at time t , the Lyapunov exponent is defined as

$$\Lambda = \lim_{t \rightarrow \infty, |\Delta \mathbf{x}_0| \rightarrow 0} \frac{1}{t} \ln \left| \frac{\Delta \mathbf{x}(t)}{\Delta \mathbf{x}_0} \right| \quad (5.10)$$

Reynolds numbers under investigation. Finally, the particle diameter investigated are provided in table 5.8 and the PAS type listed is obtained using the estimate of the minimum lubrication gap width provided in Chapter 4.

Table 5.8.: Range of interaction lengths Δ and corresponding particle radii a for which the existence of PAS is numerically investigated. With *line-like in chaotic sea* we indicate the particle accumulation structure observed in the chaotic region in vicinity of the KAM tori.

Re	PAS type	Δ	a
400	line-like in chaotic sea	0.0300	0.0201
	tubular	0.0400	0.0321
	tubular	0.0500	0.0431
	tubular	0.0600	0.0549
	single-period line-like	0.0711	0.0632
	period-doubled line-like	0.0800	0.0778
500	line-like in chaotic sea	0.0200	0.0106
	line-like in chaotic sea	0.0300	0.0201
	tubular	0.0400	0.0321
	single-period line-like	0.0493	0.0424
	no PAS	0.0550	0.0485
	no PAS	0.0600	0.0549
700	no PAS	0.0200	0.0106
	single-period line-like	0.0244	0.0143
	no PAS	0.0264	0.0162
	no PAS	0.0300	0.0201
	no PAS	0.0400	0.0321

5.3.4. Preliminary Comparison between Experiments and Simulations

All the experiments in this section are carried out at TU Wien by Haotian Wu² under the supervision of Hendrik Kuhlmann. Preliminary experimental investigations have been conducted for $Re = 400$ and $Re = 500$. A comparison with the corresponding numerical results is presented below to verify the numerical prediction of particle accumulation structures in the lid-driven cavity.

The liquid employed for the experiments is 20-cSt silicone oil (Baysilone M20) and its kinematic viscosity and density are $\rho_f = 9.5 \times 10^2 \text{kg/m}^3$ and $\nu = 2.0 \times 10^{-5} \text{m}^2/\text{s}$, respectively. The particles employed in the experiments are spherical, polyethylene, almost neutrally buoyant particles. Their radius is $a_p = 2 \text{mm}$, the particle density $\rho_p = 943 \text{kg/m}^3$ and the corresponding particle-to-fluid density ratio is $\varrho = 1.01$.

The experimental rig is the one used by Siegmann et al. [264]. The cavity is made between two horizontal co-rotating cylinders as left and right cavity walls. The free distance between the two moving walls d is therefore slightly varying with the height. In order to reduce the effect of the finite extension in z -direction, a spanwise length-to-height ratio of 10.85 is employed.

²We want to kindly acknowledge the use of this results prior to publication.

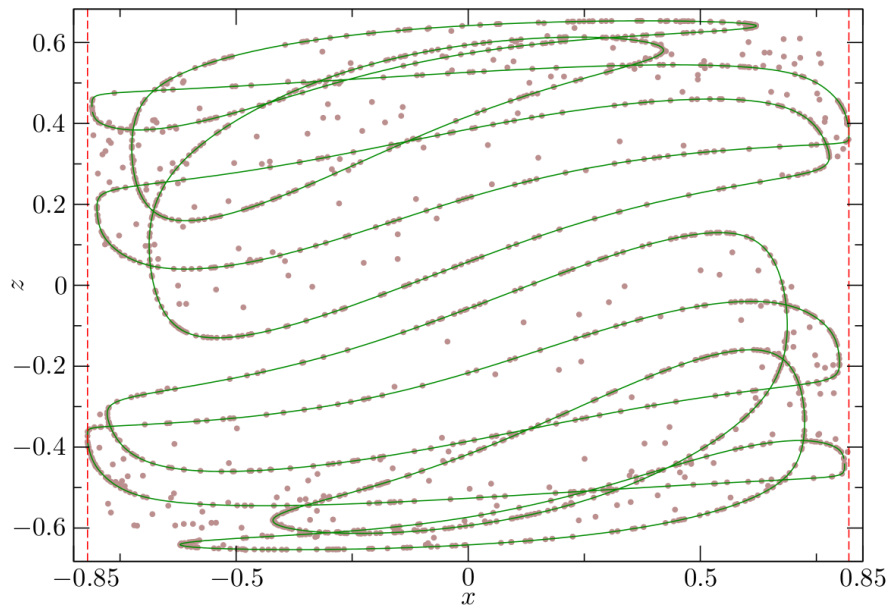


Figure 5.27.: Initially randomly distributed particles attracted to a quadruple-periodic line-like structure after $t = 1$ for $\text{Re} = 400$. The green line indicates the projection of the attractor on the (x, z) -plane and each black dot represents a particle. The interaction length adopted for the PSI model is $\Delta = 0.03$ and the prohibited regions for the particles are marked with red dashed lines.

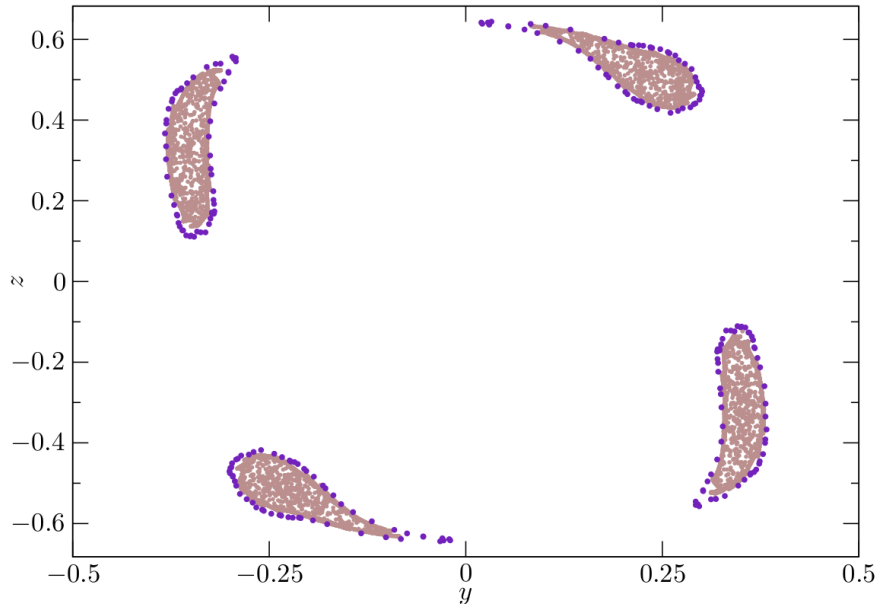


Figure 5.28.: Poincaré section on the (y, z) -plane of the initially randomly distributed particles in the last part of their trajectory ($t \in [0.75, 1]$, grey dots) for $\text{Re} = 400$. The indigo dots show the outermost KAM surface identified in Section 5.3.2. The interaction length adopted for the PSI model is $\Delta = 0.04$ and it leads to a tubular accumulation pattern.

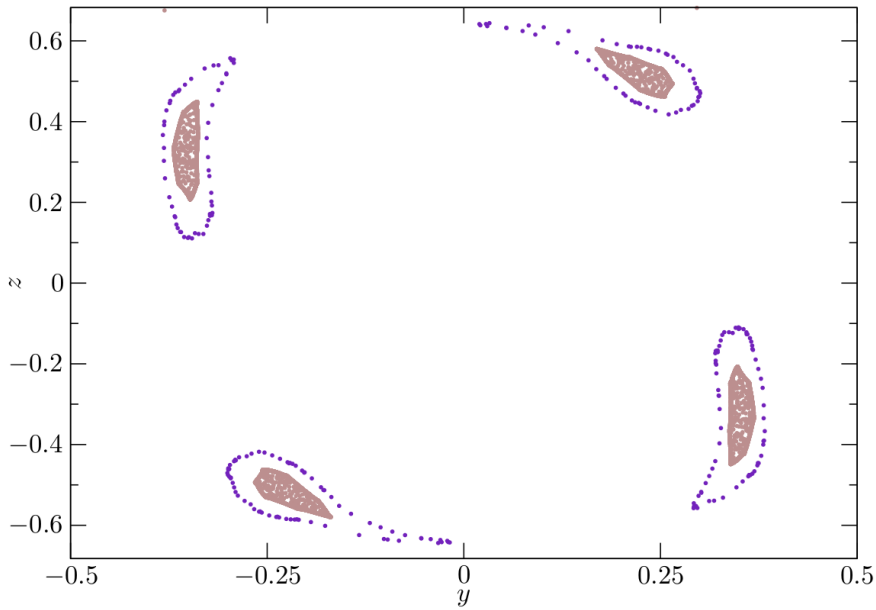


Figure 5.29.: Poincaré section on the (y, z) -plane of the initially randomly distributed particles in the last part of their trajectory ($t \in [0.75, 1]$, grey dots) for $\text{Re} = 400$. The indigo dots show the outermost KAM surface identified in Section 5.3.2. The interaction length adopted for the PSI model is $\Delta = 0.05$ and it leads to a tubular accumulation pattern.

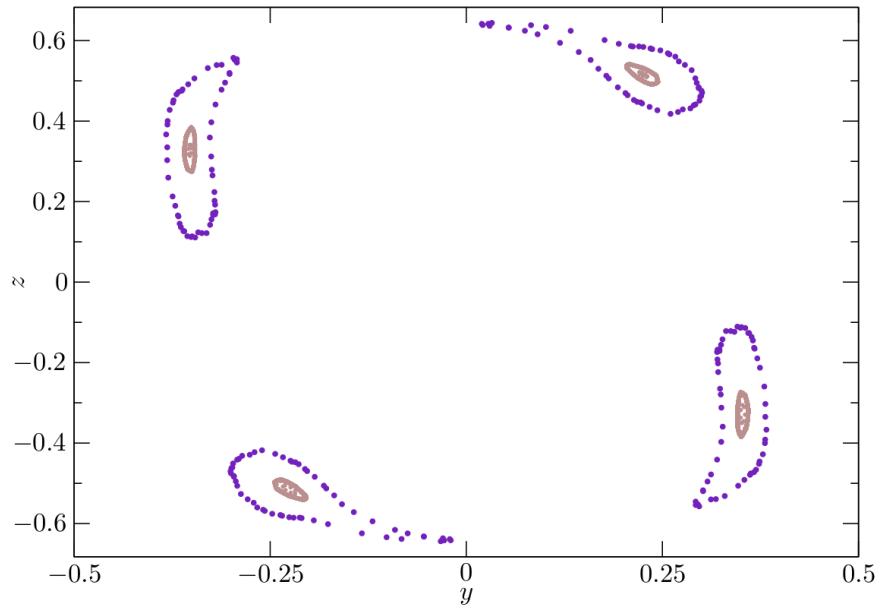


Figure 5.30.: Poincaré section on the (y, z) -plane of the initially randomly distributed particles in the last part of their trajectory ($t \in [0.75, 1]$, grey dots) for $\text{Re} = 400$. The indigo dots show the outermost KAM surface identified in Section 5.3.2. The interaction length adopted for the PSI model is $\Delta = 0.06$ and it leads to a tubular accumulation pattern.

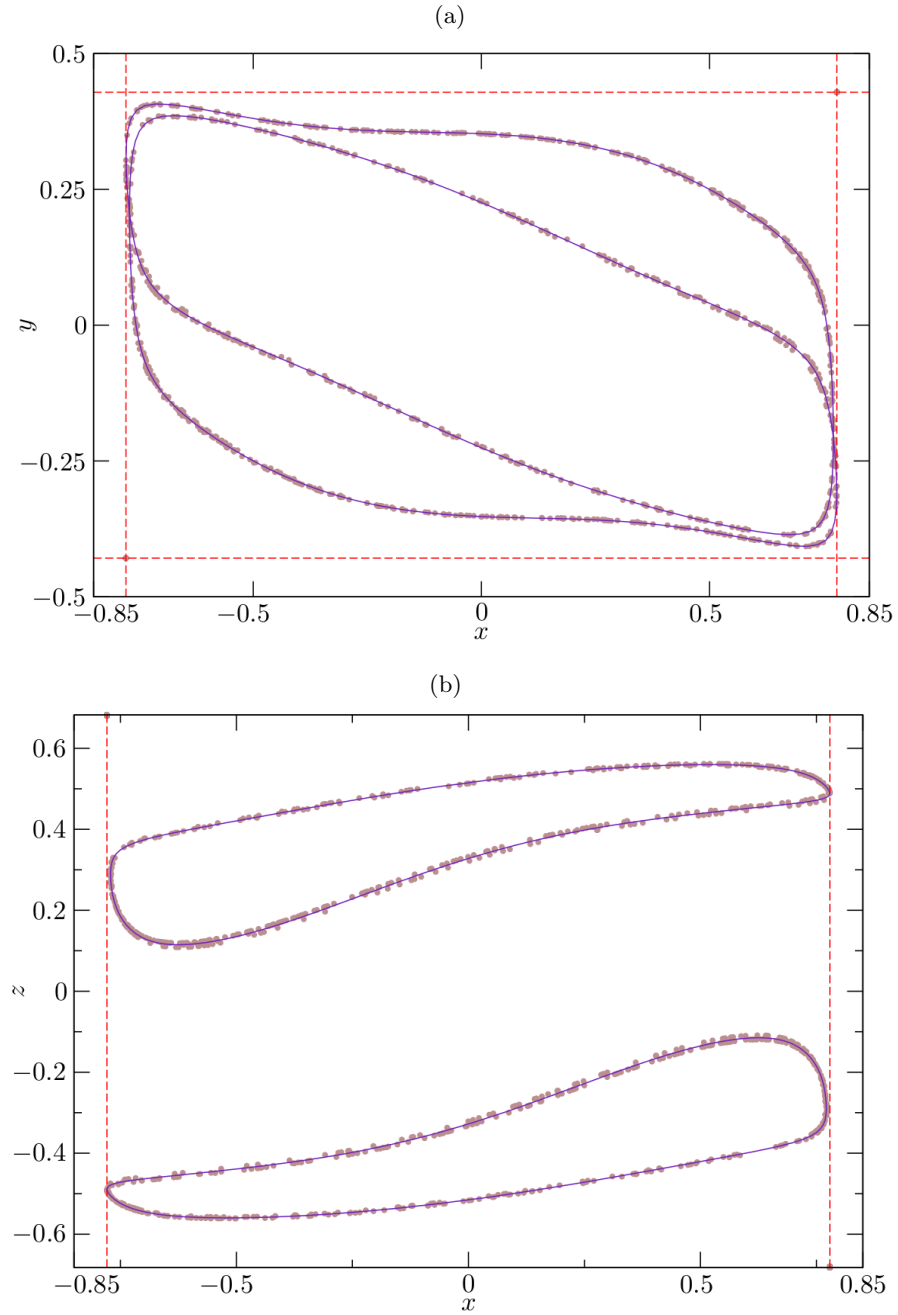


Figure 5.31.: Initially randomly distributed particles attracted to a line-like PAS along the closed streamline identified in Section 5.3.2 (indigo line). The accumulation is reported after $t = 1$ for $\text{Re} = 400$ on the (x, y) - and (x, z) -planes, (a) and (b) respectively. The prohibited regions for the particles (black dots) are marked with red dashed lines and the interaction length adopted for the PSI model is $\Delta = \Delta^{Li} = 0.0711$.

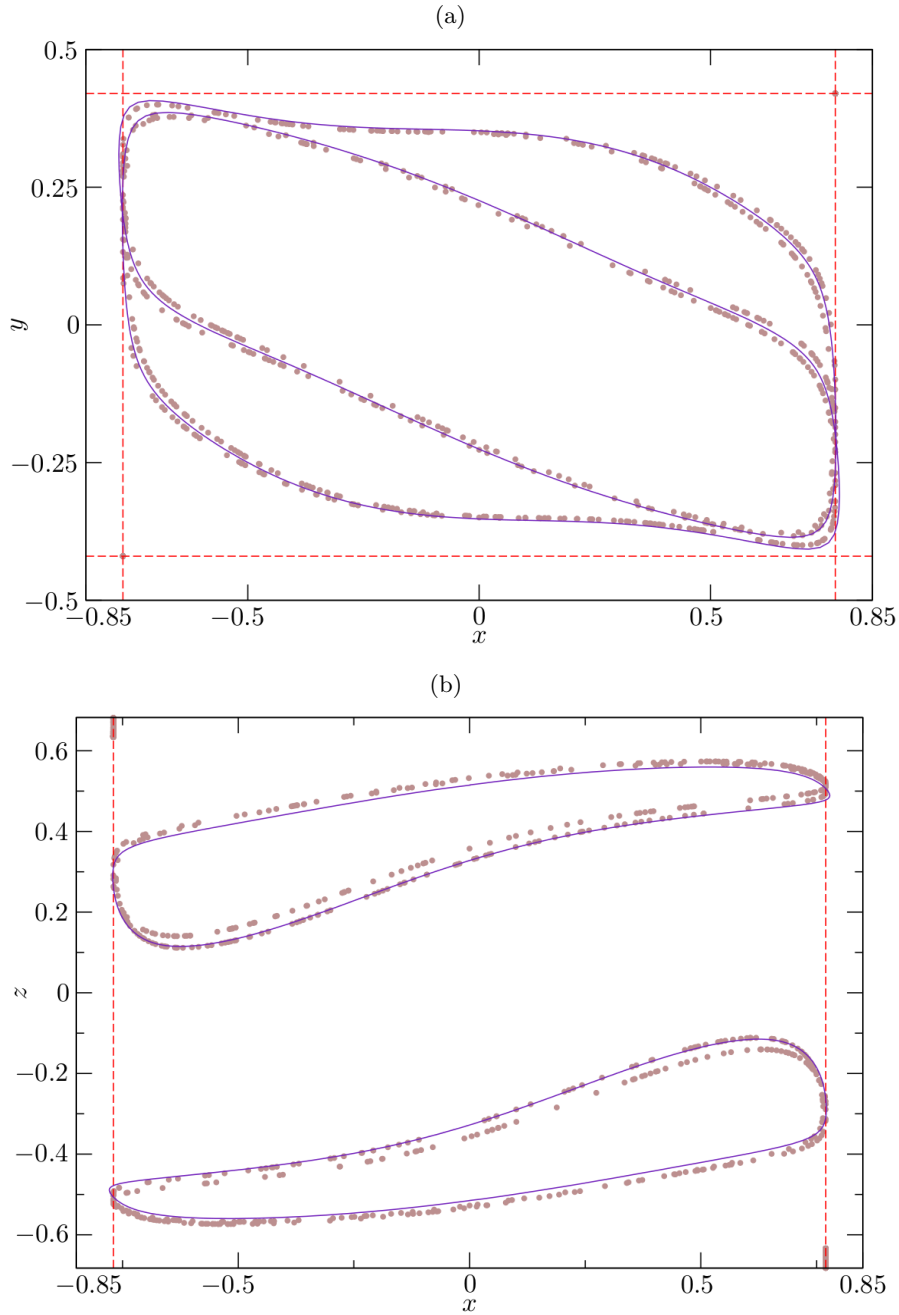


Figure 5.32.: Initially randomly distributed particles attracted to a period-doubled line-like PAS organized about the closed streamline identified in Section 5.3.2 (indigo line). The accumulation is reported after $t = 1$ for $\text{Re} = 400$ on the (x, y) - and (x, z) -planes, (a) and (b) respectively. The prohibited regions for the particles (black dots) are marked with red dashed lines and the interaction length adopted for the PSI model is $\Delta = 0.0800$.

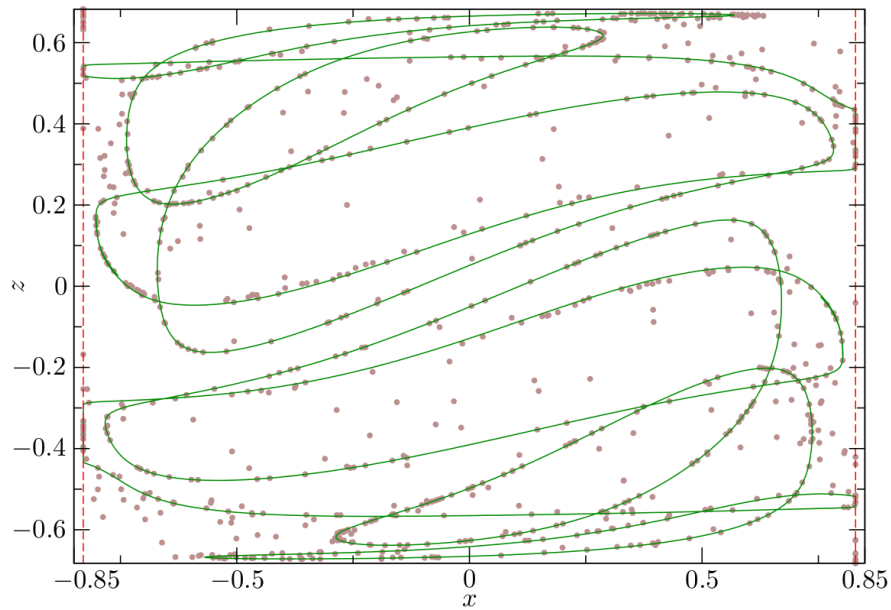


Figure 5.33.: Initially randomly distributed particles attracted to a quadruple-periodic line-like structure after $t = 1$ for $\text{Re} = 500$. The green line indicates the projection of the attractor on the (x, z) -plane and each black dot represents a particle. The interaction length adopted for the PSI model is $\Delta = 0.02$ and the prohibited regions for the particles are marked with red dashed lines.

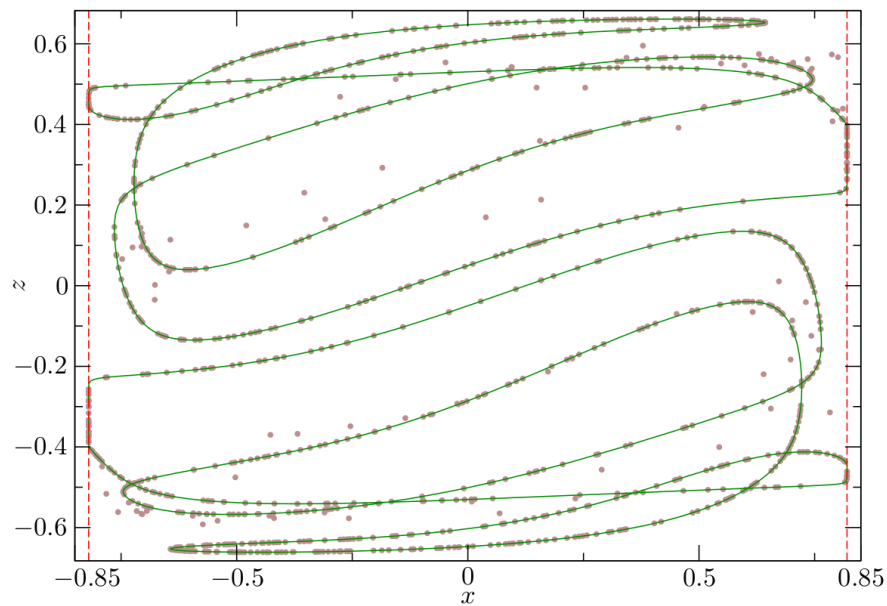


Figure 5.34.: Initially randomly distributed particles attracted to a triple-periodic line-like structure after $t = 1$ for $\text{Re} = 500$. The green line indicates the projection of the attractor on the (x, z) -plane and each black dot represents a particle. The interaction length adopted for the PSI model is $\Delta = 0.03$ and the prohibited regions for the particles are marked with red dashed lines.

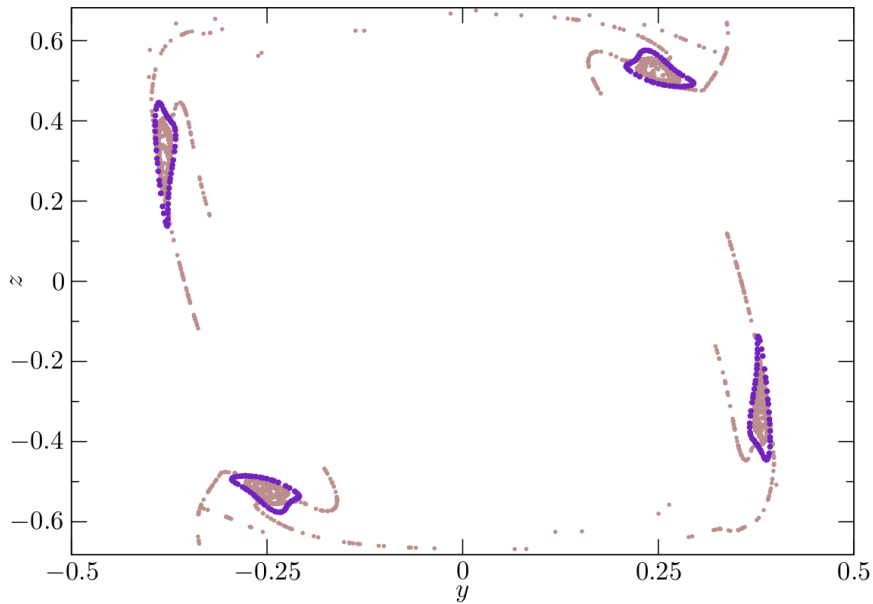


Figure 5.35.: Poincaré section on the (y, z) -plane of the initially randomly distributed particles in the last part of their trajectory ($t \in [0.75, 1]$, grey dots) for $Re = 500$. The indigo dots show the outermost KAM surface identified in Section 5.3.2. The interaction length adopted for the PSI model is $\Delta = 0.04$ and it leads to a tubular accumulation pattern.

Transparent walls made out of Perspex allow to visualize the particle trajectories. A cross-sectional aspect ratio of 1.6 is employed for the experiments and the height of the test section is $h = 40\text{mm}$. This is slightly different from the one used for numerical simulations; moreover, another important difference is represented by the curvature of the moving employed in the experiments, which is absent in our simulations. A sketch of the experimental set-up is depicted in fig. 5.38. For more extensive information about the apparatus we refer the reader to [264].

In the experiments a single particle in a periodic cell is used. Figure 5.39 depicts the experimental observation from the top view (z -axis in horizontal direction) of particle's trajectory (by long time exposure) for $Re = 400$ (a) and $Re = 500$ (b) for a tracer of radius $a_p = 2\text{mm}$. The particle trajectory is recorded for 100 seconds after 30 minutes from when the moving walls reached full speed and the images are produced with a sampling frequency of 20Hz. Figure 5.39 results from averaging them in time and a clear line-like or quasi-line-like particle accumulation can be noticed for both the investigated Reynolds numbers. The mirror image reflection on the top results from a reflection on the surface of one of the rotating cylinders. This indicates that the particle trajectory is very close to the rotating top wall.

A top view of the particle trajectory obtained by particle tracking for $Re = 400$ (a) and $Re = 500$ (b) is depicted in grey in 5.40. It is not possible to compare such trajectories one-to-one with the numerical data because of the different cross-sectional aspect ratios. Moreover the curvature of the moving walls present in the experiments is not considered in the numerical simulations. However, beyond these discrepancies, the qualitative agreement in shape and location of the attractor is very good for both the Reynolds numbers (see fig.s 5.40, 5.31 and 5.36 for comparison). A distinct difference between the computational and the experimental results is the distance of the line-like PAS from the furthest moving wall. Our one-way coupled

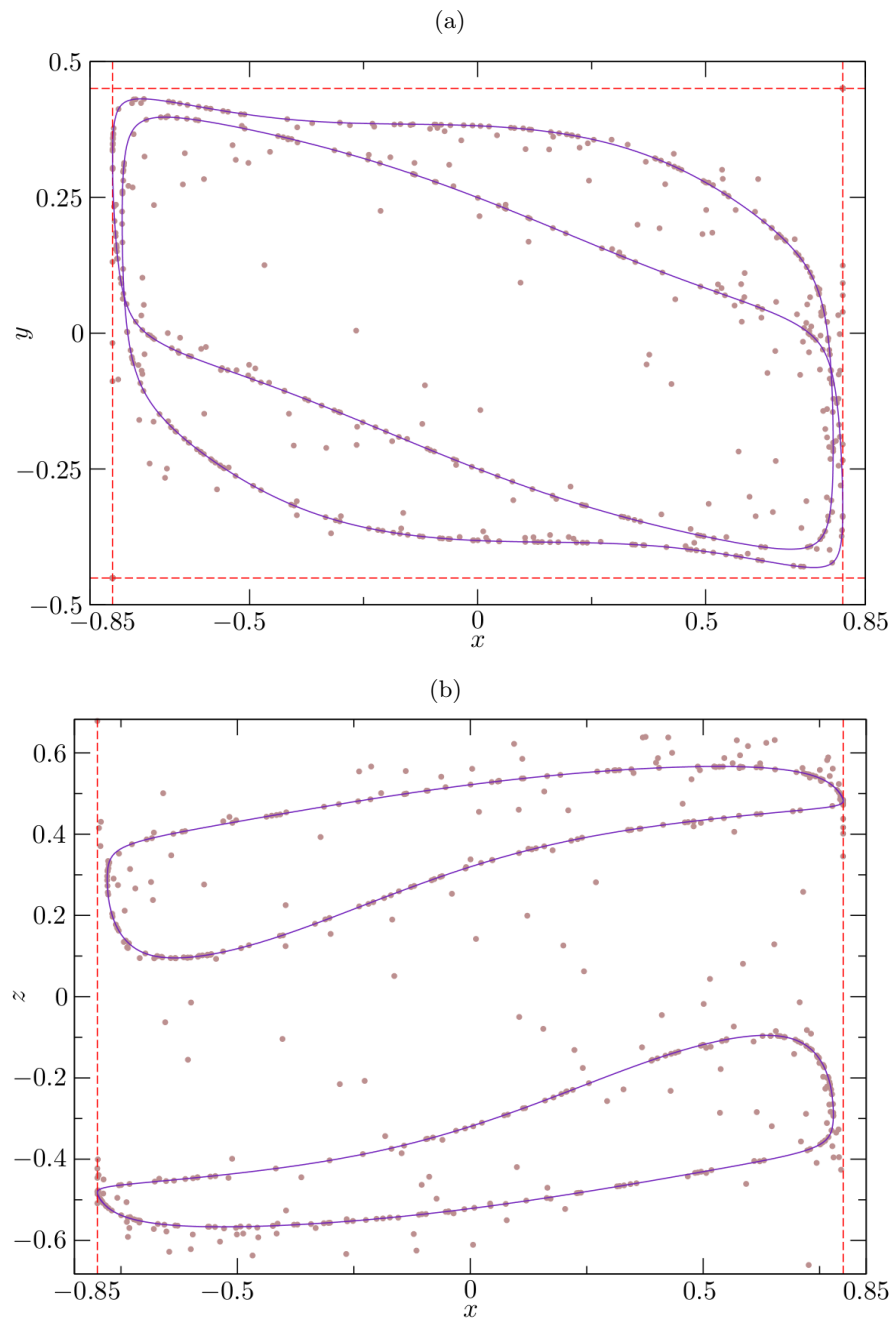


Figure 5.36.: Initially randomly distributed particles attracted to a line-like PAS along the closed streamline identified in Section 5.3.2 (indigo line). The accumulation is reported after $t = 1$ for $Re = 500$ on the (x, y) - and (x, z) -planes, (a) and (b) respectively. The prohibited regions for the particles (black dots) are marked with red dashed lines and the interaction length adopted for the PSI model is $\Delta = \Delta^{Li} = 0.0493$.

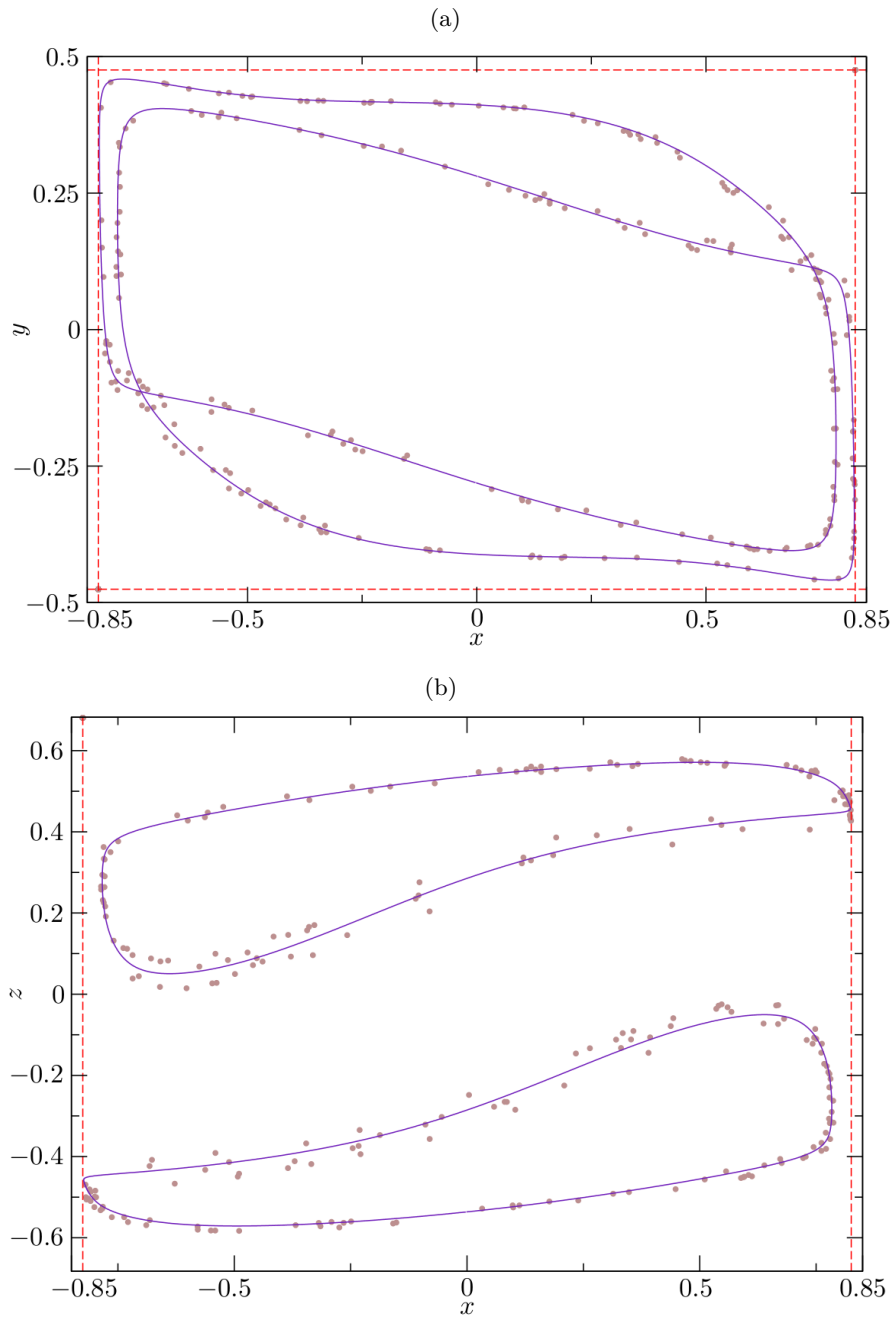


Figure 5.37.: Initially randomly distributed particles attracted to a line-like PAS along the closed streamline identified in Section 5.3.2 (indigo line). The accumulation is reported after $t = 1$ for $\text{Re} = 700$ on the (x, y) - and (x, z) -planes, (a) and (b) respectively. The prohibited regions for the particles (black dots) are marked with red dashed lines and the interaction length adopted for the PSI model is $\Delta = \Delta^{L_i} = 0.0244$.

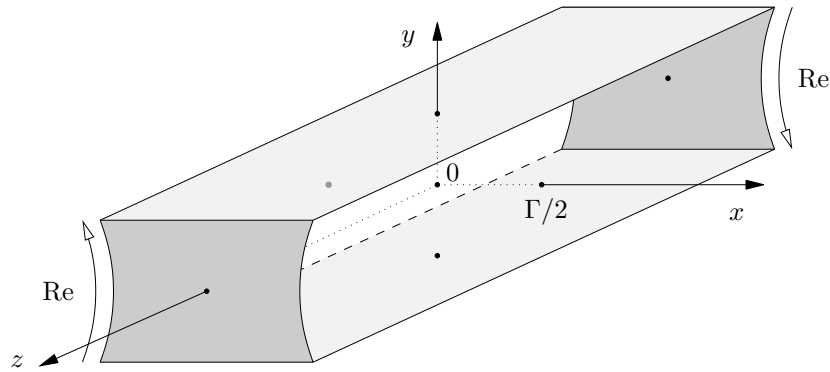


Figure 5.38.: Conceptual sketch of the experimental set-up employed for investigating PAS in a two-sided antiparallel lid-driven cavity configuration.

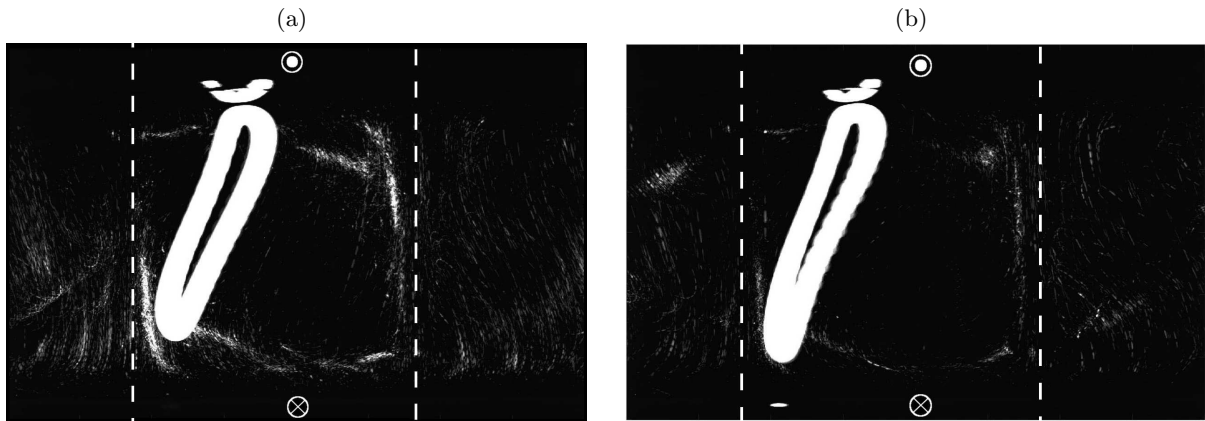


Figure 5.39.: Top view of particle accumulation structures obtained via long-exposure pictures with exposure time of 10 seconds after that a complete accumulation occurred. Two Reynolds numbers are depicted: $Re = 400$ (a) and $Re = 500$ (b). The rotating cylinders are located at the top and bottom part of the figure (\odot and \otimes indicate their rotation direction) and the dashed line shows an approximation of the periodic cell in which PAS is observed.

simulations predicted a periodic attractor which comes very close to both the moving walls, whereas the experimental accumulation shows a particle trajectory much closer to one of the rotating cylinders than to the other. The effect of the cylinders' curvature and aspect ratio have to be further investigated to figure out which changes they induce on the flow topology and on the particle limit cycle.

Figure 5.40 also shows the Poincaré sections on the $(y = 0)$ -plane obtained experimentally for the limit cycle. In table 5.8 we indicated $a = 0.0632$ and $a = 0.0424$ as the optimal particle radii for finding line-like PAS for $Re = 400$ and 500 , respectively. In the experiment such non-dimensional radii would correspond to $a_p = 2.5\text{mm}$ and $a_p = 1.7\text{mm}$, respectively. As demonstrated, a limit cycle has been experimentally found for $a_p = 2\text{mm}$. Therefore our numerical simulations can be considered sufficiently accurate for predicting the particle size for which PAS occurs in the two-sided antiparallel lid-driven cavity flow.

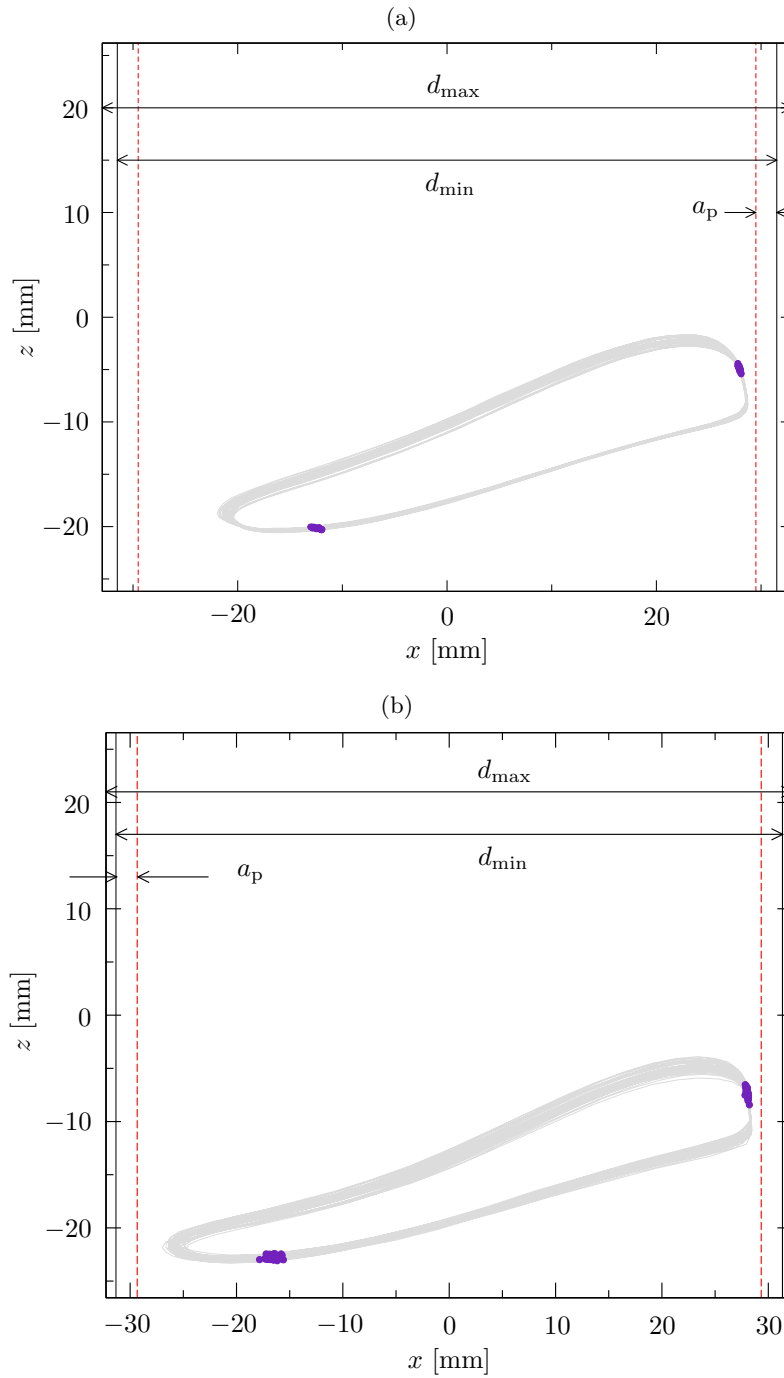


Figure 5.40.: Experimental evidence of quasi-line-like PAS obtained for a single particle in a periodic cell of the two-sided antiparallel lid-driven cavity for $\Gamma = 1.6$, $a_p = 2$ mm and $Re = 400$ (a) and $Re = 500$ (b). d_{\min} and d_{\max} indicate the extrema of the free distance between the two rotating cylinders. The grey line is the projection of the particle trajectories after a complete accumulation and the indigo dots denote the Poincaré sections of the particle trajectories on the (x, z) -plane.

5.4. Partially Liquid-Filled Rotating Drum

The last case we consider is a rotating drum configuration. The problem has been mathematically formulated in Chapter 2 and we refer the reader to it for further details about the equations and boundary conditions we impose. Among the various assumptions, it is worth to mention that we consider only the particle and the liquid phase, neglecting the gas-phase and assuming a flat shear-free surface.

The maximum liquid depth is measured at the center of the drum and set equal to $\Gamma = h/R = 0.2$ (filling ratio); the two-dimensional steady flow is found to become unstable with respect to a steady three-dimensional flow at a critical Reynolds number is $Re = 774$ (for further details we refer to [111]). The critical wavelength is $\lambda_c = 0.839$. Three supercritical Reynolds numbers will be investigated, considering $Re = 1000, 1500$ and 2000 . At all the Reynolds numbers the flow is found to be steady and three-dimensional.

Preliminary experimental observations have been conducted for proving the good approximation of the flat-interface assumption up to $Re = 2500$ and the existence of three-dimensional, steady flows for the investigated Reynolds numbers. For further details about the onset of instability we refer to [111].

The Navier–Stokes equations are solved employing `icoFoam`, a collocated transient solver which operates with laminar, incompressible flows and is implemented in the OpenFOAM[®] framework. A second-order implicit discretization in time is adopted; the computational mesh consists of ≈ 31 million grid-points, employing 450 evenly distributed cells in z -direction and 67600 cells for each cross-section. The cell distribution in the (x, y) -plane is depicted in fig. 5.41. The simulations are terminated when a stationary state is reached according to the following criterion

$$\max_{x,i} \frac{|u_i(\mathbf{x}, t) - u_i(\mathbf{x}, t - \Delta t)|}{\Delta t} \leq 10^{-7}. \quad (5.11)$$

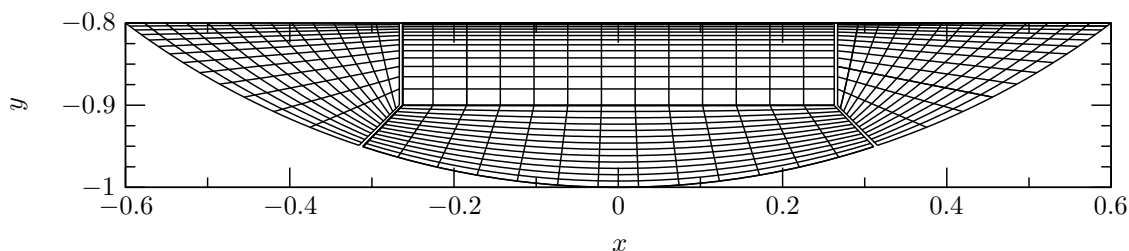


Figure 5.41.: Distribution of finite volumes for each cross-section of the liquid domain. The grid employed for the simulations is 10 times finer than the one depicted in this figure. The double lines show the four blocks which are used in OpenFOAM to assemble the computational mesh with `blockMeshDict`.

The same streamline integration method of Section 5.2.2 is here employed. The interpolation among the grid-points is linear when chaotic streamlines are computed, whereas we employ a quadratic interpolation method for computing streamlines in the regular regions. Relative and absolute tolerances for the 4th/5th-order Runge-Kutta Dormand-Prince method are set to 10^{-8} and a maximum time step of $\Delta t = 3 \times 10^{-5}$ is employed.

In order to characterize the flow, the basic state at criticality is shown in fig. 5.42. After the onset of the hydrodynamic instability a stationary flow evolves in form of periodic cells defined

by the ($z = \pm\lambda/4$)-planes. No through-flow is present across them, but, as in the case of the lid-driven cavity, the corresponding planar flow is not incompressible.

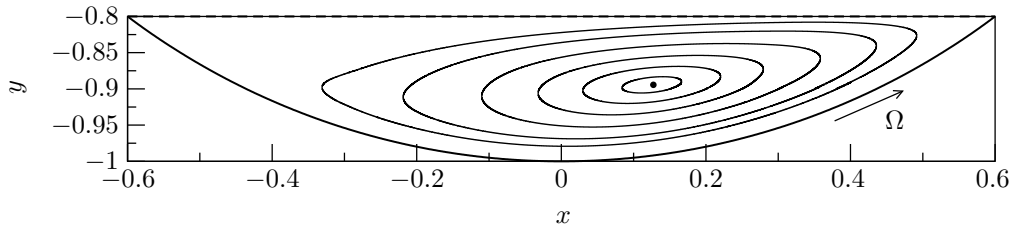


Figure 5.42.: Streamlines of the 2-D basic state in the partially liquid-filled rotating drum slightly above criticality for $\Gamma = 0.2$ and $\text{Re} = 780$. The marker (●) indicates vortex center (elliptic point).

The velocity vector field at supercritical conditions is shown in the following for $\text{Re} = 1000$, at the planes $z = -\lambda/4$ (a), $z = \lambda/4$ (b) and $x = 0$ (c). Figure 5.43a shows the counter-clockwise vortex at the center of the cell, whereas fig. 5.43b depicts how the vortex centre moves towards the top-right corner for $z = \lambda/4$. The three-dimensionality developed after the onset of the instability is evident in fig. 5.43c, where the free-surface acts transporting a fluid element from one side to the other of the periodic cell.

5.4.1. Main Topological Elements

The topology of the flow will be investigated in the following, determining the character of the critical points in the periodic cell as well as the corresponding stable and unstable manifolds. Two stagnation points are present in the cavity and both of them are located on the cell boundaries. As shown in fig. 5.44, integrating backward and forward in time the position of a single fluid element along the cell boundaries we can characterize the two critical points as saddle foci, one of them being a spiralling-in saddle focus (s_1 , fig. 5.44a) and the other one a spiralling-out saddle focus (s_2 , fig. 5.44b).

The chaos in this system is generated after breaking the heteroclinic connection holding (in the basic-state) between the sequence of elliptic points (one per each cross-section) in z -direction. A fluid element initialized nearby the spiralling-out saddle focus on the cell boundary moves towards the saddle limit cycle on $z = -\lambda/4$. From there it is ejected along the free-surface towards the saddle-limit cycle on the other side of the periodic cell. This saddle limit cycle attracts the fluid element sitting on the free-surface along z -direction and ejects it over $z = \lambda/4$. The fluid element ejected by the saddle-limit cycle will be attracted by the spiralling-in saddle focus over the cell boundary. Finally the streamline is re-ejected in the bulk along the one-dimensional unstable manifold of s_1 . A sketch of the main topological features of the supercritical flow is depicted in fig. 5.45.

5.4.2. Regular and Chaotic Regions

To complete the topological characterization of the flow, we determine the chaotic and regular embedded regions (KAM tori) in the liquid domain as function of the Reynolds number. For all the investigated cases, 1000 streamlines are initialized on the (y, z)-plane in a region nearby the rotating wall. The initial conditions are evenly distributed along five lines parallel to the y -axis in the ($x = 0$)-plane ($(y, z) \in [-0.9999, -0.9995] \times [-\lambda/4, \lambda/4]$). The trajectories are integrated up to $t = 50$ in convective time units and each streamline is assigned to chaotic or regular

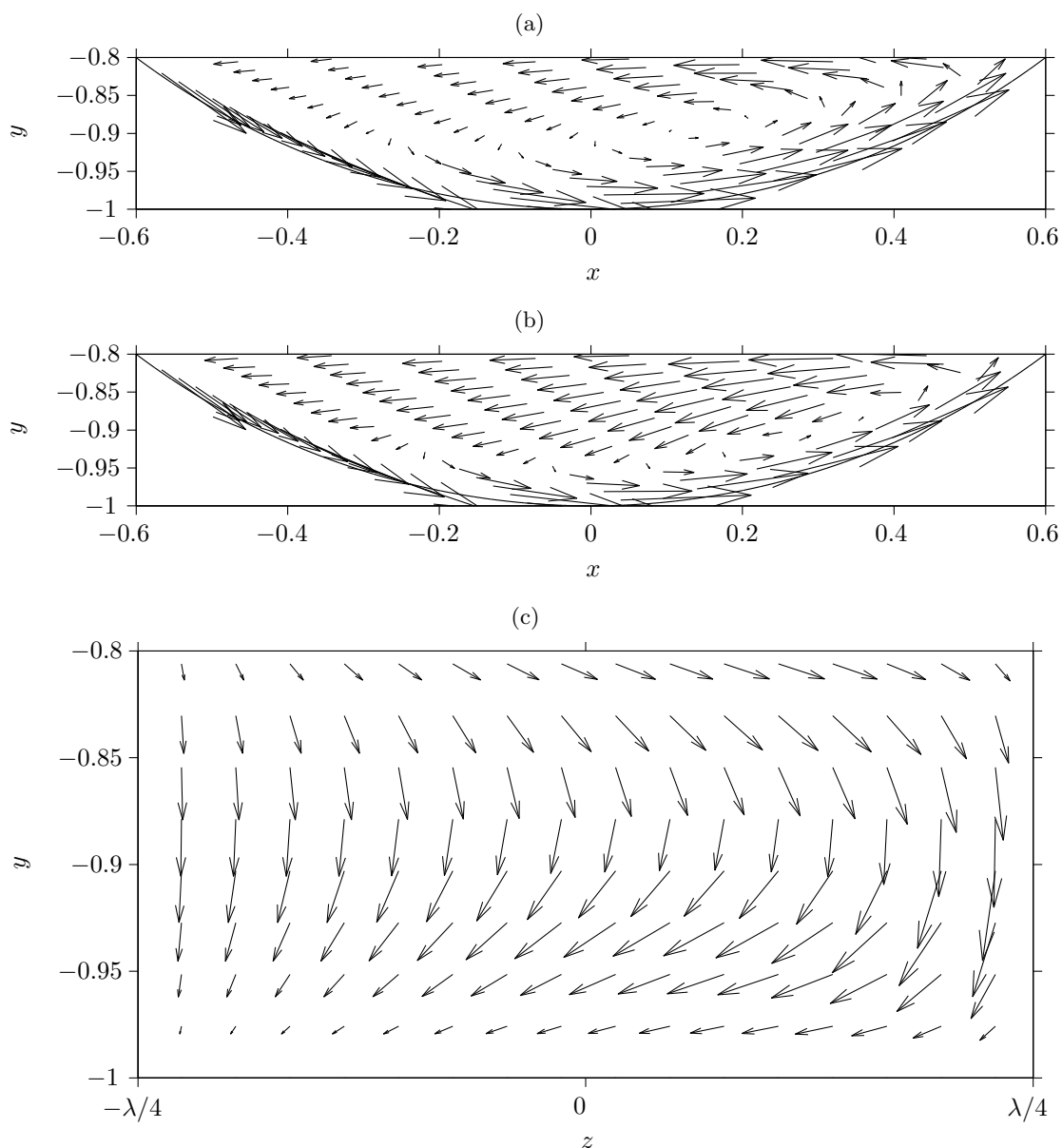


Figure 5.43.: Velocity vectors for $\text{Re} = 1000$ and $h/R = 0.2$ projected on $(z = -\lambda/4)$ - (a), $(z = \lambda/4)$ - (b) and $(x = 0)$ -planes (c).

regions in dependence on its behavior. Periodic or quasi-periodic streamlines are re-computed considering a lower relative and absolute tolerance for the 4th/5th-order Runge-Kutta scheme (10^{-9}) and a maximum time step of $\Delta t = 10^{-6}$.

For all the Reynolds numbers we investigate, $\text{Re} = 1000, 1500$ and 2000 , only single-periodic KAM tori are observed and the bigger the Reynolds number the smaller the portion of domain occupied by regular regions is. This trend is reported in fig. 5.46, where the Poincaré sections on $x = 0.15174$ are depicted. The KAM tori remain more or less localized in the same place and increasing the Reynolds number they tend to approach the boundaries.

The outermost KAM surface is always closer to the free-surface than to the rotating wall. Passing from $\text{Re} = 1000$ to $\text{Re} = 1500$ and 2000 the KAM tori tend to move towards the

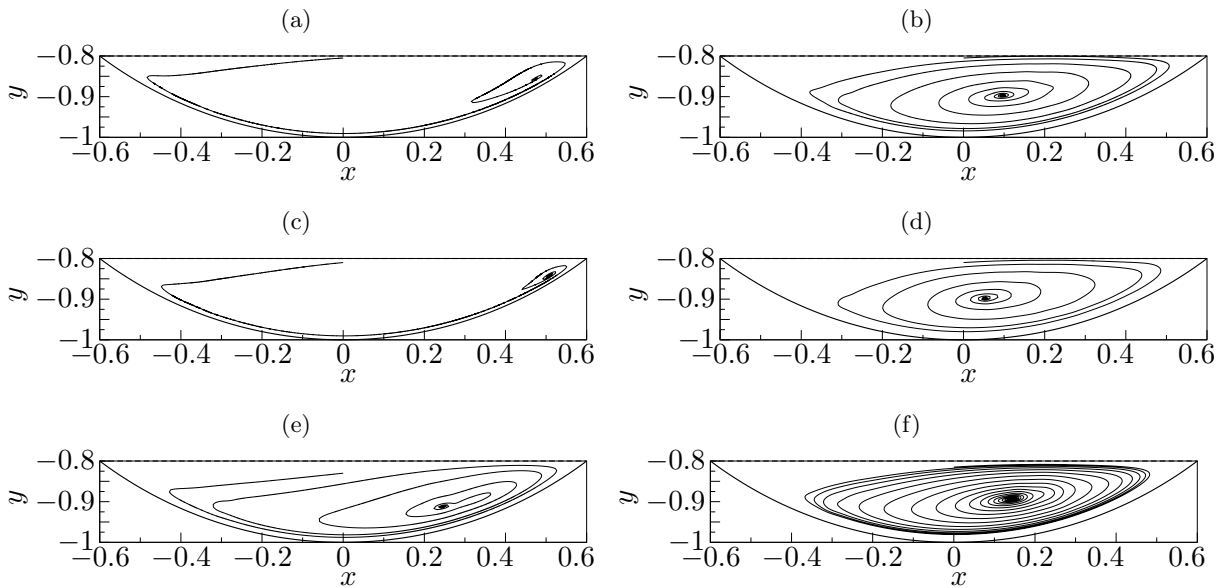


Figure 5.44.: Spiralling-in (a,c,e) and spiralling-out (b,d,f) saddle foci at the cell boundaries indicated with s_1 and s_2 , respectively. Figures (a,b) refer to $\text{Re} = 2000$, (c,d) to $\text{Re} = 1500$ and (e,f) to $\text{Re} = 1000$.

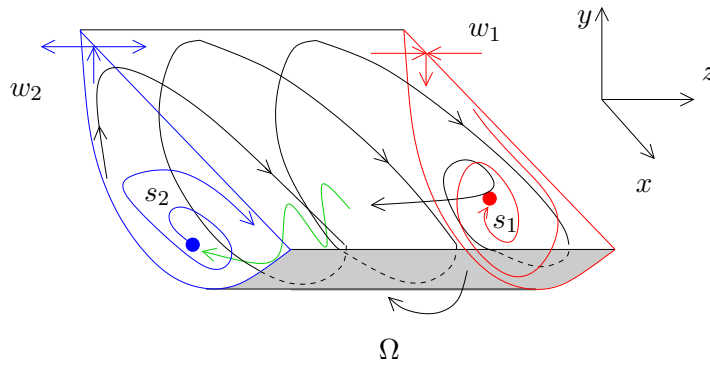


Figure 5.45.: Sketch of the major topological elements of the partially liquid-filled rotating tank in supercritical conditions. The spiralling-in saddle focus (red dot) and the saddle limit cycle on $z = \lambda/4$ are denoted by s_1 and w_1 , respectively. The spiralling-out saddle focus and the saddle limit cycle on the other cell boundary (marked in blue, $z = -\lambda/4$) are indicated by s_2 and w_2 . The grey area depicts the rotating wall.

Table 5.9.: Minimum distances from the moving wall Δ_w and the free-surface Δ_{fs} of the closed streamlines L and of the outermost KAM surfaces T . The orbit time τ of the closed streamlines are provided as well as one of two fixed points in the $(x = 0.15174)$ -Poincaré plane corresponding to L .

Re	KAM/streamline	τ	Δ_w	Δ_{fs}	Fixed point
2000	T	–	0.0291	0.0223	–
	L	6.102	0.0322	0.0329	(0.15174, –0.9553, 0.0417)
1500	T	–	0.0266	0.0179	–
	L	5.753	0.0338	0.0238	(0.15174, –0.9539, 0.0642)
1000	T	–	0.0237	0.0194	–
	L	5.120	0.0342	0.0230	(0.15174, –0.9534, 0.0702)

free-surface approaching it closer. A feature of this flow configuration is that the KAM tori are always very close to both the boundaries. This may accelerate the particle accumulation induced by particle–boundary interactions because a particle which moves close to the boundaries will experience an interaction with them twice per turn-over period (one collision with the wall, another with the free-surface).

The closed streamline in each KAM torus has been computed using the Newton–Raphson method for finding the elliptic fixed point of the Poincaré map with a relative accuracy of 10^{-4} on the $(x = 0.15174)$ -plane. The corresponding Poincaré return is indicated with a diamond marker in the Poincaré maps.

The projection of the periodic orbits on the (x, y) - and (y, z) -planes are depicted in fig. 5.47 for $Re = 1000$ (dotted line), 1500 (dashed line) and 2000 (solid line). Once again it can be noticed that the closed streamline always move very close to both the boundaries.

The closed streamline turn-over time is listed in table 5.9 as well as the minimum distance from the boundaries for the outermost KAM surface and the closed streamline. This information will be useful for numerically predicting the particle size to employ for observing PAS in experiments.

5.4.3. Particle Accumulation Structures

Particle accumulation structures in a partially liquid-filled rotating drum configuration have never been reported, so far. The perfect tracer equation supplemented by the PSI model are herein employed in the one-way coupled approach for numerically predicting PAS. Employing neutrally buoyant particles which perfectly follow the flow far away from the boundaries will make evident the role of dissipation induced by particle–boundary interactions.

In case of the particle–free-surface interaction, it must be considered that the free-surface in the rotating drum configuration is a stress-free surface. Therefore the interaction length Δ cannot be directly derived from the shear–stress-driven cavity investigated in Chapter 4. In creeping flow conditions, the forces exerted from a free-surface on a sphere moving towards the boundary are 1/4 the forces exerted on the same sphere if the free-surface were a wall. Therefore we expect a weaker repulsion from the shear–free-surface than from the wall $\Delta_w > \Delta_{fs}$ and, because of capillary forces, $\Delta_{fs} > a$. The best feasible approach to determine Δ_w and Δ_{fs} would certainly be to simulate the two-dimensional attraction to PAS for $\eta = 0.2$ in the same conditions of interest for fluid and particle parameters. This is currently in progress and we will produce our preliminary results assuming that the free-surface interaction length equals the particle radius

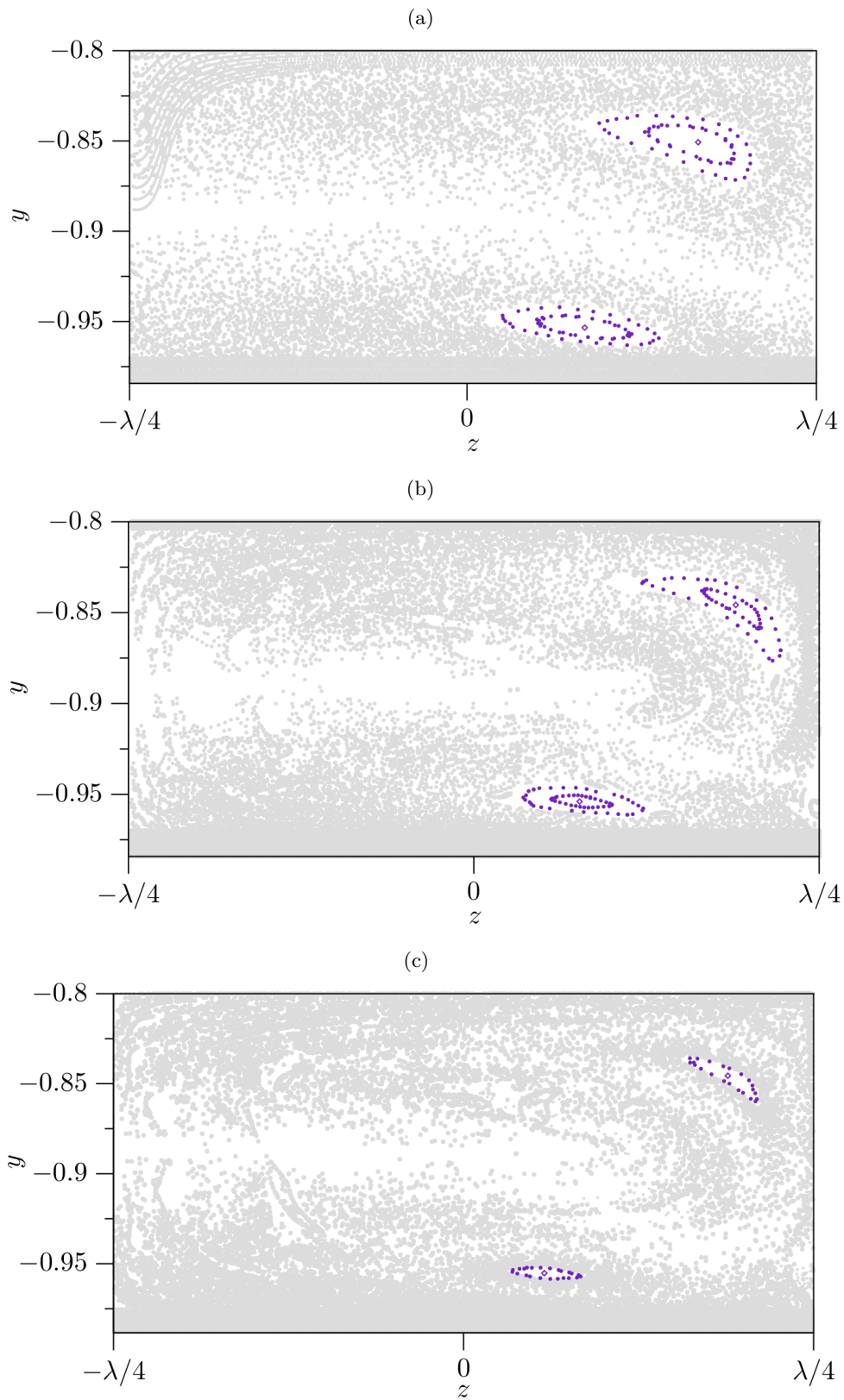


Figure 5.46.: Poincaré section of the KAM tori (indigo) embedded in the chaotic sea (grey) on $x = 0.15174$ for $\text{Re} = 1000$ (a), 1500 (b) and 2000 (c). The single-periodic orbits inside the KAM tori are marked by a diamond (\diamond).

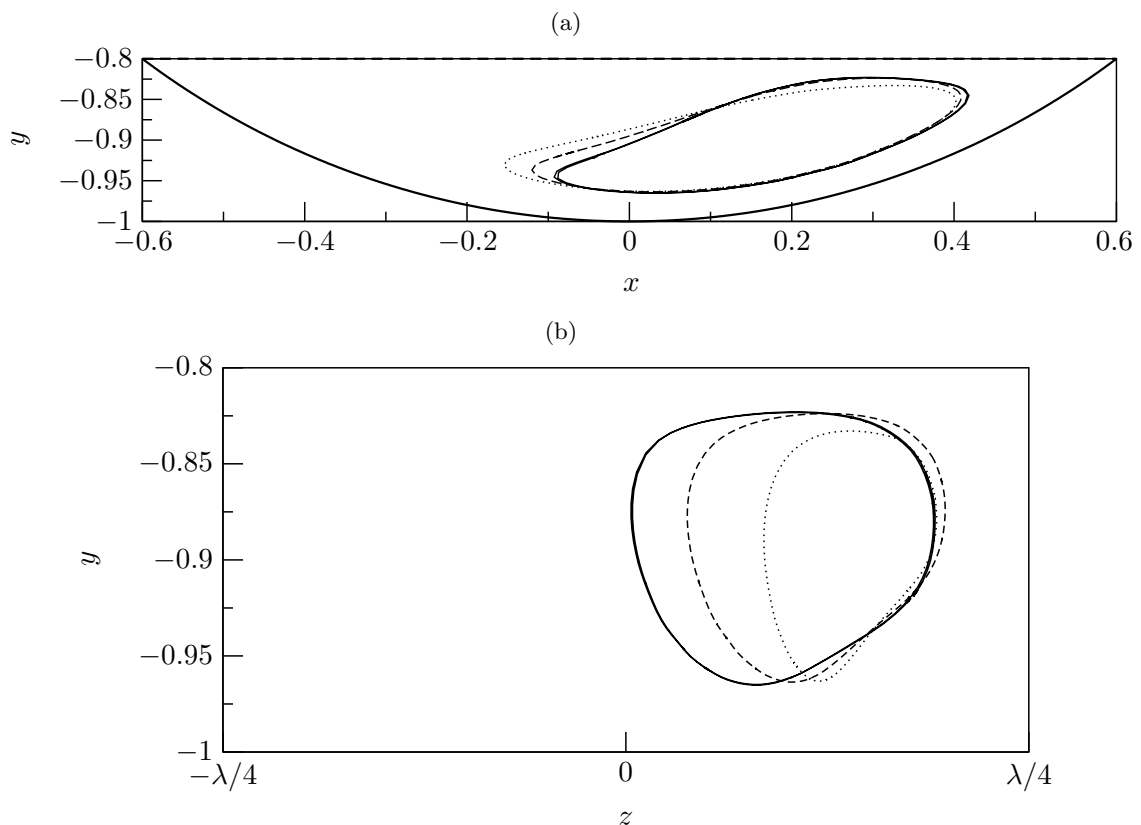


Figure 5.47.: Projection of the simple-periodic closed streamlines on the (x, y) - and (y, z) -plane, (a) and (b) respectively. The dotted, dashed and solid lines indicate the periodic orbits for $\text{Re} = 1000, 1500$ and 2000 , respectively.

($\Delta_{\text{fs}} = a$). The prediction of the minimum lubrication gap width produced in Chapter 4 is here taken into account for the interaction of a particle with the rotating wall, Δ_{w} , regardless of the curvature of driving wall itself. These results will be further improved in successive studies to give a more precise indication about the range of existence of PAS. The particle trajectories are initialized from 1500 random positions distributed in \mathcal{V}^*

$$\mathcal{V}^* = \{(x, y, z) : x^2 + y^2 \leq 1 - \Delta_{\text{w}}, y \in [-1 + \Delta_{\text{w}}, -0.8 - \Delta_{\text{fs}}], z \in [-\lambda/4, \lambda/4]\} \quad (5.12)$$

and integrated up to $t = 100$ convective time units.

The regular regions approach very close both the fluid domain boundaries, therefore it is necessary to distinguish between accumulations due to particle–wall, particle–free-surface interactions or both. This implies that, as done in the case of the liquid bridge, two distinct interaction lengths are considered for dealing with the rotating wall and the free-surface. Therefore we proceed fixing a particle radius a and deriving from it Δ_{w} and Δ_{fs} . Therefore the accumulation parameter windows are not only function of a single Δ , but combinations of Δ_{w} and Δ_{fs} .

We first investigate the range of particle radii such that $\Delta_{\text{w}} \in [\Delta_{\text{w}}^T, \Delta_{\text{w}}^L] \wedge \Delta_{\text{fs}} \in [\Delta_{\text{fs}}^T, \Delta_{\text{fs}}^L]$. In this case we can notice how the accumulation patterns are embedded in the regular regions of the flow topology. To demonstrate it we compare the Poincaré section at $x = 0.15174$ of the last quarter of particle trajectories (grey dots, $t \in [75, 100]$) and the outermost KAM surface (indigo dots) calculated to define the flow topology. When line-like structures result from the

accumulation processes, we compare them with the closed streamlines calculated in Section 5.4.2.

The results reported in fig. 5.49 and 5.52, 5.56 refer to tubular PAS. As specific case we distinguish the line-like accumulation phenomenon. In the lid-driven flow it was reported just for one value of Δ , whereas in the rotating tank we observe line-like PAS for the following condition

$$\text{single-periodic line-like PAS: } \Delta_w = \Delta_w^L \vee \Delta_{fs} = \Delta_{fs}^L. \quad (5.13)$$

The accumulation of particles along a closed periodic orbit is reported in fig.s 5.50, 5.53, 5.54, 5.57 and 5.58 for $\text{Re} = 1000, 1500$ and 2000 . The particle accumulation structures (dots) are line-like and coincide with the closed streamlines (indigo) computed in the previous section. As the particle radius increases, for $\text{Re} = 1000$ the periodic attraction is first occurring because of the interaction with the rotating wall. Vice versa, for $\text{Re} = 1500$ and 2000 , the first particle–boundary interaction inducing line-like PAS is due to the free-surface. However, further investigations are therefore needed to better describe the particle–free-surface interaction length in case of a stress-free surface.

For the particle radii considered, period doubling accumulations have not been observed and for $\Delta_w > \Delta_w^L \wedge \Delta_{fs} > \Delta_{fs}^L$ PAS does not occur in the PSI model framework. The last scenario to consider is $\Delta_w < \Delta_w^T \wedge \Delta_{fs} < \Delta_{fs}^T$ for which the creation of bigger tubular particle attractors is observed. They keep on being located nearby the KAM tori, but in this case they are not fully embedded in the outermost KAM surface. These kinds of tubular PAS are depicted in fig.s 5.48, 5.51 and 5.55 and resemble the shape of KAM tori. The same argument discussed in the lid-driven cavity case holds and the dissipation introduced by the PSI model suffices to let particles accumulate in weakly chaotic regions of the flow. The main difference with the lid-driven cavity results is that in this case a tubular PAS in the chaotic sea is observed.

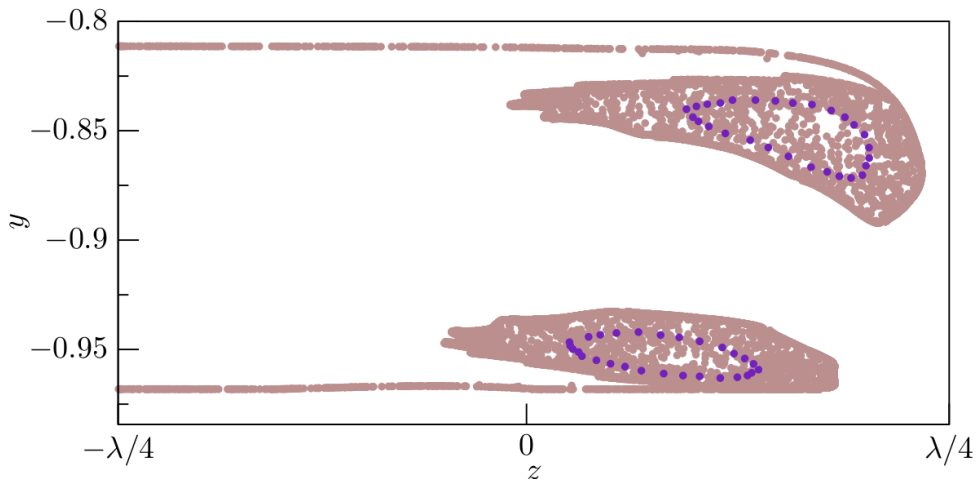


Figure 5.48.: Poincaré section on the $(x = 0.15174)$ -plane of the initially randomly distributed particles in the last part of their trajectory ($t \in [75, 100]$, grey dots) for $\text{Re} = 1000$. The indigo dots show the outermost KAM surface identified in Section 5.4.2. The selected particle radius is $a = 0.0106$ and the corresponding interaction lengths adopted for the PSI model are $\Delta_w = 0.02$ and $\Delta_{fs} = 0.0106$ and they lead to a tubular accumulation pattern developed around the outermost KAM surface.

Once again we demonstrated PAS for perfectly advected tracers undergoing to the PSI model. The clustering of particles as results of coexistence of regular and chaotic regions for the flow

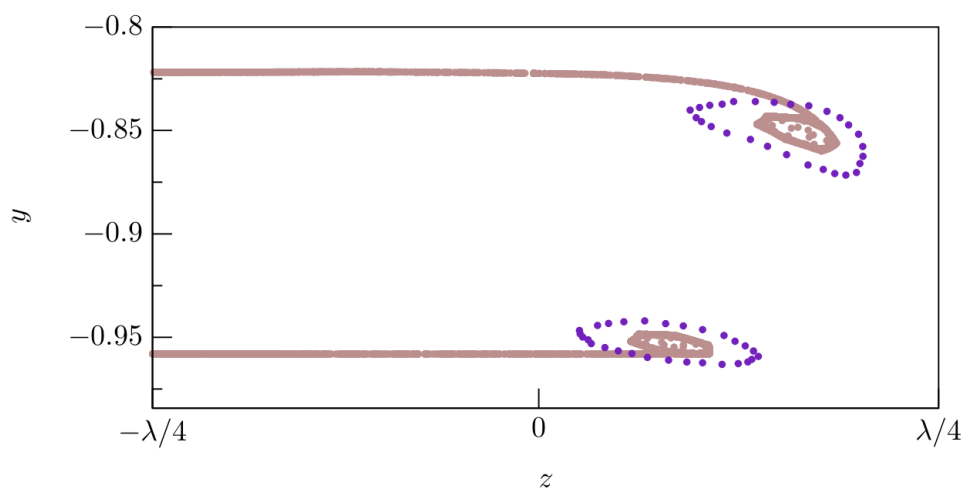


Figure 5.49.: Poincaré section on the $(x = 0.15174)$ -plane of the initially randomly distributed particles in the last part of their trajectory ($t \in [75, 100]$, grey dots) for $\text{Re} = 1000$. The indigo dots show the outermost KAM surface identified in Section 5.4.2. The selected particle radius is $a = 0.0201$ and the corresponding interaction lengths adopted for the PSI model are $\Delta_w = 0.03$ and $\Delta_{fs} = 0.0201$ and they lead to a tubular accumulation pattern embedded in the outermost KAM surface.

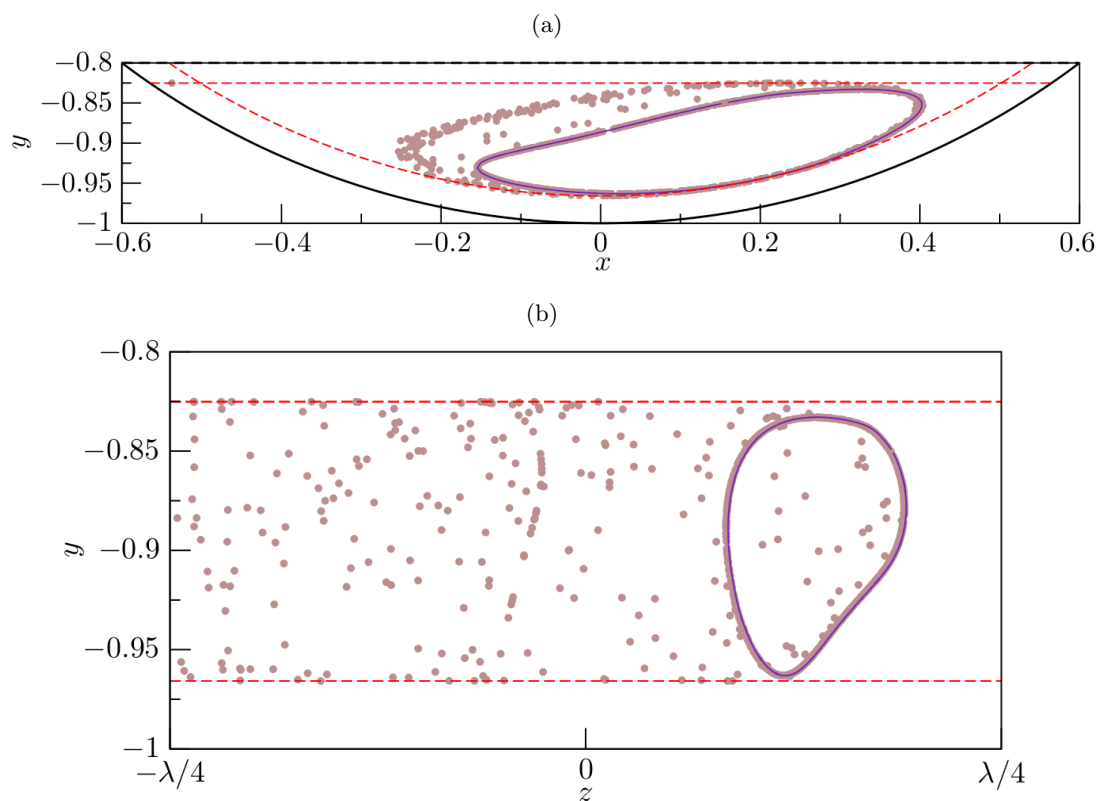


Figure 5.50.: Initially randomly distributed particles attracted to a line-like PAS along the closed streamline identified in Section 5.4.2 (indigo line). The accumulation is reported after $t = 100$ for $\text{Re} = 1000$ on the (x, y) - and (y, z) - planes, (a) and (b) respectively. The prohibited regions for the particles (black dots) are marked with red dashed lines, the selected particle radius is $a = 0.0251$ and the corresponding interaction lengths adopted for the PSI model are $\Delta_w = \Delta_w^L = 0.0342$ and $\Delta_{fs} = 0.0251$.

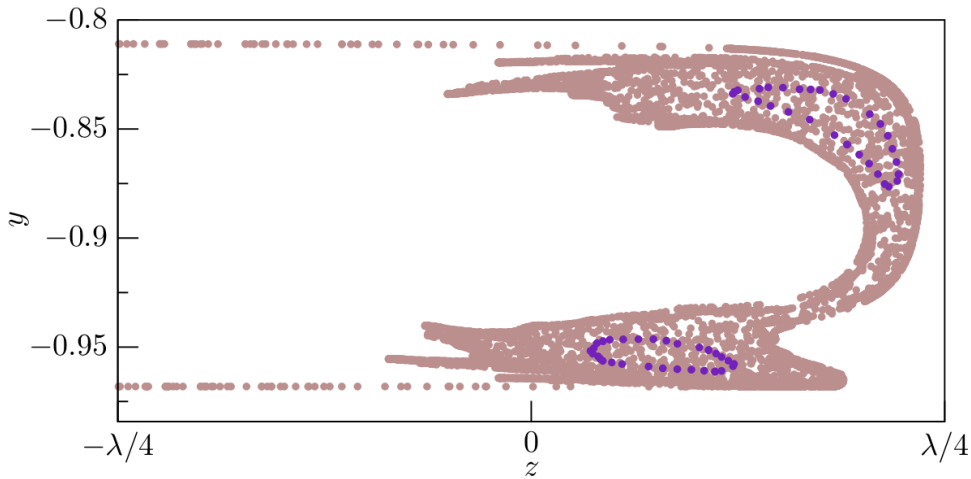


Figure 5.51.: Poincaré section on the $(x = 0.15174)$ -plane of the initially randomly distributed particles in the last part of their trajectory ($t \in [75, 100]$, grey dots) for $\text{Re} = 1500$. The indigo dots show the outermost KAM surface identified in Section 5.4.2. The selected particle radius is $a = 0.0106$ and the corresponding interaction lengths adopted for the PSI model are $\Delta_w = 0.02$ and $\Delta_{fs} = 0.0106$ and they lead to a tubular accumulation pattern developed around the outermost KAM surface.

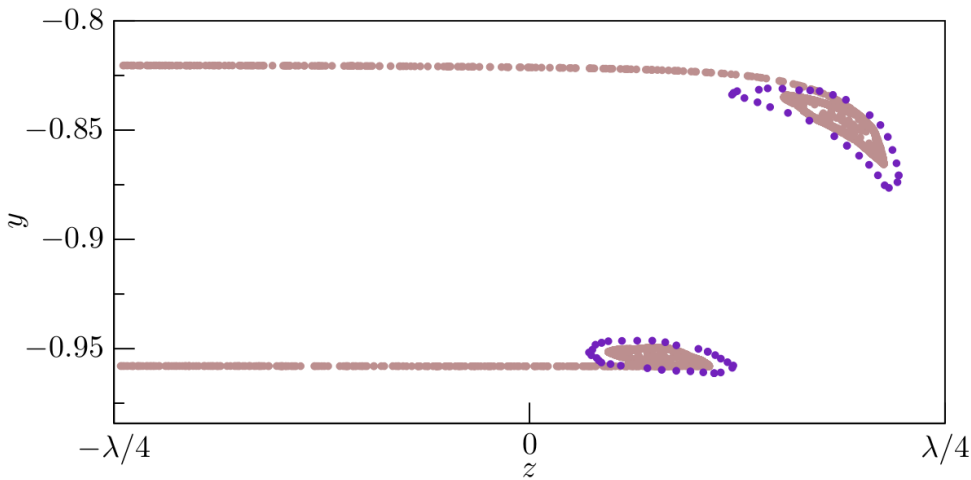


Figure 5.52.: Poincaré section on the $(x = 0.15174)$ -plane of the initially randomly distributed particles in the last part of their trajectory ($t \in [75, 100]$, grey dots) for $\text{Re} = 1500$. The indigo dots show the outermost KAM surface identified in Section 5.4.2. The selected particle radius is $a = 0.0201$ and the corresponding interaction lengths adopted for the PSI model are $\Delta_w = 0.03$ and $\Delta_{fs} = 0.0201$ and they lead to a tubular accumulation pattern embedded in the outermost KAM surface.

has been further proven, as well as the connection between the accumulation patterns and the periodic or quasi-periodic orbits of the flow. PAS has been reported for three different Reynolds numbers, $\text{Re} = 1000, 1500$ and 2000 . So far there is no experimental evidence of particle accumulation for this specific set-up. We therefore aim at indicating in table 5.10 a range of particle radii for which PAS is numerically predicted in order to facilitate experimental

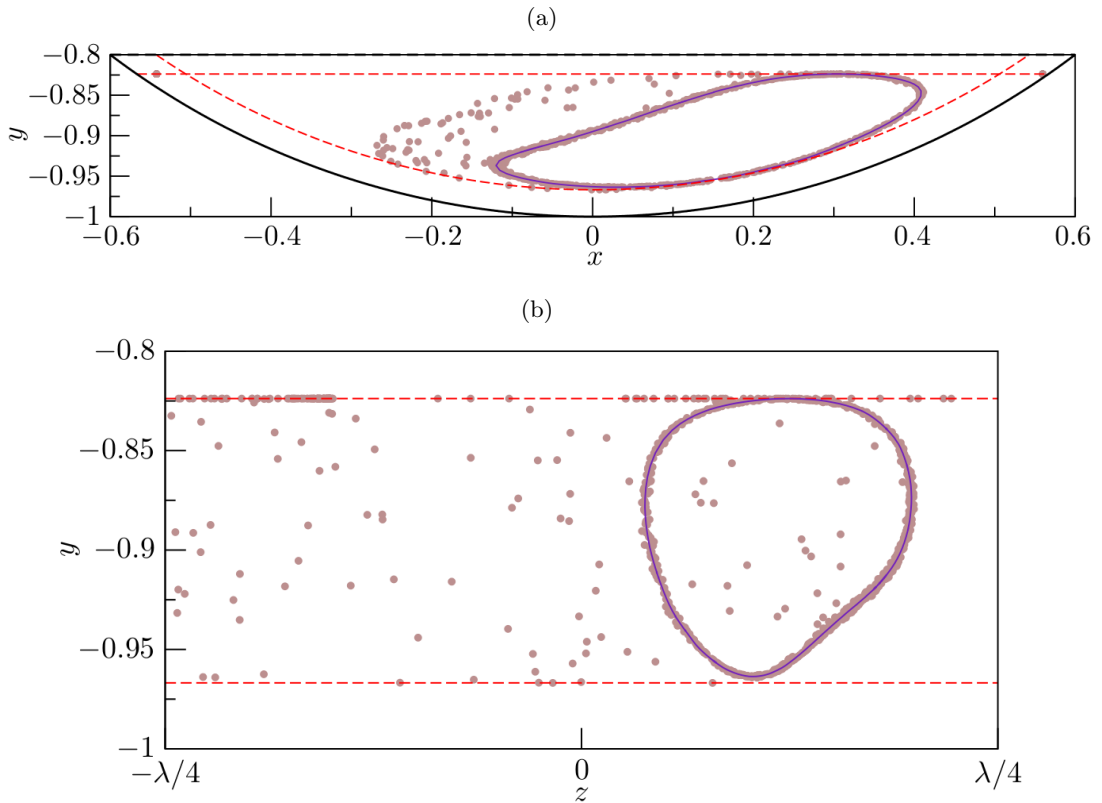


Figure 5.53.: Initially randomly distributed particles attracted to a line-like PAS along the closed streamline identified in Section 5.4.2 (indigo line). The accumulation is reported after $t = 100$ for $\text{Re} = 1500$ on the (x, y) - and (y, z) - planes, (a) and (b) respectively. The prohibited regions for the particles (black dots) are marked with red dashed lines, the selected particle radius is $a = 0.0238$ and the corresponding interaction lengths adopted for the PSI model are $\Delta_w = 0.0332$ and $\Delta_{fs} = \Delta_{fs}^L = 0.0238$.

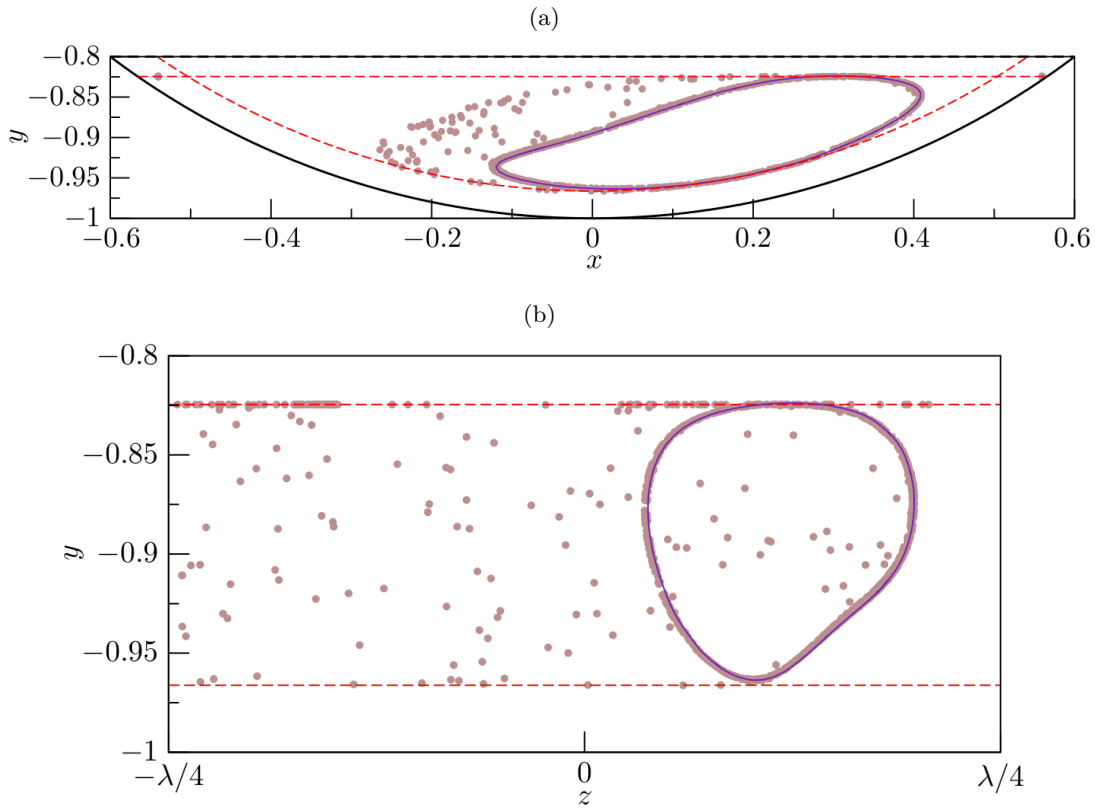


Figure 5.54.: Initially randomly distributed particles attracted to a line-like PAS along the closed streamline identified in Section 5.4.2 (indigo line). The accumulation is reported after $t = 100$ for $Re = 1500$ on the (x, y) - and (y, z) - planes, (a) and (b) respectively. The prohibited regions for the particles (black dots) are marked with red dashed lines, the selected particle radius is $a = 0.0246$ and the corresponding interaction lengths adopted for the PSI model are $\Delta_w = \Delta_w^L = 0.0338$ and $\Delta_{fs} = 0.0246$.

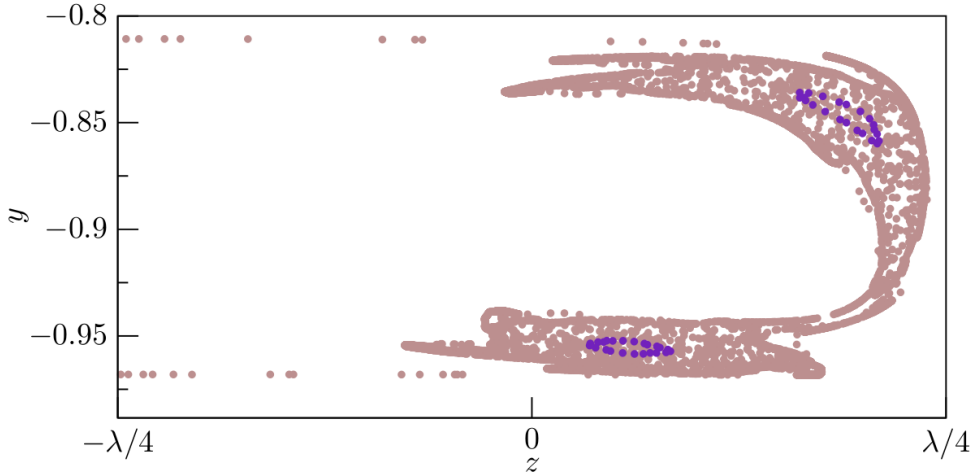


Figure 5.55.: Poincaré section on the $(x = 0.15174)$ -plane of the initially randomly distributed particles in the last part of their trajectory ($t \in [75, 100]$, grey dots) for $Re = 2000$. The indigo dots show the outermost KAM surface identified in Section 5.4.2. The selected particle radius is $a = 0.0106$ and the corresponding interaction lengths adopted for the PSI model are $\Delta_w = 0.02$ and $\Delta_{fs} = 0.0106$ and they lead to a tubular accumulation pattern developed around the outermost KAM surface.

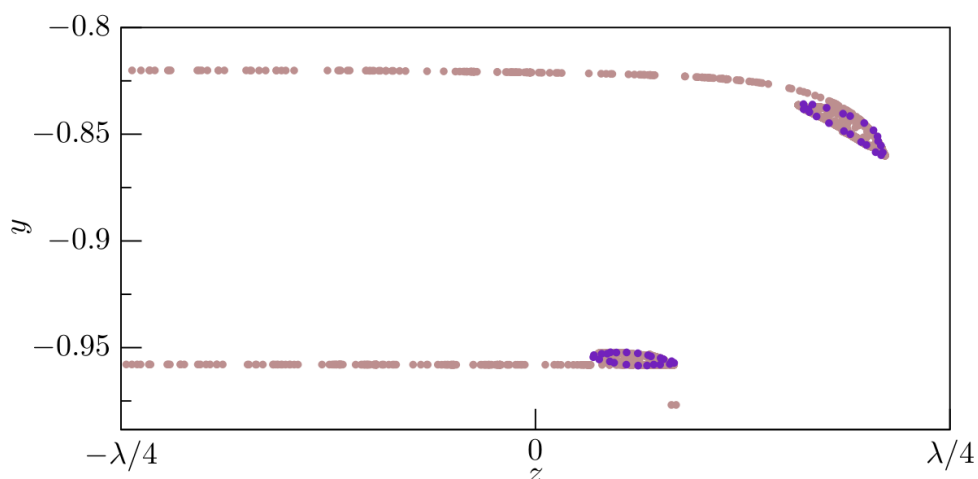
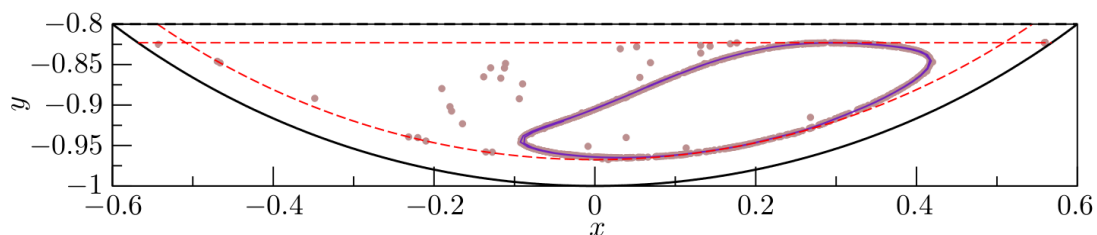


Figure 5.56.: Poincaré section on the ($x = 0.15174$)-plane of the initially randomly distributed particles in the last part of their trajectory ($t \in [75, 100]$, grey dots) for $\text{Re} = 2000$. The indigo dots show the outermost KAM surface identified in Section 5.4.2. The selected particle radius is $a = 0.0201$ and the corresponding interaction lengths adopted for the PSI model are $\Delta_w = 0.03$ and $\Delta_{fs} = 0.0201$ and they lead to a tubular accumulation pattern embedded in the outermost KAM surface.

(a)



(b)

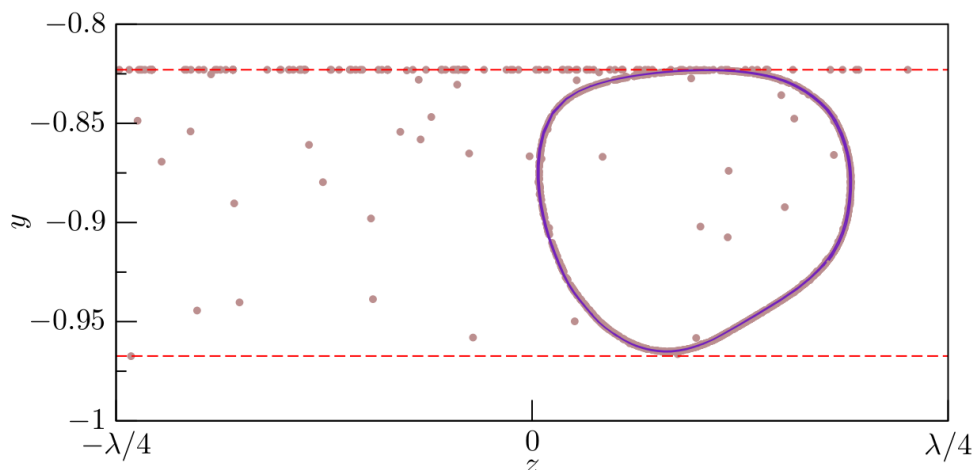


Figure 5.57.: Initially randomly distributed particles attracted to a line-like PAS along the closed streamline identified in Section 5.4.2 (indigo line). The accumulation is reported after $t = 100$ for $\text{Re} = 2000$ on the (x, y) - and (y, z) - planes, (a) and (b) respectively. The prohibited regions for the particles (black dots) are marked with red dashed lines, the selected particle radius is $a = 0.0230$ and the corresponding interaction lengths adopted for the PSI model are $\Delta_w = 0.0325$ and $\Delta_{fs} = \Delta_{fs}^L = 0.0230$.

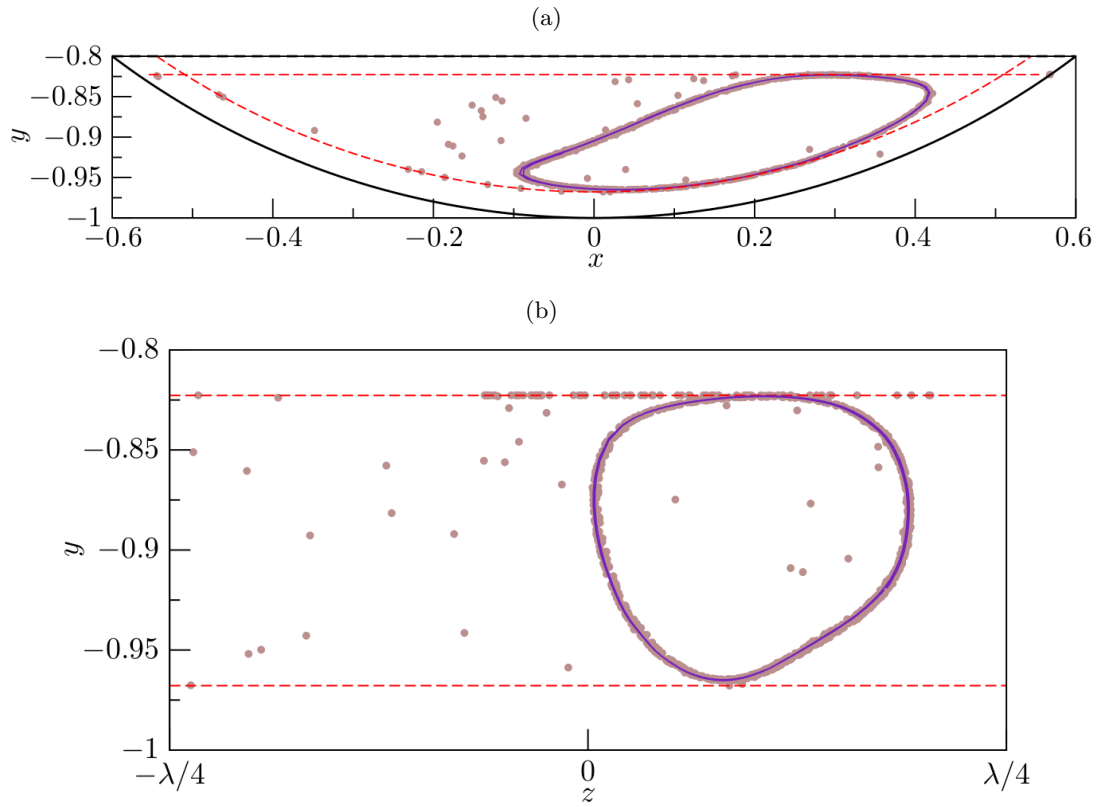


Figure 5.58.: Initially randomly distributed particles attracted to a line-like PAS along the closed streamline identified in Section 5.4.2 (indigo line). The accumulation is reported after $t = 100$ for $\text{Re} = 2000$ on the (x, y) - and (y, z) - planes, (a) and (b) respectively. The prohibited regions for the particles (black dots) are marked with red dashed lines, the selected particle radius is $a = 0.0227$ and the corresponding interaction lengths adopted for the PSI model are $\Delta_w = \Delta_w^L = 0.0322$ and $\Delta_{fs} = 0.0227$.

investigations concerning it.

Table 5.10.: Range of particle radii a and corresponding wall and free-surface interaction lengths, Δ_w and Δ_{fs} respectively, for which the existence of PAS is numerically investigated. With *tubular in chaotic sea* we indicate the tubular particle accumulation structure observed in the chaotic region about the KAM torus

Re	PAS type	$a = \Delta_{fs}$	Δ_w
1000	tubular in chaotic sea	0.0106	0.0200
	tubular in KAM	0.0201	0.0300
	single-periodic line-like	0.0251	0.0342
	no PAS	0.0321	0.0400
1500	tubular in chaotic sea	0.0106	0.0200
	tubular in KAM	0.0201	0.0300
	single-periodic line-like	0.0238	0.0332
	single-periodic line-like	0.0246	0.0338
	no PAS	0.0321	0.0400
2000	tubular in chaotic sea	0.0106	0.0200
	tubular in KAM	0.0201	0.0300
	single-periodic line-like	0.0227	0.0322
	single-periodic line-like	0.0230	0.0325
	no PAS	0.0321	0.0400

6. Summary and Conclusions

The phenomenon of particle accumulation in boundary-driven flows has been investigated in three different set-ups: a thermocapillary liquid bridge, a two-sided antiparallel lid-driven cavity and a partially liquid-filled rotating drum. This selection of the cases to study has been made in order to extend the typical research framework for PAS from thermocapillary- to more general boundary-driven flows. We aimed at demonstrating that experimental observations of PAS in a liquid bridge are not solely correlated with this system and its corresponding instabilities, but more generally with a streamline crowding near the boundaries. This is a common feature in all the flow configurations selected and has been exploited for proving the existence of particle accumulation in mechanically-driven flows, as well.

The first important results have been achieved considering non-zero-size particles in two-dimensional closed flows driven by either a constant shear-stress or a moving lid. In Chapter 4 we carried out fully-resolved simulations for a single particle in a square shear-stress- and a lid-driven cavity using the DG-FEM code developed during this project and including the rigid circular particle via SPM. Small-Stokes-number tracers with radius a equal 5 down to 1% the cavity length have been considered fully resolving fluid-flow, particle and lubrication gap scales. The main challenge was the flow resolution of the lubrication scales which ranged from $\mathcal{O}(0.01a)$ to $\mathcal{O}(a)$ for the parameters investigated. In both the systems we demonstrated the existence of a stable, global limit cycles for particles heavier than the fluid. The non-zero-size tracer is attracted to the periodic orbit due to particle–boundary interaction counteracting centrifugal inertia. When the particle moves far away from the boundaries the former dominates and centrifuges the particle out of the vortex core. On the other hand, when the rigid tracer approaches the boundaries, owing to its non-zero-size, it is repelled because of lubrication forces. These two mechanisms make the particle trajectory converge to a stable limit cycle independent of its initial position. On the attracting periodic single-particle orbit boundary repulsion and inertial centrifugal effects balance in the mean.

The fully-resolved simulations allowed to draw additional conclusions regarding the role of the particle size and density ratio ϱ in the accumulation phenomenon. In the limit of $t \rightarrow \infty$ the initial position of the particle can be disregarded. It was found that, for a constant ϱ , bigger particles are more capable of squeezing the lubrication gap ($a_1 > a_2 \Rightarrow \delta_1/a_1 < \delta_2/a_2$). Moreover, for a constant particle radius, the heavier the particle the smaller the minimum lubrication gap becomes.

The single-particle dynamics have been investigated constructing iterative Poincaré maps which gave the possibility to infer additional correlations between a , ϱ and the rate of attraction to the limit cycle. It is found that bigger particles accumulate faster than smaller ones and that the rate of attraction to the limit cycle is almost insensitive to ϱ .

Moreover, comparing the shear-stress- and the lid-driven cavities, the minimum lubrication gap for a particle moving on the limit cycle is one order of magnitude larger in the lid-driven cavities for comparable Reynolds numbers. In addition, particles in a shear-stress-driven cavity suffer a higher rate of attraction to the limit cycle, as also confirmed by experimental observations of PAS in a liquid bridge as compared to a lid-driven cavity.

The main purpose of the two-dimensional fully-coupled simulations was to quantify the interaction length Δ conceptually introduced for the first time by Mukin & Kuhlmann [194] and

defined as the minimum distance between particle centroid and boundary after a complete attraction to the limit cycle (accumulation process). The interaction length comprises of the particle radius and the minimum lubrication gap δ which has been neglected ($\delta = 0$) before our study. Herein we quantified its functional dependence on the particle radius and density ratio for both, a particle–free-surface and a particle–wall interaction. This investigation will be further developed in future studies in order to include the Reynolds number dependence on Δ and to determine the interaction length for shear–free-surfaces, as well. In view of to the high computational cost of fully-resolved simulations, even in two-dimensional flows, quantifying the interaction length Δ allowed us to simulate the accumulation process via a one-way coupling plus a particle–boundary interaction model. Such a rebound scheme (PSI model introduced in [126]) has been improved herein to take into account the minimum lubrication gap width for a particle moving on its limit cycle. In Chapter 4 it was shown the importance of δ in accurately predicting the global attracting periodic orbit in two-dimensions and the essential role of the PSI model, without which no limit cycles have been found for the two-dimensional flow considered.

The two-dimensional mechanism of accumulation has been further tested for an axisymmetric liquid bridge flow in Chapter 5. In this case we presented experimental results for single particles transported in the fluid. Experimental evidence demonstrates the existence of a limit cycle. The experiments have been satisfactorily reproduced by our one-way coupled simulations employing the Maxey–Riley equation, the PSI model and an axisymmetric finite volume solver developed during this project. Both, single-phase and multi-phase simulations have shown very good agreement with experimental results. It is remarkable the improvement of the numerical prediction accuracy when the PSI model is taking into account the estimate of δ made in Chapter 4. In particular, approximating the interaction length by a results in a very poor prediction of the minimum radial position of the particle centroid along the limit cycle. Still some open questions remain on the prediction of the particle turn-over time after complete attraction to the limit cycle. To the best of the author’s knowledge, this is the first time that a quantitative comparison between numerical and experimental data has been made for particle accumulation structures in terms of objectively defined quantities.

Using the OpenFOAM[®] solver developed during the project PARTAC [150], a further comparison between numerical simulations and experimental results in a liquid bridge has been established. Two experimental conditions have been selected for comparison because of different PAS observed (SL-I and SL-II). After the onset of instability in form of a traveling hydrothermal wave, a three-dimensional flow develops. For the selected parameters, the flow is steady with azimuthal wave number $m = 3$ and three-periodic in a reference frame rotating with the phase velocity of the wave. One-way coupled numerical simulations have been carried out in the rotating frame for reproducing the SL-I- and SL-II-PAS experimentally observed. Employing the PSI model disregarding the minimum lubrication gap width does not lead to numerically find PAS, whereas, if the estimate of Δ made in Chapter 4 is included, both the accumulation patterns reported experimentally are well predicted by our simulations. This proves once again the importance of an accurate estimate of the interaction length for simulating PAS. To the best of the author’s knowledge, this was the first time that SL-II-PAS has been numerically reproduced for $Pr = 28$.

Another important achievement of this study consisted in initiating the investigation of PAS in mechanically-driven flows. A spectral solver has been used for the lid-driven cavity fluid-phase [4] flow, whereas OpenFOAM[®] was employed for the partially liquid-filled rotating drum. In both cases, a steady three-dimensional flow develops periodic cells after the onset of instability. Numerous one-way coupled simulations have been carried out for covering the range of particle radii which may lead to particle accumulation structures for three Reynolds numbers in each

of the two set-ups. In this case we aimed at showing that PAS can be well predicted, in three-dimensions, using only the advection equation combined with the PSI model. Tubular and line-like PAS have been found in both the cases. We observe period doubling phenomena and highly-periodic accumulation orbits for the case of the lid-driven cavity. Moreover, determining the particle radius required for neutrally buoyant particles to form line-like PAS in the lid-driven cavity for $Re = 400$ and $Re = 500$ was predicted. This prediction was validated by successive experiments, even if slightly different geometrical parameters are employed in the experiments. This is the first time that PAS is numerically and experimentally reported for mechanically-driven flows. Further investigations are currently in progress to establish a quantitatively more detailed comparison as well as to verify our numerical prediction for PAS in a rotating drum.

The main achievement of this thesis work consists in further clarifying the strong correlation between flow topology and particle accumulation structures. A detailed topological study has been conducted for all the three systems under investigation, with the main purpose of accurately identifying chaotic and regular regions of the flow. The accumulation mechanism is indeed based on the transfer of the particles from the chaotic sea to the KAM tori by means of multiple particle–boundary interactions. Comparing the accumulation patterns in the liquid bridge (computed via integration of Maxey–Riley equation) and the closed streamline of the fluid-flow one may notice that the accumulation region does not only resemble the regular one, but locates on top of it. For the parameters considered, therefore, one may speculate that the inertia and finite-size effects in the bulk do not sensibly affect the final stage of accumulation of the particles. Moreover, the time scales connected with pure inertia accumulation are much longer than the ones experimentally reported. Including the particle-boundary interaction via the PSI model would already be accurate enough for an order-of-magnitude comparison with experiments in terms of PAS formation time. This is a strong indication to conclude that addressing PAS as *inertial coherent structures* (see [190, 104, 228]) is misleading. Inertia is playing a marginal role in the three-dimensional accumulation phenomenon, whereas the main dissipation mechanism is due to particle–boundary interaction. The PSI model employed for one-way coupled simulations introduces the dissipation via a discontinuity of the velocity vector field which, in the framework of dynamical systems, is classified as a Filippov system.

Finally, in the last section of Chapter 4, we proposed a mechanism for explaining the experimentally observed transfer of particles from the accumulation pattern to the bulk regions of the flow [258]. Our argument is based on the particle–particle interaction which may contribute to a transfer of the particles from the regular regions of the flow to the chaotic sea. We proposed the particle occupation ratio as non-dimensional group of interest for describing the phenomenon. Furthermore we defined a Poincaré-like stability for measuring the dispersion of particle trajectories about the single-particle attractor when mutual interactions between tracers are considered. This theoretical explanation has been analysed in the two-dimensional shear–stress-driven cavity and conceptually extended to three-dimensions. Future studies will aim to verify this hypothesis and to numerically investigate the phenomena produced by particle–particle interactions in PAS-related phenomena. To this end we will substitute the current one-way coupling with a two- or a four-way coupling approach.

A. From Prototypical to Physical Domains

In this chapter a way to transform prototypical domains into physical ones or part of it is presented. A suitable choice for building the mesh is to divide the physical domain in a set of smaller parts, elements, each of which will be referred to a prototypical element and somehow connected with the neighbor ones.

In order to proceed, transfinite interpolations are implemented for both, two- and three-dimensional geometries. They respectively deal with quadrilateral and triangular elements in 2-D, hexahedra and tetrahedra in 3-D. At the end of this chapter the nodes distribution is discussed for two-dimensional cases.

Because of convergence degrading issues, just mappings in simply connected elements will be considered, but it should be kept in mind that the transfinite interpolation technique does not have such a sort of limitations.

A.1. Transfinite Interpolation

Transfinite interpolation is a class of method for approximating multivariate functions, which is used to parametrize curved domains. In its bivariate and trivariate schemes, it is possible to build approximation lattices for describing two- and three-dimensional domains respectively, being known a parametrization of their surfaces.

Such a technique was first proposed in [62], where *Coons surfaces* have been used for computer-aided design and numerical control production of free-form surfaces like a ship's hull or an air-plane fuselage. In his paper, Coons introduces the blending-function interpolation schemes, an extension of which is the transfinite interpolation technique. One usually refers to Coons surfaces as interpolatory surfaces coinciding, on the boundary of the prototypical quadrilateral, with arbitrary curves explicitly prescribed. An extensive contribution to them was given by Forrest in [81] and [82], but the generalization to transfinite interpolation is more properly due to Gordon & Hall (see [95, 96, 97, 98, 99, 100, 101]).

They formulated the corresponding theory applying projection operators combined with each others via Boolean algebra. Indeed, in [95] it is presented how to build an algebraically maximal projector and a minimal one (tensor product) with both Lagrangian and Hermitian polynomials. Using the transfinite interpolation technique, Gordon and Hall also present some mesh and curvilinear coordinate systems generation procedures, but mainly referring to quadrilateral and hexahedral prototypical domains. A transfinite mapping for triangles [13, 14] and tetrahedron was discussed in [219] and a complete overview on the transfinite interpolation for all the prototypical domains is presented in [286]. A more recent intensive study on this topic is investigating topology, application to integral equations, to wavelet methods and regularity of the transfinite interpolation (see e.g. [235, 113, 236, 237, 238, 239]).

To motivate the choice of such an interpolation class of methods for mapping the prototypical into the physical elements, one should consider some important strengths of the transfinite mapping. For instance the high computational efficiency due to an explicit definition of the mapping, a good correlation between the boundary and the internal nodes, a direct extension from the two- to the three-dimensional case and, specially, the nondenumerability property. The latter

point gives the quality *transfinite* to the interpolation method and means that the set of points on which the interpolation exactly matches the interpolated function is nondenumerable. Such a property is particularly important for h/p -methods in order not to bound their rate of convergence or even to avoid non-physical results due to meshing approximations (see e.g. [262]). On the other hand, as main drawbacks of the transfinite interpolation technique there is the possible non-invertibility of the mapping as well as the effort required for obtaining the interpolation itself, specially in three-dimensions. For such reasons, an alternative method for providing the mapping is represented by the non-uniform rational B-spline (NURBS) interpolation, used with success in the h/p -methods field and referred as NEFEM ([262]).

In the present thesis work we will opt for the transfinite interpolation technique, some more details of which will be presented in the next subsections.

A.2. Lattice generators

The transfinite interpolation technique is based on an algebraic theory for approximating multivariate functions, whose details are extensively treated in [98]. Aim of this paragraph is just to give some fundamental notions of lattice generators without entering in details. Therefore it will be presented nothing but a framework to transfinite interpolation methods, in order to better clarify the properties of the mapping itself.

Recalling [98], for defining the class of univariate projectors of interest (herein used as lattice generators), it is considered a “normal, k -th order, linear, homogeneous, ordinary differential operator with continuous real coefficients $\alpha_i(\hat{x})$, $i = 0, 1, \dots, k$ defined over the finite interval $[a, b]$:

$$D = \alpha_0(\hat{x}) + \alpha_1(\hat{x}) \frac{d}{d\hat{x}} + \dots + \alpha_{k-1}(\hat{x}) \frac{d^{k-1}}{d\hat{x}^{k-1}} + \alpha_k(\hat{x}) \frac{d^k}{d\hat{x}^k}, \quad (\text{A.1})$$

where $\alpha_k(\hat{x}) \neq 0$ for any $\hat{x} \in [a, b]$. The null space of D is the k -dimensional linear space Φ spanned by any linearly independent set of k solutions of the homogeneous differential equation $D[\phi] = 0$.”

We can then define as projector an idempotent¹ linear transformation from a space \mathcal{Q} into the subspace Φ . Therefore P is a projector if it yields:

$$P[\cdot] = \sum_{i=1}^k \lambda_i[\cdot] \phi_i(\hat{x}), \quad (\text{A.2})$$

where $\{\lambda_i\}_{i=1}^k$ is a set of k bounded linear functionals belonging to the space C^k on $[a, b]$ and linearly independent over Φ , and $\{\phi_i\}_{i=1}^k$ is the unique basis for Φ such that $\lambda_i[\phi_j] = \delta_{ij}$.

As reported in [98], the concepts extension from univariate to multivariate functions is straightforward and nothing but a parametric extension of the operators D and P to the space of N -variate functions C^{k_1, \dots, k_N} . In the bivariate case, for instance, it holds:

$$\mathcal{D}^{\hat{x}} = D^{\hat{x}} \otimes I^{\hat{y}}, \quad \mathcal{L}_i^{\hat{x}} = \lambda_i^{\hat{x}} \otimes I^{\hat{y}}, \quad \mathcal{P}^{\hat{x}} = P^{\hat{x}} \otimes I^{\hat{y}} \quad (\text{A.3a})$$

$$\mathcal{D}^{\hat{y}} = I^{\hat{x}} \otimes D^{\hat{y}}, \quad \mathcal{L}_j^{\hat{y}} = I^{\hat{x}} \otimes \lambda_j^{\hat{y}}, \quad \mathcal{P}^{\hat{y}} = I^{\hat{x}} \otimes P^{\hat{y}}, \quad (\text{A.3b})$$

¹Being $U(\hat{x})$ an arbitrary function in C^k and π the unique function in Φ which interpolates U with respect to $\{\lambda_i\}_{i=1}^k$ such that $\pi(\hat{x}) = \sum_{i=1}^k \lambda_i[U] \phi_i(\hat{x})$, a projector P is idempotent if it yields:

$$P[P[U]] = P[U] = \pi.$$

where $D^{\hat{x}}, D^{\hat{y}}, P^{\hat{x}}, P^{\hat{y}}$ are the univariate operators D and P respectively defined for $\hat{x} \in [\hat{x}_a, \hat{x}_b]$ and $\hat{y} \in [\hat{y}_a, \hat{y}_b]$, and $I^{\hat{x}}, I^{\hat{y}}$ are the corresponding identity operator.

It is then possible to proceed with some Boolean algebra applied to the projection operators, combining them in order to obtain the lattice generators class of interest. The easiest way to build a multivariate interpolation is to compose the projectors between themselves. As shown in [95], this way conduces to an algebraically minimal projector² that, for the parametrically extended projection operators, reduces to a tensor product. In the bivariate and trivariate cases it holds:

$$T(\hat{x}, \hat{y}) = (\mathcal{P}^{\hat{x}} \circ \mathcal{P}^{\hat{y}})[F] \quad (\text{A.4a})$$

$$T(\hat{x}, \hat{y}, \hat{z}) = (\mathcal{P}^{\hat{x}} \circ \mathcal{P}^{\hat{y}} \circ \mathcal{P}^{\hat{z}})[F], \quad (\text{A.4b})$$

where $T(\hat{x}, \hat{y})$ and $T(\hat{x}, \hat{y}, \hat{z})$ are the tensor product operators for interpolating the function $F(\hat{x}, \hat{y})$ and $F(\hat{x}, \hat{y}, \hat{z})$ respectively on the point grid in \hat{x}, \hat{y} and \hat{z} . Even though T is itself a projector, its precision set consist only of the finite number of points on the generated lattices. Therefore, it cannot be classified as a transfinite interpolation operator. On the other hand, it is possible to obtain an algebraically maximal projector³ combining the projection operators $\mathcal{P}^{\hat{x}_i}$ via a Boolean sum. In the bivariate and trivariate cases, it yields:

$$\mathcal{P}^{\hat{x}} \oplus \mathcal{P}^{\hat{y}} = \mathcal{P}^{\hat{x}} + \mathcal{P}^{\hat{y}} - \mathcal{P}^{\hat{x}} \circ \mathcal{P}^{\hat{y}} \quad (\text{A.5a})$$

$$\begin{aligned} \mathcal{P}^{\hat{x}} \oplus \mathcal{P}^{\hat{y}} \oplus \mathcal{P}^{\hat{z}} &= \mathcal{P}^{\hat{x}} + \mathcal{P}^{\hat{y}} + \mathcal{P}^{\hat{z}} - \mathcal{P}^{\hat{x}} \circ \mathcal{P}^{\hat{y}} - \\ &\quad \mathcal{P}^{\hat{x}} \circ \mathcal{P}^{\hat{z}} - \mathcal{P}^{\hat{y}} \circ \mathcal{P}^{\hat{z}} + \mathcal{P}^{\hat{x}} \circ \mathcal{P}^{\hat{y}} \circ \mathcal{P}^{\hat{z}}. \end{aligned} \quad (\text{A.5b})$$

In the latter case, the obtained interpolation operator is a transfinite one because its precision set consists of the whole characteristic lines of the generated lattice. That implies that the set of points on which the interpolant exactly matches the interpolated function is nondenumerable. Such a property comes from a theorem demonstrated for bivariate Lagrange, cubic spline and trigonometric polynomial interpolation projectors ([95], [99]), but what is very essential is that the so-called *bending functions* satisfy the cardinality conditions.

In the present thesis work, just Lagrangian blending functions will be considered and the transfinite mapping to be presented are obtained using the element boundary surfaces only for the exact matching with the lattice. Further coordinate surfaces constraints can be introduced to better map the prototypical elements, but for the simple shapes of interest, this would introduce unnecessary complications.

²A projector \mathcal{P} is an algebraically minimal one when it yields:

$$\mathcal{P}^{\hat{x}_1}[\mathcal{P}] = 0, \mathcal{P}^{\hat{x}_2}[\mathcal{P}] = 0, \dots, \mathcal{P}^{\hat{x}_N}[\mathcal{P}] = 0$$

³A projector \mathcal{P} is an algebraically maximal one when it yields:

$$\mathcal{P}^{\hat{x}_1} \mathcal{P}^{\hat{x}_2} \dots \mathcal{P}^{\hat{x}_N}[\mathcal{P}] = 0$$

A.3. 2-D transfinite Lagrange interpolation

In order to clearly define the framework of a vector-valued bivariate transfinite interpolation, it can be considered the graph of the vector-valued function:

$$\mathbf{F}(\hat{x}, \hat{y}) = \begin{bmatrix} F_1(\hat{x}, \hat{y}) \\ F_2(\hat{x}, \hat{y}) \\ \vdots \\ F_n(\hat{x}, \hat{y}) \end{bmatrix}, \quad (\text{A.6})$$

where \hat{x} and \hat{y} will be used to define the prototypical domain $\hat{\Omega}$ to be mapped in the physical one Ω , or a part of it. From eq. A.6 it results that $\mathbf{F}(\hat{x}, \hat{y})$ maps, in general, \mathbb{R}^2 regions into Euclidean n -space, E^n :

$$\mathbf{F} : \mathbb{R}^2 \rightarrow E^n. \quad (\text{A.7})$$

In the following subsections just planar mappings will be considered ($n = 2$), but one should keep in mind that the bivariate transfinite interpolation does not impose any sort of constrain in the choice of E^n .

A.3.1. Edge Parametrization

The two-dimensional transfinite interpolation is built considering a parametrization of *flow lines* the lattice will be based on. Only the element edges only will be assumed as exactly matching lines with the lattice, but it stands that further constrains can be included for better adapting the interpolation as explained in [100].

It is then natural to present one-dimensional segment parametrization samples that will be employed in the following two-dimensional transfinite interpolation.

For convenience, the edges parametrization used in the quadrilateral mapping differs from the triangle one because in the first case the parameter lives in the one-dimensional prototypical domain $\gamma \in [-1, 1]$, instead, for triangles, $u \in [0, 1]$. The segment parametrization of the two cases are linked with each other through the transformation $\gamma = 2u - 1$.

The following linear and circular parametrization is extensively used during the present thesis work because of the geometry to implement for the simulations of interest. It holds, however, that transfinite interpolation methods can be used for every kind of parametrized edge.

Linear Segment: Cartesian Coordinates

$$\mathcal{T}_{edge}(u) = \begin{pmatrix} x_a \\ y_a \end{pmatrix} + u \begin{pmatrix} x_b - x_a \\ y_b - y_a \end{pmatrix} \quad (\text{A.8a})$$

$$\mathcal{T}_{edge}(\gamma) = \begin{pmatrix} x_a \\ y_a \end{pmatrix} + \frac{\gamma + 1}{2} \begin{pmatrix} x_b - x_a \\ y_b - y_a \end{pmatrix} \quad (\text{A.8b})$$

Circular Segment: Polar Coordinates

$$\mathcal{T}_{edge}(u) = \begin{pmatrix} x_C \\ y_C \end{pmatrix} + R \begin{pmatrix} \cos[\phi_a + u(\phi_b - \phi_a)] \\ \sin[\phi_a + u(\phi_b - \phi_a)] \end{pmatrix} \quad (\text{A.9a})$$

$$\mathcal{T}_{edge}(\gamma) = \begin{pmatrix} x_C \\ y_C \end{pmatrix} + R \begin{pmatrix} \cos[\phi_a + (\gamma + 1)(\phi_b - \phi_a)/2] \\ \sin[\phi_a + (\gamma + 1)(\phi_b - \phi_a)/2] \end{pmatrix} \quad (\text{A.9b})$$

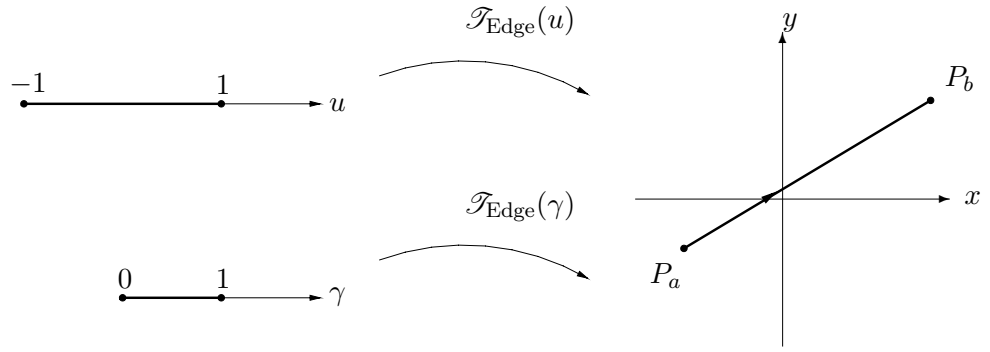


Figure A.1.: Edge mapped into a linear segment.

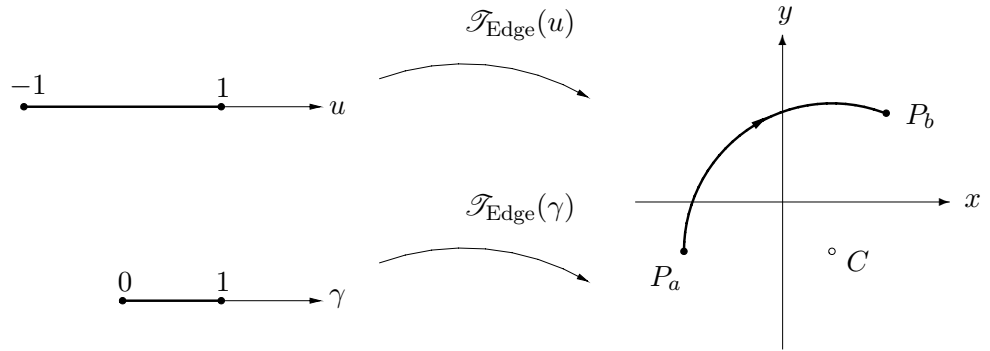


Figure A.2.: Edge mapped into a circular segment with center C.

A.3.2. Quadrilateral Mapping

In order to formally distinguish the quadrilateral mapping from the triangular one, \hat{x} and \hat{y} will be here redefined as ξ and η . For triangle transfinite interpolation they rather assume the name of r and s .

Only the element edges will be used as lattice flow lines and the resulting univariate Lagrangian blending functions are linear ([100])

$$\phi_0^\xi(\xi) = \frac{1-\xi}{2}, \quad \phi_0^\eta(\eta) = \frac{1-\eta}{2} \quad (\text{A.10a})$$

$$\phi_1^\xi(\xi) = \frac{1+\xi}{2}, \quad \phi_1^\eta(\eta) = \frac{1+\eta}{2}. \quad (\text{A.10b})$$

The bivariate projection operator can be then expressed as

$$\mathcal{P}^\xi[\mathbf{F}] = \frac{1-\xi}{2} \mathbf{F}(-1, \eta) + \frac{1+\xi}{2} \mathbf{F}(1, \eta) \quad (\text{A.11a})$$

$$\mathcal{P}^\eta[\mathbf{F}] = \frac{1-\eta}{2} \mathbf{F}(\xi, -1) + \frac{1+\eta}{2} \mathbf{F}(\xi, 1). \quad (\text{A.11b})$$

Combining this two projectors with a Boolean sum, the required lattice generator results

$$\begin{aligned}
\mathcal{T}_{Quad} = \mathcal{P}^\xi \oplus \mathcal{P}^\eta[\mathbf{F}] &= \frac{1-\eta}{2} \mathbf{F}(\xi, -1) + \frac{1+\eta}{2} \mathbf{F}(\xi, 1) + \\
&\quad \frac{1-\xi}{2} \mathbf{F}(-1, \eta) + \frac{1+\xi}{2} \mathbf{F}(1, \eta) - \\
&\quad \frac{1-\xi}{2} \frac{1-\eta}{2} \mathbf{F}(-1, -1) - \frac{1-\xi}{2} \frac{1+\eta}{2} \mathbf{F}(-1, 1) - \\
&\quad \frac{1+\xi}{2} \frac{1-\eta}{2} \mathbf{F}(1, -1) - \frac{1+\xi}{2} \frac{1+\eta}{2} \mathbf{F}(1, 1), \tag{A.12a}
\end{aligned}$$

where, referring to fig. A.3, for the edge parametrizations it yields

$$\mathbf{F}(\xi, 1) : \hat{\Gamma}_1 \rightarrow \Gamma_1, \quad \mathbf{F}(-1, \eta) : \hat{\Gamma}_2 \rightarrow \Gamma_2 \tag{A.13a}$$

$$\mathbf{F}(\xi, -1) : \hat{\Gamma}_3 \rightarrow \Gamma_3, \quad \mathbf{F}(1, \eta) : \hat{\Gamma}_4 \rightarrow \Gamma_4 \tag{A.13b}$$

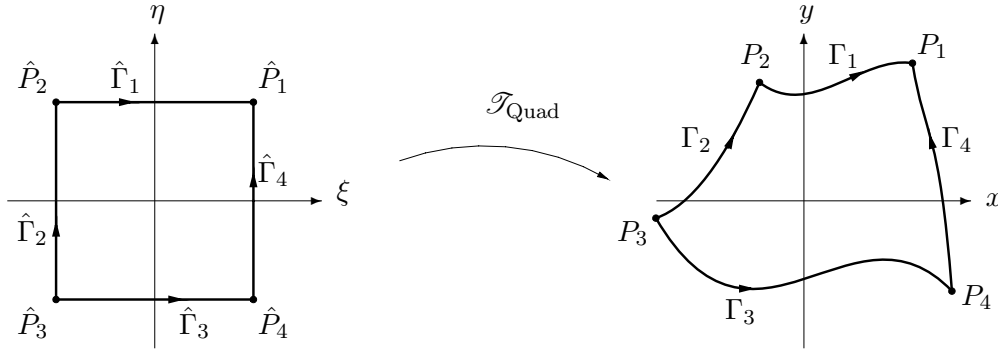


Figure A.3.: Prototypical quad mapped into a generically shaped one.

A.3.3. Triangular Mapping

As done for quadrilaterals, also in triangular mappings it is considered a set of univariate linear Lagrangian blending functions, but the edges parametrization is implemented from an unitary one-dimensional domain. This choice results from convenience in using affine coordinates instead than r and s

$$u_1 = -\frac{r+s}{2}, \quad u_2 = \frac{r+1}{2}, \quad u_3 = \frac{s+1}{2}. \tag{A.14}$$

Moreover, it is formally more compact and expressive to switch from the usage of the graph of a bivariate vector-valued function to three univariate functions verifying the compatibility conditions and parametrizing the triangle edges. Referring to fig. A.4, it yields

$$\mathbf{F}(r, -1) \longleftrightarrow \mathbf{E}_1(u) : \hat{\Lambda}_1 \rightarrow \Lambda_1 \tag{A.15a}$$

$$\mathbf{F}(r, -r) \longleftrightarrow \mathbf{E}_2(u) : \hat{\Lambda}_2 \rightarrow \Lambda_2 \tag{A.15b}$$

$$\mathbf{F}(-1, s) \longleftrightarrow \mathbf{E}_3(u) : \hat{\Lambda}_3 \rightarrow \Lambda_3, \tag{A.15c}$$

where u lives in $[0, 1]$. The triangular transfinite interpolation results

$$\begin{aligned}
\mathcal{T}_{Tri} &= u_1 [\mathbf{E}_1(u_2) + \mathbf{E}_3(1 - u_3) - \mathbf{E}_3(1)] + \\
&\quad u_2 [\mathbf{E}_2(u_3) + \mathbf{E}_1(1 - u_1) - \mathbf{E}_1(1)] + \\
&\quad u_3 [\mathbf{E}_3(u_1) + \mathbf{E}_2(1 - u_2) - \mathbf{E}_2(1)]. \tag{A.16a}
\end{aligned}$$

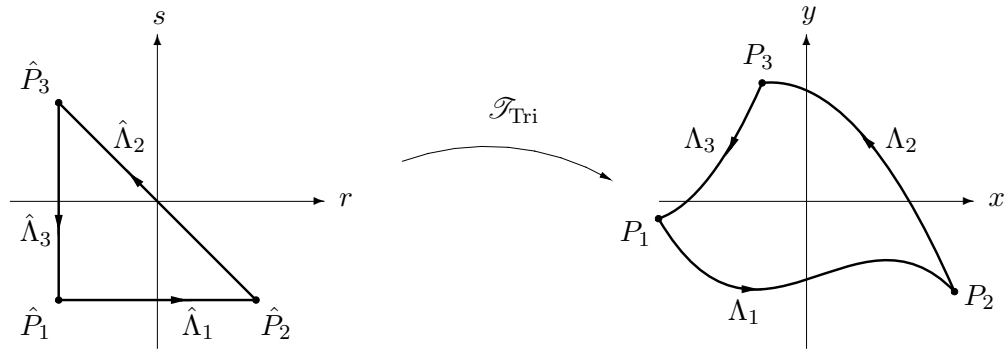


Figure A.4.: Prototypical triangle mapped into a generically shaped one.

A.3.4. 2-D Mapping Benchmarks

In order to test the correct implementation of the two-dimensional transfinite interpolations for quads and triangles, one can solve a PDE on the transformed domain and verify the expected spectral convergence.

The equations in the mapped domain are written introducing the Jacobian of the transformation. Because of its relevance in the discretization algorithm presented in Chapter 3, a Poisson's problem is chosen as benchmark and Dirichlet boundary conditions are here applied. Owing to the curved geometry, an over-integration technique is adopted in order to reduce aliasing errors (see e.g. [123]). The following problem is solved

$$\nabla^2 f = -2\pi^2 \sin(\pi x) \sin(\pi y) \quad (\text{A.17})$$

whose solution is $f_{\text{exact}} = \sin(\pi x) \sin(\pi y)$. The discretization error is here defined as $\epsilon = f_{\text{DG}} - f_{\text{exact}}$ where f_{DG} is the discrete solution obtained applying DG-FEM with one element only and the interior penalty method is employed for setting the boundary conditions.

As depicted in fig.s A.5 and A.6, both the mappings are correctly preserving the spectral convergence of DG-FEM methods, so one can conclude that the transfinite interpolations are not only properly implemented, but also a suitable choice for the selected h/p -method. However one should keep in mind that very distorted domains decrease the convergence rate because of a strong influence of the mapping Jacobian. This suggests that a suitable meshing strategy could be to prefer smooth transformations, even if this would mean smaller and more numerous elements.

A.4. 3-D Transfinite Lagrange Interpolation

As done for the two-dimensional case, one can extend the presented graph of the vector-valued function to three-dimensions

$$\mathbf{F}(\hat{x}, \hat{y}, \hat{z}) = \begin{bmatrix} F_1(\hat{x}, \hat{y}, \hat{z}) \\ F_2(\hat{x}, \hat{y}, \hat{z}) \\ \vdots \\ F_n(\hat{x}, \hat{y}, \hat{z}) \end{bmatrix}. \quad (\text{A.18})$$

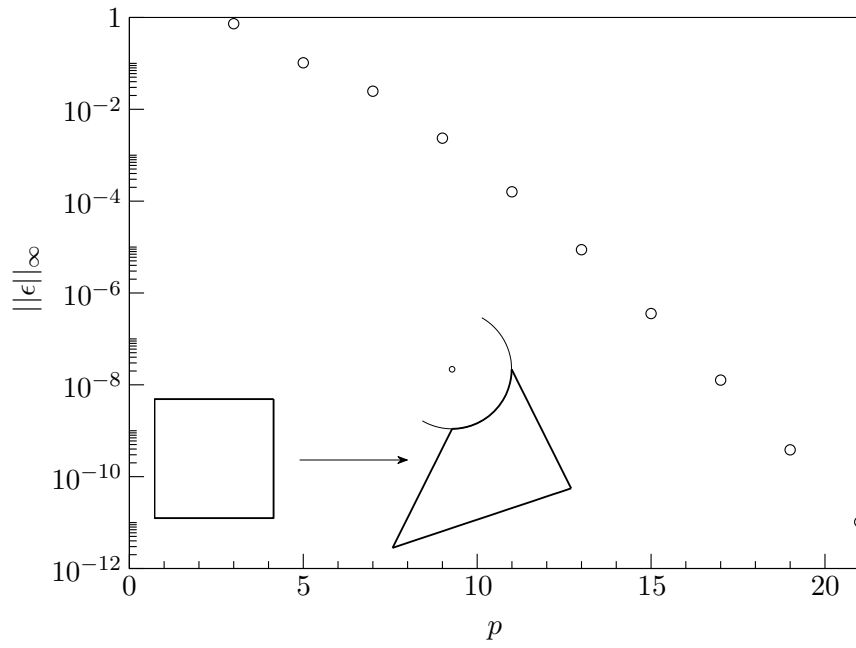


Figure A.5.: Convergence of the infinite-norm of the numerical error committed in solving an infinitely smooth Poisson problem over a mapped quadrilateral domain. The corresponding single-element DG-FEM discretization has a functional space of order p .

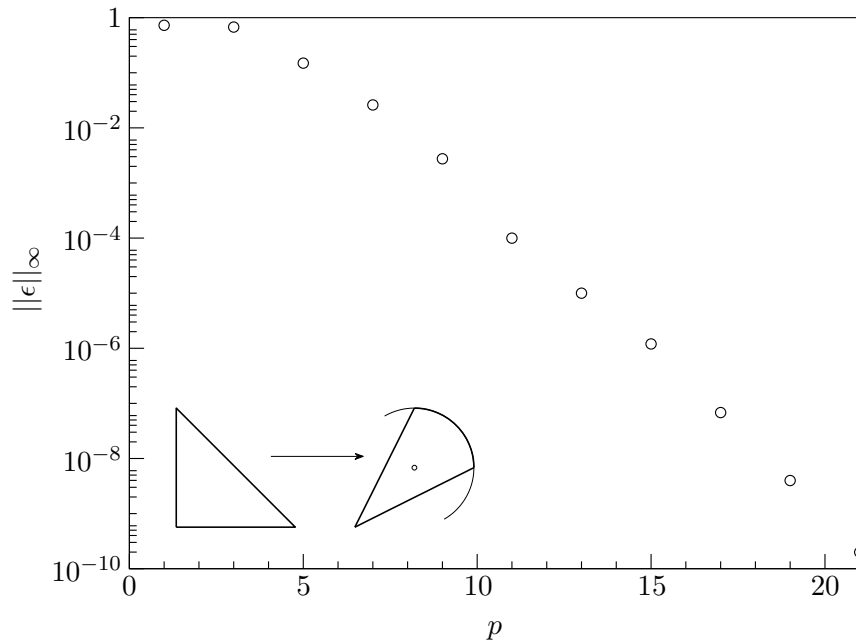


Figure A.6.: Convergence of the infinite-norm of the numerical error committed in solving an infinitely smooth Poisson problem over a mapped triangular domain. The corresponding DG-FEM discretization has a functional space of order p .

From eq. A.18 results that $\mathbf{F}(\hat{x}, \hat{y}, \hat{z})$ maps \mathbb{R}^3 regions into Euclidean n -space, E^n

$$\mathbf{F} : \mathbb{R}^3 \rightarrow E^n. \tag{A.19}$$

In the following subsections the transfinite interpolation will be restricted to three-dimensional mappings ($n = 3$). Two-dimensional transfinite Lagrange interpolations can be employed to build the 3-D ones.

A.4.1. Edge Parametrization

The following subsections extend the edge parametrization in three-dimensions.

Linear Edge: Cartesian Coordinates

$$\mathcal{T}_{edge}(u) = \begin{pmatrix} x_a \\ y_a \\ z_a \end{pmatrix} + u \begin{pmatrix} x_b - x_a \\ y_b - y_a \\ z_b - z_a \end{pmatrix} \quad (\text{A.20a})$$

$$\mathcal{T}_{edge}(\gamma) = \begin{pmatrix} x_a \\ y_a \\ z_a \end{pmatrix} + \frac{\gamma + 1}{2} \begin{pmatrix} x_b - x_a \\ y_b - y_a \\ z_b - z_a \end{pmatrix} \quad (\text{A.20b})$$

Cylindrical Edge: Cylindrical Coordinates

$$\mathcal{T}_{edge}(u) = \begin{pmatrix} x_c \\ y_c \\ z_a \end{pmatrix} + \begin{pmatrix} R \cos[\phi_a + u(\phi_b - \phi_a)] \\ R \sin[\phi_a + u(\phi_b - \phi_a)] \\ u(z_b - z_a) \end{pmatrix} \quad (\text{A.21a})$$

$$\mathcal{T}_{edge}(\gamma) = \begin{pmatrix} x_c \\ y_c \\ z_a \end{pmatrix} + \begin{pmatrix} R \cos[\phi_a + (\gamma + 1)(\phi_b - \phi_a)/2] \\ R \sin[\phi_a + (\gamma + 1)(\phi_b - \phi_a)/2] \\ (\gamma + 1)(z_b - z_a)/2 \end{pmatrix} \quad (\text{A.21b})$$

Spherical Edge: Spherical Coordinates

$$\mathcal{T}_{edge}(u) = \begin{pmatrix} x_c \\ y_c \\ z_c \end{pmatrix} + R \begin{pmatrix} \cos[\phi_a + u(\phi_b - \phi_a)] \sin[\theta_a + u(\theta_b - \theta_a)] \\ \sin[\phi_a + u(\phi_b - \phi_a)] \sin[\theta_a + u(\theta_b - \theta_a)] \\ \cos[\theta_a + u(\theta_b - \theta_a)] \end{pmatrix} \quad (\text{A.22a})$$

$$\mathcal{T}_{edge}(\gamma) = \begin{pmatrix} x_c \\ y_c \\ z_c \end{pmatrix} + R \begin{pmatrix} \cos[\phi_a + (\gamma + 1)(\phi_b - \phi_a)/2] \sin[\theta_a + (\gamma + 1)(\theta_b - \theta_a)/2] \\ \sin[\phi_a + (\gamma + 1)(\phi_b - \phi_a)/2] \sin[\theta_a + (\gamma + 1)(\theta_b - \theta_a)/2] \\ \cos[\theta_a + (\gamma + 1)(\theta_b - \theta_a)/2] \end{pmatrix} \quad (\text{A.22b})$$

A.4.2. Hexahedral Mapping

As done for quadrilateral mappings, the chosen univariate Lagrangian blending functions are linear

$$\phi_0^\xi(\xi) = \frac{1 - \xi}{2}, \quad \phi_0^\eta(\eta) = \frac{1 - \eta}{2}, \quad \phi_0^\zeta(\zeta) = \frac{1 - \zeta}{2} \quad (\text{A.23a})$$

$$\phi_1^\xi(\xi) = \frac{1 + \xi}{2}, \quad \phi_1^\eta(\eta) = \frac{1 + \eta}{2}, \quad \phi_1^\zeta(\zeta) = \frac{1 + \zeta}{2}. \quad (\text{A.23b})$$

The trivariate projection operator can be then expressed as

$$\mathcal{P}^\xi[\mathbf{F}] = \frac{1-\xi}{2} \mathbf{F}(-1, \eta, \zeta) + \frac{1+\xi}{2} \mathbf{F}(1, \eta, \zeta) \quad (\text{A.24a})$$

$$\mathcal{P}^\eta[\mathbf{F}] = \frac{1-\eta}{2} \mathbf{F}(\xi, -1, \zeta) + \frac{1+\eta}{2} \mathbf{F}(\xi, 1, \zeta) \quad (\text{A.24b})$$

$$\mathcal{P}^\zeta[\mathbf{F}] = \frac{1-\zeta}{2} \mathbf{F}(\xi, \eta, -1) + \frac{1+\zeta}{2} \mathbf{F}(\xi, \eta, 1). \quad (\text{A.24c})$$

The lattice generator is obtained combining this three projectors via a Boolean sum

$$\begin{aligned} \mathcal{I}_{Hex} = \mathcal{P}^\xi \oplus \mathcal{P}^\eta \oplus \mathcal{P}^\zeta[\mathbf{F}] &= \frac{1-\xi}{2} \mathbf{F}(-1, \eta, \zeta) + \frac{1+\xi}{2} \mathbf{F}(1, \eta, \zeta) + \\ &\frac{1-\eta}{2} \mathbf{F}(\xi, -1, \zeta) + \frac{1+\eta}{2} \mathbf{F}(\xi, 1, \zeta) + \\ &\frac{1-\zeta}{2} \mathbf{F}(\xi, \eta, -1) + \frac{1+\zeta}{2} \mathbf{F}(\xi, \eta, 1) - \\ &\frac{1-\xi}{2} \frac{1-\zeta}{2} \mathbf{F}(-1, \eta, -1) - \frac{1-\xi}{2} \frac{1+\zeta}{2} \mathbf{F}(-1, \eta, 1) - \\ &\frac{1+\xi}{2} \frac{1-\zeta}{2} \mathbf{F}(1, \eta, -1) - \frac{1+\xi}{2} \frac{1+\zeta}{2} \mathbf{F}(1, \eta, 1) - \\ &\frac{1-\xi}{2} \frac{1-\eta}{2} \mathbf{F}(-1, -1, \zeta) - \frac{1-\xi}{2} \frac{1+\eta}{2} \mathbf{F}(-1, 1, \zeta) - \\ &\frac{1+\xi}{2} \frac{1-\eta}{2} \mathbf{F}(1, -1, \zeta) - \frac{1+\xi}{2} \frac{1+\eta}{2} \mathbf{F}(1, 1, \zeta) - \\ &\frac{1-\eta}{2} \frac{1-\zeta}{2} \mathbf{F}(\xi, -1, -1) - \frac{1-\eta}{2} \frac{1+\zeta}{2} \mathbf{F}(\xi, -1, 1) - \\ &\frac{1+\eta}{2} \frac{1-\zeta}{2} \mathbf{F}(\xi, 1, -1) - \frac{1+\eta}{2} \frac{1+\zeta}{2} \mathbf{F}(\xi, 1, 1) - \\ &\frac{1-\xi}{2} \frac{1-\eta}{2} \frac{1-\zeta}{2} \mathbf{F}(-1, -1, -1) + \\ &\frac{1+\xi}{2} \frac{1-\eta}{2} \frac{1-\zeta}{2} \mathbf{F}(1, -1, -1) + \\ &\frac{1+\xi}{2} \frac{1+\eta}{2} \frac{1-\zeta}{2} \mathbf{F}(1, 1, -1) + \\ &\frac{1-\xi}{2} \frac{1+\eta}{2} \frac{1-\zeta}{2} \mathbf{F}(-1, 1, -1) + \\ &\frac{1-\xi}{2} \frac{1-\eta}{2} \frac{1+\zeta}{2} \mathbf{F}(-1, -1, 1) + \\ &\frac{1+\xi}{2} \frac{1-\eta}{2} \frac{1+\zeta}{2} \mathbf{F}(1, -1, 1) + \\ &\frac{1+\xi}{2} \frac{1+\eta}{2} \frac{1+\zeta}{2} \mathbf{F}(1, 1, 1) + \\ &\frac{1-\xi}{2} \frac{1+\eta}{2} \frac{1+\zeta}{2} \mathbf{F}(-1, 1, 1), \end{aligned} \quad (\text{A.25})$$

where, referring to fig. A.7, the face parametrization reads

$$\mathbf{F}(-1, \eta, \zeta) : \hat{\Sigma}_1 \rightarrow \Sigma_1 \quad (\text{A.26a})$$

$$\mathbf{F}(1, \eta, \zeta) : \hat{\Sigma}_2 \rightarrow \Sigma_2 \quad (\text{A.26b})$$

$$\mathbf{F}(\xi, -1, \zeta) : \hat{\Sigma}_3 \rightarrow \Sigma_3 \quad (\text{A.26c})$$

$$\mathbf{F}(1, \eta, \zeta) : \hat{\Sigma}_4 \rightarrow \Sigma_4 \quad (\text{A.26d})$$

$$\mathbf{F}(\xi, \eta, -1) : \hat{\Sigma}_5 \rightarrow \Sigma_5 \quad (\text{A.26e})$$

$$\mathbf{F}(\xi, \eta, 1) : \hat{\Sigma}_6 \rightarrow \Sigma_6. \quad (\text{A.26f})$$

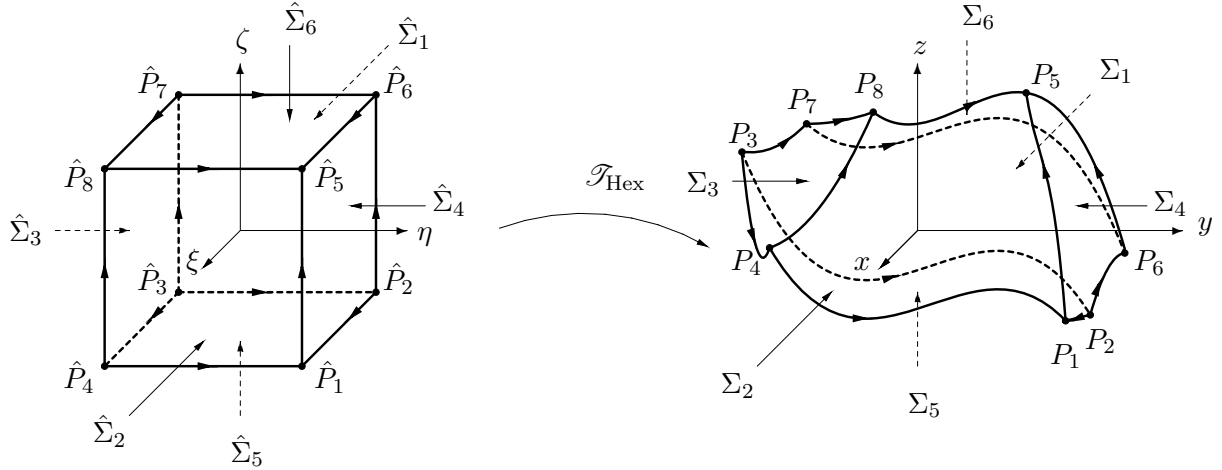


Figure A.7.: Prototypical hexahedron mapped into a generically shaped one.

A.4.3. Tetrahedral Mapping

In order to extend the triangular mapping into the tetrahedral one, the first step is to complete the set of affine coordinates in terms of r , s and t , adapting them to the three-dimensional prototypical element:

$$u_1 = -\frac{r+s+t+1}{2}, \quad u_2 = \frac{r+1}{2}, \quad u_3 = \frac{s+1}{2}, \quad u_4 = \frac{t+1}{2}. \quad (\text{A.27})$$

Referring to fig. A.8, for the parametrization of edges and faces, it yields

$$\begin{aligned} \mathbf{F}(r, -1, -1) &\longleftrightarrow \mathbf{E}_1(u) : \hat{P}_1\hat{P}_2 \rightarrow P_1P_2 \\ \mathbf{F}(r, -r, -1) &\longleftrightarrow \mathbf{E}_2(u) : \hat{P}_2\hat{P}_3 \rightarrow P_2P_3 \\ \mathbf{F}(-1, s, -1) &\longleftrightarrow \mathbf{E}_3(u) : \hat{P}_3\hat{P}_1 \rightarrow P_3P_1 \\ \mathbf{F}(-1, -1, t) &\longleftrightarrow \mathbf{E}_4(u) : \hat{P}_1\hat{P}_4 \rightarrow P_1P_4 \\ \mathbf{F}(r, -1, -r) &\longleftrightarrow \mathbf{E}_5(u) : \hat{P}_2\hat{P}_4 \rightarrow P_2P_4 \\ \mathbf{F}(-1, s, -s) &\longleftrightarrow \mathbf{E}_6(u) : \hat{P}_3\hat{P}_4 \rightarrow P_3P_4 \\ \mathbf{F}(r, s, -1) &\longleftrightarrow \mathbf{S}_1(u_1, u_2, u_3) : \hat{\Xi}_1 \rightarrow \Xi_1 \\ \mathbf{F}(r, -1, t) &\longleftrightarrow \mathbf{S}_2(u_1, u_2, u_4) : \hat{\Xi}_2 \rightarrow \Xi_2 \\ \mathbf{F}(r, s, -r-s-1) &\longleftrightarrow \mathbf{S}_3(u_2, u_3, u_4) : \hat{\Xi}_3 \rightarrow \Xi_3 \\ \mathbf{F}(-1, s, t) &\longleftrightarrow \mathbf{S}_4(u_1, u_3, u_4) : \hat{\Xi}_4 \rightarrow \Xi_4, \end{aligned} \quad (\text{A.28})$$

where u lives in $[0, 1]$.

Recalling [286], the tetrahedral transfinite interpolation can be written combining vertices, edges and faces contribution to the mapping. In [286] it is also suggested to use affine coordinates differences instead of implementing the parametrization directly in terms of u_i . In such a way the resulting interpolation is better conditioned and more robust

$$\begin{aligned}
\mathcal{T}_{Tetra} &= \mathcal{T}_{Vert} + \mathcal{T}_{Edges} + \mathcal{T}_{Faces} \\
\mathcal{T}_{Vert} &= u_1 \mathbf{F}(-1, -1, -1) + u_2 \mathbf{F}(1, -1, -1) + \\
&\quad u_3 \mathbf{F}(-1, 1, -1) + u_4 \mathbf{F}(-1, -1, 1) \\
\mathcal{T}_{Edges} &= \sum_{i=1}^6 \mathbf{E}_i^{int}(u_B - u_A) u_A u_B \\
\mathbf{E}_i^{int}(u) &= \begin{cases} \frac{4\mathbf{E}_i^0(u)}{(1-u)(1+u)} & \text{if } u \neq \pm 1 \\ 0 & \text{if } u = \pm 1 \end{cases} \\
\mathbf{E}_i^0(u) &= \mathbf{E}_i(u) - \frac{1-u}{2} \mathbf{E}_i(-1) - \frac{1+u}{2} \mathbf{E}_i(+1) \\
\mathcal{T}_{Faces} &= \sum_{i=1}^4 \mathbf{S}_i^{int}(u_B - u_A, u_C - u_A) u_A u_B u_C \\
\mathbf{S}_i^{int}(\mathbf{u}) &= \begin{cases} \frac{\mathbf{S}_i^0(\mathbf{u})}{u_A u_B u_C|_{S_i}} & \text{if } \mathbf{u} \notin \partial \mathbf{S}_i \\ 0 & \text{if } \mathbf{u} \in \partial \mathbf{S}_i \end{cases} \\
\mathbf{S}_i^0(\mathbf{u}) &= \mathbf{S}_i(\mathbf{u}) - \mathcal{T}_{Edges}|_{S_i}(\mathbf{u}) - \mathcal{T}_{Vert}|_{S_i}(\mathbf{u}), \tag{A.29}
\end{aligned}$$

where u_A , u_B and u_C are such that $u_A(\hat{P}_A) = u_B(\hat{P}_B) = u_C(\hat{P}_C)$ and $(\hat{P}_B - \hat{P}_A) \times (\hat{P}_C - \hat{P}_A)$ points out of the prototypical tetrahedron.

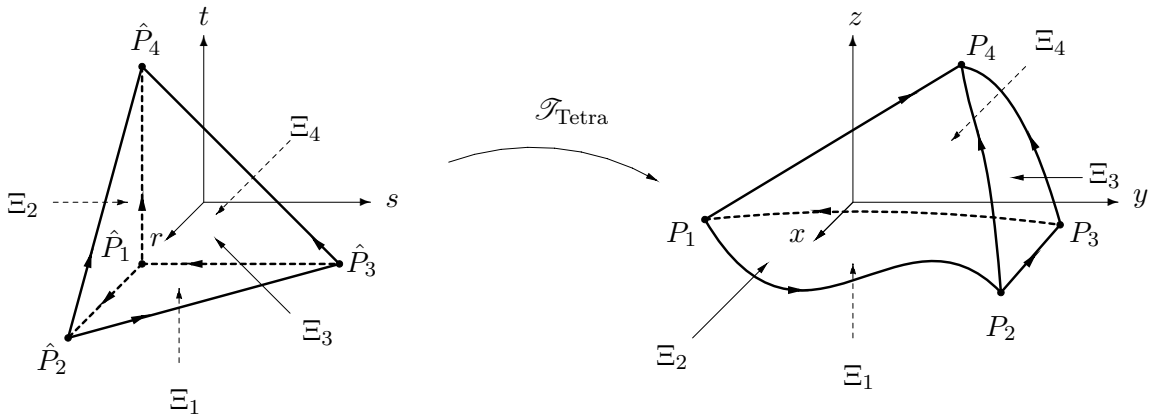


Figure A.8.: Prototypical tetrahedron mapped into a generically shaped one.

A.4.4. 3-D mapping benchmarks

For testing purpose a Poisson's problem is solved on transfinately mapped domains for both, an hexahedron and a tetrahedron. Dirichlet's boundary conditions are applied and an over-

integration technique is used for reducing aliasing issues. The Poisson problem to solve reads

$$\nabla^2 f = -3\pi^2 \sin(\pi x) \sin(\pi y) \sin(\pi z) \quad (\text{A.30})$$

whose solution is $f_{\text{exact}} = \sin(\pi x) \sin(\pi y) \sin(\pi z)$. The same definition applied for two-dimensional benchmarks is here employed for computing the discretization error and the DG-FEM solver considers one element only and the interior penalty method is employed for setting the boundary conditions.

As depicted in fig.s [A.9](#) and [A.10](#), the three-dimensional transfinite mappings are correctly implemented and exhibits the expected spectral convergence.

A.5. Distribution of Nodes

In order to conclude the description of the methodology, a short mention about node distribution is given. The choice adopted for the current investigation is discussed and for more extensive details about polynomial basis functions commonly used in literature we refer the reader to [\[123, 36, 138\]](#).

In the following, we consider prototypical or reference discretization domains, onto which to map the physical elements the computational mesh consists of. In [fig. A.11](#) a 2-D example is shown for triangular elements.

Referring to [\[139\]](#), similar constructions of polynomial basis can be used for 2- and 3-D cases for both, simplices (segments, triangles and tetrahedra) and tensorized domains (quadrilaterals and hexahedra). An accurate choice of the point sets for interpolation and quadrature assumes different node distribution among the various prototypical domains. In the following, an integration-based discontinuous Galerkin method is implemented, employing the nodal approach. Therefore nodal bases are used to determine the approximate solution as projection into nodal subspaces.

We distinguish hereafter between two sorts of point sets: quadrature and interpolation nodes. In both cases Legendre polynomials are employed, see e.g. [\[36\]](#) for more details about them.

A.5.1. Quadrature Nodes

Referring to [\[36\]](#), we recall the one-dimensional quadrature formulae, an extension of which is basically used for both, simplices and tensorized domains. For the Gaussian quadrature formulae, whose nodes are all in the interior of the reference domain, it holds

Let $x_0 < x_1 < \dots < x_N$ be the roots of the $(N + 1)$ -th orthogonal polynomial p_{N+1} , and let w_0, \dots, w_N be the solution of the linear system

$$\sum_{j=0}^N (x_j)^k w_j = \int_{-1}^1 x^k w(x) dx, \quad 0 \leq k \leq N. \quad (\text{A.31})$$

Then the weights $w_j > 0$ for $j = 0, \dots, N$ and

$$\sum_{j=0}^N p(x_j) w_j = \int_{-1}^1 p(x) w(x) dx \quad \forall p \in \mathbb{P}_{2N+1}(-1, 1), \quad (\text{A.32})$$

and it is not possible to find $x_j, w_j, j = 0, \dots, N$ such that [\(A.32\)](#) holds for all polynomials $p \in \mathbb{P}_{2N+2}$.

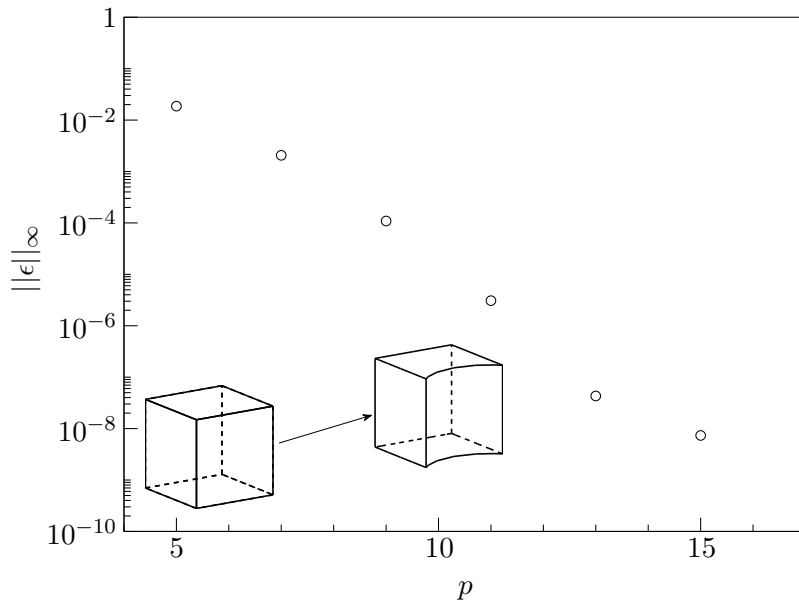


Figure A.9.: Convergence of the infinite-norm of the numerical error committed in solving an infinitely smooth Poisson problem over a mapped hexahedral domain. The corresponding single-element DG-FEM discretization has order p .

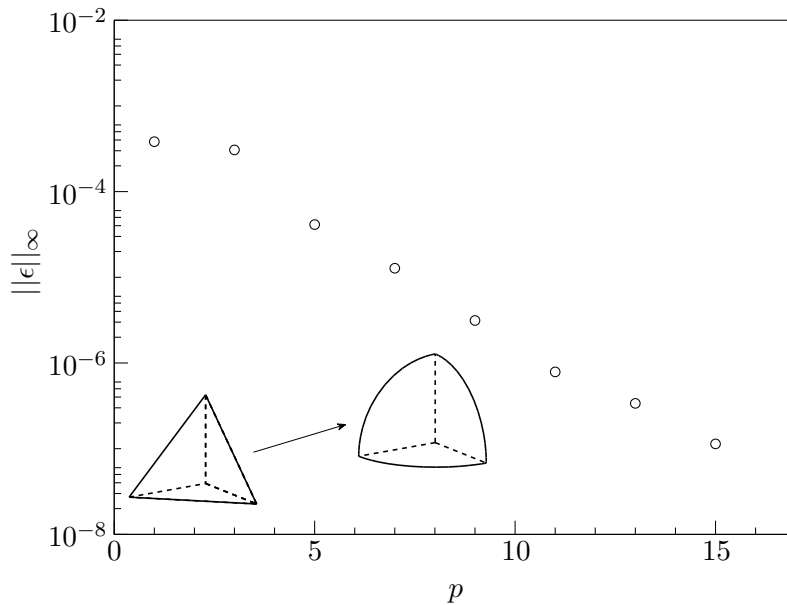


Figure A.10.: Convergence of the infinite-norm of the numerical error committed in solving an infinitely smooth Poisson problem over a mapped tetrahedral domain. The corresponding single-element DG-FEM discretization has order p .

When one of the quadrature nodes coincides with an extreme point of the domain, the Gaussian reduce to Gaussian–Radau quadrature formulae

Let $-1 = x_0 < x_1 < \dots < x_N$ be the $(N+1)$ roots of the polynomial $q(x) = p_{N+1}(x) + ap_N(x)$,

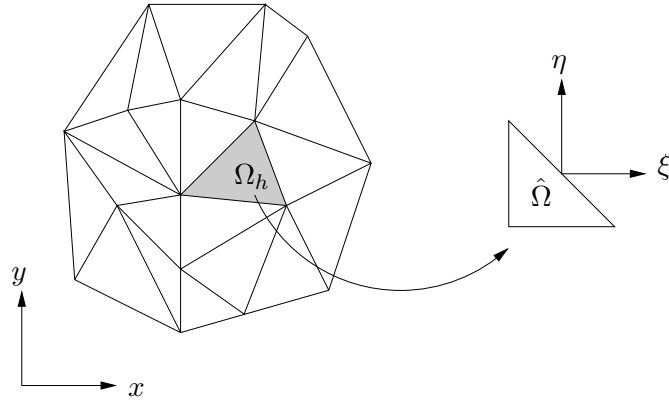


Figure A.11.: Example of element mapping from the physical (Ω_h) to the prototypical domain ($\hat{\Omega}$).

with $a = -p_{N+1}(-1)/p_N(-1)$, and let w_0, \dots, w_N be the solution of the linear system

$$\sum_{j=0}^N (x_j)^k w_j = \int_{-1}^1 x^k w(x) dx, \quad 0 \leq k \leq N. \quad (\text{A.33})$$

Then

$$\sum_{j=0}^N p(x_j) w_j = \int_{-1}^1 p(x) w(x) dx \quad \forall p \in \mathbb{P}_{2N}(-1, 1), \quad (\text{A.34})$$

and it is not possible to find $x_j, w_j, j = 0, \dots, N$ such that (A.34) holds for all polynomials $p \in \mathbb{P}_{2N+1}$.

Finally, if the nodes include both the extreme points of the domain, the Gaussian–Radau reduce to Gaussian–Lobatto quadrature formulae

Let $-1 = x_0 < x_1 < \dots < x_N = 1$ be the $(N + 1)$ roots of the polynomial $q(x) = p_{N+1}(x) + ap_N(x) + bp_{N-1}(x)$, with a and b such that $q(-1) = q(1) = 0$, and let w_0, \dots, w_N be the solution of the linear system

$$\sum_{j=0}^N (x_j)^k w_j = \int_{-1}^1 x^k w(x) dx, \quad 0 \leq k \leq N. \quad (\text{A.35})$$

Then

$$\sum_{j=0}^N p(x_j) w_j = \int_{-1}^1 p(x) w(x) dx \quad \forall p \in \mathbb{P}_{2N-1}(-1, 1), \quad (\text{A.36})$$

and it is not possible to find $x_j, w_j, j = 0, \dots, N$ such that (A.36) holds for all polynomials $p \in \mathbb{P}_{2N}$.

Based on the previous formulae, a generalized version for quadrangles and hexahedra can be obtained via tensor product (see e.g. [38, 138]). In the case of simplices, the latter extension is not so straightforward, but it can be obtained transforming the quadrature formulae of quadrangles and hexahedra via a so-called *collapsing coordinate* technique⁴ (see [138]).

⁴The usage of collapsing coordinate systems only allows generalizations of quadrature formulae that do not place nodes along the edge to be collapsed. This implies that Gauss–Lobatto integration rules cannot be extended via this technique.

Considering the 2-D case, if we refer to quadrilateral and triangular prototypical domains as \mathcal{Q}^2 and \mathcal{T}^2 respectively, it yields

$$\mathcal{Q}^2 = \{(\xi, \eta) : -1 \leq \xi, \eta \leq 1\} \quad (\text{A.37a})$$

$$\mathcal{T}^2 = \{(\xi, \eta) : -1 \leq \xi, \eta; \xi + \eta \leq 0\}. \quad (\text{A.37b})$$

The collapsed coordinate system consists in defining a transformation between the two regions that maps an edge of the quadrangles into a vertex of the triangle and viceversa, as depicted in Fig. A.12

$$\mathcal{Q}^2 \rightarrow \mathcal{T}^2, (x, y) \mapsto (\xi, \eta) = \left(\frac{(1+x)(1-y)}{2} - 1, y \right) \quad (\text{A.38a})$$

$$\mathcal{T}^2 \rightarrow \mathcal{Q}^2, (\xi, \eta) \mapsto (x, y) = \left(2\frac{1+\xi}{1-\eta} - 1, \eta \right) \quad (\text{A.38b})$$

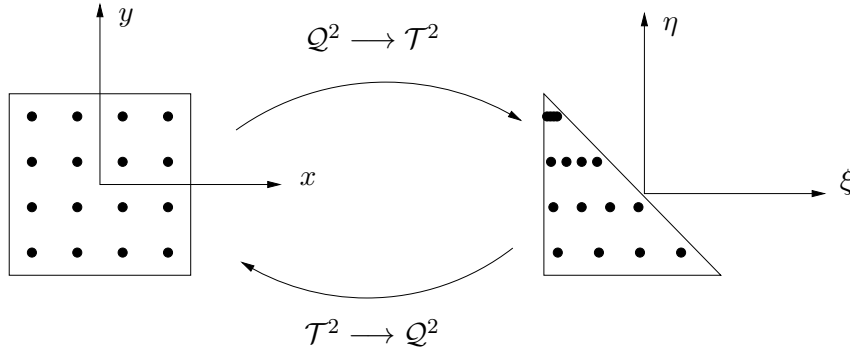


Figure A.12.: 2-D collapsed quadrilateral using a Duffy transformation.

The same technique can be used for 3-D cases, and to transform from a hexahedron to a tetrahedron, three successive collapses are employed. For details see [138]. In order to reduce aliasing errors, an over-integration technique is adopted for the quadrature formulae and both, general integration and lookup tables, are employed for implementing the cubature rules.

A.5.2. Interpolation Nodes

Aside from quadrature, the interpolation point sets have still to be defined. Because a nodal approach is followed for implementing the present discontinuous Galerkin solver, they will be used to generate the Lagrange basis on which to interpolate.

First of all the number of nodes per reference element, N_{tot} , has to be defined. Therefore, N being the number of nodes per edge, and d the dimensions of the prototypical domain, it holds

$$N_{\text{tot}} = \begin{cases} (N+1)^d - 1 & , \text{ for } \mathcal{Q}^d, \quad d = 1, 2, 3 \\ \binom{N+d}{N} - 1 & , \text{ for } \mathcal{T}^d, \quad d = 2, 3. \end{cases} \quad (\text{A.39})$$

The choice among different interpolation node sets for the associated Lagrangian basis passes through the study of the relative Lebesgue constant and, in particular, of its growth as function

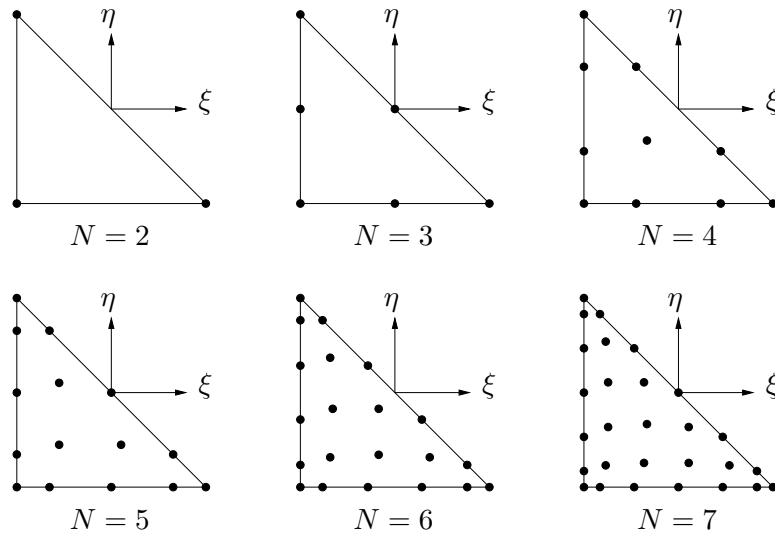


Figure A.13.: Warpblend nodes for $N = 2$ (top-left) to $N = 7$ (bottom-right).

of the interpolation order. Good rule is then to consider point sets whose Lebesgue constant does not increase so rapidly with the number of interpolation nodes and some reference studies about it can be found in [36] and [139].

In the case of tensorized domains, Gaussian points are commonly used to generate the Lagrange basis. On the other hand, there is no correspondent for simplices and many different distributions have been investigated, e.g. electrostatic [122], Fekete [271], Heinrichs [116] and warpblend [295] points.

A comparison among them can be found in [217], where the Lebesgue constant trends are investigated with respect to the number of nodes. From this data it results that Warpblend and Fekete points well behave increasing N_{tot} , therefore, owing to their explicit construction in both 2-D and 3-D cases, the *warp and blend* procedure is adopted for obtaining the interpolation point sets⁵.

The Warpblend class of nodes transforms the equidistributed points, very ill-conditioned for Galerkin methods, into a more robust distribution matching the Gauss-Lobatto points along the edges of the simplicial reference domain. In fig. A.13 the chosen interpolation nodes are depicted for various N over the two-dimensional reference domain. However, for more details, the reader is referred to [295].

⁵Fekete nodes are not available in 3-D.

B. Numerical Solver: Benchmarks

A collection of benchmarks for testing the numerical solver is here presented. At first the spatial and temporal discretization schemes applied to a single-phase flow will be validated.

Then the verification is extended to particle-laden flows with mechanical coupling only and finally we will test the numerical solver developed during the present thesis work including particle–particle interactions and thermal coupling.

B.1. Fluid Flow Benchmarks

In this section four typically used benchmarks are considered in order to validate our incompressible Navier–Stokes DG-FEM solver. The only fluid flow part of the algorithm is here tested, which correspond to Section 3.3.

At the beginning the h - and p -convergence rates are tested for an infinitely smooth solution of the Navier–Stokes system; the Taylor–Green flow solution is herein selected.

The second benchmark considers the von Kármán street generated by a cylinder with circular cross section and it is intended to test the body-fitted elements presented in the previous Appendix section for a more challenging flow structure.

Finally, because the main focus of this study is about closed flows, the lid- and thermocapillary-driven cavity benchmarks are selected for being presented hereunder.

B.1.1. Taylor–Green vortex

The Taylor–Green flow is an infinitely smooth solution of the Navier–Stokes system, therefore it can be used for testing h - and p -convergence of the discontinuous Galerkin finite element code in a rigorous manner. The exact solution which represents the Taylor–Green vortex is

$$u = -\cos(\pi x) \sin(\pi y) \exp(-2\nu\pi^2 t) \quad (\text{B.1a})$$

$$v = +\sin(\pi x) \cos(\pi y) \exp(-2\nu\pi^2 t) \quad (\text{B.1b})$$

$$p = -0.25 [\cos(2\pi x) + \cos(2\pi y)] \exp(-4\nu\pi^2 t). \quad (\text{B.1c})$$

Equations (2.16) are discretized on a square prototypical domain employing a kinematic viscosity $\nu = \text{Re}^{-1} = 10^{-2}$. The exact solution of eq. (2.16) is depicted in fig. B.1.

Dirichlet boundary conditions are enforced on the velocity field along the left and right boundaries, whereas Neumann conditions are adopted for pressure. On top and bottom boundaries Dirichlet conditions are employed for the pressure field and Neumann boundary conditions are enforced on velocity.

In order to test the h - and p -convergence, a sufficiently small Δt is chosen such that it does not induce convergence saturation and the relative error

$$\varepsilon_f = \frac{\|f_{\text{DG}} - f_{\text{exact}}\|_{\infty}}{\|f_{\text{exact}}\|_{\infty}} \quad (\text{B.2})$$

is tested at $t = 1$.

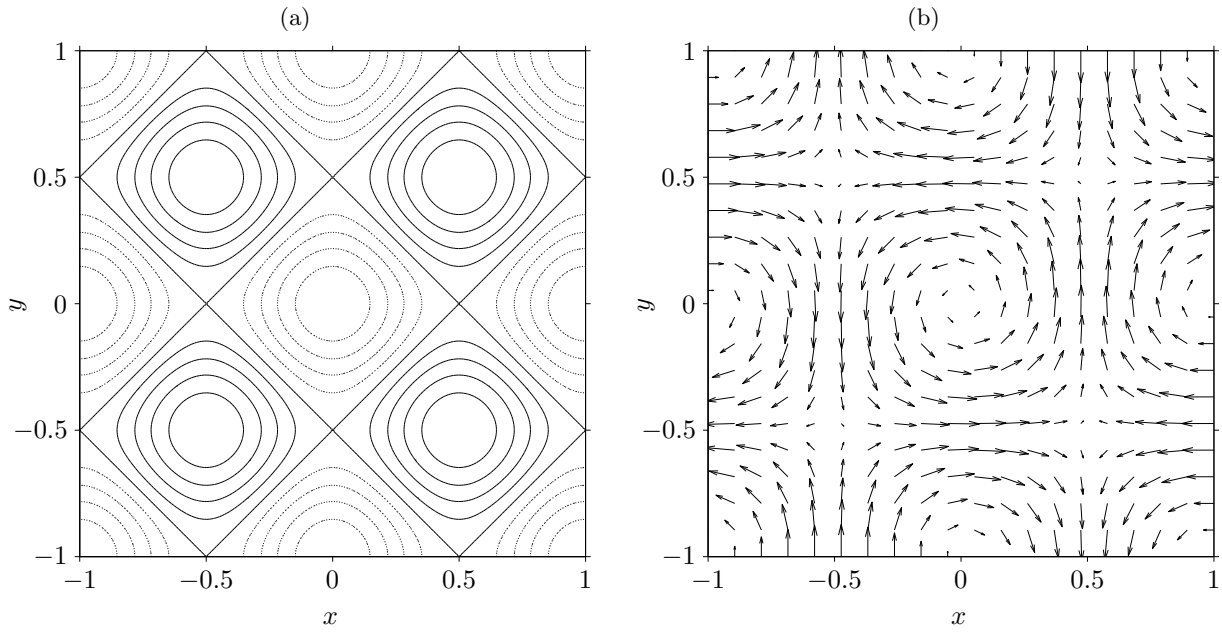


Figure B.1.: Contour lines for pressure (a) and velocity vector field (b) of the Taylor–Green flow. Solid lines indicate $p > 0$ and dotted line $p < 0$.

The tested element grids are depicted in fig. B.2, characterizing them by the size parameter h . The corresponding h - and p -convergence are demonstrated in fig. B.3, employing 6th-order polynomials for the h -convergence study, and $h = 0.25$ for the p -convergence. The results are clearly showing the expected convergence rates for both kinds of refinements.

B.1.2. Von Kármán street

A second validation of the fluid flow solver is here presented considering a classical example of hydrodynamic instability: the von Kármán street.

The case set-up for which [133] reports detailed numerical data is considered in order to compare our simulations with literature results. A graphical description of the configuration to investigate is depicted in fig. B.4, where a circular cylinder is invested by a channel flow. To initiate the von Kármán street, the cylinder is fixed in an asymmetric position with respect to the channel symmetry plane and the flow is obtained using the following time-periodic inlet velocity profile

$$U = \frac{6y(0.41 - y)}{0.41^2} \sin\left(\frac{\pi t}{8}\right). \quad (\text{B.3})$$

Discretizing this case we employ curved triangles body-fitted to the circular cylinder and compare pressure drop, drag and lift coefficients, Δp , C_D and C_L respectively, monitoring them up to $t = 8$

$$C_D = \frac{D}{(\rho_f/2)dU_{\max}^2}, \quad C_L = \frac{L}{(\rho_f/2)dU_{\max}^2}, \quad \Delta p = p(-0.05, 0.2) - p(0.05, 0.2), \quad (\text{B.4})$$

where $d = 0.1$ is the cylinder diameter, D the drag force, L the lift force and U_{\max} the maximum inlet velocity.

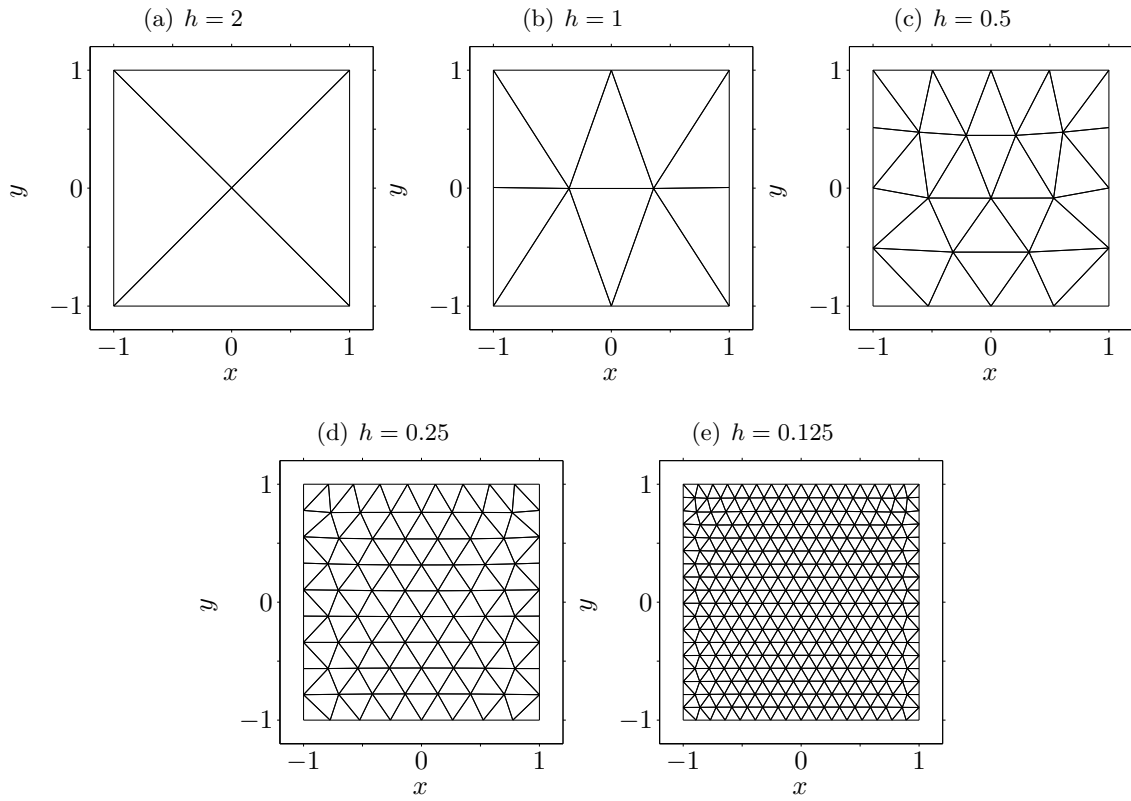


Figure B.2.: Elements distribution for obtaining the discrete Taylor–Green vortex solution via DG-FEM.

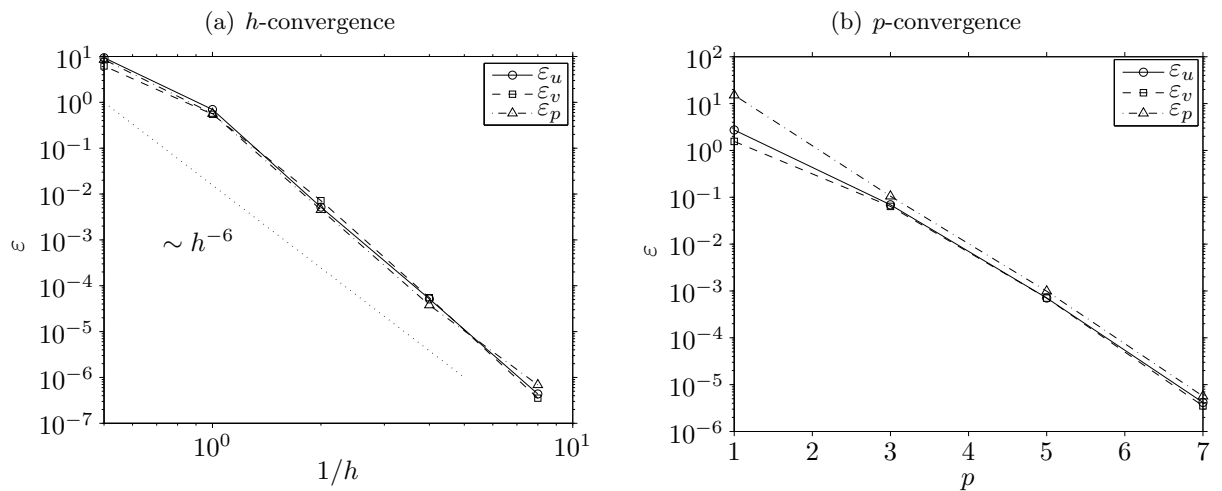


Figure B.3.: h and p -convergence expressed in terms of pressure and velocity errors for the Taylor–Green flow.

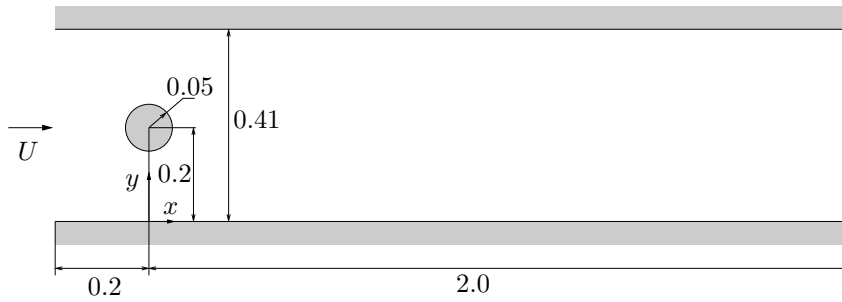


Figure B.4.: Flow past a circular cylinder located asymmetrically in a plane channel flow.

The comparison with literature data is made considering $Re = 15$, employing the mesh depicted in fig. B.5a and using 8th-order polynomial basis functions. Figure B.5b depicts the vorticity contours at time $t = 8$ and fig. B.6 shows the comparison with [133].

The good agreement with literature data is a further verification for the code developed herein.

B.1.3. Lid-Driven Cavity

One of the most common benchmarks for testing incompressible Navier–Stokes solvers is certainly represented by the lid-driven cavity set-up. In the following, it will be used to validate the implementation of continuity and momentum equations for closed-flow configurations. A further test will be proposed in the next section to include thermal effects via the internal energy balance equation. Moreover, apart from being a paradigmatic set-up for studying vortex structures in closed flows, the lid-driven cavity is extensively employed in the present study for investigating the interaction between particles and moving walls.

Our simulations are compared with literature data for the case of $Re = 1000$ [15, 32, 252, 87, 35, 105, 284, 249], which represent a typical regime of interest for the present study.

As sketched in fig. B.7, a closed liquid-filled square cavity is considered. Its boundaries are solid walls among which the only top one is moving with constant velocity U .

The cavity is infinitely extended in z -direction such to assume a two-dimensional flow, and furthermore, gravitational effects will be neglected. The mathematical problem is closed including no-slip and no-penetration boundary conditions all over the walls. The squared cavity has edge-length equal to 1 and the origin of the reference system is placed in the centre of the cavity.

In order to test the grid convergence, five evenly spaced grids are employed and in table B.1 we refer to them indicating with N_x and N_y the number of vertices per edge of the cavity. The whole data is obtained using 5th-order polynomials and it clearly shows an achieved h -convergence, plus a strong agreement with all the literature references. Following all the quoted papers, the main parameters to compare are the position of the core-vortex, $\mathbf{x}_{\min(\psi)}$, its strength, $\min(\psi)$, and the vorticity at the vortex centre, $\omega_{\min(\psi)}$. Moreover, an additional comparison between the present simulation is depicted in figs B.9. In order to characterize the flow, the streamlines are plotted in fig. B.8, where the primary vortex and the two secondary eddies at the bottom of the cavity are shown.

B.1.4. Thermocapillary-Driven Cavity

In the present section a benchmark for thermocapillary flows is considered. The following results are aimed at validating the part of the numerical solver which deals with energy transfer

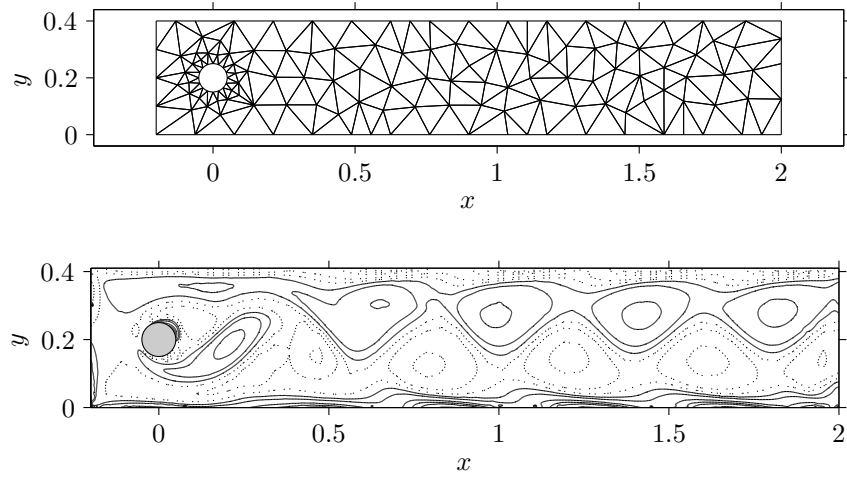


Figure B.5.: Mesh grid and vorticity contours at $t = 8$. With dotted lines $\omega < 0$ is plotted, whereas the solid lines indicate $\omega > 0$.

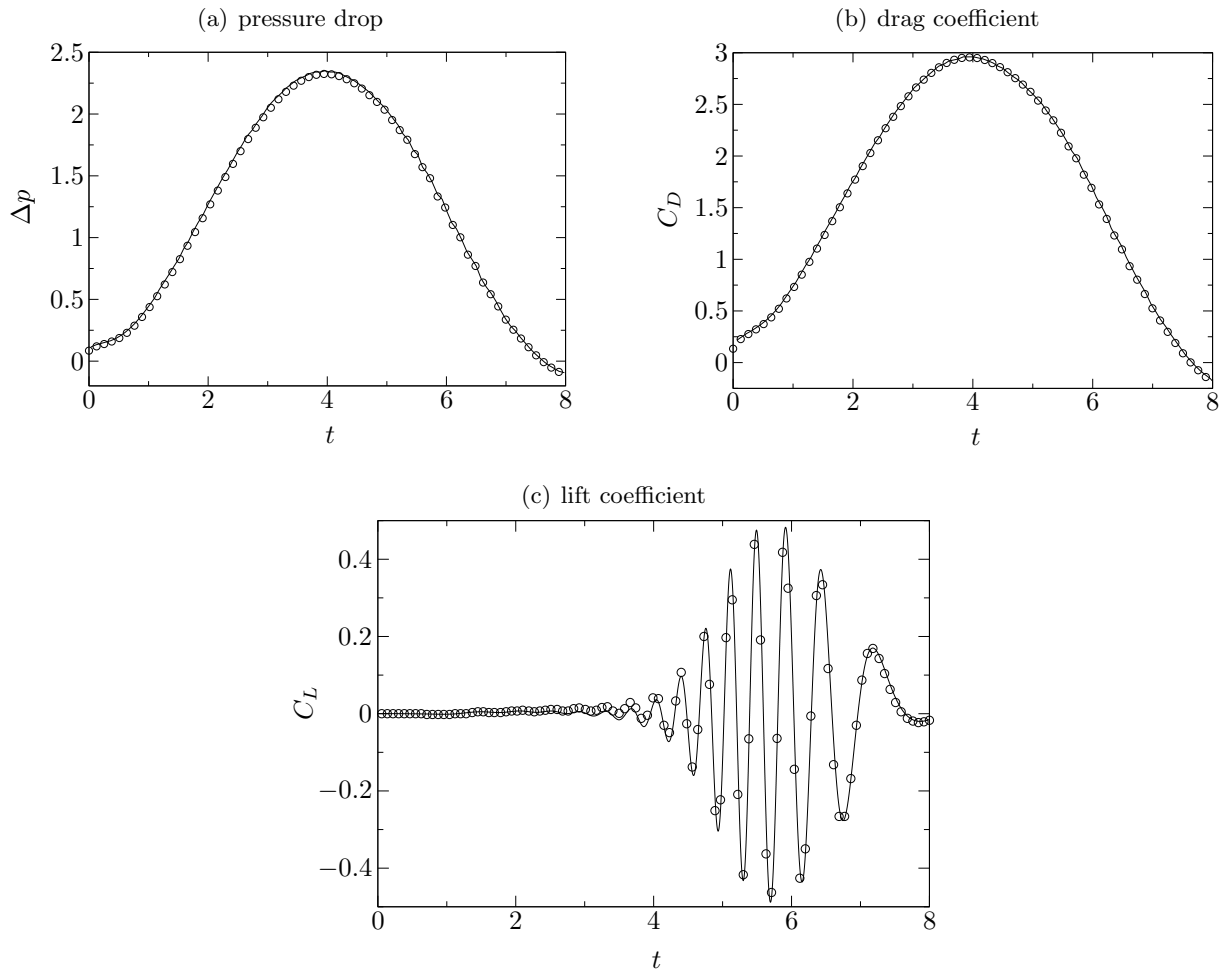


Figure B.6.: Time-dependence of the pressure drop (a), the drag (b) and the lift coefficient (c) for $t \in [0, 8]$. Full line: present result, circles: [133].

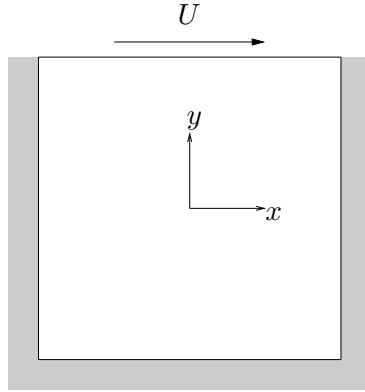


Figure B.7.: Sketch of the lid-driven cavity set-up.

Table B.1.: Convergence tests for the stream function-related quantities.

	Grid/Reference	$\min(\psi)$	$\omega_{\min(\psi)}$	$x_{\min(\psi)}$	$y_{\min(\psi)}$
	Re = 1000				
Transient ($\epsilon = 10^{-10}$)	Ref. [15]	-0.1189	–	–	–
	Ref. [32]	-0.1189	-2.0678	0.0308	0.0652
	Ref. [252]	-0.1189	-2.0677	–	–
	Ref. [87]	-0.1179	-2.0497	0.0313	0.0625
	Ref. [35]	-0.1163	–	0.0313	0.0586
	Ref. [105]	-0.1157	–	0.0312	0.0625
	Ref. [284]	-0.1173	–	0.0438	0.0625
	Ref. [249]	-0.1188	-2.0664	0.0335	0.0639
Transient ($t_{\text{fin}} = 50$)	$N_x = N_y = 10, p = 5$	-0.1138	-1.9747	0.0333	0.0667
	$N_x = N_y = 20, p = 5$	-0.1172	-2.0228	0.0316	0.0632
	$N_x = N_y = 30, p = 5$	-0.1178	-2.0391	0.0310	0.0655
	$N_x = N_y = 40, p = 5$	-0.1180	-2.0400	0.0308	0.0641
	$N_x = N_y = 50, p = 5$	-0.1182	-2.0453	0.0306	0.0653

phenomena. In particular, because shear-stress boundaries are one of the main focuses of this study, the scope of this benchmark is to prove the capability of our code in simulating the main features of thermocapillary-driven flows.

To such a purpose, the typical thermocapillary-driven cavity set-up is considered and the simulation results will be compared with literature data ([39], [40], [298], [216], [148]) for three different cases.

An open liquid-filled square cavity is considered. As depicted in fig. B.10, the top boundary of the cavity represents the free-surface and all the other boundaries are walls. In order to drive the flow, the lateral walls of the cavity are isothermal and kept at a constant temperature difference of ΔT whereas the basement is adiabatic. This results in thermocapillary stresses acting on the free-surface and responsible for driving the flow from the hot to the cold side (because $\partial\sigma/\partial T < 0$). In addition, buoyancy effects will be included as contribution to the momentum balance.

As basic assumptions we consider the case of large mean surface tensions σ_0 , in the asymptotic

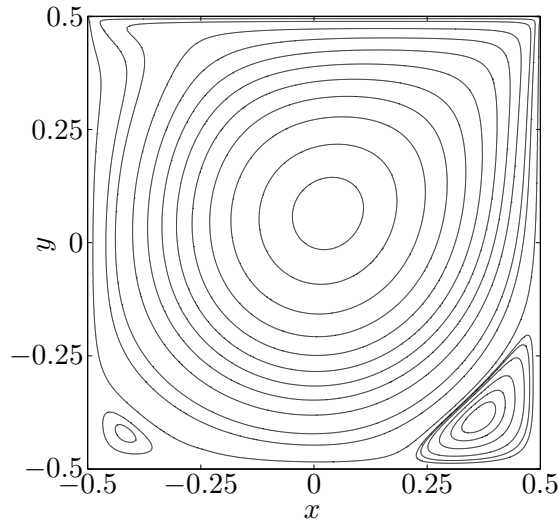


Figure B.8.: Streamlines in a square lid-driven cavity for $Re = 1000$.

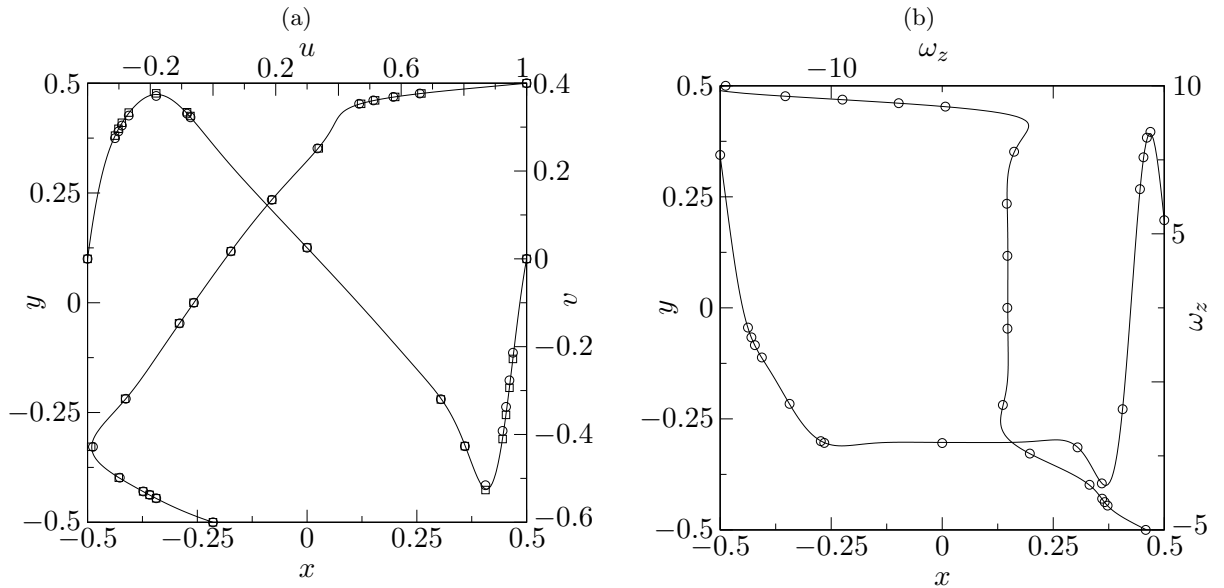


Figure B.9.: Comparison of velocities (a) and vorticity (b) along $x = 0$ and $y = 0$ in a square lid-driven cavity for $Re = 1000$. The circle markers are the results of [32], the square markers are reported in [87] and the solid line are obtained with out DG-FEM solver.

limit of vanishing capillary number

$$Ca = \frac{\gamma \Delta T}{\sigma_0} \rightarrow 0, \quad (\text{B.5})$$

where Ca is the capillary number and $\gamma = -\partial\sigma/\partial T$ the surface tension coefficient. The substantial simplification resulting from it is that the free-surface deformations dynamically induced by the flow are absent ([147]). A second assumption regarding the cavity geometry assumes it in-

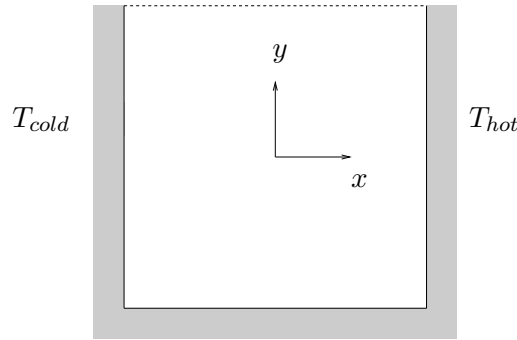


Figure B.10.: Sketch of the thermocapillary-cavity set-up.

finitely extended in z -direction, reducing the flow from three- to two-dimensional. Furthermore, the density variation is described by the mean of an incompressible model, that excludes its dependency on the pressure, but takes into account the variation of density with temperature. We therefore employ the Boussinesq approximation

$$\frac{\delta\rho}{\rho_0} = -\beta\delta T \quad (\text{B.6})$$

where β is the thermal expansion coefficient.

Adopting a viscous scaling, we recall the definitions of the Prandtl, thermocapillary Reynolds and Grashof numbers

$$\text{Pr} = \frac{\nu}{k}, \quad \text{Gr} = \frac{g\beta\Delta Th^3}{\nu^2}, \quad \text{Re} = \frac{\gamma\Delta Th}{\rho\nu^2} \quad (\text{B.7})$$

being h the cavity height.

The closure of the problem is then achieved defining the boundary conditions. The side walls are assumed perfectly conductive such that their temperature can be fixed, the bottom boundary is adiabatic and the free-surface is considered in the limit of vanishing Biot number (absence of heat exchange between free-surface and ambient).

As anticipated, three different cases are adopted as benchmark in dependence on the three dimensionless groups ruling the phenomenon. In the first case a high-thermocapillary Reynolds number flow is investigated, neglecting buoyancy effects and assuming kinematic viscosity equal to the thermal diffusivity. The latter assumption is adopted in the third case, as well, but halving the Reynolds number and including gravity effects. In order to better characterize them, a dynamic Bond number is employed because it focuses on the ratio between buoyancy and thermocapillary effects ([148]):

$$\text{Bd} = \frac{\text{Gr}}{\text{Re}} = \frac{\rho g \beta h^2}{\gamma}. \quad (\text{B.8})$$

Finally, the second case focuses on simulating a high-Marangoni number flow, combining a high Prandtl with a moderate Reynolds number

$$\text{Ma} = \text{RePr} = \frac{\gamma\Delta Th}{\rho\nu k}. \quad (\text{B.9})$$

Five literature sources are used as references, namely [39], [40], [298], [216] and [148], and in all of them, a steady-state numerical simulation is performed. As significant quantities for

the present benchmark, three main aspects of the flow are considered. The Nusselt number is employed for characterizing the temperature field and, referring to [39], the following definition is adopted

$$\text{Nu} = \int_{-\frac{1}{2}}^{+\frac{1}{2}} \left(u\theta - \frac{\partial\theta}{\partial x} \right) dy. \quad (\text{B.10})$$

To compare the cavity vortex-linked quantities, position, strength and vorticity of the vortex core are considered. Finally, to completely characterize the flow, a further comparison is made in terms of free-surface velocity.

All our simulations are transient starting from rest and stopped at $t = 0.1$. This suffices for producing reliable comparisons with steady solvers for all our data, except for the temperature-linked quantities for $\text{Pr} = 30$ (gray rows in table B.2). Even though such a high Marangoni number is employed, the time required to reach a pseudo-steady-state for the free-surface velocity and the streamfunctions-referred quantities seems already achieved after $t = 0.1$. On the other hand, because of the high Prandtl number, the temperature evolution is much slower than in the other cases, so a comparison in terms of steady-state Nusselt numbers is not so meaningful. In fact, the temporal convergence is expected at $t \sim 10$ and, because of computational cost reasons, we will limit the comparison of the second case to streamfunction and free-surface velocity only.

Because of the characteristic features of thermocapillary flows, the computational mesh is chosen to cluster its elements nearby the hot and the cold corners of the free-surface. Therefore, in order to prove the h -convergence of the code, a global grid parameter is assumed for controlling all the elements size. All the simulations are performed using 5th-order polynomials and the data in tables B.2, B.3 and B.4 demonstrates a clear grid convergence of our solver for all the quantities under investigation. Moreover, a very good agreement is shown between the literature references and the present simulations.

In order to characterize the flow, isolines for temperature and streamfunction are plotted in fig. B.11.

B.2. Multiphase Flow Benchmarks

In this section seven different configurations are employed as benchmark to validate the incompressible Navier–Stokes DG-FEM solver coupled with SPM. Having tested the fluid flow part of the algorithm in the previous section, the focus will be on the particulate-phase.

At first, different configurations will be investigated considering the only mechanical coupling between a single particle and the fluid-phase. In them it is tested the prediction of forces and torques exerted by the fluid on the particle for prescribed particle motions. The second class of benchmarks will consider freely-falling particle and colloidal forces. Finally, the thermal coupling between particulate- and fluid-phase will be tested, including particle–particle interactions in the validation process.

B.2.1. Static Cylinder in a Channel Flow

As first benchmark, the flow field past a static circular cylinder in a channel is considered. Figure B.12 depicts the simulation set-up we consider in this case, enforcing a fully developed Poiseuille flow at the inlet. Adopting a convective scaling, the inflow velocity is given by

$$U = \left(1 - \frac{y}{2d} \right) \left(1 + \frac{y}{2d} \right) \quad (\text{B.11})$$

Table B.2.: Convergence tests for the heat transfer-related quantities.

	Grid/Reference	Nu($x = -0.5$)	Nu($x = 0$)	Nu($x = 0.5$)
Re = 10000, Pr = 1, Bd = 0				
Steady	Ref. [40]	4.33	4.40	4.36
	Ref. [298]	4.36	–	4.36
	Ref. [216]	4.44	4.36	4.30
	Ref. [148]	4.36	4.36	4.36
Transient ($t_{\text{fin}} = 0.1$)	$h = 0.07, p = 5$	4.3918	4.3735	4.3367
	$h = 0.06, p = 5$	4.3830	4.3971	4.3357
	$h = 0.05, p = 5$	4.3767	4.3518	4.3650
	$h = 0.04, p = 5$	4.3737	4.3516	4.3664
	$h = 0.03, p = 5$	4.3698	4.3572	4.3663
	$h = 0.02, p = 5$	4.3695	4.3573	4.3663
Re = 2000, Pr = 30, Bd = 0				
Steady	Ref. [40]	6.60	6.29	6.42
	Ref. [298]	6.61	–	6.61
	Ref. [216]	6.69	6.71	7.14
	Ref. [148]	6.23	6.23	6.23
Transient ¹ ($t_{\text{fin}} = 0.1$)	$h = 0.035, p = 5$	8.4867	4.5361	2.1310
	$h = 0.030, p = 5$	11.6968	4.5746	2.2250
	$h = 0.025, p = 5$	8.9348	4.4233	2.1883
	$h = 0.020, p = 5$	8.5163	4.4599	2.1665
	$h = 0.015, p = 5$	8.3809	4.4620	2.1665
Re = 5000, Pr = 1, Bd = 10				
Steady	Ref. [39]	4.17	4.15	4.14
	Ref. [148]	4.55	4.545	4.55
Transient ($t_{\text{fin}} = 0.1$)	$h = 0.07, p = 5$	4.6669	4.5316	4.4055
	$h = 0.06, p = 5$	4.6746	4.5231	4.3865
	$h = 0.05, p = 5$	4.6572	4.5548	4.4477
	$h = 0.04, p = 5$	4.6488	4.5687	4.4496
	$h = 0.03, p = 5$	4.6420	4.5693	4.4531
	$h = 0.02, p = 5$	4.6349	4.5694	4.4590

¹ Results not comparable with steady-state simulations.

Table B.3.: Convergence tests for the stream function-related quantities.

	Grid/Reference	$\max(\psi)$	$\omega_{\max(\psi)}$	$x_{\max(\psi)}$	$y_{\max(\psi)}$
Re = 10000, Pr = 1, Bd = 0					
Steady	Ref. [40]	32.3	697	-0.08	0.12
	Ref. [298]	32.1	701	-0.07	0.13
	Ref. [216]	32.4	729	–	–
	Ref. [148]	32.2	702	-0.07	0.13
Transient ($t_{\text{fn}} = 0.1$)	$h = 0.07, p = 5$	32.2252	704.8684	-0.0754	0.1299
	$h = 0.06, p = 5$	32.2280	704.9873	-0.0744	0.1296
	$h = 0.05, p = 5$	32.2220	702.9726	-0.0738	0.1313
	$h = 0.04, p = 5$	32.2316	704.1387	-0.0736	0.1299
	$h = 0.03, p = 5$	32.2307	705.5564	-0.0720	0.1280
	$h = 0.02, p = 5$	32.2250	704.8051	-0.0726	0.1286
Re = 2000, Pr = 30, Bd = 0					
Steady	Ref. [40]	4.26	148	–	–
	Ref. [298]	3.38	125.4	-0.07	0.28
	Ref. [216]	3.64	130.6	–	–
	Ref. [148]	2.87	109	0.10	0.28
Transient ($t_{\text{fn}} = 0.1$)	$h = 0.035, p = 5$	3.3676	122.9027	0.0553	0.2757
	$h = 0.030, p = 5$	2.8925	111.7138	0.0884	0.2801
	$h = 0.025, p = 5$	3.0896	118.2184	0.0744	0.2797
	$h = 0.020, p = 5$	3.1801	121.2661	0.0723	0.2807
	$h = 0.015, p = 5$	3.1802	120.1964	0.0729	0.2793
Re = 5000, Pr = 1, Bd = 10					
Steady	Ref. [39]	16.45	248.5	–	–
	Ref. [148]	16.36	230.6	-0.15	0.15
Transient ($t_{\text{fn}} = 0.1$)	$h = 0.07, p = 5$	15.6705	226.2956	-0.1555	0.1643
	$h = 0.06, p = 5$	15.6826	230.6119	-0.1570	0.1615
	$h = 0.05, p = 5$	15.7183	231.0978	-0.1573	0.1619
	$h = 0.04, p = 5$	15.7134	228.4487	-0.1559	0.1646
	$h = 0.03, p = 5$	15.7231	226.9731	-0.1550	0.1614
	$h = 0.02, p = 5$	15.7158	228.8274	-0.1559	0.1637

Table B.4.: Convergence tests for the free-surface velocity-related quantities.

	Grid/Reference	$u_{fs}(x=0)$	$\max(u_{fs})$	$x_{\max(u_{fs})}$
Re = 10000, Pr = 1, Bd = 0				
Steady	Ref. [40]	-296	–	–
	Ref. [298]	-305	–	–
	Ref. [216]	-306	–	–
	Ref. [148]	-304	-712	-0.496
Transient ($t_{fin} = 0.1$)	$h = 0.07, p = 5$	-304.62	-680.84	-0.496371
	$h = 0.06, p = 5$	-304.48	-678.80	-0.496179
	$h = 0.05, p = 5$	-304.73	-690.90	-0.495564
	$h = 0.04, p = 5$	-304.78	-691.06	-0.495528
	$h = 0.03, p = 5$	-304.83	-688.77	-0.495867
	$h = 0.02, p = 5$	-304.83	-689.19	-0.495753
Re = 2000, Pr = 30, Bd = 0				
Steady	Ref. [40]	-37.2	–	–
	Ref. [298]	-29.8	–	–
	Ref. [216]	-32.2	–	–
	Ref. [148]	-24.0	-225	-0.499
Transient ($t_{fin} = 0.1$)	$h = 0.035, p = 5$	-31.16	-279.75	-0.499664
	$h = 0.030, p = 5$	-22.96	-243.93	-0.499770
	$h = 0.025, p = 5$	-26.35	-283.41	-0.499733
	$h = 0.020, p = 5$	-27.65	-265.84	-0.499804
	$h = 0.015, p = 5$	-27.64	-254.64	-0.499853
Re = 5000, Pr = 1, Bd = 10				
Steady	Ref. [39]	-179	–	–
	Ref. [148]	-176	-420	-0.492
Transient ($t_{fin} = 0.1$)	$h = 0.07, p = 5$	-169.48	-423.57	-0.492936
	$h = 0.06, p = 5$	-169.69	-423.25	-0.492144
	$h = 0.05, p = 5$	-169.73	-421.54	-0.492032
	$h = 0.04, p = 5$	-169.82	-422.85	-0.492425
	$h = 0.03, p = 5$	-169.94	-422.87	-0.492418
	$h = 0.02, p = 5$	-169.98	-422.89	-0.492658

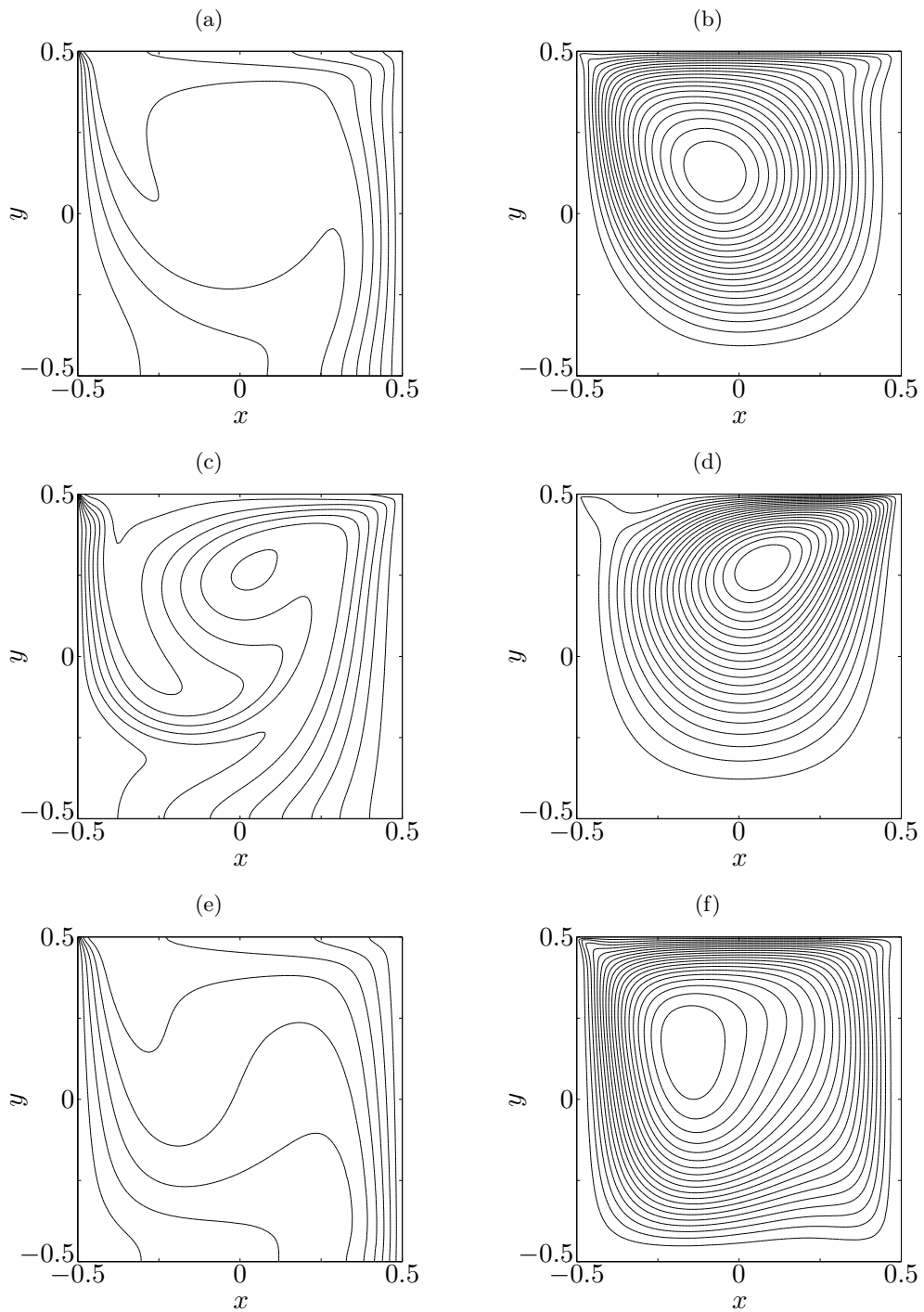


Figure B.11.: Temperature isolines (left) and streamlines (right) in a square thermocapillary-driven cavity for $Re = 10000$, $Pr = 1$, $Bd = 0$ (a and b), $Re = 2000$, $Pr = 30$, $Bd = 0$ (c and d) and $Re = 5000$, $Pr = 1$, $Bd = 10$ (e and f).

where $d = 2a = 1$ the radius of the cylinder. To close the mathematical problem, no-slip and no-penetration boundary conditions are imposed on the channel walls and outflow (uniform pressure and zero-gradient velocity) is enforced on the right boundary of the simulation domain.

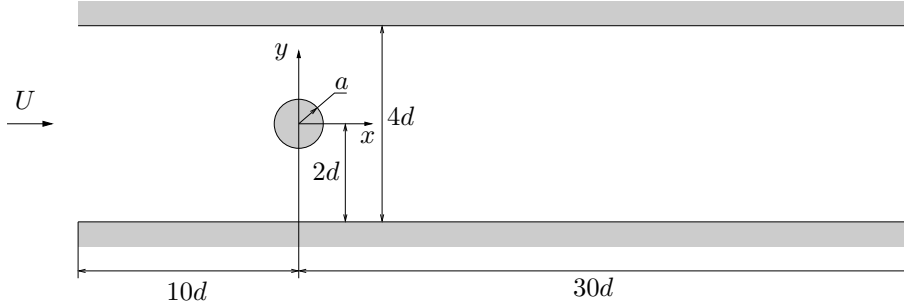


Figure B.12.: Static cylinder on the centerline of a channel.

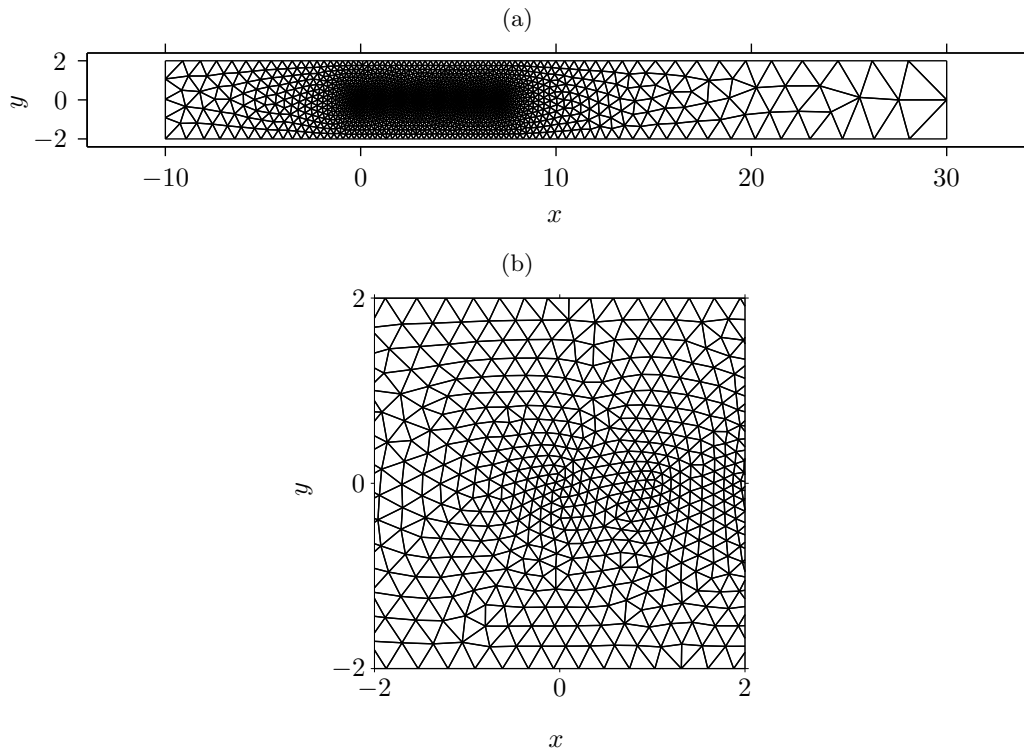


Figure B.13.: Elements of the computational mesh for simulating a circular cylinder in channel flow with SPM.

The benchmark consists of comparing force coefficients and vorticity for four different Reynolds numbers, simulating the presence of the cylinder with body-fitted elements (as done in Section B.1.2) and with SPM. The two kinds of simulation are compared for $t = 5$, 5th-order polynomials are employed as basis functions for the spatial DG-FEM discretization and $\xi = 0.15a$ is set as interface thickness layer for the SPM method. The element distribution employed for all the simulations using SPM is depicted in fig. B.13.

For most of the cases herein a moderate Reynolds number is employed and a von Kármán street will not develop, hence the main force coefficient to consider is certainly the drag coefficient

of the cylinder

$$C_D = \frac{D}{(\rho_f/2)U_{\max}^2 d}, \quad (\text{B.12})$$

where U_{\max} is the inlet velocity along the centreline and D the force exerted by the fluid on the cylinder in x -direction.

The comparison between the body-fitted DG-FEM (no SPM) and the DG-FEM plus SPM solvers is depicted in fig. B.14, showing a very good agreement between the two results with a maximum relative deviations inferior than $\pm 1\%$.

A further comparison is here shown to critically comment the application of no-penetration and specially no-slip boundary conditions implicitly enforced using the smoothed profile method. In fact, the fluid flow vorticity is generated by the no-slip conditions along the walls and the cylinder surface, therefore a comparison in terms of vorticity field is depicted in fig. B.15 at time $t = 5$ for $\text{Re} = 50$. As it can be noticed, the SPM provides a good approximation of the explicitly enforced no-slip boundary condition and it can be considered a good result in terms of fluid- and particle-phase coupling conditions.

The last investigation we propose on this set-up considers $\text{Re} = 100$. For this moderate Reynolds number the cylinder wake runs into von Kármán vortex-street instability and the comparison with body-fitted element simulations is extended to the lift coefficient

$$C_L = \frac{L}{(\rho_f/2)U_{\max}^2 d}, \quad (\text{B.13})$$

where L is the lift force exerted by the fluid on the cylinder.

A non completely satisfactory agreement is reported in fig. B.16 between body-fitted element and SPM simulations. The initial transient of the instability is well captured by the SPM method, at least up to $t = 1$. After the initial phase of evolution of the wake, the approximated no-slip boundary condition enforced by the SPM slows down the growth rate of the perturbation and the von Kármán street develops with an evident delay. Together with this effect, the softening of the boundary condition imposed by the SPM approximation, significantly reduces the vortex-shedding frequency predicted by DG-FEM plus SPM. Regardless of this issues, fig. B.16 shows the good agreement of the drag and lift force coefficients extrema for the whole time of the simulation ($t = 10$).

B.2.2. Circular Cylinder Harmonically In-Line Oscillating

The second benchmark for the particle-laden flow solver deals with prediction of forces exerted by the fluid on a circular cylinder forced to periodically oscillate with frequency f . The radius of the cylinder is $a = d/2$ and the fluid flow far away from the cylinder is at rest (see fig. B.17).

The oscillations are harmonically enforced in x -direction with the following functional dependency

$$x_p(t) = -\frac{U_{\max}}{2\pi f} \sin(2\pi ft), \quad (\text{B.14})$$

where $(x_p, 0)$ defines centroid position of the cylinder and U_{\max} is the maximum velocity of the forced oscillations. Also for this benchmark a convective scaling is adopted and two non-dimensional groups of interest are used to completely define the case: the Reynolds number and the Keulegan–Carpenter number

$$\text{Re} = \frac{U_{\max} d}{\nu}, \quad \text{KC} = \frac{U_{\max}}{fd}. \quad (\text{B.15})$$

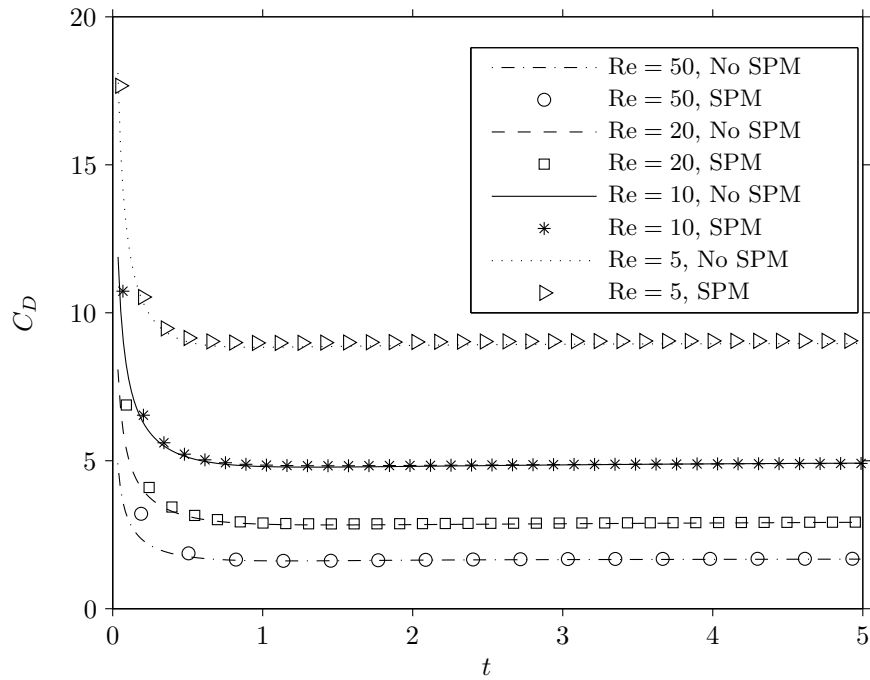


Figure B.14.: Comparison of the drag coefficient for a circular cylinder in a channel flow predicted employing body-fitted DG-FEM simulations (lines) and DG-FEM plus SPM (symbols).

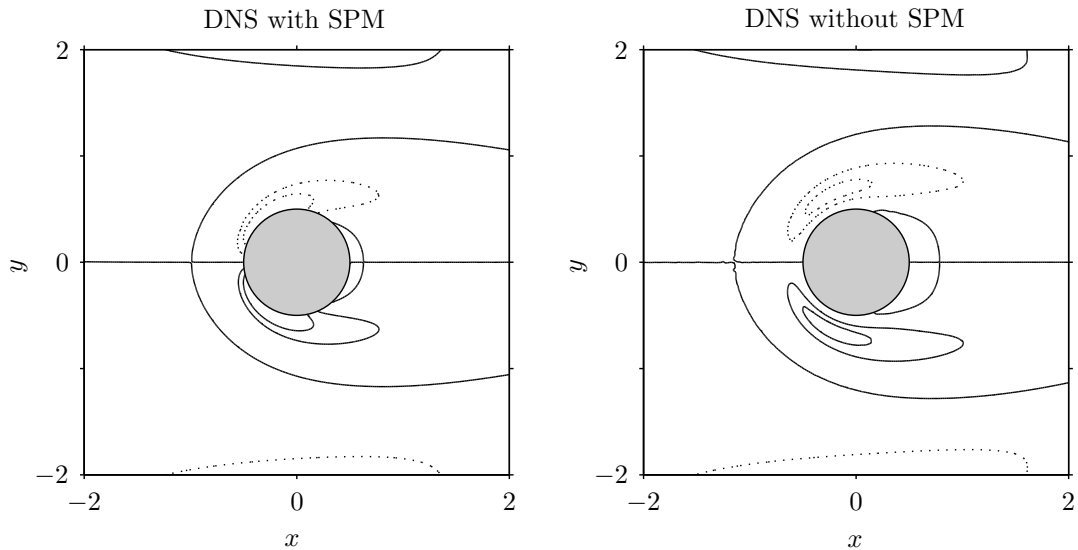


Figure B.15.: Vorticity contours for circular cylinder in channel flow. The vorticity values $\omega_z = 0, 2.5$ and 5 are represented in solid line, whereas $\omega_z = -5$ and -2.5 is shown in dotted line.

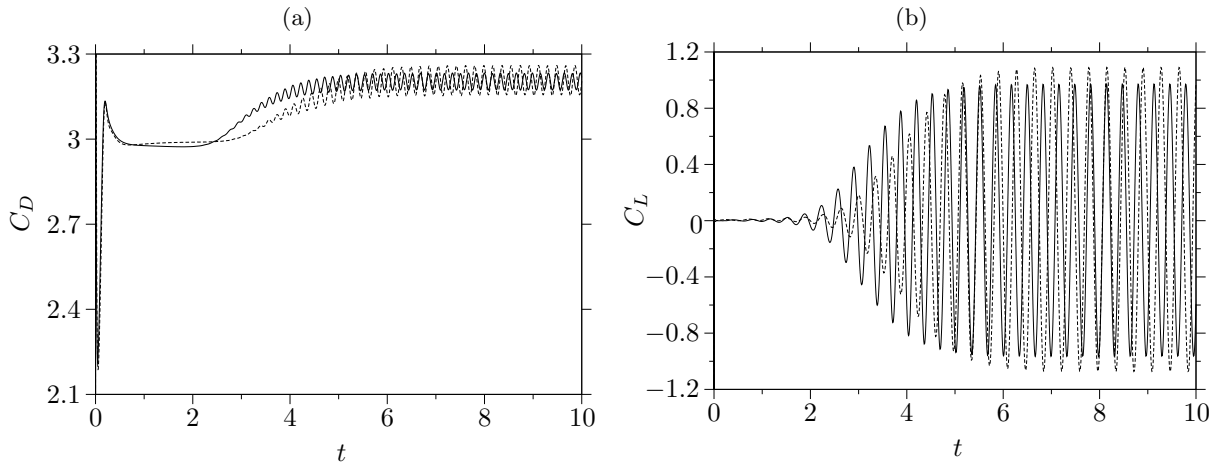


Figure B.16.: C_D (a) and C_L (b) of a circular cylinder symmetrically placed in a channel flow during the development of a vortex-shedding phenomenon. The dashed-lines indicate the DG-FEM plus SPM simulations, whereas the solid lines refer to DG-FEM with body-fitted elements.

According to what reported in [75] a square computational domain of edge-length $100a$ is enough for modelling the flow field far away from the cylinder without making the simulation results domain-size dependent. Zero-gradient boundary conditions are applied on the velocity field and a constant pressure is enforced on the domain boundaries. Because an SPM approach is adopted, no boundary conditions are explicitly needed to match the two phases; the mesh employed is presented in fig. B.18, 8th-order polynomials are used and ξ is fixed to $0.15a$.

The comparison with the experimental and numerical data of [75] is made on the drag coefficient

$$C_D = \frac{D}{(\rho_f/2)U_{\max}^2 d} \quad (\text{B.16})$$

and it is reported in fig. B.17 for $\text{Re} = 100$ and $\text{KC} = 5$ after the transient phase. Both the data sets of Dütsch et al. are reported in only one set of markers because the agreement their experiments and numerical simulations have makes the two data sets equal to each other within the marker size. From fig. B.17 one can notice the good agreement between our DG-FEM plus SPM code results and the experimental and numerical drag coefficient reported in [75].

B.2.3. Circular Cylinder Harmonically Oscillatory Rotating

In this benchmark we want to test the code in predicting torques exerted by the fluid-phase on the particles. Hence a circular cylinder periodically rotating in an unbounded domain is considered, enforcing an harmonic law for its angular velocity

$$\Omega_p(t) = \Omega_{\max} \sin(2\pi ft). \quad (\text{B.17})$$

A sketch of the problem of interest is shown in fig. B.19.

The convective scaling adopted in this benchmark is based on the maximum peripheral velocity $U_{\max} = \Omega_{\max} a$. The corresponding Reynolds number is defined as in the previous benchmark and to completely define the simulated case, the non-dimensional rotation frequency has to be

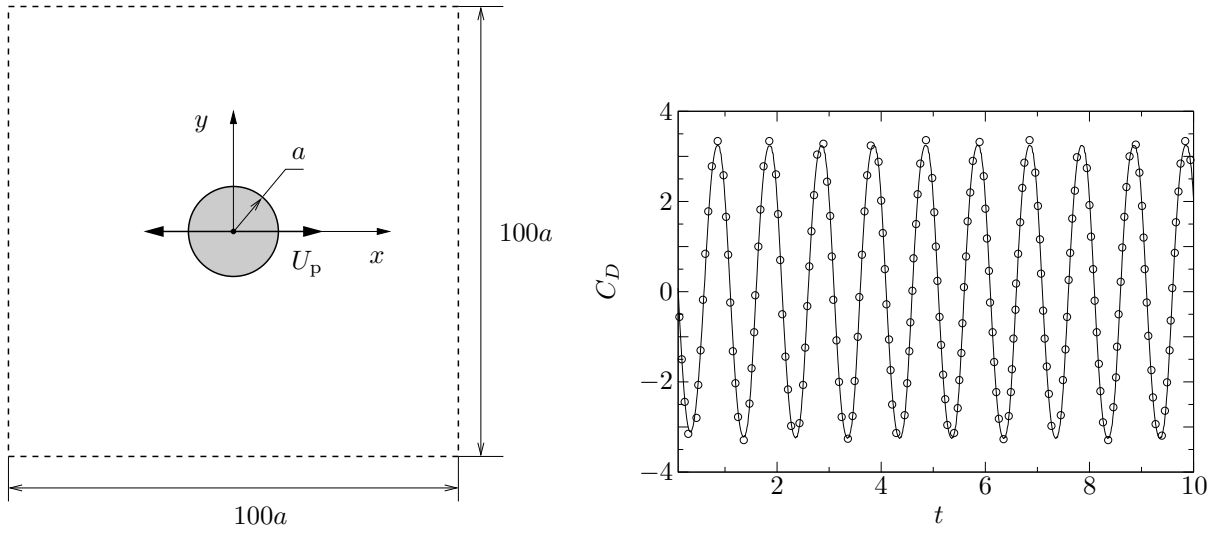


Figure B.17.: Forced harmonic oscillations of a circular cylinder in quiescent flow (left). Comparison of drag coefficient for a cylinder in quiescent fluid oscillating harmonically in x -direction (b).

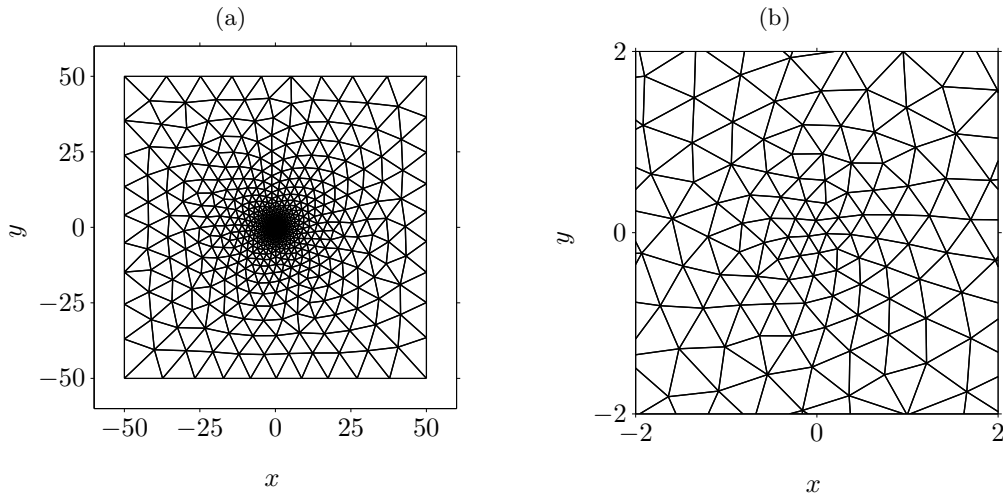


Figure B.18.: Element distribution used for simulating a harmonically oscillating circular cylinder in quiescent flow.

set. The same domain, boundary conditions, polynomial order of the basis function, interface thickness and computational mesh of Section B.2.2 are employed.

The results of the DG-FEM plus SPM solver are compared in terms of torque coefficient

$$C_T = \frac{T}{(\rho_f/2)U_{\max}^2 d^2}, \quad (\text{B.18})$$

where T is the torque exerted by the fluid on the circular cylinder, for $\text{Re} = 300$ and $f = 0.2$. The literature data for this comparison are reported in [144] and, as it is shown in fig. B.19, they very well compare with our prediction.

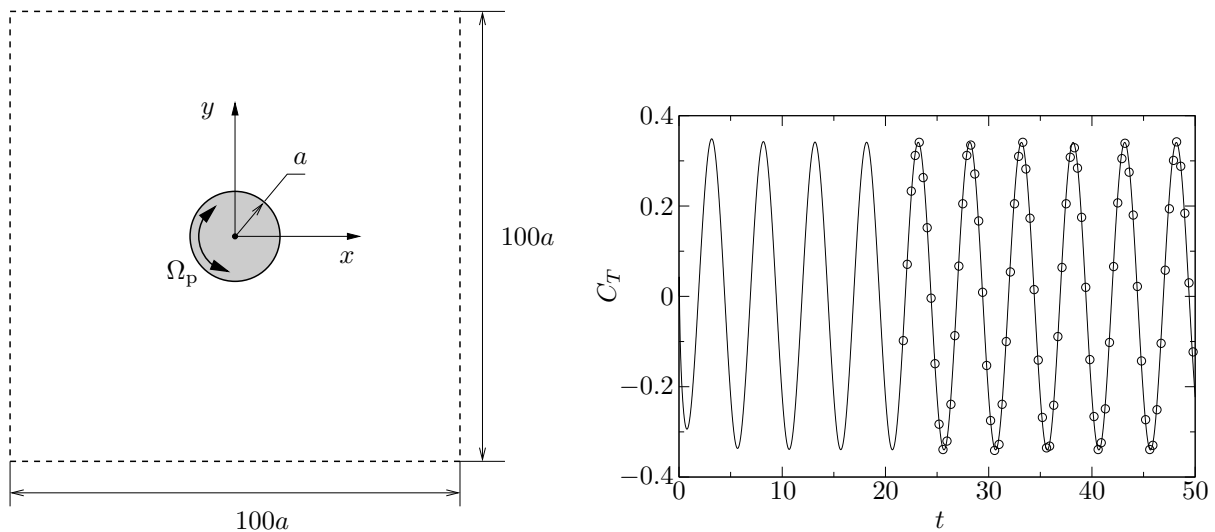


Figure B.19.: Circular cylinder forced to harmonically oscillate in a quiescent flow (left). Comparison of the torque coefficient for a cylinder harmonically rotating in quiescent fluid (right).

B.2.4. Cylinder Falling in a Channel

This benchmark is included to test the correct implementation of the algorithm part which calculate the particle trajectories and velocities. A circular cylinder is placed on the centreline of a straight vertical channel of width $W = 4d$, where $d = 2a$ is the cylinder diameter. When the cylinder is released, the fluid is initially at rest and because of gravity acceleration, the cylinder of density ρ_p starts falling down asymptotically approaching a certain velocity which implies the equilibrium between gravitational and viscous forces. Following [224], we set $L = 40d$ ¹ and all the boundaries are modelled as walls. A sketch of the problem to simulate is reported in fig. B.20.

The most appropriate scaling to adopt for this benchmark is a gravity scaling. This is because the phenomenon is fully driven by gravity forces and the arising non-dimensional groups are the particle-to-fluid density ratio and the Galileo number

$$\varrho = \frac{\rho_p}{\rho_f}, \quad \text{Ga} = \frac{\sqrt{|\varrho - 1|gd^3}}{\nu}, \quad (\text{B.19})$$

where for all the presented simulations ϱ is set equal to 3. The corresponding momentum equation reads

$$\frac{\partial \mathbf{u}}{\partial t} + (\mathbf{u} \cdot \nabla) \mathbf{u} = -\nabla p + \frac{1}{\text{Ga}} \nabla^2 \mathbf{u} - \frac{\mathbf{e}_y}{|\varrho - 1|} + \mathbf{f}_s. \quad (\text{B.20})$$

The comparison with literature data is made on a wide range of Galileo numbers ($\text{Ga} \in [0.01, 10]$) and the termination criterion for the calculation is set as follows

$$\left| \frac{U_c^n - U_c^{n-1}}{U_c^n} \right| < 10^{-4}. \quad (\text{B.21})$$

¹According to [172], having a channel length bigger than 30 times the cylinder diameter is enough to have a good approximation to an infinite channel.

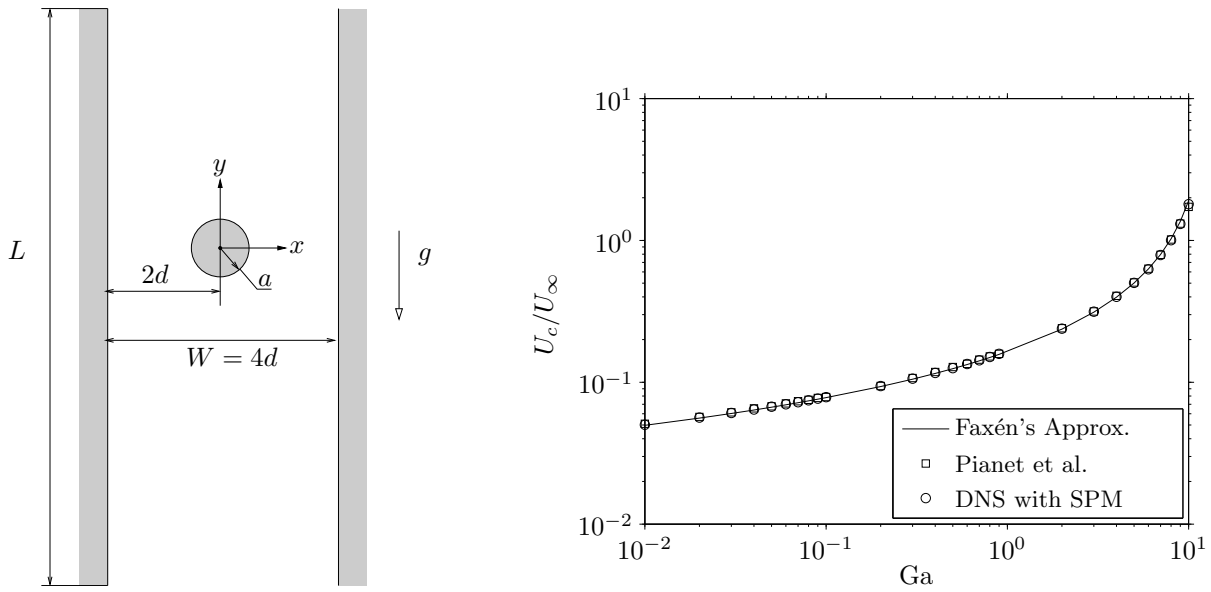


Figure B.20.: Circular cylinder falling in vertical channel starting from rest (left). Comparison of the terminal velocity for a circular cylinder settling in a vertical channel in quiescent fluid (right).

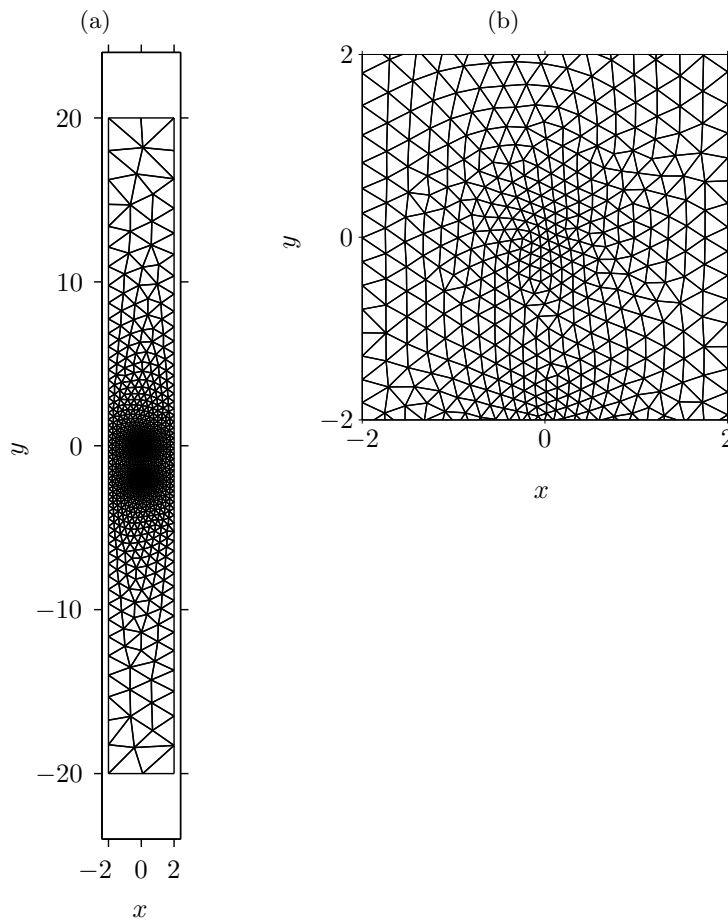


Figure B.21.: (a) Example of the element distribution employed for simulating the circular cylinder settling in a vertical channel in quiescent flow. (b) Zoom in the highly refined region.

where U_c is the terminal velocity of the cylinder.

Two sources of data are here employed for comparison: the theoretical approximation of Faxén and the numerical simulations of [224], which simulate the same problem using the immersed boundary method applied to finite volume discretization. Pianet et al. proved that the theory of Faxén gives a good prediction of the settling velocity, even though its hypothesis are not properly verified. The terminal velocity of a confined cylinder is defined as follows

$$U_c^{\text{Faxén}} = (1 - \varrho) \frac{gd^2}{\nu} f(k_x), \quad (\text{B.22a})$$

where $f(k_x)$ is the Faxén's correction factor

$$f(k_x) = -0.9157 - \ln(k_x) + 1.7244k_x^2 - 1.7302k_x^4, \quad (\text{B.22b})$$

where $k_x = d/W = 0.25$ is the blockage ratio in wall-normal direction. Following Pianet et al., we scale the velocity of the cylinder settling between two vertical parallel walls with the terminal velocity in the case of a falling circular cylinder in unbounded domain. The latter, U_∞ , can be obtained using the Oseen–Lamb approximation and it represents a good estimate of the former one for low Galileo numbers

$$U_\infty = -\frac{\text{Ga}^2\nu}{16\gamma d} \sum_{i=0}^n \delta_i [\ln(\text{Ga})]^i. \quad (\text{B.23})$$

The higher the Galileo number, the longer the distance the cylinder has to travel for reaching the settling velocity is. Hence, to efficiently simulate the whole range of Galileo numbers targeted in this benchmark, we employ h -adaptivity making sure that the particle always moves in a highly refined grid region. For all the cases, 5th-order polynomial basis functions are used, ξ equals $0.1a$ and fig. B.21 shows an example of the computational grid we employ.

The results in terms of scaled terminal velocity, U_c/U_∞ , is depicted in fig. B.20 as function of Ga . It is evident a very good agreement with both the literature sources, being it confined to less than 2% in terms of relative difference. Moreover, the deviation from Faxén's theory found by our numerical data and by Pianet et al. has the same trend.

B.2.5. Cylinder Settling in a Bounded Geometry

In this benchmark the capability of our DG-FEM plus SPM code in accurately computing colloidal forces will be tested. The problem to simulate consists in a circular cylinder of radius $a = d/2$ initially located at the centre of a square cavity of edge-length $2L$ filled with a fluid initially at rest. The cylinder is released at time $t = 0$ and it starts settling due to inertial forces as in the previous benchmark. A sketch of the problem is presented in fig. B.22. Once again a gravity scaling is adopted, the Galileo number and the cylinder-to-fluid density ratio are kept both constant ($\text{Ga} = 0.1566$, $\varrho = 3$) and the simulations investigate the role of the containment parameter

$$k = k_x = k_y = \frac{a}{L} \in [0.1, 0.85]. \quad (\text{B.24})$$

Figure B.22 shows the computational mesh consisting of 1682 equal-sized triangles (30 triangle vertices per edge of the cavity), 5th-order polynomial basis functions are employed and the interface thickness layer is $\xi = 0.1a$.

The results of our code is compared with Faxén's theory (see eq. (B.21)) and the numerical data reported in [224]. The target quantity is the asymptotic settling velocity U_c^m the cylinder will

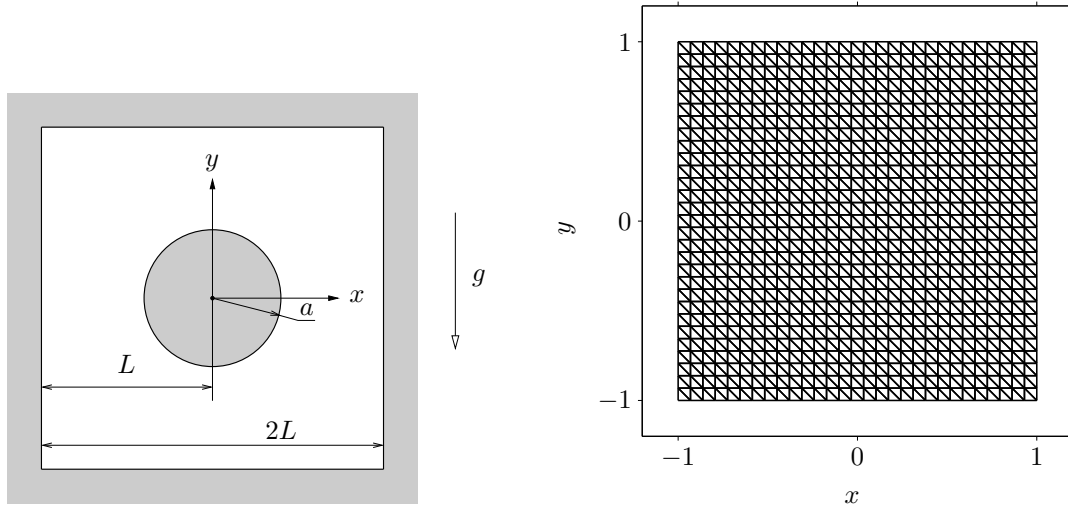


Figure B.22.: Circular cylinder settling in a square cavity filled with a fluid initially at rest (left). Element distribution of the computational mesh employed for simulating a circular cylinder settling in a square cavity. The case depicted refers to $k = 0.5$ (right).

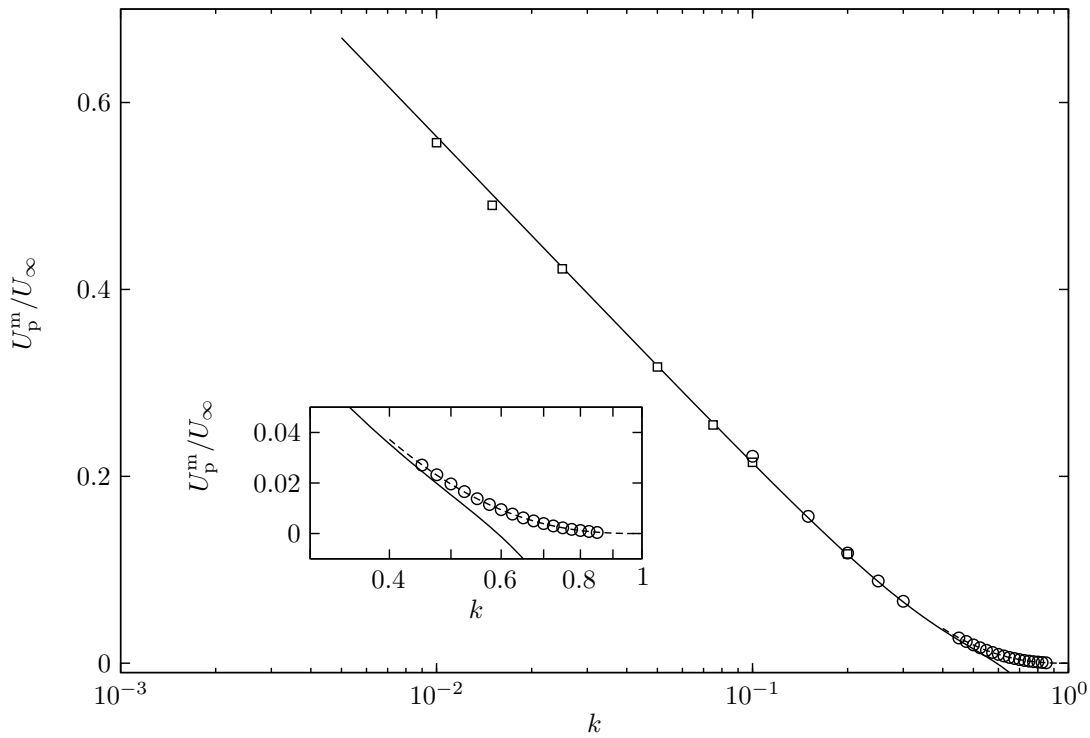


Figure B.23.: Comparison of the asymptotic terminal velocity U_p^m of a circular cylinder settling in a square box of containment parameter k . The results of DG-FEM plus SPM are represented by circles, the numerical data of [224] by squares, Faxén's theory is depicted in solid line and Pianet's correlation with dashed line.

reach before that the lubrication effects due to the presence of the bottom wall become sensible. The aforementioned comparison is depicted in fig. B.23 and confirms the good agreement between our prediction and the other literature sources. Either the DG-FEM plus SPM code or the data by Pianet et al. clearly agree with Faxén’s theory for a moderate containment parameter ($k < 0.4$), however, because Faxén’s law does not include the effect of the bottom wall, [224] suggested the correlation to improve the prediction made with eq. (B.21)

$$\frac{U_p^m}{U_\infty} = \sum_{i=1}^2 \vartheta_i (1-k)^{2.8i}, \quad (\text{B.25})$$

where ϑ_i are coefficients reported in [224] and U_p^m is the maximum asymptotic velocity reached by the settling particle.

A very good agreement is here reported between our data and Pianet’s. When colloidal forces become important in determining the settling velocity, our numerical simulation sits on the correlation function of [224] (see zoom-in region of fig. B.23).

B.2.6. Calibration of a Hot-Wire Probe

The mechanical coupling between the fluid- and the particulate-phase has been, so far, extensively tested. Hence, the following two benchmark will focus on the thermal coupling.

In this case we simulate the calibration process of an hot wire probe which operates at constant heat flux. The heat transfer is here considered for a circular cross-section wire of radius a within a square confined domain of size $60a \times 60a$. The wire is at the center of the domain, the horizontal boundaries are isothermal walls at $T = T_0$, and the flow is going from left (inlet) to right (outlet). A sketch of this set-up is depicted in fig. B.24. To model the inflow conditions, Dirichlet boundary conditions are applied on both, velocity and temperature ($\mathbf{u} = U\hat{\mathbf{e}}_x$ and $T = T_0$), whereas the outflow considers a constant pressure and homogeneous Neumann boundary conditions for temperature and velocity. A source-strength distribution is assumed for modelling the heat flux due to constant electric current in the hot-wire and it is defined as follows

$$q = \phi(\mathbf{x}, t). \quad (\text{B.26})$$

As fluid the simulations are considering air, fixing $\text{Pr}_f = 0.72$, $\text{Gr} = 1.5 \times 10^{-6}$, and $\text{Pr}_p = 3\text{Pr}_f$. The other non-dimensional groups which are arising in the problem are

$$\text{Re} = \frac{Ud}{\nu}, \quad \text{Nu} = \frac{a}{\theta_w - \theta_\infty} \int_0^{2\pi} \frac{\partial \theta}{\partial \mathbf{n}} d\varphi, \quad (\text{B.27})$$

where U denotes the inlet velocity, and θ_w and θ_∞ represents the non-dimensional temperatures on the wire surface and on the walls, respectively. To evaluate them, θ_w is obtained averaging the temperature over the hot-wire surface and θ_∞ is set to 1. The Nusselt number after reaching steady-state is used as comparison parameter between the numerical prediction of our DG-FEM plus SPM code and the calibration curves proposed by [61] for $\text{Re} \in [0.02, 44]$

$$\text{Nu} \left(1 + \frac{\theta_w - 1}{2} \right)^{-0.17} = 0.24 + 0.56\text{Re}^{0.45}. \quad (\text{B.28})$$

As initial conditions, the fluid is considered at rest and constant temperature T_0 . At the beginning of the simulation, $t = 0$, the heat source within the hot-wire is suddenly switched on as well as the incoming flow. The same grid of Section B.2.2 is employed, using 5th-order polynomials and setting the interface layer thickness $\xi = 0.05a$. Investigating the problem for a wide range of Reynolds numbers, a very good agreement with the experimental correlation law by Collins et al. is found (maximum difference always below 2%) and reported in fig. B.25.

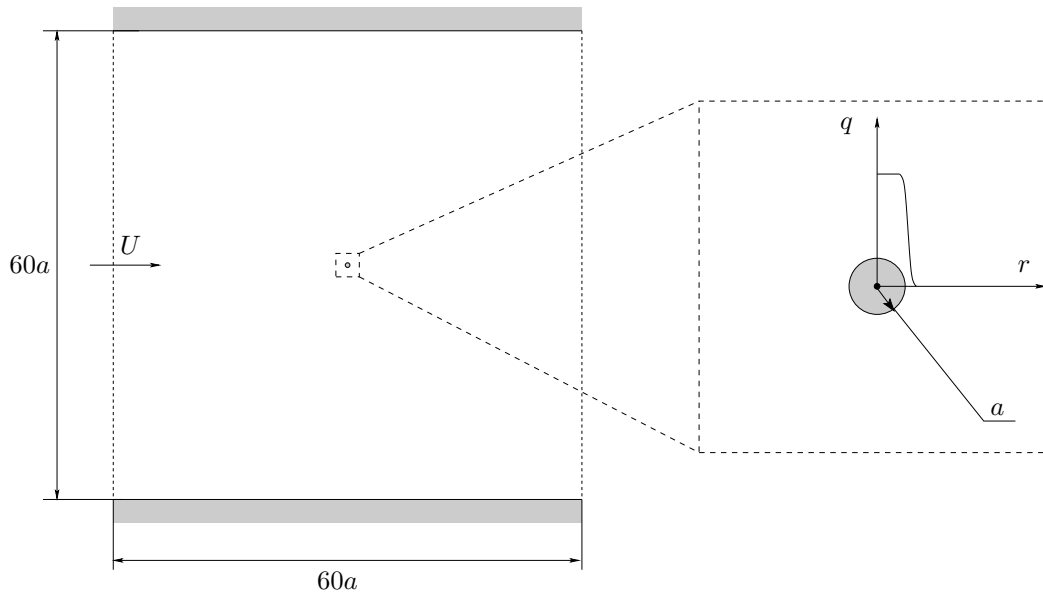


Figure B.24.: Sketch of the hot-wire probe calibration problem.

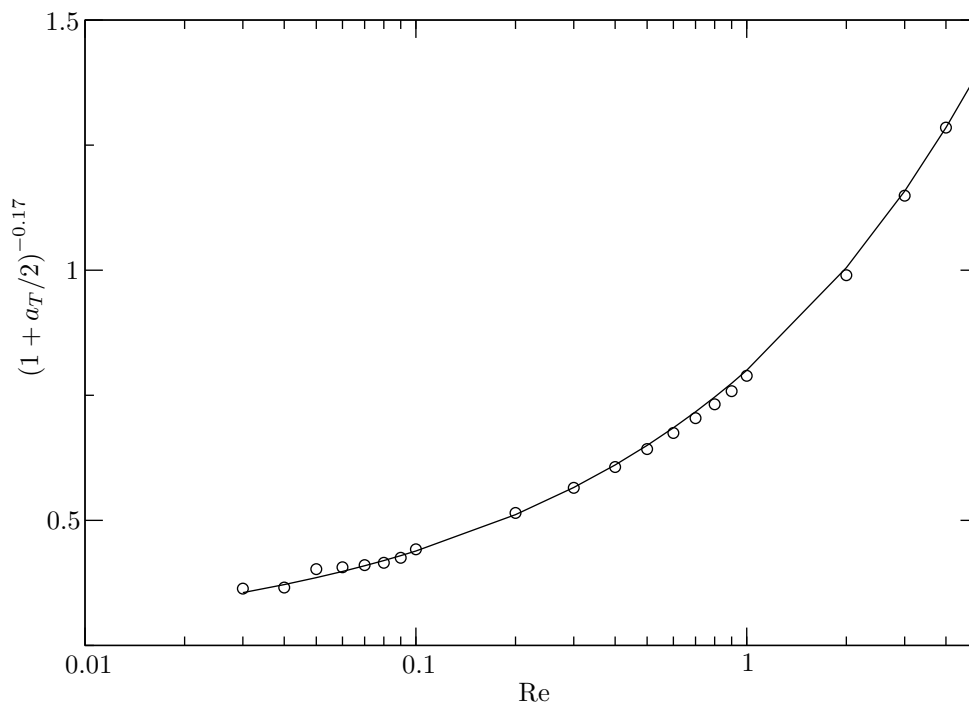


Figure B.25.: Comparison of the Reynolds-Nusselt number correlation for a hot wire probe in steady state air flow; $a_T = (\theta_w - 1) / 2$. The solid line depicts the correlation law of Collins & Williams whereas the markers are the results of our DG-FEM plus SPM code.

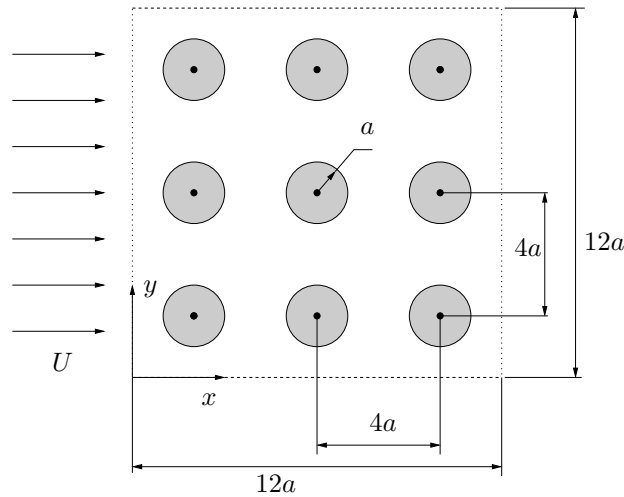


Figure B.26.: Setup of the heat-exchanger problem.

B.2.7. Heat Exchanger

The last benchmark we report is still concerning the thermal coupling between fluid- and particle-phase, but in the case of multiple particles involved in the simulations.

The forced convection problem targeted in this section considers a classic in-line circular-pin heat exchanger invested by a fully developed flow. The pins shape is circular, of radius a , and their arrangement is such that their centroid distances are equal to $4a$ either in horizontal or in vertical direction. A sketch of the case is reported in fig. B.26.

Because the pins are supposed fixed, the only non-dimensional groups of interest are the Reynolds and the Nusselt number, defined as in the previous section using as reference velocity and temperature the maximum incoming velocity and inlet temperature, respectively. The numerical simulations are made enforcing periodic boundary conditions on the left and on the right edge of the domain, whereas on top and bottom boundaries, symmetric boundary conditions are employed.

As computational mesh we adopt 70 evenly distributed element vertices per domain boundary, 5th-order polynomials and $\xi = 0.05a$. The comparison with the literature data by Behnia et al. ([25]) for isothermal pins are tabulated in table B.5 and a very good agreement is found also in this case for all the three investigated Reynolds numbers.

Therefore, after presenting several benchmarks for various flow conditions, we consider the numerical code developed in the present thesis work extensively verified and validated.

Table B.5.: Comparison of the Nusselt number for an in-line heat exchanger with circular pins changing the Reynolds number.

Grid/Reference	$N = 70$	ref. [25]
Re = 100	10.39	10.1
Re = 200	12.0	11.7
Re = 300	12.1	12.0

C. One-Way Coupling Simulations

The numerical method employed for simulating the axisymmetric liquid bridge flow of Section 5.2.1 is discussed and validated in this chapter of the Appendix.

In Chapter 5 this fluid flow solver has been employed for the one-way coupled simulations for numerically investigating the experimental evidences reported in [255]. A similar approach was adopted by [151].

C.1. Fluid Flow Discretization

The numerical flow field solver presented in this section discretize the steady-state Navier–Stokes equations written adopting the thermocapillary scaling. The reference problem to simulate is a statically deformed axisymmetric liquid bridge flow, including temperature dependent kinematic viscosity and thermal diffusivity. We refer to Chapter 2 for a more detailed problem formulation.

The Newton–Raphson method is used to deal with non-linearities by the mean of successive linearizations

$$\mathbf{J}(\mathbf{y}^k) \cdot \delta \mathbf{y} = -\mathbf{f}(\mathbf{y}^k), \quad (\text{C.1a})$$

$$\mathbf{y}^{k+1} = \mathbf{y}^k + \delta \mathbf{y}, \quad (\text{C.1b})$$

where $\mathbf{y} = (u, v, p, T)^\top$ is the solution vector, $\mathbf{J}(\mathbf{y}^k)$ represents the Jacobian of the Navier–Stokes equations at the iteration step k , $\delta \mathbf{y}$ is the increment of the solution between two successive iterations and $\mathbf{f}(\mathbf{y}^k)$ is the nonlinear residual. Writing the problem to solve in explicit form and linearizing with respect to the solution increment, it yields

$$\nabla \cdot \delta \mathbf{u} = -\nabla \cdot \mathbf{u}^k, \quad (\text{C.2a})$$

$$\begin{aligned} \text{Re} \left(\delta \mathbf{u} \cdot \nabla \mathbf{u}^k + \mathbf{u}^k \cdot \nabla \delta \mathbf{u} \right) + \nabla \delta p - \nabla \cdot (\nu / \nu_0 \nabla \delta \mathbf{u}) - \text{Bd} \delta T \mathbf{e}_z = \\ -\text{Re} \left(\mathbf{u}^k \cdot \nabla \mathbf{u}^k \right) - \nabla p^k + \nabla \cdot \left[\nu(T^k) / \nu_0 \nabla \mathbf{u}^k \right] + \text{Bd} T^k \mathbf{e}_z, \end{aligned} \quad (\text{C.2b})$$

$$\begin{aligned} \text{Ma} \left(\delta \mathbf{u} \cdot \nabla T^k + \mathbf{u}^k \cdot \nabla \delta T \right) - \nabla \cdot (\kappa / \nu_0 \nabla \delta T) = \\ -\text{Ma} \left(\mathbf{u}^k \cdot \nabla T^k \right) + \nabla \cdot \left[\kappa(T^k) / \nu_0 \nabla T^k \right]. \end{aligned} \quad (\text{C.2c})$$

The Jacobian can be computed using the Newton’s linearization of the convective terms

$$\nabla \cdot (\mathbf{u} \mathbf{u}) \approx \nabla \cdot (\mathbf{u} \mathbf{u}^k) + \nabla \cdot (\mathbf{u}^k \mathbf{u}). \quad (\text{C.3})$$

The code is implemented using a second order finite volume method discretized in primitive variables on a structured staggered grid (see e.g. [297]).

The local mesh refinement is provided using an hyperbolic-tangent stretching of the computational cells, increasing the accuracy along all the four boundaries (see [285, 273] for details). In fig. C.1 an example of the computational grid is depicted.

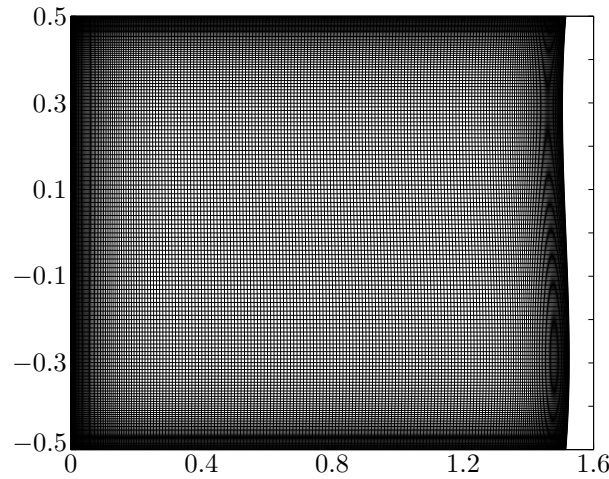


Figure C.1.: Computational mesh which consists of 169×169 nodes. The grid refinement follows a hyperbolic-tangent distribution and employs a stretching factor of 1.05.

Only statical deformations are considered in the the free-surface shape $h(z)$ of the liquid bridge, therefore the Young–Laplace equation is to be solved and it can be written in form of a system of three ordinary first-order differential equations as follows

$$b' = (\Gamma^2 + b^2) \left[\frac{1}{h} - \frac{\Delta p_s - \text{Bo}z}{\Gamma^2} \sqrt{\Gamma^2 + b^2} \right], \quad (\text{C.4a})$$

$$h' = b, \quad (\text{C.4b})$$

$$\Delta p'_s = 0. \quad (\text{C.4c})$$

This non-linear system is solved by Newton–Raphson method discretized via central finite differences and prescribing the liquid bridge volume ratio \mathcal{V} , as indicated in Chapter 2.

C.2. Verification of the Numerical Solver

Two main part of the FVM solver are to be tested: the static free-surface deformation and the internal fluid flow. Owing to the decoupling already discussed in Chapter 2, the free-surface shape does not depend on the fluid flow and it can be separately tested. To verify it, a closed-form solution in case of absence of gravity is represented by the catenoidal profile [212]

$$h^{\text{cat}}(z) = h_0 \cosh \left(\frac{\Gamma z}{h_0} \right), \quad (\text{C.5})$$

where $h_0 \cosh(\Gamma/2h_0) = 1$. In fig. C.2 a convergence study of our solver is shown for a liquid bridge of $\Gamma = 1$. The grid study is conducted for an even distribution of the nodes N_z , testing the L_∞ and L_2 norms of the error

$$\epsilon = h^{\text{cat}}(z) - h^{\text{FD}}(z), \quad (\text{C.6})$$

where $h^{\text{FD}}(z)$ is the finite difference numerical solution. A clear second-order convergence rate is shown, consistently with the employed discretization.

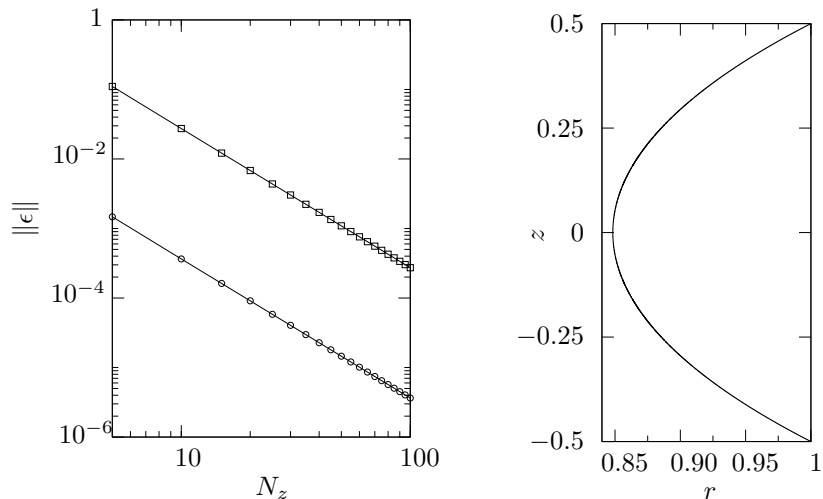


Figure C.2.: Convergence rate of the free-surface shape solver (left) for a closed-form solution of a liquid bridge deformation with $\Gamma = 1$ (right). Squares and circles denote L_2 - and infinite-norms, respectively.

The second benchmark for the fluid flow solver is made comparing the main representative quantities of the flow structures with literature data for many different parameters. Our numerical results are confronted with the ones published in [205] and [167]. The maximum absolute value of the Stokes stream-function $\psi^{\text{St}} = r\psi$ is considered for a upstraight cylindrical liquid bridge with aspect ratio one under weightlessness. The comparison with literature data is made for a wide range of Reynolds and Prandtl numbers employing a hyperbolic-tangent distribution of the computational mesh with a stretching factor of 1.05. The results of our fluid flow solver are reported in table C.1 and they very well agree with literature data.

Table C.1.: Maximum value of the Stokes' stream function $|\psi^{\text{St}}|$ for a cylindrical liquid bridge under weightlessness with $\Gamma = 1$.

Re	1000	3000	5000	7000	Grid/Reference
Pr = 0.02	8.93	7.18	6.31	5.65	[167]
			6.28		[205]
	9.0200	7.1059	6.2178	5.6301	112×112
	9.0210	7.1102	6.2240	5.6384	169×169
	9.0226	7.1101	6.2249	5.6391	266×266
	9.0238	7.1114	6.2256	5.6401	366×366
Pr = 4	2.35	2.09	1.97	1.86	[167]
			2.03		[205]
	2.4692	2.1875	2.0752	1.9894	112×112
	2.4684	2.1781	2.0612	1.9749	169×169
	2.4691	2.1778	2.0609	1.9727	266×266
	2.4698	2.1783	2.0605	1.9735	366×366

Bibliography

- [1] Abe, Y., Ueno, I., and Kawamura, H. (2007). Effect of shape of HZ liquid bridge on particle accumulation structure (PAS). *Microgravity Sci. Technol.*, 19:84–86.
- [2] Abe, Y., Ueno, I., and Kawamura, H. (2009). Dynamic particle accumulation structure due to thermocapillary effect in noncylindrical half-zone liquid bridge. *Ann. N. Y. Acad. Sci.*, 1161:240–245.
- [3] Albensoeder, S. and Kuhlmann, H. C. (2002). Linear stability of rectangular cavity flows driven by anti-parallel motion of two facing walls. *Journal of Fluid Mechanics*, 458:153–180.
- [4] Albensoeder, S. and Kuhlmann, H. C. (2005). Accurate three-dimensional lid-driven cavity flow. *Journal of Computational Physics*, 206(2):536–558.
- [5] Albensoeder, S., Kuhlmann, H. C., and Rath, H. J. (2001). Multiplicity of steady two-dimensional flows in two-sided lid-driven cavities. *Theor. Comp. Fluid Dyn.*, 14:223–241.
- [6] Angilella, J.-R. (2007). Asymptotic analysis of chaotic particle sedimentation and trapping in the vicinity of a vertical upward streamline. *Physics of Fluids*, 19(7):07330.
- [7] Angilella, J.-R. (2010). Dust trapping in vortex pairs. *Physica D: Nonlinear Phenomena*, 239(18):1789–1797.
- [8] Arnold, D., Brezzi, F., Cockburn, B., and Marini, L. (2002). Unified analysis of discontinuous galerkin methods for elliptic problems. *SIAM Journal on Numerical Analysis*, 39(5):1749–1779.
- [9] Atkins, H. L. and Shu, C.-W. (1998). Quadrature-free implementation of discontinuous galerkin method for hyperbolic equations. *AIAA Journal*, 36:775–782.
- [10] Babiano, A., Cartwright, J. H. E., Piro, O., and Provenzale, A. (2000). Dynamics of a small neutrally buoyant sphere in a fluid and targeting in hamiltonian systems. *Phys. Rev. Lett.*, 84:5764–5767.
- [11] Babuška, I. (1971). Error-bounds for finite element method. *Numerische Mathematik*, 16(4):322–333.
- [12] Bajer, K. (1994). Hamiltonian formulation of the equations of streamlines in three-dimensional steady flows. *Chaos, Solitons & Fractals*, 4(6):895–911.
- [13] Barnhill, R. E., Birkhoff, G., and Gordon, W. J. (1973). Smooth interpolation in triangles. *Journal of Approximation Theory*, 8(2):114–128.
- [14] Barnhill, R. E. and Gregory, J. A. (1975). Compatible smooth interpolation in triangles. *Journal of Approximation Theory*, 15(3):214–225.
- [15] Barragy, E. and Carey, G. (1997). Stream function-vorticity driven cavity solution using p finite elements. *Computers and Fluids*, 26(5):453–468.

- [16] Bassi, F., Crivellini, A., Pietro, D. A. D., and Rebay, S. (2006a). An artificial compressibility flux for the discontinuous galerkin solution of the incompressible navier–stokes equations. *Journal of Computational Physics*, 218(2):794–815.
- [17] Bassi, F., Crivellini, A., Pietro, D. A. D., and Rebay, S. (2006b). A high-order discontinuous galerkin solver for 3d aerodynamic turbulent flows. Delft University of Technology ECCOMAS.
- [18] Bassi, F., Crivellini, A., Pietro, D. A. D., and Rebay, S. (2007). An implicit high-order discontinuous galerkin method for steady and unsteady incompressible flows. *Computers and Fluids*, 36(10):1529–1546.
- [19] Bassi, F., Crivellini, A., Rebay, S., and Savini, M. (2005). Discontinuous galerkin solution of the reynolds-averaged navier–stokes and $k - \omega$ turbulence model equations. *Computers and Fluids*, 34(4–5):507–540.
- [20] Bassi, F. and Rebay, S. (1997a). A high-order accurate discontinuous finite element method for the numerical solution of the compressible navier–stokes equations. *Journal of Computational Physics*, 131(2):267–279.
- [21] Bassi, F. and Rebay, S. (1997b). High-order accurate discontinuous finite element solution of the 2d euler equations. *Journal of Computational Physics*, 138(2):251–285.
- [22] Baumann, C. E. (1997). *An hp-Adaptive Discontinuous Finite Element Method for Computational Fluid Dynamics*. PhD thesis, University of Texas at Austin.
- [23] Baumann, C. E. and Oden, J. T. (1999). A discontinuous hp finite element method for convection–diffusion problems. *Computer Methods in Applied Mechanics and Engineering*, 175(3–4):311–341.
- [24] Becker, A. and aus der Wiesche, S. (2013). Experimental study of rimming flows of two liquids in a partially filled horizontally rotating cylinder. In *ASME 2013 Fluids Engineering Division Summer Meeting*, page V01BT16A001. American Society of Mechanical Engineers.
- [25] Behnia, M., Copeland, D., and Soodphakdee, D. (1998). A comparison of heat sink geometries for laminar forced convection: Numerical simulation of periodically developed flow. In *Thermal and Thermomechanical Phenomena in Electronic Systems, ITherm '98*. The Sixth Intersociety Conference, pages 310–315.
- [26] Beskok, A. and Warburton, T. (2001a). Arbitrary lagrangian eulerian analysis of a bidirectional micro-pump using spectral elements. *International Journal of Computational Engineering Science*, 02(01):43–57.
- [27] Beskok, A. and Warburton, T. (2001b). An unstructured hp finite-element scheme for fluid flow and heat transfer in moving domains. *Journal of Computational Physics*, 174(2):492–509.
- [28] Beyer, R. P. and LeVeque, R. J. (1992). Analysis of a one-dimensional model for the immersed boundary method. *SIAM Journal on Numerical Analysis*, 29(2):332–364.
- [29] Blohm, C. (2001). *Experimentelle Untersuchung stationärer und zeitabhängiger Strömungen im zweiseitig angetriebenen Rechteckbehälter*. PhD thesis, University of Bremen.
- [30] Blohm, C. H. and Kuhlmann, H. C. (2002). The two-sided lid-driven cavity: experiments on stationary and time-dependent flows. *Journal of Fluid Mechanics*, 450:67–95.

-
- [31] Botella, O. (1998). *Résolution numérique de problèmes de Navier-Stokes singuliers par une méthode de projection Tchebychev*. PhD thesis, Université de Nice.
- [32] Botella, O. and Peyret, R. (1998). Benchmark spectral results on the lid-driven cavity flow. *Computers and Fluids*, 27(4):421–433.
- [33] Breugem, W.-P. (2012). A second-order accurate immersed boundary method for fully resolved simulations of particle-laden flows. *Journal of Computational Physics*, 231(13):4469–4498.
- [34] Brezzi, F. (1974). On the existence, uniqueness and approximation of saddle-point problems arising from lagrangian multipliers. *ESAIM: Mathematical Modelling and Numerical Analysis - Modélisation Mathématique et Analyse Numérique*, 8(R2):129–151.
- [35] Bruneau, C.-H. and Jouron, C. (1982). An efficient scheme for solving steady incompressible navier–stokes equations. *Journal of Computational Physics*, 89(2):389–413.
- [36] Canuto, C., Hussaini, M., Quarteroni, A., and Zang, T. (1988). *Spectral Methods in Fluid Dynamics*. Springer-Verlag.
- [37] Canuto, C., Hussaini, M., Quarteroni, A., and Zang, T. (2007). *Spectral Methods: Evolution to Complex Geometries and Applications to Fluid Dynamics*. Springer.
- [38] Canuto, C. and Quarteroni, A. (2004). *Spectral Methods*. Encyclopedia of Computational Mechanics.
- [39] Carpenter, B. M. and Homsy, G. M. (1989). Combined buoyant thermocapillary flow in a cavity. *Journal of Fluid Mechanics*, 207:121–132.
- [40] Carpenter, B. M. and Homsy, G. M. (1990). High marangoni number convection in a square cavity, part ii. *Physics of Fluids A*, 2:137–149.
- [41] Cartwright, J. H. E., Feudel, U., Károlyi, G., de Moura, A., Piro, O., and Tél, T. (2010). Dynamics of finite-size particles in chaotic fluid flows. In *Nonlinear Dynamics and Chaos: Advances and Perspectives*, pages 51–87. Springer.
- [42] Castillo, P., Cockburn, B., Schötzau, D., and Schwab, C. (2002). Optimal a priori error estimates for the hp-version of the local discontinuous galerkin method for convection–diffusion problems. *Mathematics of Computation*, 71:455–478.
- [43] Chavent, G. and Cockburn, B. (1987). The local projection p0-p1-discontinuous galerkin finite element for scalar conservation laws. *IMA Preprints Series*, 2209(341).
- [44] Chavent, G. and Salzano, G. (1982). A finite element method for the 1d flooding problem with gravity. *Journal of Computational Physics*, 45:307–344.
- [45] Chorin, A. J. (1968). Numerical solution of the navier–stokes equations. *Mathematics of Computation*, 22:745–762.
- [46] Climent, E. and Maxey, M. R. (2003). Numerical simulations of random suspensions at finite reynolds numbers. *International Journal of Multiphase Flow*, 29(4):579–601.
- [47] Climent, E. and Maxey, M. R. (2009). The force coupling method: a flexible approach for the simulation of particulate flows. *Theoretical Methods for Micro Scale Viscous Flows*.

- [48] Cockburn, B. and Guzmán, J. (2008). Error estimates for the runge–kutta discontinuous galerkin method for the transport equation with discontinuous initial data. *SIAM Journal on Numerical Analysis*, 46(3):1364–1398.
- [49] Cockburn, B., Hou, S., and Shu, C.-W. (1990). The runge-kutta local projection discontinuous galerkin finite element method for conservation laws. iv. the multidimensional case. *Mathematics of Computation*, 54:545–581.
- [50] Cockburn, B., Kanschat, G., and Schötzau, D. (2005a). The local discontinuous galerkin method for linearized incompressible fluid flow: a review. *Computers and Fluids*, 34(4–5):491–506.
- [51] Cockburn, B., Kanschat, G., and Schötzau, D. (2005b). A locally conservative ldg method for the incompressible navier–stokes equations. *Mathematics of Computation*, 74:1067–1095.
- [52] Cockburn, B., Kanschat, G., and Schötzau, D. (2009). An equal-order dg method for the incompressible navier–stokes equations. *Journal of Scientific Computing*, 40(1–3):188–210.
- [53] Cockburn, B., Kanschat, G., Schötzau, D., and Schwab, C. (2002). Local discontinuous galerkin methods for the stokes system. *SIAM Journal on Numerical Analysis*, 40(1):319–343.
- [54] Cockburn, B., Karniadakis, G. E., and Shu, C.-W. (2000). The development of discontinuous galerkin methods. In Cockburn, B., Karniadakis, G. E., and Shu, C.-W., editors, *Discontinuous Galerkin Methods*, volume 11 of *Lecture Notes in Computational Science and Engineering*, pages 3–50. Springer Berlin Heidelberg.
- [55] Cockburn, B., Lin, S.-Y., and Shu, C.-W. (1989). Tvb runge-kutta local projection discontinuous galerkin finite element method for conservation laws iii: One-dimensional systems. *Journal of Computational Physics*, 84(1):90–113.
- [56] Cockburn, B., Luskin, M., Shu, C.-W., and Süli, E. (2003). Enhanced accuracy by post-processing for finite element methods for hyperbolic equations. *Mathematics of Computation*, 72:577–606.
- [57] Cockburn, B. and Shu, C.-W. (1988). The runge-kutta local projection p1-discontinuous-galerkin finite element method for scalar conservation laws. *1st National Fluid Dynamics Conference*, pages 636–656.
- [58] Cockburn, B. and Shu, C.-W. (1989). Tvb runge-kutta local projection discontinuous galerkin finite element method for conservation laws. ii. general framework. *Mathematics of Computation*, 52:411–435.
- [59] Cockburn, B. and Shu, C.-W. (1998a). The local discontinuous galerkin method for time-dependent convection-diffusion systems. *SIAM Journal on Numerical Analysis*, 35(6):2440–2463.
- [60] Cockburn, B. and Shu, C.-W. (1998b). The runge–kutta discontinuous galerkin method for conservation laws v: Multidimensional systems. *Journal of Computational Physics*, 141(2):199–224.
- [61] Collis, D. C. and Williams, M. J. (1959). Two-dimensional convection from heated wires at low reynolds numbers. *Journal of Fluid Mechanics*, 6:357–384.

-
- [62] Coons, S. A. (1967). Surfaces for computer-aided design of space forms. Technical report.
- [63] Crowe, C. T., Schwarzkopf, J. D., Sommerfeld, M., and Tsuji, Y. (2011). *Multiphase flows with droplets and particles*. CRC press.
- [64] Curtin, S., Kirby, R., Ryan, J., and Shu, C.-W. (2008). Post-processing for the discontinuous galerkin method over non-uniform meshes. *SIAM Journal on Scientific Computing*, 30(1):272–289.
- [65] Cuthill, E. and McKee, J. (1969). Reducing the bandwidth of sparse symmetric matrices. In *Proceedings of the 1969 24th National Conference*, ACM '69, pages 157–172. Association for Computing Machinery.
- [66] Dance, S. L. and Maxey, M. R. (2003). Incorporation of lubrication effects into the force-coupling method for particulate two-phase flow. *Journal of Computational Physics*, 189(1):212–238.
- [67] Demkowicz, L., Kurtz, J., Pardo, D., Paszynski, M., Rachowicz, W., and Zdunek, A. (2006). *Computing with hp-Adaptive Finite Elements: Vol. 1, One and Two Dimensional Elliptic and Maxwell Problems, Applied Mathematics and Nonlinear Science*. Chapman and Hall/CRC.
- [68] Demkowicz, L., Kurtz, J., Pardo, D., Paszynski, M., Rachowicz, W., and Zdunek, A. (2007). *Computing with Hp-Adaptive Finite Elements, Vol. 2: Frontiers Three Dimensional Elliptic and Maxwell Problems with Applications*. Chapman and Hall/CRC.
- [69] Domesi, S. (2006). Particle dynamics in the axisymmetric toroidal flow in thermocapillary liquid bridges: towards understanding PAS. *Microgravity Sci. Technol.*, 18:137–140.
- [70] Domesi, S. (2008). *Numerical analysis of particle dynamics in the thermocapillary flow of liquid bridges*. PhD thesis, University of Bremen.
- [71] Donea, J., Giuliani, S., and Halleux, J. P. (1982). An arbitrary lagrangian-eulerian finite element method for transient dynamic fluid-structure interactions. *Computer Methods in Applied Mechanics and Engineering*, 33(1–3):689–723.
- [72] Dong, S., Liu, D., Maxey, M. R., and Karniadakis, G. E. (2004). Spectral distributed lagrange multiplier method: Algorithm and benchmarktests. *Journal of Computational Physics*, 195(2):695–717.
- [73] Dormand, J. R. and Prince, P. J. (1980). A family of embedded runge-kutta formulae. *Journal of Computational and Applied Mathematics*, 6(1):19–26.
- [74] Dumbser, M. and Käser, M. (2006). An arbitrary high-order discontinuous galerkin method for elastic waves on unstructured meshes - ii. the three-dimensional isotropic case. *Geophysical Journal International*, 167(1):319–336.
- [75] Dütsch, H., Durst, F., Becker, S., and Lienhart, H. (1998). Low-reynolds-number flow around an oscillating circular cylinder at low keulegan-carpenter numbers. *Journal of Fluid Mechanics*, 360:249–271.
- [76] Faldun, E., Verzicco, R., Orlandi, P., and Mohd-Yusof, J. (2000). Combined immersed-boundary finite-difference methods for three dimensional complex flow simulations. *Journal of Computational Physics*, 161:30–60.

- [77] Ferrer, E. (2012). *A High-Order Discontinuous Galerkin-Fourier Incompressible 3D Navier-Stokes Solver with Rotating Sliding Meshes for Simulating Cross-Flow Turbines*. PhD thesis, University of Oxford.
- [78] Ferrer, E. and Willden, R. H. J. (2011). A high order discontinuous galerkin finite element solver for the incompressible navier-stokes equations. *Computers and Fluids*, 46(1):224–230.
- [79] Filippov, A. F. (2013). *Differential equations with discontinuous righthand sides: control systems*, volume 18. Springer Science & Business Media.
- [80] Fogelson, A. L. and Peskin, C. S. (1988). A fast numerical method for solving the three-dimensional stokes' equations in the presence of suspended particles. *Journal of Computational Physics*, 79(1):50–69.
- [81] Forrest, A. R. (1968). *Curves and Surfaces for Computer Aided Design*. PhD thesis, Cambridge University.
- [82] Forrest, A. R. (1971). Coons surfaces and multivariable functional interpolation. *Cambridge University CAD Group Document 38*.
- [83] Funaro, D. (1986). A multidomain spectral approximation of elliptic equations. *Numerical Methods for Partial Differential Equations*, 2(3):187–205.
- [84] Funaro, D. and Gottlieb, D. (1988). A new method of imposing boundary conditions in pseudospectral approximations of hyperbolic equations. *Mathematics of Computation*, 51:599–613.
- [85] Funaro, D. and Gottlieb, D. (1991). Convergence results for pseudospectral approximations of hyperbolic systems by a penalty-type boundary treatment. *Mathematics of Computation*, 57:585–596.
- [86] Geurts, B. J., Clercx, H., and Uijtewaal, W., editors (2007). *Particle-laden flow : from geophysical to Kolmogorov scales*, volume 11 of *ERCOfTAC series ; 11*. Springer, Berlin, Germany.
- [87] Ghia, U., Ghia, K. N., and Shin, C. T. (1982). High-re solutions for incompressible flow using the navier-stokes equations and a multigrid method. *Journal of Computational Physics*, 48(3):387–411.
- [88] Gilmanov, A. and Sotiropoulos, F. (2005). A hybrid cartesian/immersed boundary method for simulating flows with 3d, geometrically complex, moving bodies. *Journal of Computational Physics*, 207(2):457–492.
- [89] Giraldo, F. X., Hesthaven, J. S., and Warburton, T. (2002). Nodal high-order discontinuous galerkin methods for the spherical shallow water equations. *Journal of Computational Physics*, 181(2):499–525.
- [90] Glowinski, R., Pan, T.-W., Hesla, T. I., and Joseph, D. D. (1999). A distributed lagrange multiplier/fictitious domain method for particulate flows. *International Journal of Multiphase Flow*, 25(5):755–794.
- [91] Glowinski, R., Pan, T.-W., Hesla, T. I., Joseph, D. D., and Periaux, J. (2000). A distributed lagrange multiplier/fictitious domain method for the simulation of flow around moving rigid bodies: Application to particulateflow. *Computer Methods in Applied Mechanics and Engineering*, 184(2–4):241–267.

-
- [92] Glowinski, R., Pan, T.-W., Hesla, T. I., Joseph, D. D., and Périaux, J. (2001). A fictitious domain approach to the direct numerical simulation of incompressible viscous flow past moving rigid bodies: Application to particulate flow. *Journal of Computational Physics*, 169(2):363–426.
- [93] Goda, K. (1979). A multistep technique with implicit difference schemes for calculating two- or three-dimensional cavity flows. *Journal of Computational Physics*, 30(1):76–95.
- [94] Goldstein, D., Handler, R., and Sirovich, L. (1993). Modeling a no-slip flow boundary with an external force field. *Journal of Computational Physics*, 105(2):354–366.
- [95] Gordon, W. J. (1969a). Distributive lattices and the approximation of multivariate functions. *Approximation with Special Emphasis on Spline Functions*, pages 223–277.
- [96] Gordon, W. J. (1969b). Free-form surface interpolation through curve networks. Technical report.
- [97] Gordon, W. J. (1969c). Spline-blended surface interpolation through curve networks. *Journal of Mathematics and Mechanics*, 18(10):931–952.
- [98] Gordon, W. J. (1971). Blending-function methods of bivariate and multivariate interpolation and approximation. *SIAM Journal on Numerical Analysis*, 8(1):158–177.
- [99] Gordon, W. J. and Hall, C. A. (1973a). Construction of curvilinear co-ordinate systems and applications to mesh generation. *International Journal for Numerical Methods in Engineering*, 7(4):461–477.
- [100] Gordon, W. J. and Hall, C. A. (1973b). Transfinite element methods: Blending-function interpolation over arbitrary curved element domains. *Numerische Mathematik*, 21(2):109–129.
- [101] Gordon, W. J. and Thiel, L. C. (1982). Transfinite mappings and their application to grid generation. *Applied Mathematics and Computation*, 10–11(0):171–233.
- [102] Gotoda, M., Melnikov, D. E., Ueno, I., and Shevtsova, V. (2016a). Experimental study on dynamics of coherent structures formed by inertial solid particles in three-dimensional periodic flows. *Chaos*, 26(7):073106.
- [103] Gotoda, M., Sano, T., Kaneko, T., and Ueno, I. (2015). Evaluation of existence region and formation time of particle accumulation structure (pas) in half-zone liquid bridge. *The European Physical Journal Special Topics*, 224(2):299–307.
- [104] Gotoda, M., Toyama, A., Ishimura, M., Sano, T., Suzuki, M., Kaneko, T., and Ueno, I. (2016b). Experimental study on dynamics of finite-size particles in coherent structures induced by thermocapillary effect in deformable liquid bridge. *Phys. Rev. Fluids*.
- [105] Goyon, O. (1996). High-reynolds number solutions of navier–stokes equations using incremental unknowns. *Computer Methods in Applied Mechanics and Engineering*, 130(3–4):319–335.
- [106] Guckenheimer, J. and Holmes, P. (1983). *Nonlinear Oscillations, Dynamical Systems, and Bifurcations of Vector Fields*, volume 42 of *Applied Mathematical Sciences*. Springer.
- [107] Guermond, J. L., Mineev, P., and Shen, J. (2006). An overview of projection methods for incompressible flows. *Archive for Rational Mechanics and Analysis*, 195(44–47):6011–6045.

- [108] Guermond, J. L. and Shen, J. (2003a). A new class of truly consistent splitting schemes for incompressible flows. *Journal of Computational Physics*, 192(1):262–276.
- [109] Guermond, J. L. and Shen, J. (2003b). Velocity-correction projection methods for incompressible flows. *SIAM Journal on Numerical Analysis*, 41(1):112–134.
- [110] Haddad, W. M. and Sadikhov, T. (2013). Dissipative differential inclusions, set-valued energy storage and supply rate maps, and stability of discontinuous feedback systems. *Nonlinear Analysis: Hybrid Systems*, 8:83–108.
- [111] Hajisharifi, A. (2016). Topology of three-dimensional steady cellular flow in a partially liquid-filled rotating drum. Master’s thesis, TU Wien and University of Pisa.
- [112] Haller, G. and Sapsis, T. (2008). Where do inertial particles go in fluid flows? *Physica D: Nonlinear Phenomena*, 237(5):573–583.
- [113] Harbrecht, H. and Randrianarivony, M. (2010). From computer aided design to wavelet bem. *Computing and Visualization in Science*, 13(2):69–82.
- [114] Hartmann, R. and Houston, P. (2006a). Symmetric interior penalty dg methods for the compressible navier–stokes equations i: Goal-oriented a posteriori error estimation. *International Journal of Numerical Analysis and Modeling*, 3:141–162.
- [115] Hartmann, R. and Houston, P. (2006b). Symmetric interior penalty dg methods for the compressible navier–stokes equations i: Method formulation. *International Journal of Numerical Analysis and Modeling*, 3:1–20.
- [116] Heinrichs, W. (2005). Improved lebesgue constants on the triangle. *Journal of Computational Physics*, 207(2):625–638.
- [117] Hesthaven, J. (1997). A stable penalty method for the compressible navier–stokes equations: Ii. one-dimensional domain decomposition schemes. *SIAM Journal on Scientific Computing*, 18(3):658–685.
- [118] Hesthaven, J. (1998). A stable penalty method for the compressible navier–stokes equations: Iii. multidimensional domain decomposition schemes. *SIAM Journal on Scientific Computing*, 20(1):62–93.
- [119] Hesthaven, J. (2000). Spectral penalty methods. *Applied Numerical Mathematics*, 33(1–4):23–41.
- [120] Hesthaven, J. and Gottlieb, D. (1996). A stable penalty method for the compressible navier–stokes equations: I. open boundary conditions. *SIAM Journal on Scientific Computing*, 17(3):579–612.
- [121] Hesthaven, J. and Gottlieb, D. (1999). Stable spectral methods for conservation laws on triangles with unstructured grids. *Computer Methods in Applied Mechanics and Engineering*, 175(3–4):361–381.
- [122] Hesthaven, J. and Teng, C. (2000). Stable spectral methods on tetrahedral elements. *SIAM Journal on Scientific Computing*, 21(6):2352–2380.
- [123] Hesthaven, J. S. and Warburton, T. (2007). *Nodal Discontinuous Galerkin Methods: Algorithms, Analysis, and Applications*. Springer Science and Business Media.

-
- [124] Hirt, C. W. (1971). An arbitrary lagrangian-eulerian computing technique. In Holt, M., editor, *Proceedings of the Second International Conference on Numerical Methods in Fluid Dynamics*, volume 8 of *Lecture Notes in Physics*, pages 350–355. Springer Berlin Heidelberg.
- [125] Hirt, C. W., Amsden, A. A., and Cook, J. L. (1974). An arbitrary lagrangian-eulerian computing method for all flow speeds. *Journal of Computational Physics*, 14(3):227–253.
- [126] Hofmann, E. and Kuhlmann, H. C. (2011). Particle accumulation on periodic orbits by repeated free surface collisions. *Physics of Fluids (1994-present)*, 23(7):072106.
- [127] Houston, P., Schwab, C., and Süli, E. (2002). Discontinuous hp-finite element methods for advection-diffusion-reaction problems. *SIAM Journal on Numerical Analysis*, 39(6):2133–2163.
- [128] Hu, H. H. (1996). Direct simulation of flows of solid-liquid mixtures. *International Journal of Multiphase Flow*, 22(2):335–352.
- [129] Hu, H. H., Patankar, N. A., and Zhu, M. Y. (2001). Direct numerical simulations of fluid–solid systems using the arbitrary lagrangian–eulerian technique. *Journal of Computational Physics*, 169(2):427–462.
- [130] Huang, H. and Takagi, S. (2003). Physalis: a new method for particle flow simulation. part iii: Convergence analysis of two-dimensional flows. *Journal of Computational Physics*, 189(2):493–511.
- [131] Hughes, T. J. R., Liu, W. K., and Zimmermann, T. K. (1981). Lagrangian-eulerian finite element formulation for incompressible viscous flows. *Computer Methods in Applied Mechanics and Engineering*, 29(3):329–349.
- [132] Jafari, S., Yamamoto, R., and Rahnama, M. (2011). Lattice-boltzmann method combined with smoothed-profile method for particulate suspensions. *Physical Review E*, 83:026702.
- [133] John, V. (2004). Reference values for drag and lift of a two-dimensional time-dependent flow around a cylinder. *International Journal for Numerical Methods in Fluids*, 44(7):777–788.
- [134] Johnson, A. A. and Tezduyar, T. E. (1997). 3d simulation of fluid-particle interactions with the number of particles reaching 100. *Computer Methods in Applied Mechanics and Engineering*, 145(3–4):301–321.
- [135] Johnson, A. A. and Tezduyar, T. E. (1999). Advanced mesh generation and update methods for 3d flow simulations. *Computational Mechanics*, 23(2):130–143.
- [136] Johnson, C. and Pitkäranta, J. (1986). An analysis of the discontinuous galerkin method for a scalar hyperbolic equation. *Mathematics of Computation*, 46(173):1–26.
- [137] Kang, S. and Suh, Y. K. (2011). Direct simulation of flows with suspended paramagnetic particles using one-stage smoothed profile method. *Journal of Fluids and Structures*, 27(2):266–282.
- [138] Karniadakis, G. and Sherwin, S. (1999). *Spectral/hp Element Methods for CFD, Numerical Mathematics and Scientific Computation*. Clarendon Press.
- [139] Karniadakis, G. and Sherwin, S. (2013). *Spectral/hp Element Methods in Computational Fluid Dynamics*. Oxford University Press.

- [140] Karniadakis, G. E. and Hesthaven, J. H. (2006). Spectral interpolation in non-orthogonal domains: Algorithms and applications. *Journal of Engineering Mathematics*, 56(3):201–202.
- [141] Karniadakis, G. E., Israeli, M., and Orszag, S. A. (1991). High-order splitting methods for the incompressible navier–stokes equations. *Journal of Computational Physics*, 97(2):414–443.
- [142] Kim, J. and Moin, P. (1985). Application of a fractional-step method to incompressible navier–stokes equations. *Journal of Computational Physics*, 59(2):308–323.
- [143] Kim, K., Nakayama, Y., and Yamamoto, R. (2005). A smoothed profile method for simulating charged colloidal dispersions. *Computer Physics Communications*, 169(1–3):104–106.
- [144] Kim, K., Nakayama, Y., and Yamamoto, R. (2006). Direct numerical simulations of electrophoresis of charged colloids. *Physical Review Letters*, 96:208302.
- [145] Kim, K. and Yamamoto, R. (2005). Efficient simulations of charged colloidal dispersions: A density functional approach. *Macromolecular Theory and Simulations*, 14(4):278–284.
- [146] Kuhlmann, H. and Lemée, T. (2016). Particle accumulation in the jeremi experiment: Definition of necessary flow and particle parameters. FFG: ASAP 9 3604313, TU Wien.
- [147] Kuhlmann, H. C. (1999). *Thermocapillary Convection in Models of Crystal Growth*. Springer Tracts in Modern Physics.
- [148] Kuhlmann, H. C. and Albensoeder, S. (2008). Three-dimensional flow instabilities in a thermocapillary-driven cavity. *Physical Review E*, 77:036303.
- [149] Kuhlmann, H. C., Lappa, M., Melnikov, D., Mukin, R., Muldoon, F. H., Pushkin, D., Shevtsova, V., and Ueno, I. (2014a). The JEREMI-project on thermocapillary convection in liquid bridges. Part a: Overview of particle accumulation structures. *Fluid Dyn. Mat. Proc.*, 10:1–36.
- [150] Kuhlmann, H. C. and Lemée, T. (2015a). Particle accumulation in the jeremi experiment: Definition of necessary flow and particle parameters. ASAP9 840119, FFG.
- [151] Kuhlmann, H. C. and Lemée, T. (2015b). Particle-depletion dynamics in axisymmetric thermocapillary flows. *Eur. Phys. J. Special Topics*, 224:309–318.
- [152] Kuhlmann, H. C., Mukin, R. V., Sano, T., and Ueno, I. (2014b). Structure and dynamics of particle-accumulation in thermocapillary liquid bridges. *Fluid Dyn. Res.*, 46(4):041421.
- [153] Kuhlmann, H. C. and Muldoon, F. H. (2012a). Comment on “Ordering of small particles in one-dimensional coherent structures by time-periodic flows”. *Phys. Rev. Lett.*, 108(24):249401.
- [154] Kuhlmann, H. C. and Muldoon, F. H. (2012b). Particle-accumulation structures in periodic free-surface flows: Inertia versus surface collisions. *Phys. Rev. E*, 85:046310.
- [155] Kuhlmann, H. C. and Muldoon, F. H. (2013). On the different manifestations of particle accumulation structures (PAS) in thermocapillary flows. *Eur. Phys. J. Special Topics*, 219:59–69.
- [156] Kuhlmann, H. C. and Muldoon, F. H. (2014). Comment on “Synchronization of finite-size particles by a traveling wave in a cylindrical flow” [Phys. Fluids 25, 092108 (2013)]. *Phys. Fluids*, 26(9):099101.

-
- [157] Kuhlmann, H. C., Wanschura, M., and Rath, H. J. (1997). Flow in two-sided lid-driven cavities: non-uniqueness, instabilities, and cellular structures. *Journal of Fluid Mechanics*, 336:267–299.
- [158] Lai, M.-C. and Peskin, C. S. (2000). An immersed boundary method with formal second-order accuracy and reduced numerical viscosity. *Journal of Computational Physics*, 160(2):705–719.
- [159] Landmann, B., Kessler, M., Wagner, S., and Krämer, E. (2008). A parallel, high-order discontinuous galerkin code for laminar and turbulent flows. *Computers and Fluids*, 37(4):427–438.
- [160] Lappa, M. (2013a). Assessment of the role of axial vorticity in the formation of particle accumulation structures in supercritical marangoni and hybrid thermocapillary-rotation-driven flows. *Phys. Fluids*, 25:012101.
- [161] Lappa, M. (2013b). On the existence and multiplicity of one-dimensional solid particle attractors in time-dependent Rayleigh-Bénard convection. *Chaos*, 23(1):013105.
- [162] Lappa, M. (2013c). On the variety of particle accumulation structures under the effect of g-jitters. *J. Fluid Mech.*, 726:160–195.
- [163] Lappa, M. (2014). Stationary solid particle attractors in standing waves. *Phys. Fluids*, 26(1):013305.
- [164] Lee, L. and LeVeque, R. J. (2003). An immersed interface method for incompressible navier–stokes equations. *SIAM Journal on Scientific Computing*, 25(3):832–856.
- [165] LeSaint, P. and Raviart, P. (1974). On a finite element method for solving the neutron transport equation. *Mathematical Aspects of Finite Elements in Partial Differential Equations*, pages 89–145.
- [166] LeVeque, R. J. and Li, Z. (1997). Immersed interface methods for stokes flow with elastic boundaries or surface tension. *SIAM Journal on Scientific Computing*, 18(3):709–735.
- [167] Leypoldt, J., Kuhlmann, H. C., and Rath, H. J. (2000). Three-dimensional numerical simulation of thermocapillary flows in cylindrical liquid bridges. *Journal of Fluid Mechanics*, 414:285–314.
- [168] Li, B. Q. (2006). *Discontinuous Finite Elements in Fluid Dynamics and Heat Transfer*. Springer Science and Business Media.
- [169] Li, Z. and Lai, M.-C. (2001). The immersed interface method for the navier–stokes equations with singular forces. *Journal of Computational Physics*, 171(2):822–842.
- [170] Lin, G. and Karniadakis, G. E. (2006). A discontinuous galerkin method for two-temperature plasmas. *Computer Methods in Applied Mechanics and Engineering*, 195(25–28):3504–3527.
- [171] Lin, Q. and Zhou, A. H. (1993). Convergence of the discontinuous galerkin method for a scalar hyperbolic equation. *Acta Mathematica Scientia*, 13(2):207–210.
- [172] Liu, A. W., Bornside, D. E., Armstrong, R. C., and Brown, R. A. (1998). Viscoelastic flow of polymer solutions around a periodic, linear array of cylinders: comparisons of predictions for microstructure and flow fields. *Journal of Non-Newtonian Fluid Mechanics*, 77(3):153–190.

- [173] Liu, D., Maxey, M. R., and Karniadakis, G. E. (2002). A fast method for particulate microflows. *Journal of Microelectromechanical Systems*, 11(6):691–702.
- [174] Liu, D., Maxey, M. R., and Karniadakis, G. E. (2003). Fcm-spectral element method for simulating colloidal micro-devices. *Computational Fluid and Solid Mechanics*, pages 1413–1416.
- [175] Liu, D. and Zheng, Y. (2014). Modal spectral element solutions to incompressible flows over particles of complex shape. *Journal of Computational Engineering*, pages 1–11.
- [176] Liu, J.-G. and Shu, C.-W. (2000). A high-order discontinuous galerkin method for 2d incompressible flows. *Journal of Computational Physics*, 160(2):577–596.
- [177] Liu, L., Zheng, H., Williams, L., Zhang, F., Wang, R., Hertzberg, J., and Shandas, R. (2008). Development of a custom-designed echo particle image velocimetry system for multi-component hemodynamic measurements: system characterization and initial experimental results. *Physics in Medicine and Biology*, 53(5):1397–1412.
- [178] Löhner, R. and Yang, C. (1998). Improved ale mesh velocities for moving bodies. *Communications in Numerical Methods in Engineering*, (12):599–608.
- [179] Lomholt, S. and Maxey, M. R. (2003). Force-coupling method for particulate two-phase flow: Stokes flow. *Journal of Computational Physics*, 184(2):381–405.
- [180] Lomtev, I. (1999). *A Discontinuous Galerkin Method for the Compressible Navier-Stokes Equations in Stationary and Moving 3D Domains*. PhD thesis, Brown University.
- [181] Lomtev, I. and Karniadakis, G. E. (1999). A discontinuous galerkin method for the navier-stokes equations. *International Journal for Numerical Methods in Fluids*, 29(5):587–603.
- [182] Lomtev, I., Kirby, R. M., and Karniadakis, G. E. (1999). A discontinuous galerkin ale method for compressible viscous flows in moving domains. *Journal of Computational Physics*, 155(1):128–159.
- [183] Luo, H., Baum, J. D., and Löhner, R. (2007). A hermite weno-based limiter for discontinuous galerkin method on unstructured grids. *Journal of Computational Physics*, 225(1):686–713.
- [184] Luo, X., Beskok, A., and Karniadakis, G. E. (2010a). Modeling electrokinetic flows by the smoothed profile method. *Journal of Computational Physics*, 229(10):3828–3847.
- [185] Luo, X., Chrysosostomidis, C., and Karniadakis, G. E. (2009a). Fast 3d flow simulations of a waterjet propulsion system. In *Proceedings of the 2009 Grand Challenges in Modeling & Simulation Conference*, GCMS '09, pages 112–120. Society for Modeling & Simulation International.
- [186] Luo, X., Chrysosostomidis, C., and Karniadakis, G. E. (2010b). Spectral element/smoothed profile method for turbulent flow simulations of waterjet propulsion systems. In *Proceedings of the 2010 Conference on Grand Challenges in Modeling and Simulation*, GCMS '10, pages 129–135. Society for Modeling and Simulation International.
- [187] Luo, X., Maxey, M. R., and Karniadakis, G. E. (2009b). Smoothed profile method for particulate flows: Error analysis and simulations. *Journal of Computational Physics*, 228(5):1750–1769.

-
- [188] Maxey, M. R. and Patel, B. K. (2001). Localized force representations for particles sedimenting in stokes flow. *International Journal of Multiphase Flow*, 27(9):1603–1626.
- [189] Maxey, M. R. and Riley, J. J. (1983). Equation of motion for a small rigid sphere in a nonuniform flow. *Physics of Fluids*, 26(4):883–889.
- [190] Melnikov, D. E., Pushkin, D. O., and Shevtsova, V. M. (2013). Synchronization of finite-size particles by a traveling wave in a cylindrical flow. *Physics of Fluids*, 25(9):092108.
- [191] Mizev, A., Trofimenko, A., Schwabe, D., and Viviani, A. (2013). Instability of Marangoni flow in the presence of an insoluble surfactant. experiments. *Eur. Phys. J. Special Topics*, 219:89–98.
- [192] Montlaur, A., Fernandez-Mendez, S., and Huerta, A. (2008). Discontinuous galerkin methods for the stokes equations using divergence-free approximations. *International Journal for Numerical Methods in Fluids*, 57(9):1071–1092.
- [193] Mozolevski, I., Süli, E., and Bösing, P. R. (2007). Discontinuous galerkin finite element approximation of the two-dimensional navier–stokes equations in stream-function formulation. *Communications in Numerical Methods in Engineering*, 23(6):447–459.
- [194] Mukin, R. V. and Kuhlmann, H. C. (2013). Topology of hydrothermal waves in liquid bridges and dissipative structures of transported particles. *Physical Review E*, 88:053016.
- [195] Muldoon, F. H. and Kuhlmann, H. C. (2013a). Coherent particulate structures by boundary interaction of small particles in confined periodic flows. *Physica D: Nonlinear Phenomena*, 253:40–65.
- [196] Muldoon, F. H. and Kuhlmann, H. C. (2013b). Numerical error in modeling of particle-accumulation structures in periodic free-surface flows. *Computers & Fluids*, 88:43–50.
- [197] Muldoon, F. H. and Kuhlmann, H. C. (2016). Origin of particle accumulation structures in liquid bridges: particle–boundary interactions versus inertia. *Phys. Fluids*, 28(7).
- [198] Nakayama, Y., Kim, K., and Yamamoto, R. (2006). Hydrodynamic effects in colloidal dispersions studied by a new efficient direct simulation. *Flow Dynamics*, 832:245–250.
- [199] Nakayama, Y., Kim, K., and Yamamoto, R. (2008). Simulating (electro)hydrodynamic effects in colloidal dispersions: Smoothed profile method. *The European Physical Journal E*, 26(4):361–368.
- [200] Nakayama, Y., Kim, K., and Yamamoto, R. (2010). Direct simulation of flowing colloidal dispersions by smoothed profile method. *Advanced Powder Technology*, 21(2):206–211.
- [201] Nakayama, Y. and Yamamoto, R. (2005). Simulation method to resolve hydrodynamic interactions in colloidal dispersions. *Physical Review E*, 71:036707.
- [202] Neitzel, G. P., Chang, K. T., Jankowski, D. F., and Mittelman, H. D. (1992). Linear-stability theory of thermocapillary convection in a model of the float-zone crystal-growth process. *Physics of Fluids A*, 5(1):108–114.
- [203] Nguyen, N., Persson, P.-O., and Peraire, J. (2007). Rans solutions using high order discontinuous galerkin methods. volume 25.

- [204] Nguyen, N. C., Peraire, J., and Cockburn, B. (2011). An implicit high-order hybridizable discontinuous galerkin method for the incompressible navier–stokes equations. *Journal of Computational Physics*, 230(4):1147–1170.
- [205] Nienhüser, C. H. and Kuhlmann, H. C. (2002). Stability of thermocapillary flows in non-cylindrical liquid bridges. *Journal of Fluid Mechanics*, 458:35–73.
- [206] Niigaki, Y. and Ueno, I. (2013). Formation of particle accumulation structure (PAS) in half-zone liquid bridge under an effect of thermo-fluid flow of ambient gas. *Trans. Jap. Soc. Aeronaut. Space Sci.*, 10:Ph33–Ph37.
- [207] Nobile, F. (2001). *Numerical Approximation of Fluid–Structure Interaction Problems with Application to Haemodynamics*. PhD thesis, École Polytechnique Fédérale de Lausanne.
- [208] Oden, J. T., Babuška, I., and Baumann, C. E. (1998). A discontinuous hp finite element method for diffusion problems. *Computer Methods in Applied Mechanics and Engineering*, 146(2):491–519.
- [209] Oliver, T. and Darmofal, D. (2007). An unsteady adaptation algorithm for discontinuous galerkin discretizations of the rans equations.
- [210] Orszag, S. T., Israeli, M., and Deville, M. O. (1986). Boundary conditions for incompressible flows. *Journal of Scientific Computing*, 1(1):75–111.
- [211] Ottino, J. M. and Khakhar, D. V. (2000). Mixing and segregation of granular materials. *Annu. Rev. Fluid Mech.*, 32:55–91.
- [212] Padday, J. F. (1976). Capillary forces and stability in zero-gravity environments. In Battrick, B., editor, *ESA Special Publication*, volume 114 of *ESA Special Publication*, pages 447–454.
- [213] Pan, T.-W., Joseph, D. D., Bai, R., Glowinski, R., and Sarin, V. (2002). Fluidization of 1204 spheres: simulation and experiment. *Journal of Fluid Mechanics*, 451:169–191.
- [214] Pan, T. W., Joseph, D. D., and Glowinski, R. (2001). Modelling rayleigh–taylor instability of a sedimenting suspension of several thousand circular particles in a direct numerical simulation. *Journal of Fluid Mechanics*, 434:23–37.
- [215] Patankar, N. A., Singh, P., Joseph, D. D., Glowinski, R., and T.-W.Pan (2000). A new formulation of the distributed lagrange multiplier/fictitious domain method for particulate flows. *International Journal of Multiphase Flow*, 26(9):1509–1524.
- [216] Peltier, L. J. and Biringen, S. (1993). Time-dependent thermocapillary convection in a rectangular cavity: Numerical results for a moderate prandtl number fluid. *Journal of Fluid Mechanics*, 257:339–357.
- [217] Pena, G. (2009). *Spectral Element Approximation of the Incompressible Navier–Stokes Equations in a Moving Domain and Applications*. PhD thesis, École Polytechnique Fédérale de Lausanne.
- [218] Pena, G., Prud’homme, C., and Quarteroni, A. (2012). High order methods for the approximation of the incompressible navier–stokes equations in a moving domain. *Computer Methods in Applied Mechanics and Engineering*, 209–212(0):197–211.

-
- [219] Perronnet, A. (1998). Interpolation transfinie sur le triangle, le tétraèdre et le pentaèdre. application à la création de maillages et à la condition de dirichlet. *Comptes Rendus de l'Académie des Sciences - Series I - Mathematics*, 326(1):117–122.
- [220] Persson, P.-O., Bonet, J., and Peraire, J. (2009). Discontinuous galerkin solution of the navier–stokes equations on deformable domains. *Computer Methods in Applied Mechanics and Engineering*, 198(17–20):1585–1595.
- [221] Perugia, I. and Schötzau, D. (2002). An hp-analysis of the local discontinuous galerkin method for diffusion problems. *Journal of Scientific Computing*, 17:561–571.
- [222] Peskin, C. S. (2002). The immersed boundary method. *Acta Numerica*, 11:479–517.
- [223] Peterson, T. (1991). A note on the convergence of the discontinuous galerkin method for a scalar hyperbolic equation. *SIAM Journal on Numerical Analysis*, 28(1):133–140.
- [224] Pianet, G. and Arquis, E. (2008). Simulation of particles in fluid: a two-dimensional benchmark for a cylinder settling in a wall-bounded box. *European Journal of Mechanics - B/Fluids*, 27(3):309–321.
- [225] Pietro, D. A. D. and Ern, A. (2011). *Mathematical Aspects of Discontinuous Galerkin Methods*. Springer Science and Business Media.
- [226] Pikovsky, A., Rosenblum, M., and Kurths, J. (2003). *Synchronization: a universal concept in nonlinear sciences*, volume 12. Cambridge university press.
- [227] Prosperetti, A. and guz, H. O. (2001). Physalis: A new $\mathcal{O}(n)$ method for the numerical simulation of disperse systems: Potential flow of spheres. *Journal of Computational Physics*, 167(1):196–216.
- [228] Pushkin, D. O., Melnikov, D. E., and Shevtsova, V. M. (2011). Ordering of small particles in one-dimensional coherent structures by time-periodic flows. *Physical Review Letters*, 106:234501.
- [229] Qiu, J. and Shu, C.-W. (2004). Hermite weno schemes and their application as limiters for runge–kutta discontinuous galerkin method: One-dimensional case. *Journal of Computational Physics*, 193(1):115–135.
- [230] Qiu, J. and Shu, C.-W. (2005a). A comparison of troubled-cell indicators for runge–kutta discontinuous galerkin methods using weighted essentially nonoscillatory limiters. *SIAM Journal on Scientific Computing*, 27(3):995–1013.
- [231] Qiu, J. and Shu, C.-W. (2005b). Hermite weno schemes and their application as limiters for runge–kutta discontinuous galerkin method ii: Two dimensional case. *Computers and Fluids*, 34(6):642–663.
- [232] Qiu, J. and Shu, C.-W. (2005c). Hermite weno schemes for hamilton–jacobi equations. *Journal of Computational Physics*, 204(1):82–99.
- [233] Qiu, J. and Shu, C.-W. (2005d). Runge-kutta discontinuous galerkin method using weno limiters. *SIAM Journal on Scientific Computing*, 26(3):907–929.
- [234] Quarteroni, A. and Valli, A. (2008). *Numerical Approximation of Partial Differential Equations*. Springer.

- [235] Randrianarivony, M. (2006). *Geometric Processing of CAD Data and Meshes as Input of Integral Equation Solvers*. PhD thesis.
- [236] Randrianarivony, M. (2008a). Tetrahedral transfinite interpolation with b-patch faces: Construction and regularity. *INS Preprint*, (0803).
- [237] Randrianarivony, M. (2008b). Topological transfinite interpolations in the multidimensional simplex and hypercube. *INS Preprint*, (0808).
- [238] Randrianarivony, M. (2009). On global continuity of coons mappings in patching cad surfaces. *Computer Aided Design*, 41:782–791.
- [239] Randrianarivony, M. (2011). Coons’ generalization for polytopes. *INS Preprint*.
- [240] Reed, W. H. and Hill, T. R. (1973). Triangular mesh methods for the neutron transport equation. Technical report, Los Alamos Scientific Laboratory Report.
- [241] Rivière, B. (2008). *Discontinuous Galerkin Methods For Solving Elliptic And Parabolic Equations: Theory and Implementation*. Society for Industrial and Applied Mathematics.
- [242] Roman, F., Napoli, E., Milici, B., and Armenio, V. (2009). An improved immersed boundary method for curvilinear grids. *Computers & Fluids*, 38(8):1510–1527.
- [243] Romanò, F., Albensoeder, S., and Kuhlmann, H. C. (2016a). Topology of three-dimensional steady cellular flow in a two-sided anti-parallel lid-driven cavity. *Journal of Fluid Mechanics*, (submitted).
- [244] Romanò, F. and Kuhlmann, H. C. (2016a). Numerical investigation of the interaction of a finite-size particle with a tangentially moving boundary. *International Journal of Heat and Fluid Flow*, (accepted).
- [245] Romanò, F. and Kuhlmann, H. C. (2016b). Smoothed-profile method for momentum and heat transfer in particulate flows. *International Journal of Numerical Methods in Fluids*, (accepted).
- [246] Romanò, F., Kuhlmann, H. C., Ishimura, M., and Ueno, I. (2016b). Particle–free-surface interaction in thermocapillary flows. prediction and observation of limit cycles in axisymmetric flow. (in preparation).
- [247] Ryan, J., Shu, C., and Atkins, H. (2005). Extension of a post processing technique for the discontinuous galerkin method for hyperbolic equations with application to an aeroacoustic problem. *Journal of Computational Physics*, 26(3):821–843.
- [248] Rybicki, A. and Floryan, J. M. (1987). Thermocapillary effects in liquid bridges. I. Thermocapillary convection. *Phys. Fluids*, 30:1956–1972.
- [249] Sahin, M. and Owens, R. G. (2003). A novel fully implicit finite volume method applied to the lid-driven cavity problem – part i: High reynolds number flow calculations. *International Journal for Numerical Methods in Fluids*, 42(1):57–77.
- [250] Sapsis, T. and Haller, G. (2010). Clustering criterion for inertial particles in two-dimensional time-periodic and three-dimensional steady flows. *Chaos: An Interdisciplinary Journal of Nonlinear Science*, 20(1):017515.

-
- [251] Savino, R. and Monti, R. (1996). Three-dimensional numerical simulation of thermocapillary instabilities in floating zones. *Applied Scientific Research*, 56(1):19–41.
- [252] Schreiber, R. and Keller, H. B. (1983). Driven cavity flows by efficient numerical techniques. *Journal of Computational Physics*, 49(2):310–333.
- [253] Schwabe, D. (1988). Surface-tension-driven flow in crystal growth melts. In Freyhardt, H. C., editor, *Crystals*, volume 11, pages 75–112. Springer.
- [254] Schwabe, D. and Frank, S. (1999). Particle accumulation structures (pas) in the toroidal thermocapillary vortex of a floating zone — model for a step in planet-formation? *Advances in Space Research*, 23(7):1191–1196.
- [255] Schwabe, D., Hintz, P., and Frank, S. (1996). New features of thermocapillary convection in floating zones revealed by tracer particle accumulation structures (pas). *Microgravity sci. technol.*, IX(3):163–168.
- [256] Schwabe, D., Mizev, A., Tanaka, S., and Kawamura, H. (2006). Particle accumulation structures in time-dependent thermocapillary flow in a liquid bridge under microgravity. *Microgravity - Science and Technology*, 18(3):117–127.
- [257] Schwabe, D. and Mizev, A. I. (2011). Particles of different density in thermocapillary liquid bridges under the action of travelling and standing hydrothermal waves. *The European Physical Journal Special Topics*, 192(1):13–27.
- [258] Schwabe, D., Mizev, A. I., Udhayasankar, M., and Tanaka, S. (2007). Formation of dynamic particle accumulation structures in oscillatory thermocapillary flow in liquid bridges. *Physics of Fluids*, 19(7):072102.
- [259] Schwabe, D. and Scharmann, A. (1988). Marangoni and buoyant convection in an open cavity under reduced and under normal gravity. *Adv. Space Res.*, 8(12):175–185.
- [260] Seetharaman, S. (2013). *Treatise on Process Metallurgy Process Phenomena*. Elsevier.
- [261] Seo, J. H. and Mittal, R. (2011). A sharp-interface immersed boundary method with improved mass conservation and reduced spurious pressure oscillations. *Journal of computational physics*, 230(19):7347–7363.
- [262] Sevilla, R. (2009). *NURBS-Enhanced Finite Element Method (NEFEM)*. PhD thesis, Universitat Politècnica de Catalunya.
- [263] Shahbazi, K., Fischer, P. F., and Ethier, C. R. (2007). A high-order discontinuous galerkin method for the unsteady incompressible navier–stokes equations. *Journal of Computational Physics*, 222(1):391–407.
- [264] Siegmund-Hegerfeld, T., Albensoeder, S., and Kuhlmann, H. C. (2008). Two- and three-dimensional flows in nearly rectangular cavities driven by collinear motion of two facing walls. *Experiments in Fluids*, 45(5):781–796.
- [265] Silicone, S.-E. (2016). Shin-etsu silicone oil catalog. Catalog of silicone fluid properties.
- [266] Smith, M. K. and Davis, S. H. (1983). Instabilities of dynamic thermocapillary liquid layers. part 1. convective instabilities. *Journal of Fluid Mechanics*, 132:119–144.

- [267] Squires, K. D. and Eaton, J. K. (1991). Preferential concentration of particles by turbulence. *Physics of Fluids A*, 3(5):1169–1178.
- [268] Takagi, S., guz, H. N. O., Zhang, Z., and Prosperetti, A. (2003). Physalis: a new method for particle simulation: Part ii: Two-dimensional navier–stokes flow around cylinders. *Journal of Computational Physics*, 187(2):371–390.
- [269] Takashi, N. and Hughes, T. J. R. (1992). An arbitrary lagrangian-eulerian finite element method for interaction of fluid and a rigid body. *Computer Methods in Applied Mechanics and Engineering*, 95(1):115–138.
- [270] Tanaka, S., Kawamura, H., Ueno, I., and Schwabe, D. (2006). Flow structure and dynamic particle accumulation in thermocapillary convection in a liquid bridge. *Physics of Fluids*, 18:067103.
- [271] Taylor, M., Wingate, B., and Vincent, R. (2000). An algorithm for computing feketé points in the triangle. *SIAM Journal on Numerical Analysis*, 38(5):1707–1720.
- [272] Témam, R. (1969). Sur l’approximation de la solution des Équations de navier–stokes par la méthode des pas fractionnaires (ii). *Archive for Rational Mechanics and Analysis*, 33(5):377–385.
- [273] Thompson, J. F., Warsi, Z. U., and Mastin, C. W. (1985). *Numerical grid generation: foundations and applications*, volume 45. North-holland Amsterdam.
- [274] Thoroddsen, T. S. and Mahadevan, L. (1997). Experimental study of coating flows in a partially-filled horizontally rotating cylinder. *Experiments in Fluids*, 23(1):1–13.
- [275] Timmermans, L. J. P., Mineev, P. D., and Vosse, F. N. V. D. (1996). An approximate projection scheme for incompressible flow using spectral elements. *International Journal for Numerical Methods in Fluids*, 22(7):673–688.
- [276] Tryggvason, G., Bunner, B., Esmaeeli, A., Juric, D., Al-Rawahi, N., Tauber, W., Han, J., Nas, S., and Jan, Y.-J. (2001). A front-tracking method for the computations of multiphase flow. *Journal of Computational Physics*, 169(2):708–759.
- [277] Udaykumar, H. S., Kan, H., Shyy, W., and Tran-Son-Tay, R. (1997). Multiphase dynamics in arbitrary geometries on fixed cartesian grids. *Journal of Computational Physics*, 137(2):366–405.
- [278] Ueno, I. (2016). (private communication).
- [279] Ueno, I., Abe, Y., Noguchi, K., and Kawamura, H. (2008). Dynamic particle accumulation structure (PAS) in half-zone liquid bridge – reconstruction of particle motion by 3-D PTV. *Adv. Space Res.*, 41:2145–2149.
- [280] Ueno, I., Ono, Y., Nagano, D., Tanaka, S., and Kawamura, H. (2000). Modal oscillatory structure and dynamic particle accumulation in liquid-bridge marangoni convection. *Proceedings of the JSME-KSME Thermal Engineering Conference*, 3:265–270.
- [281] Uhlmann, M. (2005). An immersed boundary method with direct forcing for the simulation of particulate flows. *Journal of Computational Physics*, 209(2):448–476.

- [282] Uranga, A., Persson, P.-O., Drela, M., and Peraire, J. (2011). Implicit large eddy simulation of transition to turbulence at low reynolds numbers using a discontinuous galerkin method. *International Journal for Numerical Methods in Engineering*, 87(1–5):232–261.
- [283] van Kan, J. (1986). A second-order accurate pressure-correction scheme for viscous incompressible flow. *SIAM Journal on Scientific and Statistical Computing*, 7(3):870–891.
- [284] Vanka, S. P. (1986). Block-implicit multigrid solution of navier–stokes equations in primitive variables. *Journal of Computational Physics*, 65(1):138–158.
- [285] Vinokur, M. (1983). On one-dimensional stretching functions for finite-difference calculations. *Journal of Computational Physics*, 50(2):215–234.
- [286] Šolín, P., Segeth, K., and Doležel, I. (2004). *Higher-order Finite Element Methods*. Chapman and Hall/CRC.
- [287] Wallraff, M. and Leicht, T. (2014). 3d application of higher order multigrid algorithms for a rans- $k - \omega$ dg-solver. In *High Order Nonlinear Numerical Schemes for Evolutionary PDEs*, volume 99 of *Lecture Notes in Computational Science and Engineering*, pages 77–88. Springer International Publishing.
- [288] Wang, S., Stewart, R. L., Metcalfe, G., and Wu, J. (2014). Kinematics of clustering. *arXiv preprint arXiv:1407.2331*.
- [289] Wanschura, M., Kuhlmann, H. C., and Rath, H. J. (1996). Three-dimensional instability of axisymmetric buoyant convection in cylinders heated from below. *Journal of Fluid Mechanics*, 326:399–415.
- [290] Wanschura, M., Kuhlmann, H. C., and Rath, H. J. (1997). Linear stability of two-dimensional combined buoyant-thermocapillary flow in cylindrical liquid bridges. *Phys. Rev. E*, 55:7036–7042.
- [291] Wanschura, M., Shevtsova, V. M., Kuhlmann, H. C., and Rath, H. J. (1995). Convective instability mechanisms in thermocapillary liquid bridges. *Physics of Fluids*, 7(5):912–925.
- [292] Warburton, A. B. T. (1998). Micro-fluidic design and fluid structure interaction analysis of a micropump. *Proceedings of ASME IMECE, CA, DSC*, 66:77–84.
- [293] Warburton, T. (1999). *Spectral/hp Methods on Polymorphic Multi-Domains: Algorithms and Applications*. PhD thesis, Brown University.
- [294] Warburton, T. (2000). Application of the discontinuous galerkin method to maxwell’s equations using unstructured polymorphic hp-finite elements. In Cockburn, B., Karniadakis, G. E., and Shu, C.-W., editors, *Discontinuous Galerkin Methods*, volume 11 of *Lecture Notes in Computational Science and Engineering*, pages 451–458. Springer Berlin Heidelberg.
- [295] Warburton, T. (2006). An explicit construction of interpolation nodes on the simplex. *Journal of Engineering Mathematics*, 56(3):247–262.
- [296] Warburton, T. and Karniadakis, G. E. (1997). Spectral simulations of flow past a cylinder close to a free surface. *ASME, FEDSM97-3389*.
- [297] Wesseling, P. (2009). *Principles of computational fluid dynamics*. Springer Science and Business Media.

- [298] Xu, J. and Zebib, A. (1998). Oscillatory two- and three-dimensional thermocapillary convection. *Journal of Fluid Mechanics*, 364:187–209.
- [299] Xu, J.-J. (1984). Steady axisymmetric thermocapillary motion of a short melting column. *Scientia Sinica A*, 27:372–391.
- [300] Yamamoto, R., Kim, K., and Nakayama, Y. (2007). Strict simulations of non-equilibrium dynamics of colloids. *Colloids and Surfaces A: Physicochemical and Engineering Aspects*, 311(1–3):42–47.
- [301] Yamamoto, R., Nakayama, Y., and Kim, K. (2005). A method to resolve hydrodynamic interactions in colloidal dispersions. *Computer Physics Communications*, 169(1–3):301–304.
- [302] Yamamoto, R., Nakayama, Y., and Kim, K. (2009). Smoothed profile method to simulate colloidal particles in complex fluids. *International Journal of Modern Physics C*, 20(09):1457–1465.
- [303] Yang, J. and Stern, F. (2014). A sharp interface direct forcing immersed boundary approach for fully resolved simulations of particulate flows. *Journal of Fluids Engineering*, 136(4):040904.
- [304] Zayernouri, M., Park, S.-W., Tartakovsky, D. M., and Karniadakis, G. E. (2013). Stochastic smoothed profile method for modeling random roughness in flow problems. *Computer Methods in Applied Mechanics and Engineering*, 263(0):99–112.
- [305] Zhang, Z. and Prosperetti, A. (2003). A method for particle simulation. *Journal of Applied Mechanics*, 70:64–74.
- [306] Zhang, Z. and Prosperetti, A. (2005). A second-order method for three-dimensional particle simulation. *Journal of Computational Physics*, 210(1):292–324.
- [307] Zienkiewicz, O. C., Taylor, R. L., Sherwin, S. J., and Peiró, J. (2003). On discontinuous galerkin methods. *International Journal for Numerical Methods in Engineering*, 58(8):1119–1148.

List of Publications

1. F. Romanò and H. C. Kuhlmann (2015). Interaction of a finite-size particle with the moving lid of a cavity, *PAMM*, **15** (1) 519–520.
2. F. Romanò and H. C. Kuhlmann (2016). Smoothed-profile method for momentum and heat transfer in particulate flows, *Int. J. Numer. Meth. Fluids*, <http://dx.doi.org/10.1002/flid.4279>
3. F. Romanò and H. C. Kuhlmann (2016). Numerical investigation of the interaction of a finite-size particle with a tangentially moving boundary, *Int. J. Heat Fluid Fl.*, <http://dx.doi.org/10.1016/j.ijheatfluidflow.2016.07.011>
4. F. Romanò, S. Albensoeder and H. C. Kuhlmann. Topology of three-dimensional steady cellular flow in a two-sided anti-parallel lid-driven cavity, *JFM*, **submitted**
5. C. Kuehn, F. Romanò and H. C. Kuhlmann. Tracking particles in flows near invariant manifolds via balance functions, *SIAM*, **submitted**
6. F. Romanò and H. C. Kuhlmann. Particle–free-surface interaction in a shear-driven cavity flow, *Theor. Comp. Fluid Dyn.*, **submitted**
7. H. C. Kuhlmann, F. Romanò, H. Wu and S. Albensoeder. Particle-motion attractors due to particle–boundary interaction in incompressible steady three-dimensional flows, *20th AFMC*, **submitted**
8. F. Romanò, H. C. Kuhlmann, M. Ishimura and I. Ueno. Particle–free-surface interaction in thermocapillary flows. Prediction and observation of limit cycles in axisymmetric flow, **in preparation**
9. F. Romanò, A. Hajisharifi and H. C. Kuhlmann. Topology of three-dimensional steady cellular flow in a partially liquid-filled rotating drum, **in preparation**